Environmental impact of amino acids on the stability of layered double hydroxides after immobilized selenate and iodide

王，梦梦

Environmental impact of amino acids on the stability of layered double hydroxides after immobilized selenate and iodide

By

Wang Mengmeng

A thesis submitted to

Kyushu University

for the degree of Ph.D.

Department of Earth Resources Engineering

Graduate School of Engineering

Kyushu University

September 2021

CONTENTS

Abstract

Selenium-79 (^{79}Se) and iodide-129 (^{129}I) as one of radioactive isotopes of selenium (Se) and iodide (I) with a 3.77×10^5 years and 1.57×10^7 years half-life. In aqueous environments, Se and I species behave as anionic species, which can be immobilized in layered double hydroxides (LDHs). Soil organic matter (SOM) is known to be a risk to affect the stability of minerals in pedosphere where low-level radioactive wastes are buried. If the radioactive wastes are released into soil environment from cementitious materials, the adsorbed radionuclides might be possibly contacted with SOM. However, the releasing behaviors of SeO_4^{2-} and I^- from LDHs are still unclear, but important to evaluate its effectiveness. Five amino acids were selected as the model of SOM to investigate on the environmental impact.

In **Chapter 1**, overviewed the background information of low-level radionuclides, occurrence and characteristics of SOM including its relation with amino acids, characteristics of Se and I anionic species, and their immobilization is overviewed, where LDHs are key matrix for removal of anionic species as well as byproducts in the aging of cement. The reason why five amino acids were selected as simplified models to represent the environmental factors there was also described. Density functional theory (DFT) calculation is an important approach in the present work to simulate the stable configurations of ion-exchanged amino acids in LDHs.

All the methodology in the present work was introduced in **Chapter 2**, including the solution analysis (inductively coupled plasma optical emission spectrometry (ICP-OES), inductively coupled plasma mass spectrometry (ICP-MS), ion chromatography (IC), High-performance liquid chromatography (HPLC)), solid characterization (X-ray diffraction (XRD), X-ray fluorescence (XRF), Scanning electron microscope (SEM), and CHN analysis) and DFT simulation.

In **Chapter 3,** hydrocalumite immobilized iodide (Ca$_2$Al-LDH(I)) was synthesized through co-precipitation. Ca$_2$Al-LDH(I) was very fragile compared with Ca$_2$Al-LDH(SeO$_4$) and Mg$_2$Al-LDH(SeO$_4$), which are discussed in subsequent chapters. It is probably due to a small charge and

hydrophobicity of I^-. Cysteine (H_2Cys) and aspartic acid (H_2Asp) accelerated the release rate of I^- from I-hydrocalumite than other amino acids. H_2Cys caused ion-exchange with I^- on hydrocalumite more preferentially than H_2Asp. The intercalation of Cys^{2-} was evidenced by XRD of the solid residues, which was supported by DFT calculation predicting the interaction force is ascribed to the hydrogen and Ca-O chemical bonds between carboxyl groups in amino acid and metallic hydroxide layers in LDH.

The more stable LDH, hydrotalcite immobilized selenate (Mg_2Al-LDH(SeO_4)) was synthesized to examine the effect of amino acids (**Chapter 4)**, Glycine (HGly), H_2Cys, and H_2Asp, showed intercalation, causing to release SeO_4^{2-}, which tryptophan (HTrp) and phenylalanine (HPhe) did not. Clear differences were verified by solution data as well as XRD, which resulted from several factors including ionic sizes, hydrophilicity, and charge numbers of amino acids. DFT simulation well demonstrated a layer spacing value caused by singly stacked HGly molecules and the layer spacing of the main and shoulder peaks caused by doubly stacked HGly molecules. Specific interaction of Cys^{2-} with Mg^{2+} was also predicted through the thiol group in Cys^{2-}, which explained the experimental results suppressing Mg^{2+} dissolved.

To get closer to a more realistic system, hydrocalumite immobilized SeO_4^{2-} (Ca_2Al-LDH) was prepared and investigated in **Chapter 5**. With increase in the loading amounts of amino acids on Ca_2Al-LDH, release of SeO_4^{2-} increased in the presence of HGly, H_2Asp, and H_2Cys, but not in HPhe and HTrp series. DFT simulation exemplified that Asp^{2-} in the interlayer of Ca_2Al-LDH has several possible configurations, and the stability of SeO_4^{2-} in LDH is more strongly affected by CO_3^{2-} in hydrocalumite, compared with hydrotalcite.

As an analogical model of the realistic matrix that stabilizes selenate, the fly ash blended cement was supplied for the leaching test in the presence of amino acids in **Chapter 6**. During the aging period, anionic exchangers such as hydrocalumite and ettringite were produced in the cement. H_2Asp and H_2Cys enhanced the dissolution of selenate because of ion-exchange on hydrocalumite.

Other anionic pollutant species from fly ash such as arsenate, chromate, borate, and fluoride did not exceed the environmental standard except for selenate, indicating Se oxoanions are difficult species to immobilize.

So one measure was tried to stabilize Se oxoanions by mixing zero-valent iron (ZVI) with the fly ash blended cement in **Chapter 7**. Under the present condition, Se oxoanions were not effectively stabilized probably because ZVI was spent for reduction of coexisting Cr(VI) and As(V) species, which have the higher standard redox potentials. It can be predicted that Se(VI)/Se(IV) oxoanions can be reductively immobilized on ZVI in the absence of competing species.

Finally, the main conclusion of this thesis was summarized in **Chapter 8**. Environmental impact of amino acids on the stability of selenate and iodide in LDHs was investigated in experimental and the DFT approaches. Smaller sized amino acids have more serious risk to unstabilize selenate and iodide. Carbonate is also another environmentally important threatening factor to the stability of selenate. The necessity of engineering measures to improve stability was emphasized.

List of tables

List of figures

Chapter 1 Introduction

1.1 Low-level radioactive wastes

Radioactive wastes is defined as "any material that contains or is contaminated by radionuclides at concentrations or radioactivity levels greater than the exempted quantities established by the competent authorities and for which no use is foreseen" (Sokol and Cooper, 1979). International atomic energy agency (IAEA) proposed the categorization depending on their half-life to classify into exempt waste low low-level waste (shorter than 100 days), low-level waste (shorter than 30 years), intermediate-level waste (longer than 30 years), and high-level waste.

Low-level radioactive waste is nuclear waste that does not fall into the categories of intermediate-level waste, high-level waste, spent nuclear fuel, transuranic waste, or certain byproduct materials such as uranium mill tailings. Every year, society generates 0.4 Mt of radioactive waste, the majority of which is generated by the world's nuclear power plants and fuel cycle support facilities. Low-level radioactive waste is the most common type of radioactive waste, accounting for up to 95% of all radioactive wastes. Low-level radionuclides with low-level radioactivity exist naturally and artificially, which can be introduced into the ecological environment as a result of nuclear energy activities, nuclear research, coal, and earth rare-earth mining, nuclear weapons reprocessing, nuclear power plant accidents, and other ways (Baca and Florkowski, 2000; Cazzola et al., 2004; Todorov and Ilieva, 2006). Low-level radioactivity is associated with those radioactive sources of ionizing radiation that have low activities. The activity may not always represent the total amount of radionuclides but rather their concentration. In other case, the total activity may be enough high, but we can only measure a small portion of material. The most threatening source for environment is nuclear power plant accidents which can release a large amount of low-level radioactive nuclides into atmosphere, soil, and water environments, and finally affect human health. Released radionuclides are mobile in the natural environment, and

they may be taken up by microbes, algae, plankton, plants, or crops and further accumulated through cascaded food chains via soil and water medias and finally pose a significant impact on human health (Ikemoto and Magara, 2011). Radioactive substances can cause damage to the central nervous system, neuroendocrine system, and blood system; cause changes in vascular permeability, leading to bleeding and concurrent infections. Radiation can also damage genetic material, mainly in causing gene mutations and chromosomal aberrations, which can damage one generation or even several generations (Battist, 1979; Yamada, 2012).

Through direct discharge, dry and wet atmospheric deposition, a large number of low-level radionuclides entered the soil environment. Cesium (Cs) and iodine (I) are the most important radionuclides of the radiation exposure and have been intensively studied, but many other radionuclides also were released into environment, such as iodine-129 (^{129}I) and selenium-79 (^{79}Se). Depending on their radioactivity in each accident, ^{129}I and ^{79}Se as low-level radionuclides have been investigated about their mobility, sorption affinities with natural minerals and sorption behavior in cementitious materials (Um and Serne, 2005; Rojo et al., 2018). The researches show ^{79}Se present in the low- and intermediated-level radioactive wastes as the prevail ingredient, especially in the cementitious near field (Johnson et al., 2000; Berner, 2002; Baur and Johnson, 2003; Wersin et al., 2003; Zhang and Reardon, 2003; Bonhoure et al., 2006; Hummel, 2017). Cement has been a common binder to immobilize low-, intermediate-, and high-level radioactive wastes. The cement matrices for incorporation of low-level radioactive wastes, including Portland cement, alkali-activated slag cement, calcium sulfoaluminate cement have been widely utilized due to they are simple to operate, performance stably, low cost, and environmentally friendly. The cement solidification of radioactive wastes uses cement as the main inorganic gel material, based on this, different admixtures such as pozzolanic active mixtures, fly ash, blast furnace slag, and zeolite also can be included in different ratios to mix with water. Utilizing the hydraulic properties of cement and admixtures, the mixed slurry is expected to form a solidified body with certain

strength and durability after a certain curing period. During the curing process, hydration reactions will happen and several hydration products can be formed. The mainly chemical compositions of Portland cement are calcium oxide (CaO), silicon dioxide (SiO_2), aluminium oxide (Al_2O_3), ferric oxide (Fe_2O_3), magnesium oxide (MgO), sulfur trioxide (SO_3) corresponding to the content of 60-65%, 21-24%, 3-8%, 3-8%, 0-2%, and 1-4%, respectively. Thus calcium silicate hydrate (C-S-H), portlandite ($Ca(OH)_2$), hydrocalumite ($3CaO·Al_2O_3·CaSO_4·nH_2O$), and ettringite ($3CaO·Al_2O_3·3CaSO_4·32H_2O$) are mainly hydration products which contribute to the immobilization of radionuclides oxyanions in cement systems (Gougar et al., 1996; Zhang and Reardon, 2003; Aimoz et al., 2012; Rojo et al., 2018).

After immobilized into cement systems, low-level radioactive wastes were produced. The disposal methods suitable for low-level radioactive wastes include trench disposal (bury in the shallow ground without artificial structures), pit disposal (bury in the shallow ground with concrete pits), medium depth disposal (bury at a depth $\geq$ 70 meters), and deep geological disposal (bury in the underground $\geq$ 300 meters) (**Scheme 1.1**). In the normal situation, low-level radioactive wastes are stored in a drum at the geological repository which needs careful management to prevent those wastes from contacting the external environment, like soil and water (Kim et al., 2020). Due to the relatively high mobility in the soil environment of [79]Se and [129]I, they were investigated using chemical reagents ensuring the safety as the low-level radionuclides and radioactive wastes in soil environment.
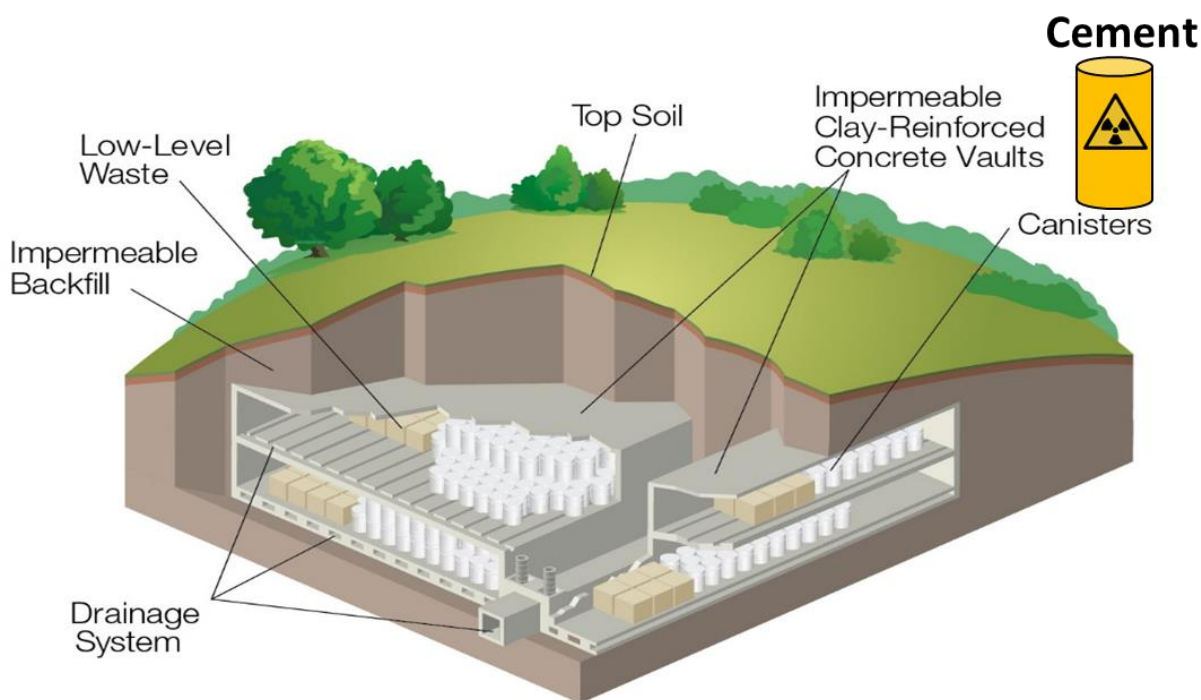
Scheme 1.1 Low-level radioactive waste disposal site (U.S.NRC,2017).

1.2 Soil chemistry

The radionuclides have different behavior in environmental systems, such as adsorption, precipitation in soil environment depending on the complicated soil conditions and their species. Silicon (Si) is one of the most abundant elements in soil which combines with oxygen (O) to be silica (SiO_2) to constitute the framework of soil. Normally, the natural soil pH is in the range of 2.0 to 11.0 (Survey, 1993; Batjes, 1995) which is influenced by the existing acid (H^+, Al^{3+}, Fe^{2+}, Fe^{3+}) and base ions (Ca^{2+}, Mg^{2+}, K^+, Na^+). The zeta potential of SiO_2 nanoparticles in different pH has been investigated as shown in **Fig. 1.1** (Xu et al., 2006). At pH 2-3, the zeta potential of SiO_2 is near zero which indicates silanol (-Si-O-H) groups created equally negative and positive charges on the surface of SiO_2. As the soil pH higher than 4, the zeta potential shows negative values indicating the negative charges increase on the SiO_2 surface. Therefore, under natural soil environment, negative minerals would like to exist. This can contribute to the removal of positively charged radionuclides like Cs^+ and strontium(II) (Sr^{2+}). However, for radionuclides

anions, it is difficult to be adsorbed by natural minerals so that they possess high mobility in soil

environment as shown in **Scheme 1.2**.
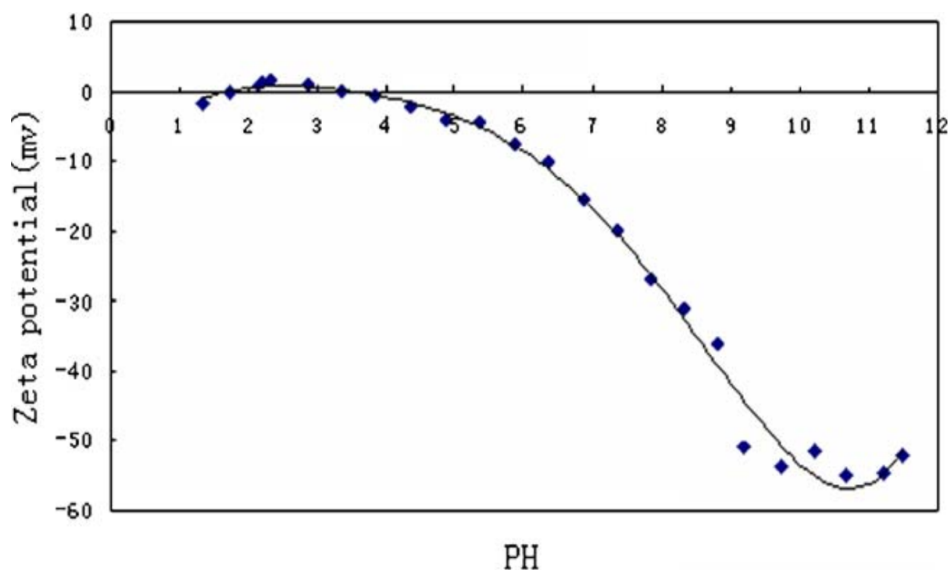
Fig. 1.1 The zeta potential of the SiO_2 nanoparticles at different pH values (Xu et al., 2006).
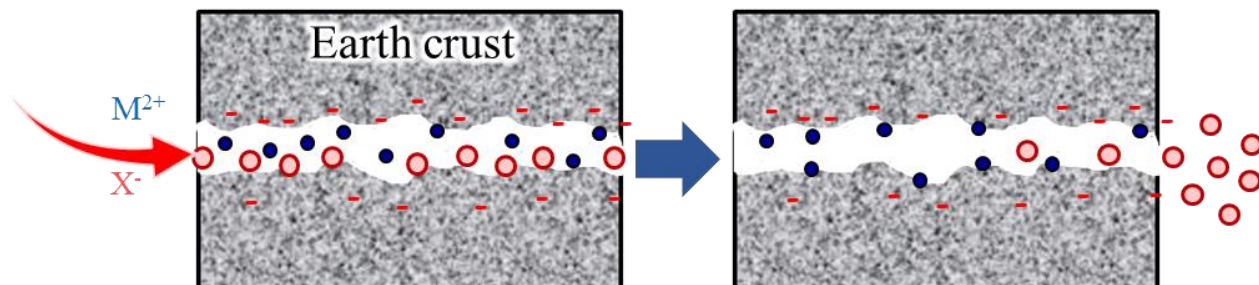
Scheme 1.2 Schematic diagram of the solidification of radioactive anions in the earth crust.

1.2.1 Soil organic matter (SOM)

In the soil environment, pH, redox potential, natural minerals, organic matters and other factors

influence the species of radionuclides, mobility and bioavailability. Soil organic matter (SOM) is

a broad term for all organic compounds in the soil, including all animals and plant residues, both

naturally occurring and introduced, as well as their decomposition and synthesis products. Soil

microbial residues, animal residues and secretions such as earthworms, ants, rodents, insects, plant

residues, and organic matter applied to the soil such as organic fertilizers and soil organic pollutants are the primary sources of SOM.

Soil organic matter is divided into two types: humus and non-humus. Humus is a dark-colored, amorphous, difficult-to-degrade, and complex high-molecular-weight organic matter that is transformed into a series of reactions by the residues of animals and plants under the action of soil microorganisms. Humus contains a variety of functional groups including carboxyl, phenolic hydroxyl, alcoholic hydroxyl, carbonyl and others. The surface of humus is charged, usually negatively charged, due to the dissociation of carboxyl and other groups on the molecule's surface and the protonation of amine groups. Humic acid is an important component of humus, and the surface of the molecule contains a large number of functional groups that bind soil nutrients. The solubility of Huminin decreases due to its strong interaction with inorganic components such as iron-aluminum compounds and clay minerals, and its chemical structure is extremely complex. Non-humic substances are simple byproducts of biological residues decomposition that include organic acids, carbohydrates, fats, resins, waxes, lignin, and other non-nitrogenous organic substances as well as protein-based nitrogen-containing organic compounds. The main nitrogen-containing compound in animal and plant residues is protein, which is the main component of protoplasm and cell nucleus. The elemental composition of protein includes carbon (C), hydrogen (H), oxygen (O), and nitrogen (N), with some also containing sulfur (S) or phosphorus (P). Protein is made up of various amino acids.

Humic acid is a common SOM is which has been confirmed it was highly reactive toward minerals surface, changing surface properties and further influencing the migration of anionic ions in soil (De Cristofaro et al., 2000; Luo et al., 2006; Tian and Chen, 2011). On the other hand, it has complicated structures with many functional groups as shown in **Scheme 1.3**. Therefore, simplified models of SOM have been studied in the behavior of radioactive oxyanions in soil.
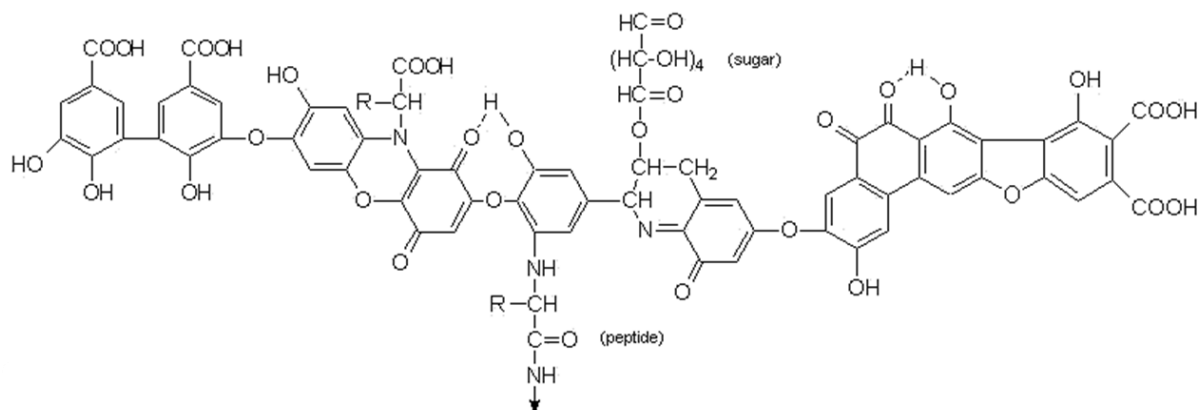
Scheme 1.3 Model structure of humic acid (Stevenson, 1982).

1.2.2 Amino acids

Amino acids are the monomers of proteins. Proteins come from the degradation of plants, microorganisms, and animals, which are large biomolecules in soil environment. The generic formula of amino acids presents as $H_2NCHRCOOH$. From the structure, we can see the center of α carbon (C) atom connects to the amino group ($-NH_2$) by a covalent bond, to the carboxyl group (-COOH), to the hydrogen (H) atom as well as to a variable side chain group (R group) in different directions. There are 20 kinds of natural amino acids and can be classified into hydrophobic, hydrophilic, and amphipathic amino acids according to different side chain groups. Hydrophobic amino acid is an amino acid assembly with high hydrophobicity in the side chain, like aliphatic or aromatic groups. Hydrophobicity refers to the tendency of non-polar molecules to leave the water phase and enter non-polar phase. Hydrophobic interaction, hydrogen bonding, electrostatic interaction, and van der Waals interaction are all non-bonding interactions. Hydrophilic amino acids prefer to be surrounded by water, so the side chains can participate in hydrogen bond formation with another polar group by donating or accepting a proton. Some amino acids are sometimes called amphipathic due to their ability to have both polar and nonpolar character. Also, some amino acids are chiral molecules. Except for glycine, the α C atoms at the center of other

amino acids are the asymmetric center of molecule. These α C atoms connect four different functional groups to make the amino acids be chiral molecules which possess optical activity. The chiral amino acids who have the property of deflecting the polarization plane of the passing light to the left are called levorotatory (L)-amino acids. In the same way, those chiral amino acids who can deflect the polarization plane of the passing light to the right are called dextrorotatory (D)-amino acids. For natural amino acids, except glycine, other amino acids adopt the levorotatory configuration.

The properties of amino acids such as acid-base, double electricity, and polar and non-polar significantly affect the behavior of amino acids in radionuclides behavior. The acidic -COOH groups of amino acids molecules can dissociate into $-COO^-$ and H^+, and the basic $-NH_2$ groups can accept protons become amine ($-NH_3^+$) groups. Therefore, amino acids are also amphoteric substances. The charged condition of amino acids molecules depends on the relationship of acid dissociation constants (pK_a) of each functional group and solution pH. pK_a is a strength quantitative measure of acid and can reveal the deprotonation/protonation state of a molecule in a specific solvent. When the solution pH is higher than pK_a value, deprotonation will happen. In contrast, the protonation would like to happen when the pK_a value is higher than solution pH. The basic information of amino acids like pK_a values, are shown in **Table 1.2**. Five amino acids selected in this thesis were shown in **Table 1.1**.

Table 1.1 Selected five types of amino acids in the present work.
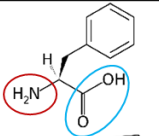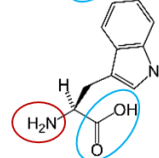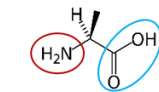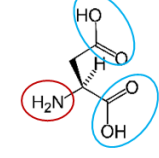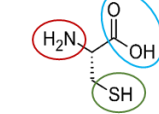
Amino acid	Molecular structure	$pK_{a(-COOH)}$	$pK_{a(-NH3)}$	$pK_{a(side\ chain)}$
L-phenylalanine (HPhe)		1.83	9.13	-
L-tryptophan (HTrp)		2.83	9.39	-
Glycine (HGly)		2.34	9.60	-
L-aspartic acid (H_2Asp)		1.88	9.60	3.65
L-cysteine (H_2Cys)		1.96	10.28	8.18

Table 1.2 Information of 20 types of amino acids.

Type	Amino acids	Abbreviation	Molecular formula	pK_a (-COOH)	pK_a (-NH$_3^+$)	pK_a (side chain)
Hydrophobic	Alanine	HAla	$C_3H_7NO_2$	2.34	9.69	
	Valine	HVal	$C_5H_{11}NO_2$	2.32	9.62	
	Leucine	HLeu	$C_6H_{13}NO_2$	2.36	9.68	
	Isoleucine	HIle	$C_6H_{13}NO_2$	2.36	9.68	
	Proline	HPro	$C_5H_9NO_2$	1.99	10.6	
	Phenylalanine	HPhe	$C_9H_{11}NO_2$	1.83	9.13	
Hydrophilic	Aspartic acid	H$_2$Asp	$C_4H_7NO_4$	2.09	9.82	3.86
	Glutamic acid	H$_2$Glu	$C_5H_9NO_4$	2.19	9.67	4.25
	Glycine	HGly	$C_2H_5NO_2$	2.34	9.60	
	Serine	HSer	$C_3H_7NO_3$	2.21	9.15	
	Threonine	HThr	$C_4H_9NO_3$	2.63	10.43	
	Cysteine	H$_2$Cys	$C_3H_7NO_2S$	1.96	10.28	8.18
	Asparagine	HAsn	$C_4H_8N_2O_3$	2.02	8.8	
	Glutamine	HGln	$C_5H_{10}N_2O_3$	2.17	9.13	
	Arginine	H$_2$Arg	$C_6H_{14}N_4O_2$	2.17	9.04	12.48
	Histidine	H$_2$His	$C_6H_9N_3O_2$	1.82	9.17	6.00
Amphipathic	Methionine	HMet	C5H11NO2S	2.28	9.21	
	Tyrosine	H$_2$Tyr	$C_9H_{11}NO_3$	2.2	9.11	10.07
	Tryptophan	HTrp	$C_{11}H_{12}N_2O_2$	2.38	9.39	
	Lysine	H$_2$Lys	$C_6H_{14}N_2O_2$	2.18	8.95	10.53

(Reference D.R. Lide, Handbook of Chemistry and Physics, 72nd Edition, CRC Press, Boca Raton, FL, 1991)

1.3 Anionic radioactive species

1.3.1 Selenium

Selenium (Se) is ranked 67th among the most abundant elements in the Earth's crust and the 145th toxic element among the hazardous substances by Agency of toxic substances and Disease Registry as well as No. 125 in the US Environmental Protection Agency's priority pollutants list (EPAToxic; ATSDR, 2007; Naik and Dubey, 2017). Se shares similar chemistry with sulfur (S), tellurium (Te), and polonium (Po). Like sulfur (S), Se possesses four possible oxidation states (**Fig. 1.3**). Under high redox conditions, Se exists with Se(VI) dominated in the form of selenate (SeO_4^{2-}). Under the lower redox conditions, Se(IV) exists in the forms of selenite (SeO_3^{2-}) and biselenite ($HSeO_3^-$). In the strongly redox potential conditions, Se(VI) and Se(IV) can reduced to elemental selenium (Se(0)) or selenide (Se^{2-}). In the soil environment, Se(VI), Se(IV), and Se(0) are the dominant speciation that is strongly dependent on the soil redox potential. SeO_3^{2-} is much more reactive and by forming inner-sphere complexes on minerals, such as Fe/Al oxyhydroxides, while SeO_4^{2-} adsorb weakly at the minerals surface through electrostatic interactions creating the outer-sphere complexes (Manceau and Charlet, 1994; Peak, 2006; Eich-Greatorex et al., 2010). SeO_3^{2-} has asymmetric hydration shells (as shown in **Scheme 1.4**) due to the presence of free electron pair in the fourth tetrahedron vortex (Eklund and Persson, 2014). Therefore, in the soil environment, SeO_4^{2-} has the higher mobility than SeO_3^{2-}. Se isotopes include ^{72}Se, ^{73}Se, ^{75}Se, ^{79}Se, and others with different half-life, while most of them are short-lived, and the physical half-life is in the range of 17 seconds (^{86}Se) to 127 days (^{75}Se). ^{79}Se is the only long-lived β-emitting radioactive isotope of Se with a 3.77×10^5 years half-life, which is low-yield fission and activation products related with the irradiated reactor fuel and construct fission reactors materials (Shaw and Ashworth, 2006). ^{79}Se is formed from the fission of ^{235}U and the neutron activation of ^{78}Se. In the earth's crust, naturally, Se is in the concentration between 0.05 and 0.09 mg/kg. If ^{79}Se leaked into

the environment in a small amount, it is expected to behave like the naturally Se to exist as a trace element in the ecosystem. However, Se has a narrow gap between deficiency and toxicity to living organism, so if the leakage accident of nuclear power plants or radioactive waste repositories happened, a large amount of ^{79}Se is possibly released into ecological environment and pose significant threat to human health in the long term run (Supriatin et al., 2015). Generally, consumption of Se-rich food will pose a health risk to human bodies, however, the radioactivity can cause serious health problems, like chromosome aberration and cancers (Shahid et al., 2018). Therefore, the mobility of SeO_4^{2-} in soil makes the removal of ^{79}Se been an important subject of environmental research (Chen et al., 1999).
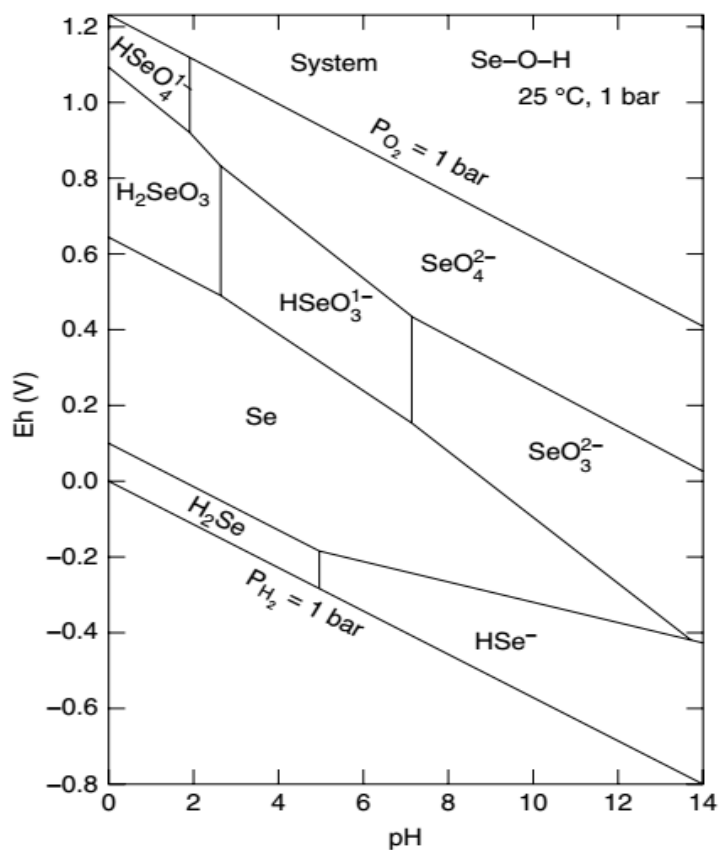
Fig. 1.2 *E*h/pH stability diagram for selenium in aqueous systems (Shaw and Ashworth, 2006).
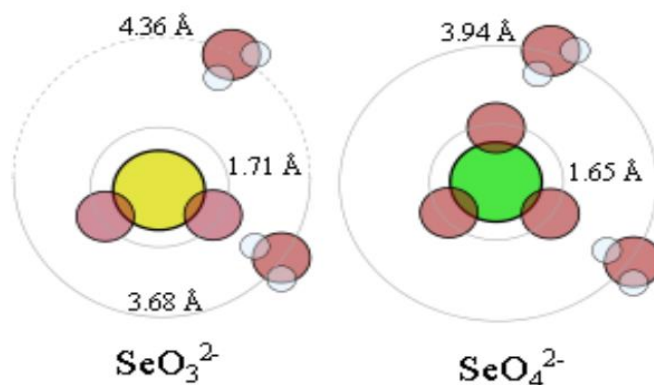
Scheme 1.4 Asymmetric structure of selenite and symmetric structure of selenate (Eklund and Persson, 2014).

1.3.2 Iodine

Iodine (I) was discovered by French chemist Bernard Courtois in 1811 (Fuge and Johnson, 1986). In the periodic stable, I as halogens is the heaviest stable member of group 17 with an aromatic weight of 126.9. In Earth's crust, the content of I is between 0.25 mg/kg and 0.3 mg/kg which as an ultra-trace element (Fuge, 1988; Muramatsu and Wedepohl, 1998). In natural aqueous environment, the predominant states of I are iodide (I^-) and iodate (IO_3^-) (as shown in **Fig. 1.3 and Scheme 1.5**). In the oxidizing environment, I occurs as the reactive anion IO_3^-. Under the reducing conditions, I usually present as the mobile anion I^-. Radioactive I comes from nuclear power plant and reactors emission and ash from atmospheric nuclear tests. Its isotopes with half-life more than 10 min start from ^{123}I to ^{135}I continuously, while only ^{129}I possesses long half-life of 1.57×10^7 years. ^{129}I is one of the important nuclear fission product with a high-abundance fission yield of 0.9% from ^{235}U and 1.6% ^{239}Pu (Hu and Moran, 2011). The mainly forms of I^- and IO_3^- make ^{129}I possesses high mobility in the environment and the long half-life ^{129}I has been identified as the important concern in the studies of radionuclides on environment pollution and ecosystems. The uncontrolled release of radioactive I can pose a direct threat to human health due to its

accumulation in the human thyroid which mainly manifested as damage to thyroid function, changes in the histopathology of the glands, and finally induce thyroid tumors (VanMiddlesworth et al., 2000).
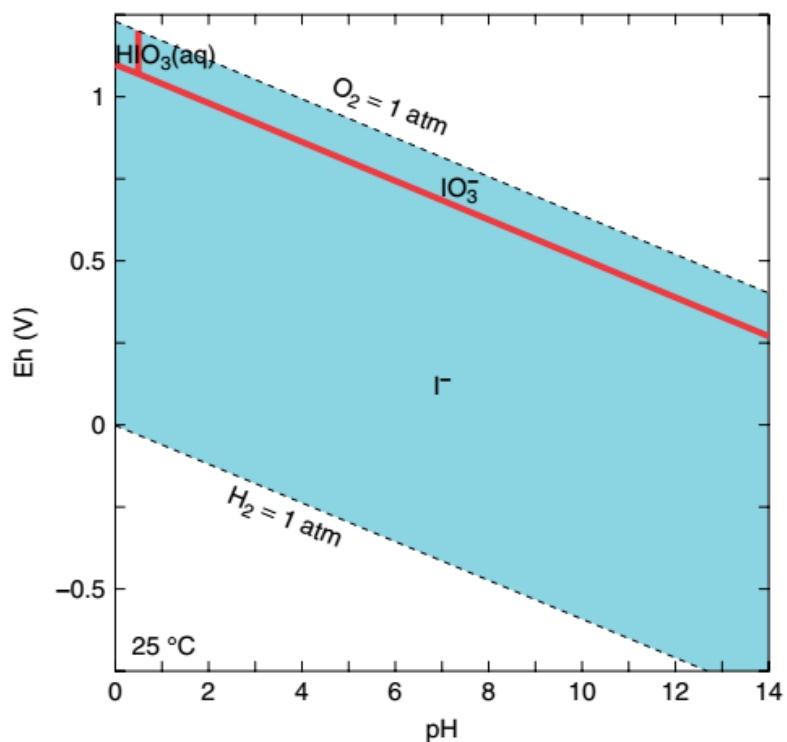
Fig. 1.3 *E*h/pH diagram for iodine, 25 °C (Hu and Moran, 2011).
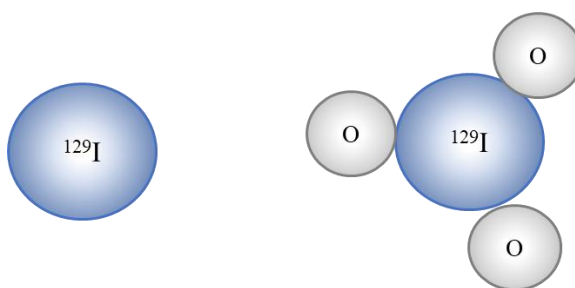
Scheme 1.5 Atomic structure of iodide and iodate.

1.4 Layered double hydroxides

The cement systems produce different hydration products, among them, one material named layered double hydroxides (LDHs) which are positively charged play an important role in immobilizing ^{79}Se and ^{129}I anionic species during cement hydration process.

1.4.1 Structures

Layered double hydroxides (LDHs) are a class of ionic lamellar compounds based on $M(OH)_6$ octahedral units sharing edges to build $M(OH)_2$ brucite-like layers with interlayers region. The octahedral units contain divalent and trivalent metallic cations, and the vertexes contain hydroxide ions to form infinite 2D sheets. The whole structure of LDHs is constituted through the stacking of such sheets as shown in **Scheme 1.6**. The basal layers of LDHs are positively charged, and the generic formula of LDHs can be displayed as $[M_{1-x}^{2+}M_x^{3+}(OH)_2][A^{n-}]_{x/n} \cdot nH_2O$, where A^{n-} represents inorganic or organic anions to balance the positive charges. The M^{2+} and M^{3+} mainly belong to the third and fourth periods of the periodic tables where Mg, Mn, Fe, Co, Ni, Cu, Zn with the ionic radius 0.65-0.80 Å contribute to M^{2+} and Al, Mn, Fe, Co, Ni, Cr, Ga with the ionic radius 0.50-0.69 Å contribute to M^{3+}. The possible anions can be (1) oxo-anions, such as carbonate (CO_3^{2-}), nitrate (NO_3^-), sulphate (SO_4^{2-}), bromate (BrO_3^-), etc; (2) halides, such as fluoride (F^-), chloride (Cl^-), iodide (I^-) and etc; (3) organic anions, such as carboxylates (RCO_2^-), alkyl sulphates (RSO_4^-), etc. LDHs interlayer occupied by anions and water molecules, but in most cases, between interlayer anions and the basal layers only weak bonding exist which gives them ion-exchange ability. So their variable metallic cations and layers charge density, and very reactive interlayer spaces, as well as the water swelling and colloidal properties, make LDHs a mineral family. LDHs also can be recognized as anionic clays which have been widely explored to remove radioactive oxyanions. Hydrotalcite usually refers to MgAl-LDH (Mg^{2+}/Al^{3+} = 2, 3, 4) where chloride (Cl^-),

carbonate (CO_3^{2-}), and nitrate (NO_3^-) as anions (Grover et al., 2009). Hydrocalumite belongs to CaAl layered double hydroxides which is normally found in cement pastes and also can be easily synthesized (Kalinichev and Kirkpatrick, 2002; Brown and Bothe Jr, 2004; Renaudin et al., 2004; Wu et al., 2010). The octahedral structure of hydrocalumite group is different from hydrotalcite. That is because the radius of Ca^{2+} is high, the octahedral coordination is changed through opening one side of the octahedron caused one additional coordination with one interlayer water molecule.
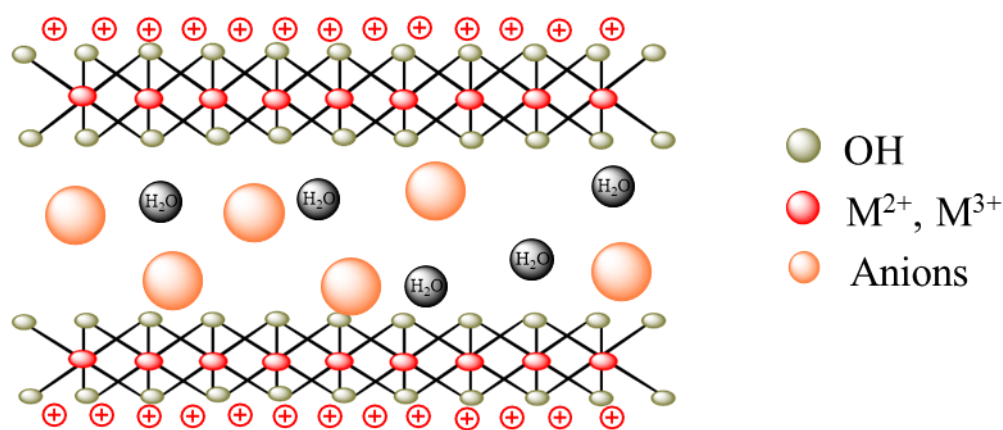
Scheme 1.6 Schematic diagram of layered double hydroxides (LDHs).

1.4.2 Synthetic methods

There are several methods to synthesize LDHs, the most widely utilized are co-precipitation, urea hydrolysis, and ion-exchange. Co-precipitation method is the most utilized one based on the condensation of hexa-aquo complexes in aqueous to build the LDHs structures. The synthesis steps usually follow the next steps. Firstly, the specific proportions of divalent and trivalent metals salts are mixed, and then totally dissolved the mixed solution should slowly dropwise into a reactor containing water. Meanwhile, the second solution which provides anions is added into the reactor slowly and NaOH is used to maintain the necessary formation pH conditions of target LDHs. Secondly, the mixture suspension gel should be aged for several hours under room temperature or high temperatures to get well crystallized LDHs phases.

Urea hydrolysis method is frequently used for synthesis of highly crystalline LDHs where CO_3^{2-} be the interlayer anion. The divalent and trivalent metal salts in specific M^{2+}/M^{3+} ratios as well as urea are dissolved in water, and then this mixed solution is putted into Teflon inner vessels, each in a stainless-steel jacket. These vessels are placed in a furnace or an oven to keep heating at the target temperatures for several hours. After cooling down to room temperature, products from vessels should be washed and dried.

Ion-exchange method is based on the different affinity with host layers of LDHs and is useful when the co-precipitation method cannot be used. In this method, the original LDHs should be synthesized using other methods and then the guest cations or anions are exchanged with the original LDHs to produce specific LDHs which contain the guest ions.

1.4.3 Applications

LDHs were explored for several pollutants and also the mechanisms were clear. Anion exchange between host anions in the interlayer region of LDHs and pollutant anions in aqueous solution is the primary adsorption mechanism, generally coupled with chemical bond formation. According to this property of LDHs, a large number of researches have been studied. Ma Bin et al. (2017a) synthesized two types CaAl-LDH, CaAl-SO$_4$-LDH, and CaAl-Cl-LDH, to adsorb SeO_3^{2-}. Finally, the inner-sphere complexe CaAl-SeO$_3$-LDH was produced by exchange with SO_4^{2-} and Cl$^-$ to form hydrogen bonds, while it is found thermodynamics unstable. Under the same experimental conditions, MgAl-LDH and ZnAl-LDH were synthesized to remove SeO_3^{2-} and SeO_4^{2-}. The adsorption results showed the adsorption trends of them on LDHs were similar and affinity of SeO_3^{2-} on ZnAl-LDH was higher than on MgAl-LDH (You et al., 2001). ZnAl-NO$_3$-LDH was developed to remove As(V) from pH 12 wastewater, the results showed As(V) has a large binding energy with LDH sheets so that the removal efficiency almost reached 100%, but the pH was decreased to 7.4 (Meng et al., 2016). Lazaridis et al. (2004) prepared MgAl-CO$_3$-LDH to remove

Cr(VI) mainly through anion exchange between $HCrO_4^-$, CrO_4^{2-} and CO_3^{2-}. Due to the excellent intercalation property of hydrotalcite and the strong covalent bonds of sulfides with soft heavy metals, the sulfide-based material MgAl-MoS$_4$-LDH was synthesized to remove heavy metals, such as Co^{2+}, Ni^{2+}, Cu^{2+}, Zn^{2+}, Ag^+, Pb^{2+}, and Hg^{2+}. The sorption results showed MgAl-MoS$_4$-LDH decreased the concentrations of Cu^{2+}, Pb^{2+}, Hg^{2+}, Ag^+ from ppm levels to lower than 1 ppb trace levels mainly ascribed to the chemisorption of forming heavy metal-S bonds (Ma et al., 2016). Behbahani at al. (2021) proposed ionic metal polysulfide FeMoS$_4$ loaded on the surface of Fe$_3$O$_4$ into the interlayer and surface of MgAl-LDH to remove Pb(II), Cd(II), and Cu(II). The formation of coordination complexes in Fe$_3$O$_4$/FeMoS$_4$/MgAl-LDH interlayer and electrostatic attraction allowed Fe$_3$O$_4$/FeMoS$_4$/MgAl-LDH can be one of the promising materials for wastewater heavy metals remediation.

Considering hydrocalumite, the dissolution-reprecipitation (DR) also is an important mechanism for LHDs application. The DR mechanism can apply to cation removal. Liu et al. (2011)utilized the hydrocalumite to remove zinc (Zn) from ZnSO$_4$, Zn(NO$_3$)$_2$, and ZnCl$_2$ solutions. Combing with simulation results, hydrocalumite happened dissolution to release Ca^{2+}, $Al(OH)_4^-$ and Cl^- which provided for Zn to form new ZnAl-Cl-LDH, ZnAl-SO$_4$-LDH phases. The performance of LDHs also depends on the concentration of pollutants. Takaki, et al. (2016) explored two types of hydrocalumite on the removal of arsenate. Under low concentrations, intercalation of arsenate into high crystallinity hydrocalumite contributed to its great adsorption ability. When arsenate was in high concentrations, the fragile property of Mg-doped hydrocalumite enhanced dissolution-reprecipitation (DR) to increase the great adsorption values.

And also the investigation of LDHs to remove SeO_4^{2-} and I^- from environment haven been conducted as shown in **Table 1.2**. For SeO_4^{2-}, the mainly involved mechanisms are ion-exchanging, reconstruction, and reduction. SeO_4^{2-} has high charge density and large affinity with host layers of LDHs. Hydrocalumite was explored mainly comes from the immobilization of Se during the

process of cement hydration for hazardous wastes disposal. Hydrotalcite and other LDHs were investigated based on Lab scale and soil or wastewater pollutions.

Table 1. 3 Application of LDHs for removal of selenium and iodine.

LDHs material	Interlayer anion	Adsorbate	pH	Adsorption mechanism	References
CaAl-LDH	Cl^-	SeO_4^{2-}	8	Ion-exchange	(Wu et al., 2010)
MgAl-LDH	CO_3^{2-}	SeO_4^{2-}	5	Ion-exchange	(Chubar, 2014)
MgAl-LDH/C-dot	NO_3^-	SeO_4^{2-}	5.95	Ion-exchange	(Koilraj et al., 2017)
ZnFe-LDH	SO_4^{2-}	SeO_4^{2-}	2.3-14	Ion-exchange	(Hongo et al., 2008)
MgAl-LDH	CO_3^{2-}	SeO_4^{2-}	2.3-14	Ion-exchange	(Hongo et al., 2008)
MgAl-LDH	CO_3^{2-}	SeO_4^{2-}	3-11	Ion-exchange	(Li et al., 2018)
NZVI/LDH	/	SeO_4^{2-}	4.8-7.2	Reduction	(Hu et al., 2017b)
FeFe-LDH	Cl^-	SeO_4^{2-}	8	Reduction	(Schellenger et al., 2021)
MgAl-LDH	MoS_4	SeO_4^{2-}	/	Ion-exchange; precipitation	(Ma et al., 2017b)
MgAl-LDH	/	SeO_4^{2-}		Memory effect(reconstruction)	(Constantino et al., 2017)
CaAl-LDH	Cl^-	SeO_4^{2-}	11.58; 12.23	Ion exchange	(Grangeon et al., 2019)
CaAl-LDH	SO_4^{2-}	I^-	/	Ion exchange	(Aimoz et al., 2012)
ZnAl-LDH	CO_3^{2-}	I^-	/	Memory effect(reconstruction)	(Theiss et al., 2012)
MgAl-LDH	/	I^-	/	Reconstruction	(Theiss et al., 2017)
MgAl-LDH	/	I^-	/	Coprecipitation	(Iglesias et al., 2016)
CaMgAl-LDH	$C_6H_5COO^-$	I^-	/	Ion-exchange	(Iglesias et al., 2016)
CaAl-LDH	/	I^-	/	Coprecipitation	(Nedyalkova et al., 2020)

1.4.4 Problems

The radioactive waste disposal programme requires not only geologists but also physicist, biologists, chemists, media experts and lawyers, etc (Alexander et al., 2015). It is obviously that in any geological environment, the uncertainty of natural environment conditions and processes is probably related to the flow of groundwater, the contents of environmental factors and low-level radionuclides transport in the waste repositories (Miller et al., 2000). However, the activities of the geological environment, like earthquake, and the durability of cement systems both should be considered in the investigation of long-term stability of radioactive wastes.

LDHs as the important adsorbent components in radionuclides not only is one of the cementitious materials but also widely explored for environmentally friendly adsorbents, their properties seem sensitive to the changing of environment. LDHs are strongly influenced by the pH of environment depending on the types of LDHs and target pollutants. They as one of the positively charged materials, when the solution pH is higher than the zeta potential, the surface of LDHs will be negatively charged, in contrast, when pH is lower than the zeta potential, the charge of surface will be positive. However, the very low or high pH should be avoided which might destroy the structures of LDHs or induce a competitive relationship of OH^- with target anions (Goh et al., 2008). LiAl-LDH(Cl) has been reported the sensitive pH range was 4-7 when it was used to adsorb As(V) while the adsorption of As(V) onto MgAl-LDH was sensitive to pH 2-11 in a wide range (Yang et al., 2005; Liu et al., 2006). MgAl-LDH was synthesized to adsorb sodium dodecyl benzene sulfonate (SDBS), the adsorption amount was decreased as the temperature increased from 298 K to 313 K where higher temperature resulted in less negative values of electrokinetic potentials. While as the pH changed from 7.0 to 9.0, the adsorption values also increased. That is because higher pH provided more hydroxyl anions made micelles less stable, and the adsorption process on MgAl-LDH continues until reached saturation (dos Reis et al., 2004). The chemical stability of SeO_4-hydrocalumite also was investigated in water with different initial solution pH.

Very small leaching concentrations around 0.3-0.4 % of SeO_4^{2-} under pH 4, 7 and 10 were found, and 97.6-99.2% selenate was still stabilized in Cl-hydrocalumite even under initial pH 13.0. That is because hydrocalumite has a high neutralization capacity to adjust solution pH to maintain the hydrocalumite phases. Under lower pH, the framework $Ca(OH)_2$ is partially dissolved leading initial pH increased to 11.0, and under high pH 13.0, the framework $Al(OH)_3$ is partially dissolved to anti-alkaline leading pH decreased to 11.6 to prevent SeO_4^{2-} leaching out (Wu et al., 2010).

The ion-exchanging ability of LDHs makes it perform well in the removal of oxyanions, whereas this property makes more competitive anions to affect the target pollutants adsorption. The anions which possess higher valence generally have higher affinity with host layers of LDHs than the monovalent anions in the adsorption of oxyanions. This also means competitive anions have an interfering effect on the adsorption ability of LDHs. Due to different charge densities, the divalent anions of SeO_3^{2-} and SO_4^{2-} performed a profound interfering effect to PO_4^{3-} adsorption using LDHs than monovalent anions Cl^- and NO_3^- (Das et al., 2006). The behavior of Se(IV) on MgAl-LDH was dependent on the type of co-existing anions. In the adsorption systems, SeO_3^{2-} will be desorbed completely from MgAl-LDH if CO_3^{2-} exists (You et al., 2001). Not only inorganic ions were studied but also SOM was considered for the real contaminated soils or waters. Fang et al. (2015) found the prevailing negative charge property of humic and fulvic acids make it play an enhancement role on the adsorption of Ni(II) by calcined MgAl-LDH. Contrarily, when LDHs were used for the removal of CrO_4^{2-}, SeO_4^{2-} and AsO_4^{2-}, their adsorption amount could be decreased by negatively charged organic acids (Hu et al., 2017a). Therefore, the complicated environmental factors in cement systems or natural environment might threaten the stability of LDHs after incorporated pollutants. However, only very few reports and unclear mechanisms have been explored the environmental effects of SOM on the stability of LDHs after immobilized oxyanions, especially the low molecular weight SOM.

1.5 DFT simulation

For the complex anions intercalation LDH system, it is still difficult to confirm the arrangement of the interlayer anions. The arrangement of water molecules in the interlayer structure is not known from the experimental results. Furthermore, there are still considerable difficulties in accurately exploring the microstructure of LDHs from an experimental point of view. At the same time, it is difficult to explore the essence of supramolecular interactions between metal ions and hydroxyl groups in LDHs laminates, between host laminates and guest anions as well as water molecules.

In recent years, theoretical simulation calculation has been developed as an effective research method in the study of the microstructure, mechanics, and thermal properties of LDHs materials. Among them, computer simulation research can be divided into two categories: quantum mechanics (QM) and molecular mechanics (MM) methods according to the difference in simulation scale, theoretical basis, and research properties. It is considered to be the third type of scientific research in this century besides theoretical analysis and experimental observation, called "computer experiments". Density functional theory (DFT) takes the electron density instead of the wave function as the basic variable, and describes the electronic system by solving the electron density differential equation (Kohn-Sham equation), which is a QM method for studying the electronic structure of multi-electron systems. DFT is used to study the coordination between metal ions and hydroxyl groups in LDHs material laminates, the microstructure of simple anion intercalation, ion exchange performance, reaction mechanism, etc (Greenwell et al., 2003a; Wei et al., 2008).

Molecular dynamics simulation (MD) is one MM method which ignores the movement of electrons to calculates various properties of molecules based on the force field of molecules and interaction potential between atoms. This method has been widely used in simulating the molecular arrangement and orientation of amino acids between layers of LDHs, DNA and proteins

(Aicken et al., 1997; Newman et al., 1998; Greenwell et al., 2003b; Boulet et al., 2006; Li et al., 2006; Yan et al., 2008).

According to the electron's density, it has been recognized that the electronic structure govers the properties of adsorbent materials. The electronic structure theory has been developed and combined with the improved software making accurate materials simulations almost become routine. *Ab* initio simulation is an integral tool for the investigation of materials, in order to support experimental data and explain experimental results, as well as guide the experimental design. This application origins from the Thomas-Fermi uniform electron gas model (Fermi, 1927; Thomas, 1927), based on Hohenberg-Kohn theorem (Hohenberg and Kohn, 1964). But the build of Kohn-Sham equations make DFT get widely application. In 1965, Kohn and Sham (Kohn and Sham, 1965) proposed a scheme to get the ground state density and solve the energy from the ground state density where a hypothetical non-interacting multi-electron system with the same electron density as the interacting multi-electron system is introduced, and all the complex interactions are placed in the exchange-related action terms, and the kinetic energy term can be carried out by the kinetic energy of the non-interacting system description. Through the calculation of this non-interacting system, the electron density and energy of interacting system.

Kohn-Sham equation converts the multi-electron system ground state problem formally into an effective single-electron problem, but the exchange-correlation energy (the repulsion between electrons of the same spin) and exchange-correlation potential (the correlation between spintronics) should be well done before this equation. The eneral approximation for exchange and correlation is generalized-gradient approximations (GGAs) including the PW91 and PBE (Becke, 1988; Perdew et al., 1996). GGA has greatly improved the calculation accuracy of the exchange-related energy of atoms, and has been widely used in the field of chemistry. At present, a large number of quantum chemistry and molecular simulation software based on density functional theory have been developed, such as Gaussian, Cambridge Serial Total Energy Package (Castep), and Vienna

Ab-inito Simulation Package (VASP), etc. The present work was based on VASP which is a software package for ab initio simulation using plane-wave pseudopotential method.

1.6 Objectives

Layered double hydroxides (LDHs) have been explored for their adsorption capacities and mechanisms in the application of removing anionic species. SOM has also been shown to have effects on minerals that possess the ability to remove anionic pollutants. So the stability of low-level radionuclides of ^{79}Se and ^{129}I after immobilized in LDHs attracted our attention. If radionuclides from radioactive wastes repositories are released into an environment where many SOM abundant, the products which adsorbed ^{79}Se and ^{129}I are possible to contact with them. Depending on the properties of SOM, they might have some influences on the migration of anionic species of ^{79}Se and ^{129}I by affecting the stability of LDHs. In order to investigate this potential problem, we selected five amino acids which have simple functional groups but with different physical and chemical properties to be the simplified model of SOM. MgAl-LDH, the most common hydrotalcite, and hydrocalumite (CaAl-LDH), the special LDH were focused as the adsorbent for Se and I to explore their stability in the presence of amino acids. Furthermore, the influenced mechanisms of amino acids were explored by combing with DFT simulation. Six chapters are included in this thesis.

Background information of radionuclides producing, soil environment including amino acids are presented in **Chapter 1**. After that, the low-level radionuclides and the application of LDHs as well as existing problems of them on pollutants removal are introduced. Finally, the DFT simulation in LDHs was elaborated.

Chapter 2, summarized the solution analysis, solid characterizations, and DFT simulation methods.

Chapter 3 explored the releasing behavior of iodide (I^-) from Ca_2Al-LDH in the presence of amino acids. The most reactive amino acids which affected the I^- releasing speed were investigated.

Chapter 4 explored the releasing behavior of selenate (SeO_4^{2-}) after it adsorbed into Mg_2Al-LDH in the presence of amino acids. The chemical bonds and possible configurations of amino acids were studied using glycine (HGly) and aspartic acid (H_2Asp) as the model of amino acids in DFT calculation.

Chapter 5 uses Ca_2Al-LDH to immobilize SeO_4^{2-} and after that the effects of amino acids on it were explored combing with DFT simulation. In this chapter, H_2Asp and cysteine (H_2Cys) were selected as the model of amino acids to support our experimental results and mechanisms.

Based on the above results in our model experiments, **Chapter 6** was constructed using the real fly ash cement blocks after added Ca additives to check the anionic species leaching behavior in the presence of selected amino acids. The effect of pH, the leaching behavior of anionic species with amino acids were discussed. Furthermore, **Chapter 7** investigated the effects of ZVI on the leaching behavior of anionic species during the cement hydration process.

The conclusions of this thesis are summarized and some recommendations are made for future research in **Chapter 8**.

References

Adeleke, R., Nwangburuka, C., Oboirien, B., 2017. Origins, roles and fate of organic acids in soils: A review. S. Afr. J. Bot. 108, 393-406.

Aicken, A.M., Bell, I.S., Coveney, P.V., Jones, W., 1997. Simulation of layered double hydroxide intercalates. Adv. Mater. 9, 496-500.

Aimoz, L., Wieland, E., Taviot-Guého, C., Dähn, R., Vespa, M., Churakov, S.V., 2012. Structural insight into iodide uptake by AFm phases. Environ. Sci. Technol. 46, 3874-3881.

Alexander, W.R., Reijonen, H.M., McKinley, I.G., 2015. Natural analogues: studies of geological processes relevant to radioactive waste disposal in deep geological repositories. Swiss J. of Geosci. 108, 75-100.

Atsdr, U., 2007. CERCLA priority list of hazardous substances. http://www. atsdr. cdc. gov/cercla/07list. html.

Baca, T.E., Florkowski, T.eds., 2000. The environmental challenges of nuclear disarmament (Vol.29). Springer Science & Business Media.

Banfield, J.F., Barker, W.W., Welch, S.A., Taunton, A., 1999. Biological impact on mineral dissolution: application of the lichen model to understanding mineral weathering in the rhizosphere. Proc. Natl. Acad. Sci. 96, 3404-3411.

Batjes, N., 1995. A global data set of soil pH properties. International Soil Reference and Information Centre.

Battist, L., 1979. Population Dose and Health Impact of the Accident at the Three Mile Island Nuclear Station: Preliminary Estimates Prepared by the Ad Hoc Interagency Dose Assessment Group. US Nuclear Regulatory Commission.

Baur, I., Johnson, C.A., 2003. Sorption of selenite and selenate to cement minerals. Environ. Sci. Technol. 37, 3442-3447.

Becke, A.D., 1988. Density-functional exchange-energy approximation with correct asymptotic behavior. Phys Rev A 38, 3098.

Behbahani, E.S., Dashtian, K., Ghaedi, M., 2021. Fe_3O_4-$FeMoS_4$: Promise magnetite LDH-based adsorbent for simultaneous removal of Pb (II), Cd (II), and Cu (II) heavy metal ions. J. Hazard. Mater. 410, 124560.

Berner, U., 2002. Project Opalinus Clay-Radionuclide concentration limits in the near-field of a repository for spent fuel and vitrified high-level waste. Paul Scherrer Institute PSI.

Bonhoure, I., Baur, I., Wieland, E., Johnson, C.A., Scheidegger, A.M., 2006. Uptake of Se (IV/VI) oxyanions by hardened cement paste and cement minerals: An X-ray absorption spectroscopy study. Cem. Concr. Res. 36, 91-98.

Boulet, P., Greenwell, H., Stackhouse, S., Coveney, P., 2006. Recent advances in understanding the structure and reactivity of clays using electronic structure calculations. Journal of Molecular Structure: THEOCHEM 762, 33-48.

Brown, P., Bothe Jr, J., 2004. The system CaO-Al_2O_3-$CaCl_2$-H_2O at 23±2 °C and the mechanisms of chloride binding in concrete. Cem. Concr. Res. 34, 1549-1553.

Cazzola, P., Cena, A., Ghignone, S., Abete, M.C., Andruetto, S., 2004. Experimental system to displace radioisotopes from upper to deeper soil layers: chemical research. Environ. Health 3, 1-10.

Chen, F., Burns, P.C., Ewing, R.C., 1999. [79]Se: geochemical and crystallo-chemical retardation mechanisms. J. Nucl. Mater. 275, 81-94.

Chubar, N., 2014. EXAFS and FTIR studies of selenite and selenate sorption by alkoxide-free sol-gel generated Mg-Al-CO_3 layered double hydroxide with very labile interlayer anions. J. Mater. Chem. A 2, 15995-16007.

Constantino, L.V., Quirino, J.N., Monteiro, A.M., Abrão, T., Parreira, P.S., Urbano, A., Santos, M.J., 2017. Sorption-desorption of selenite and selenate on Mg-Al layered double hydroxide in competition with nitrate, sulfate and phosphate. Chemosphere 181, 627-634.

Dakora, F.D., Phillips, D.A., 2002. Root exudates as mediators of mineral acquisition in low-nutrient environments. Food security in nutrient-stressed environments: Exploiting plants' genetic capabilities, 201-213.

Das, J., Patra, B., Baliarsingh, N., Parida, K., 2006. Adsorption of phosphate by layered double hydroxides in aqueous solutions. Appl. Clay Sci. 32, 252-260.

De Cort, M., 1998. Atlas of caesium deposition on Europe after the Chernobyl accident.

De Cristofaro, A., He, J., Zhou, D., Violante, A., 2000. Adsorption of Phosphate and Tartrate on Hydroxy-Aluminum-Oxalate Precipitates. Soil Sci. Soc. Am. J. 64, 1347-1355.

Dinh, Q.T., Li, Z., Tran, T.A.T., Wang, D., Liang, D., 2017. Role of organic acids on the bioavailability of selenium in soil: A review. Chemosphere 184, 618-635.

dos Reis, M.J., Silvério, F., Tronto, J., Valim, J.B., 2004. Effects of pH, temperature, and ionic strength on adsorption of sodium dodecylbenzenesulfonate into Mg-Al-CO_3 layered double hydroxides. J Phys Chem Solids 65, 487-492.

Eich-Greatorex, S., Krogstad, T., Sogn, T.A., 2010. Effect of phosphorus status of the soil on selenium availability. J. Plant. Nutr. Soil. Sci. 173, 337-344.

Eklund, L., Persson, I., 2014. Structure and hydrogen bonding of the hydrated selenite and selenate ions in aqueous solution. Dalton Trans. 43, 6315-6321.

EPAToxic, U., Toxic and Priority Pollutants Under the Clean Water Act. US EPAAvailable online: https://www. epa. gov/eg/toxic-and-priority-pollutants-under-clean-water-act (accessed on 24 January 2021).

Eklund, L. and Persson, I., 2014. Structure and hydrogen bonding of the hydrated selenite and selenate ions in aqueous solution. Dalton Transactions, 43(17), pp.6315-6321.

Fang, L., Li, W., Chen, H., Xiao, F., Huang, L., Holm, P.E., Hansen, H.C.B. and Wang, D., 2015. Synergistic effect of humic and fulvic acids on Ni removal by the calcined Mg/Al layered double hydroxide. RSC Adv. 5(24),18866-18874.

Fermi, E., 1927. Statistical method to determine some properties of atoms. Rend. Accad. Naz. Lincei 6, 5.

Fuge, R., 1988. Sources of halogens in the environment, influences on human and animal health. Environ. Geochem. Health 10, 51-61.

Fuge, R., Johnson, C.C., 1986. The geochemistry of iodine-a review. Environ. Geochem. Health 8, 31-54.

Goh, K.-H., Lim, T.-T., Dong, Z., 2008. Application of layered double hydroxides for removal of oxyanions: a review. Water Res. 42, 1343-1368.

Gougar, M., Scheetz, B., Roy, D., 1996. Ettringite and C-S-H Portland cement phases for waste ion immobilization: A review. Waste Manage. 16, 295-303.

Grangeon, S., Marty, N.C., Maubec, N., Warmont, F., Claret, F., 2019. Selenate Sorption by Hydrated Calcium Aluminate (AFm): Evidence for Sorption Reversibility and Implication for the Modeling of Anion Retention. ACS Earth Space Chem. 4, 229-240.

Greenwell, H., Jones, W., Newman, S., Coveney, P., 2003a. Computer simulation of interlayer arrangement in cinnamate intercalated layered double hydroxides. J. Mol. Struct. 647, 75-83.

Greenwell, H.C., Stackhouse, S., Coveney, P.V., Jones, W., 2003b. A density functional theory study of catalytic trans-esterification by tert-butoxide MgAl anionic clays. J. Phys. Chem. B 107, 3476-3485.

Grover, K., Komarneni, S., Katsuki, H., 2009. Uptake of arsenite by synthetic layered double hydroxides. Water Res. 43, 3884-3890.

Hohenberg, P., Kohn, W., 1964. Inhomogeneous electron gas. Phys. Rev. 136, B864.

Hongo, T., Iemura, T., Yamazaki, A., 2008. Adsorption ability for several harmful anions and thermal behavior of Zn-Fe layered double hydroxide. J. Ceram. Soc. Japan 116, 192-197.

Hu, B., Chen, G., Jin, C., Hu, J., Huang, C., Sheng, J., Sheng, G., Ma, J., Huang, Y., 2017a. Macroscopic and spectroscopic studies of the enhanced scavenging of Cr (VI) and Se (VI) from water by titanate nanotube anchored nanoscale zero-valent iron. J. Hazard. Mater. 336, 214-221.

Hu, B., Ye, F., Jin, C., Ma, X., Huang, C., Sheng, G., Ma, J., Wang, X., Huang, Y., 2017b. The enhancement roles of layered double hydroxide on the reductive immobilization of selenate by nanoscale zero valent iron: Macroscopic and microscopic approaches. Chemosphere 184, 408-416.

Hu, Q., Moran, J.E., 2011. Iodine: radionuclides. Encyclopedia of Inorganic and Bioinorganic Chemistry.

Hummel, W., 2017. Chemistry of selected dose-relevant radionuclides. Paul Scherrer Institute (PSI).

Iglesias, L., Walther, C., Medina, F., Hölzer, A., Neumann, A., Lozano-Rodriguez, M.J., Álvarez, M.G., Torapava, N., 2016. A comprehensive study on iodine uptake by selected LDH phases via coprecipitation, anionic exchange and reconstruction. J. Radioanal. Nucl. Chem. 307, 111-121.

Ikemoto, T., Magara, Y., 2011. Measures against impacts of nuclear disaster on drinking water supply systems in Japan. Water Pract. Technol. 6.

Jiang, H., Li, T., Han, X., Yang, X., He, Z., 2012. Effects of pH and low molecular weight organic acids on competitive adsorption and desorption of cadmium and lead in paddy soils. Environ. Monit. Assess. 184, 6325-6335.

Johnson, E.A., Rudin, M.J., Steinberg, S.M., Johnson, W.H., 2000. The sorption of selenite on various cement formulations. Waste Manage. 20, 509-516.

Jones, D., Dennis, P., Owen, A., Van Hees, P., 2003. Organic acid behavior in soils–misconceptions and knowledge gaps. Plant Soil 248, 31-41.

Kalinichev, A.G., Kirkpatrick, R.J., 2002. Molecular dynamics modeling of chloride binding to the surfaces of calcium hydroxide, hydrated calcium aluminate, and calcium silicate phases. Chem. Mater. 14, 3539-3549.

Kim, M., Kim, H.G., Kim, S., Yoon, J.H., Sung, J.Y., Jin, J.S., Lee, M.H., Kim, C.W., Heo, J., Hong, K.S., 2020. Leaching behaviors and mechanisms of vitrified forms for the low-level radioactive solid wastes. J. Hazard. Mater. 384, 121296.

Kohn, W., Sham, L.J., 1965. Self-consistent equations including exchange and correlation effects. Phys. Rev. 140, A1133.

Koilraj, P., Kamura, Y., Sasaki, K., 2017. Carbon-dot-decorated layered double hydroxide nanocomposites as a multifunctional environmental material for co-immobilization of SeO_4^{2-} and Sr^{2+} from aqueous solutions. ACS Sustain. Chem. Eng. 5, 9053-9064.

Lazaridis, N., Pandi, T., Matis, K., 2004. Chromium (VI) removal from aqueous solutions by Mg-Al-CO_3 hydrotalcite: sorption-desorption kinetic and equilibrium studies. Ind. Eng. Chem. Res. 43, 2209-2215.

Li, H., Ma, J., Evans, D.G., Zhou, T., Li, F., Duan, X., 2006. Molecular dynamics modeling of the structures and binding energies of α-nickel hydroxides and nickel-aluminum layered double hydroxides containing various interlayer guest anions. Chem. Mater. 18, 4405-4414.

Li, M., Dopilka, A., Kraetz, A.N., Jing, H., Chan, C.K., 2018. Layered double hydroxide/chitosan nanocomposite beads as sorbents for selenium oxoanions. Ind. Eng. Chem. Res. 57, 4978-4987.

Liu, Q., Li, Y., Zhang, J., Chi, Y., Ruan, X., Liu, J., Qian, G., 2011. Effective removal of zinc from aqueous solution by hydrocalumite. Chem. Eng. J. 175, 33-38.

Liu, Y.T., Wang, M.K., Chen, T.Y., Chiang, P.N., Huang, P.M., Lee, J.F., 2006. Arsenate sorption on lithium/aluminum layered double hydroxide intercalated by chloride and on gibbsite: sorption isotherms, envelopes, and spectroscopic studies. Environ. Sci. Technol. 40, 7784-7789.

Luo, L., Zhang, S., Shan, X.Q., Zhu, Y.G., 2006. Effects of oxalate and humic acid on arsenate sorption by and desorption from a Chinese red soil. Water Air Soil Pollut. 176, 269-283.

Ma, B., Fernandez-Martinez, A., Grangeon, S., Tournassat, C., Findling, N., Claret, F., Koishi, A., Marty, N.C., Tisserand, D., Bureau, S., 2017a. Evidence of multiple sorption modes in layered double hydroxides using Mo as structural probe. Environ. Sci. Technol. 51, 5531-5540.

Ma, L., Islam, S.M., Xiao, C., Zhao, J., Liu, H., Yuan, M., Sun, G., Li, H., Ma, S., Kanatzidis, M.G., 2017b. Rapid simultaneous removal of toxic anions $[HSeO_3]^-$, $[SeO_3]^{2-}$, and $[SeO_4]^{2-}$, and metals Hg^{2+}, Cu^{2+}, and Cd^{2+} by MoS_4^{2-} intercalated layered double hydroxide. J. Am. Chem. Soc. 139, 12745-12757.

Ma, L., Wang, Q., Islam, S.M., Liu, Y., Ma, S., Kanatzidis, M.G., 2016. Highly selective and efficient removal of heavy metals by layered double hydroxide intercalated with the MoS_4^{2-} ion. J. Am. Chem. Soc. 138, 2858-2866.

Manceau, A., Charlet, L., 1994. The mechanism of selenate adsorption on goethite and hydrous ferric oxide. J. Colloid Interface Sci. 168, 87-93.

Meng, Z., Lv, F., Li, X., Zhang, Q., Chu, P.K., Komarneni, S., Zhang, Y., 2016. Simultaneous arsenate and alkali removal from alkaline wastewater by in-situ formation of Zn-Al layered double hydroxide. Microporous Mesoporous Mater. 227, 137-143.

Miller, W., Alexander, R., Chapman, N., McKinley, J.C., Smellie, J.A.T. eds., 2000. Geological disposal of radioactive wastes and natural analogues (Vol.2). Elsevier.

Mimmo, T., Ghizzi, M., Marzadori, C., Gessa, C., 2008. Organic acid extraction from rhizosphere soil: effect of field-moist, dried and frozen samples. Plant Soil 312, 175-184.

Naik, M.M., Dubey, S.K., 2017. Marine pollution and microbial remediation. Springer.

Nedyalkova, L., Lothenbach, B., Geng, G., Mäder, U., Tits, J., 2020. Uptake of iodide by calcium aluminate phases (AFm phases). Appl. Geochemistry 116, 104559.

Newman, S.P., Williams, S.J., Coveney, P.V., Jones, W., 1998. Interlayer arrangement of hydrated MgAl layered double hydroxides containing guest terephthalate anions: Comparison of simulation and measurement. J. Phys. Chem. B 102, 6710-6719.

Peak, D., 2006. Adsorption mechanisms of selenium oxyanions at the aluminum oxide/water interface. J. Colloid Interface Sci. 303, 337-345.

Perdew, J.P., Burke, K., Ernzerhof, M., 1996. Generalized gradient approximation made simple. Phys. Rev. Lett. 77, 3865.

Perminova, I.V., Frimmel, F.H., Kudryavtsev, A.V., Kulikova, N.A., Abbt-Braun, G., Hesse, S., Petrosyan, V.S., 2003. Molecular weight characteristics of humic substances from different environments as determined by size exclusion chromatography and their statistical evaluation. Environ. Sci. Technol. 37, 2477-2485.

United Nations Scientific Committee on the Effects of Atomic Radiation, 1996. Sources and Effects of Ionizing Radiation, United Nations Scientific Committee on the Effects of Atomic Radiation (UNSCEAR) 1996 Report: Report to the General Assembly, with Scientific Annexes. United Nations.

United Nations Scientific Committee on the Effects of Atomic Radiation, 2008. Effects of Ionizing Radiation, United Nations Scientific Committee on the Effects of Atomic Radiation (UNSCEAR) 2006 Report, Volume I: Report to the General Assembly, Scientific Annexes A and B. United Nations.

Renaudin, G., Rapin, J.P., Elkaim, E., François, M., 2004. Polytypes and polymorphs in the related Friedel's salt $[Ca_2Al(OH)_6]^+[X\cdot 2H_2O]^-$ halide series. Cem. Concr. Res. 34, 1845-1852.

Rojo, H., Scheinost, A., Lothenbach, B., Laube, A., Wieland, E., Tits, J., 2018. Retention of selenium by calcium aluminate hydrate (AFm) phases under strongly-reducing radioactive waste repository conditions. Dalton Trans. 47, 4209-4218.

Schellenger, A.E., Choi, S., Onnis-Hayden, A., Larese-Casanova, P., 2021. Selenium oxyanion exchange with Mg(II)-Fe(III) and Fe(II)-Fe(III) layered double hydroxides. Appl. Clay Sci. 200, 105959.

Shahid, M., Niazi, N.K., Khalid, S., Murtaza, B., Bibi, I., Rashid, M.I., 2018. A critical review of selenium biogeochemical behavior in soil-plant system with an inference to human health. Environ. Pollut. 234, 915-934.

Shaw, G., Ashworth, D., 2006. Selenium: radionuclides. Encyclopedia of Inorganic Chemistry.

Sokol, J.P., Cooper, M.H., 1979. Radioactive waste in perspective. Proceedings of the American Power Conference.

Stevenson, F.J. 1982. Humus Chemistry: Genesis, Composition, Reactions. Wiley & Sons, New York, NY

Supriatin, S., Weng, L., Comans, R.N., 2015. Selenium speciation and extractability in Dutch agricultural soils. Sci. Total Environ. 532, 368-382.

United States. Division of Soil Survey, 1993. Soil survey manual (No. 18). US Department of Agriculture.

Takaki, Y., Qiu, X., Hirajima, T., Sasaki, K., 2016. Removal mechanism of arsenate by bimetallic and trimetallic hydrocalumites depending on arsenate concentration. Appl. Clay Sci. 134, 26-33.

Theiss, F.L., Ayoko, G.A., Frost, R.L., 2017. Sorption of iodide (I^-) from aqueous solution using Mg/Al layered double hydroxides. Mater. Sci. Eng. C 77, 1228-1234.

Theiss, F.L., Sear-Hall, M.J., Palmer, S.J., Frost, R.L., 2012. Zinc aluminium layered double hydroxides for the removal of iodine and iodide from aqueous solutions. Desalination Water Treat. 39, 166-175.

Thomas, L.H., 1927. The calculation of atomic fields. Mathematical proceedings of the Cambridge philosophical society (Vol.23, No.5). Cambridge University Press, 542-548.

Todorov, P.T., Ilieva, E.N., 2006. Contamination with uranium from natural and antropological sources. Romanian J. Phys. 51, 27.

Um, W., Serne, R.J., 2005. Sorption and transport behavior of radionuclides in the proposed low-level radioactive waste disposal facility at the Hanford site, Washington. Radiochim. Acta 93, 57-63.

UNSCEAR, 2000. Sources and Effects of Ionizing Radiation, United Nations Scientific Committee on the Effects of Atomic Radiation. Report to the General Assembly with Scientific Annexes. Exposures from natural radiation sources, 84-141.

VanMiddlesworth, L., Handle, J., Johns, P., 2000. Iodine-129 in thyroid glands: A sensitive biological marker of fission product exposure. J. Radioanal. Nucl. Chem. 243, 467-472.

Wei, M., Pu, M., Guo, J., Han, J., Li, F., He, J., Evans, D.G., Duan, X., 2008. Intercalation of l-Dopa into layered double hydroxides: enhancement of both chemical and stereochemical stabilities of a drug through host-guest interactions. Chem. Mater. 20, 5169-5180.

Wersin, P., Johnson, L., Schwyn, B., Berner, U., Curti, E., 2003. Redox Conditions in the Near Field of a Repository for SF/HLW and ILW in Opalinus Clay. TECHNISCHER BERICHT-NAGRA NTB.

Wu, Y., Chi, Y., Bai, H., Qian, G., Cao, Y., Zhou, J., Xu, Y., Liu, Q., Xu, Z.P., Qiao, S., 2010. Effective removal of selenate from aqueous solutions by the Friedel phase. J. Hazard. Mater. 176, 193-198.

Xu, P., Wang, H., Tong, R., Du, Q., Zhong, W., 2006. Preparation and morphology of SiO$_2$/PMMA nanohybrids by microemulsion polymerization. Colloid. Polym. Sci. 284, 755-762.

Yan, D., Lu, J., Wei, M., Li, H., Ma, J., Li, F., Evans, D.G., Duan, X., 2008. In Situ Polymerization of the 4-Vinylbenzenesulfonic Anion in Ni-Al-Layered Double Hydroxide and Its Molecular Dynamic Simulation. J. Phys. Chem. A 112, 7671-7681.

Yang, L., Shahrivari, Z., Liu, P.K., Sahimi, M., Tsotsis, T.T., 2005. Removal of trace levels of arsenic and selenium from aqueous solutions by calcined and uncalcined layered double hydroxides (LDH). Ind. Eng. Chem. Res. 44, 6804-6815.

Yasunari, T.J., Stohl, A., Hayano, R.S., Burkhart, J.F., Eckhardt, S. and Yasunari, T., 2011. Cesium-137 deposition and contamination of Japanese soils due to the Fukushima nuclear accident. Proc. Natl. Acad. Sci. 108(49), 19530-19534.

You, Y., Vance, G.F., Zhao, H., 2001. Selenium adsorption on Mg-Al and Zn-Al layered double hydroxides. Appl. Clay Sci. 20, 13-25.

Zhang, M., Reardon, E.J., 2003. Removal of B, Cr, Mo, and Se from wastewater by incorporation into hydrocalumite and ettringite. Environ. Sci. Technol. 37, 2947-2952.

Chapter 2 Methodology

2.1 Solution analysis

2.1.1 Inductively coupled plasma optical emission spectrometry

Inductively coupled plasma optical emission spectrometry (ICP-OES, Optima 8300, Perkin Elmer, Boston Waltham, US) was adopted to quantify the concentrations of Ca, Mg, Al, and Se.

2.1.2 Inductively coupled plasma mass spectrometry

Inductively coupled plasma mass spectrometry (ICP-MS, Agilent 7500c, Santa Clara, US) was used to determine the concentrations of Mg, Al, Se, As, B, Cr which lower than ICP-OES limitation.

2.1.3 Ion chromatography

The concentrations of I^-, NO_3^-, and F^- were determined by an ion chromatography (IC, ICS-2100, Thermo Scientific, Yokohama, Japan).

2.1.4 High-performance liquid chromatography

Concentrations of amino acids were determined by HPLC LC-Net II/ADC, which is equipped with a column (Shim-pack GIST-HP C18 column, Shimadzu, Kyoto, Japan) and a UV detector (UV-2075 plus, JASCO, Hachioji, Japan). First, 0.1 mL 1.0 M triethylamine and 0.1 mL 0.2 M phenyl isothiocyanate (PITC) were mixed with 0.2 mL of the sample solution and standstill for 1 h. Then, 0.4 mL of *n*-hexane was added and shaken by a Vortex mixer for 10 s. Finally, 0.2 mL of lower-layer phase was taken and mixed with 0.8 mL ultra-pure water for determination

(Heinrikson and Meredith, 1984; Scholze, 1985; Cohen et al., 1986; Lippincott et al., 1988; Gunawan et al., 1990).

The adsorption density of each amino acid was calculated by **Eq. (2.1)**:

$$Q_e = (C_0 - C_e) \cdot V/m \tag{2.1}$$

where Q_e (mmol g^{-1}) is the amino acid sorption amount in LDH after 24 h, C_0 (mM) is the initial concentration of amino acid, C_e (mM) is the equilibrium concentration of amino acid after the interaction, V (L) is the volume of solution and m (g) is the mass of LDH.

2.1.5 Zeta potential

The zeta potential of LDHs was measured by observation of the colloidal vibration current (CVC) which can be determined by electroacoustic measurement using Zetasizer NANO-ZS (Malvern Panalytical Ltd., Worcestershire, UK).

2.2 Solid characterization

2.2.1 X-ray diffraction

The solid residues were characterized by X-ray diffraction (Rigaku Ultima IV XRD, Akishima, Japan) using Cu Kα radiation (40 kV, 40 mA, λ=1.54184 Å) with Ni filter at a scanning speed of 2°/min, a scanning step of 0.02°.

2.2.2 X-ray fluorescence spectroscopy

X-ray fluorescence (XRF) was adopted to determine the elemental compositions of the samples using a Rigaku ZSX Primus II (Akishima, Japan) in the wavelength dispersive mode: Rh-anode (3 or 4 kV, 60 kV).

2.2.3 CHN analysis

The carbon (C), hydrogen (H), nitrogen (N) contents in LDH were determined by a CHN analyzer (CHN MT-5, Yanaco Technical Science Co. Ltd., Tokyo, Japan).

2.2.4 Scanning electron microscope

The morphology of the samples was characterized using a field emission scanning electron microscope (SEM, FlexSEM 1000, Hitachi, Japan) at 20 kV.

2.3 Density functional theory (DFT)

The projector augmented-wave (PAW) method (Blöchl, 1994; Kresse and Joubert, 1999) was employed with the PBEsol exchange-correlation functional within the generalized gradient approximation (GGA) (Perdew et al., 1996, 1997; Perdew et al., 2008) and D3 van der Waals correction (Grimme et al., 2010; Grimme et al., 2011) as implemented in the VASP code (Kresse and Hafner, 1993a, 1993b; Kresse and Furthmüller, 1996a, 1996b). Standard PAW datasets were used with a plane-wave cutoff energy of 550 eV.

References

Blöchl, P.E., 1994. Projector augmented-wave method. Phys. Rev. B 50, 17953.

Cohen, S.A., Bidlingmeyer, B.A., Tarvin, T.L., 1986. PITC derivatives in amino acid analysis. Nature 320, 769-770.

Grimme, S., Antony, J., Ehrlich, S., Krieg, H., 2010. A consistent and accurate ab initio parametrization of density functional dispersion correction (DFT-D) for the 94 elements H-Pu. J. Chem. Phys. 132, 154104.

Grimme, S., Ehrlich, S., Goerigk, L., 2011. Effect of the damping function in dispersion corrected density functional theory. J. Comput. Chem. 32, 1456-1465.

Gunawan, S., Walton, N.Y., Treiman, D.M., 1990. High-performance liquid chromatographic determination of selected amino acids in rat brain by precolumn derivatization with phenylisothiocyanate. J. Chromatogr. A 503, 177-187.

Heinrikson, R.L., Meredith, S.C., 1984. Amino acid analysis by reverse-phase high-performance liquid chromatography: precolumn derivatization with phenylisothiocyanate. Anal. Biochem. 136, 65-74.

Kresse, G., Furthmüller, J., 1996a. Efficiency of ab-initio total energy calculations for metals and semiconductors using a plane-wave basis set. Comput. Mater. Sci 6, 15-50.

Kresse, G., Furthmüller, J., 1996b. Efficient iterative schemes for ab initio total-energy calculations using a plane-wave basis set. Phys. Rev. B 54, 11169.

Kresse, G., Hafner, J., 1993a. Ab initio molecular dynamics for liquid metals. Phys. Rev. B 47, 558.

Kresse, G., Hafner, J., 1993b. Ab initio molecular dynamics for open-shell transition metals. Phys. Rev. B 48, 13115.

Kresse, G., Joubert, D., 1999. From ultrasoft pseudopotentials to the projector augmented-wave method. Phys. Rev. B 59, 1758.

Lippincott, S.E., Friedman, A.L., Siegel, F.L., Pityer, R.M., Chesney, R.W., 1988. HPLC analysis of the phenylisothiocyanate (PITC) derivatives of taurine from physiologic samples. J. Am. Coll. Nutr. 7, 491-497.

Perdew, J.P., Burke, K., Ernzerhof, M., 1996. Generalized gradient approximation made simple. Phys. Rev. Lett. 77, 3865.

Perdew, J.P., Ruzsinszky, A., Csonka, G.I., Vydrov, O.A., Scuseria, G.E., Constantin, L.A., Zhou, X., Burke, K., 2008. Restoring the density-gradient expansion for exchange in solids and surfaces. Phys. Rev. Lett. 100, 136406.

Scholze, H., 1985. Determination of phenyltiocarbamyl amino acids by reversed-phase high-performance liquid chromatography. J. Chromatogr. A 350, 453-460.

Chapter 3 Environmental impact of amino acids on the leaching behavior of iodide intercalated in hydrocalumite

3.1 Introduction

The stability of I^- in the Ca_2Al-LDH interlayer is always affected by the presence of other anions which have higher affinity with Ca_2Al-LDH. In the contaminated soil and wastewater, there are always many competitive inorganics and organic ions which possibly exist in cementitious materials after immobilizing target pollutants (Dai et al., 2009; Emerson et al., 2014; Xu et al., 2015; Li et al., 2017). Generally, the effects of inorganic ions such as Cl^-, OH^-, CO_3^{2-} and SO_4^{2-} on the stability of hydrocalumite have been explored. Aimoz et al. (Aimoz et al., 2012) explored the retention behavior of I^- in AFm phase, and found that the Cl^- and CO_3^{2-} show a competitive relationship with I- to intercalate into AFm interlayer and reduce the stability of I-AFm and I-SO4-AFm. Nedyalkova et al. (Nedyalkova et al., 2020) also confirmed the capability of AFm bearing I^- becomes weakly due to the formation of monocarbonate as the reaction time going. However, the effects of organic matters on the stability of I-hydrocalumite have not yet been explored. Amino acids as the elementary units of proteins which exist in free single molecules and degradation products of soil small animals, plants as well as microorganisms in the pedosphere. Amino acids contain amino ($-NH_2$) and carboxyl ($-COOH$) functional groups and can be classified into hydrophobic, neutral and hydrophilic depends on their specific side chains (R group). Therefore, to some extent, the chemical properties of amino acids can represent complicated organic molecules (Gao et al., 2014).

In the present work, I-hydrocalumite (Ca_2Al-LDH(I)) was prepared through co-precipitation. Five amino acids were selected to explore the stability of Ca_2Al-LDH(I), considering the molecular size, the charge number, the functional groups, and hydrophilicity. Based on Ca and Al oxides hydration in alkaline conditions, released behavior of I^-, adsorption behavior of amino acids,

and solid residues phases changing were elaborated. Density functional theory (DFT) simulation was applied to find out the possible configurations and support the experimental results and possible releasing mechanisms of I$^-$ in the presence of amino acids.

3.2 Experimental

3.2.1 Materials

All reagents used in the present work were purchased from Wako Chemicals (Osaka, Japan). Inorganic reagents including CaCO$_3$ (98%), Al$_2$O$_3$ (99%), NaOH (97%), CaI$_2\cdot n$H$_2$O (99.5%) are in an analytical grade.

There are 20 types of amino acids exist in nature. Depending on their specific side chain groups, hydrophilic, hydrophobic, and amphipathic can be classified. L-phenylalanine (HPhe, C$_9$H$_{11}$NO$_2$, 99%) and L-tryptophan (HTrp, C$_{11}$H$_{12}$N$_2$O$_2$, 99%) have aromatic groups which make them more hydrophobic than L-cysteine (H$_2$Cys, C$_3$H$_7$NO$_2$S, 99%), L-aspartic acid (H$_2$Asp, C$_4$H$_7$NO$_4$, 99%), and glycine (HGly, C$_2$H$_5$NO$_2$, 99%) which have hydrophilic side chain groups. Each amino acid has different acid dissociation constants (pK_a), depending on the relationship between solution pH and pK_a, the different negative charge numbers for each amino acid can be produced. Under the present experimental condition where pH is higher than 12.0, HGly, HTrp, and HPhe are one negative charge but H$_2$Cys and H$_2$Asp are two negative charges. Hence, different behaviors can be expected. H$_2$Cys, H$_2$Asp, HGly, HTrp, and HPhe are used in a special grade. For HPLC analysis (**2.1.4 section**), the phenyl isothiocyanate (PITC, 98%) in a special grade, acetonitrile, methanol, *n*-hexane in HPLC grade were used. All the solutions were prepared using decarbonized Milli-Q water (integral water purification system, Millipore) boiled with purging N$_2$ gas for 2 h.

3.2.2 Synthesis of Ca$_2$Al-LDH(I)

Tricalcium aluminate, Ca$_3$Al$_2$O$_6$ (C$_3$A) was prepared by calcining the mixture of 30.027 g CaCO$_3$ and 10.196 g Al$_2$O$_3$ at a molar ratio of 3:1 for 72 h at 1300 °C in a furnace as described in Atkins (Atkins et al., 1992; Ma et al., 2017). Thereafter, the obtained solid was provided for the following experiments. I-hydrocalumite, 3CaO·Al$_2$O$_3$·CaI$_2$·10H$_2$O, also formulated as Ca$_4$Al$_2$(OH)$_{12}$I$_2$·4H$_2$O, was prepared by the co-precipitation method using 0.02 mol C$_3$A and 0.02 mol CaI$_2$·nH$_2$O stirring at 600 rpm in a glovebox (95% N$_2$, 5% H$_2$, COY, M-160, US) to avoid carbon dioxide (CO$_2$) contamination. After 72 h, the suspension was centrifuged to separate the solid residues, which were rinsed with decarbonized water, freeze-drying for 24 h, and then stored for further use.
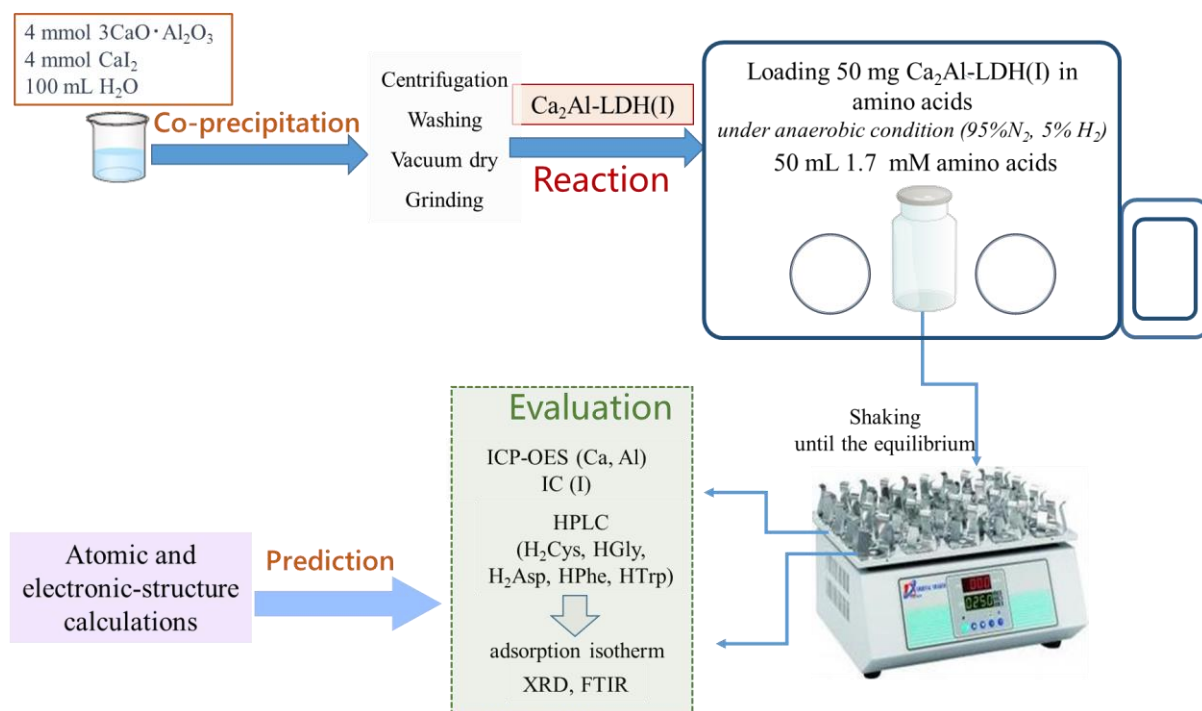
Scheme 3.1 Experimental procedure of Ca$_2$Al-LDH(I) with different amino acids.

3.2.3 Reaction of Ca_2Al-LDH(I) with amino acids

50 mg of the synthesized Ca_2Al-LDH(I) were suspended into 50 mL of solutions with and without 1.7 mM amino acids. The initial pH of each solution was adjusted to pH 12.0 by 3 M NaOH. pH of 12.0 was selected to simulate the alkalinity condition in a real cement system. The suspensions in polyethylene plastic bottles were shaken at 100 rpm for different time intervals from 0.5 to 24 h followed by collection of leaching solutions using disposable syringes and solid residues by filtration using 0.2 μm membrane filters to freeze-drying for 12 h. The solubility of Ca_2Al-LDH(I) in ultrapure water was separately evaluated without adding amino acids. After reacting with amino acids, the soluble fraction of I^- was evaluated.

3.2.4 Chemical analysis and solid characterizations

As shown in 2.1, 2.2 sections.

The solubility fraction was calculated based on concentrations of Ca^{2+}, $Al(OH)_4^-$ and I^- following **Eq. (3.1)**:

Dissolved fraction (%) $= C_t/C_0 \times 100$ (3.1)

where the C_t (mmol) is the released amount of ions in solution at time t (h), C_0 (mmol) is the amount of ions in pristine I-hydrocalumite solid.

3.2.5 DFT simulation

As shown in 2.3 section.

Density functional theory (DFT) simulation was applied to predict the intercalation of amino acids as well as the possible interaction between amino acids and hydrocalumite. Due to the expanded peaks appeared in XRD patterns only appeared in the presence of Asp^{2-} and Cys^{2-}, which means the intercalation behavior Asp^{2-} and Cys^{2-} might have occurred. So Asp^{2-} and Cys^{2-} were

selected as the model of amino acids in DFT simulation. The states as valence electrons are: 1s for H; 2s and 2p for C, N, and O; 3s and 3p for Al and S; 3p and 4s for Ca.

Initial structural models were prepared as follows. Firstly, the structural model of positively charged hydroxides layers for Ca_2Al-LDH was constructed for the computer simulation. The hydroxide layers of Ca_2Al-LDH used in the simulations were set using atomic coordinates extracted from the previously reported crystal structure of hydrocalumite with the composition of $[Ca_8Al_4(OH)_24(CO_3)(Cl)_2 \cdot 10H_2O]$ (Sacerdoti and Passaglia, 1988). By removing the intercalated carbonate (CO_3^{2-}) and chloride (Cl^-) ions, an "empty" LDH model was created. Since the composition of the LDH layer is $[Ca_2Al(OH)_6]^+$, the number of Al atoms corresponds to the positive charge of the empty LDH model. Secondly, specific Asp^{2-} and Cys^{2-} anions and water molecules are placed in the interlayer space of the empty LDH layers with random positions and rotation angles by using the pymatgen python library (Ong et al., 2013) so as to neutralize the positive charge of the empty LDH models. Thus, more than ten simulated unit cells consisting of the positively charged hydroxide layers of $[Ca_2Al(OH)_6]^+$ and desired intercalated anions were constructed. Relaxation of lattice constants and internal coordinates was performed until the residual stress and force decreased to 4 MPa and 1 meV/Å, respectively. The pymatgen python library was used to extract the structural information such as interlayer spacing and the number of chemical bonds from the optimized structures (Ong et al., 2013). The VESTA code was used to visualize the optimized structures (Momma and Izumi, 2011).

3.3 Results and discussion

3.3.1 Characterizations of pristine Ca_2Al-LDH(I)

Fig. 3.1 (a, b) presents the XRD patterns of the calcined C_3A (PDF#32-0149) and Ca_2Al-LDH(I) (PDF#042-1474). The solid phase of C_3A is consistent with the previous report (Sánchez-Herrero et al., 2012). After co-precipitate with $CaI_2 \cdot nH_2O$ for 72 h, Ca_2Al-LDH(I) was formed in

a pure phase with a d_{003} value of 8.75 Å at the angle of 10.101° which is consistent with the published works (Aimoz et al., 2012; Nedyalkova et al., 2020). In **Fig. 3.4(b)**, SEM micrographs of the Ca$_2$Al-LDH(I) show hexagonal morphology with sharp edges as another hydrocalumite family (Choi et al., 2012) and further, the mole ratio of Ca/Al is 1.87 in **Table 3.1**. Therefore, considering the above results, the formation of Ca$_2$Al-LDH(I) is displayed using the following reaction (**Eq. (3.2)**):

$$3CaO \cdot Al_2O_3 + CaI_2 + 10H_2O \rightarrow Ca_4Al_2(OH)_{12}I_2 \cdot 4H_2O \tag{3.2}$$

Table 3.1 Elemental composition of synthesized Ca$_2$Al-LDH(I).

LDHs	Chemical formula	Ca/mmol·g^{-1}	Al/mmol·g^{-1}	I/mmol·g^{-1}	Ca/Al
Ca$_2$Al-LDH(I)	Ca$_{6.0}$·Al$_{3.2}$·(OH)$_{18}$·(I)$_{2.19}$·6H$_2$O	6.0	3.2	2.19	1.87
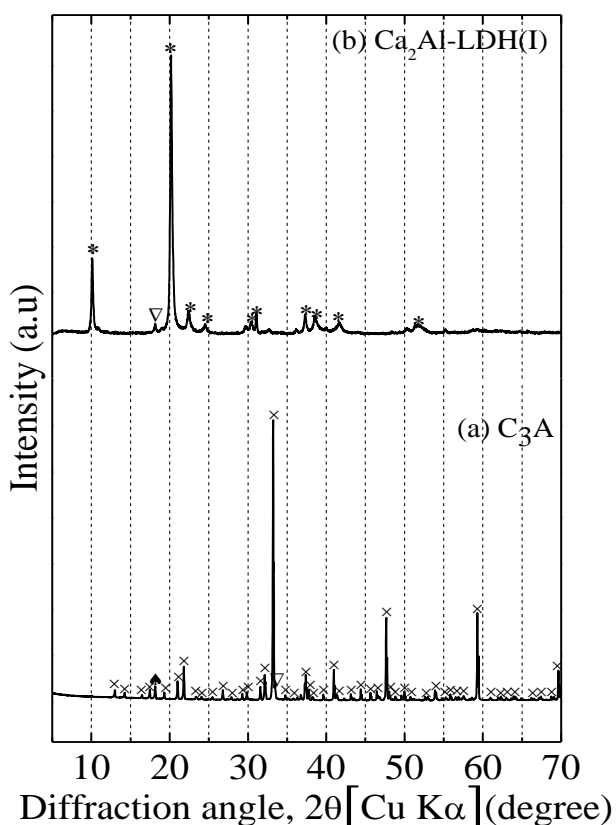
Fig. 3.1 XRD patterns of (a) tricalcium aluminate (C$_3$A), (b) I-hydrocalumite (Ca$_2$Al-LDH(I)). Symbols: ∗, calcium aluminum iodide oxide hydrate (3CaO·Al$_2$O$_3$·CaI$_2$·10H$_2$O, PDF#42-1474); ×, tricalcium aluminate (3CaO·Al$_2$O$_3$, PDF#32-0149); ♠, mayenite (12CaO·7Al$_2$O$_3$, PDF#78-0910); ▽, unknown.

3.3.2 Dissolution of Ca_2Al-LDH(I) in alkaline solutions

The changes in I^-, Ca^{2+}, $Al(OH)_4^-$, pH, and amino acids at different suspension times were shown in **Fig. 3.2**. Without any amino acids, after Ca_2Al-LDH(I) was suspended into alkaline solution for 0.5 h, the leaching amount of I^- reached 50.0% of the total amount in pristine Ca_2Al-LDH(I). As the reaction time going, the concentration of released I^- reached 2.00 mM (91.0%) and the dissolution equilibrium was almost achieved after 6 h. The concentrations of released Ca^{2+} (**Fig. 3.2(b)**) and $Al(OH)_4^-$ (**Fig. 3.2(c)**) reached 5.37 and 2.78 mM after 24 h, respectively. Besides, the ratio of released Ca/Al is always within 1.85-1.95 which is close to the Ca/Al ratio in pristine Ca_2Al-LDH(I). This indicates the metallic hydroxide layer structure of Ca_2Al-LDH(I) was unstable to dissolve simply even though under strongly alkaline conditions (**Eq. (3.3)**).

$$Ca_4Al_2(OH)_{12}I_2 \cdot 4H_2O \rightarrow 4Ca^{2+} + 2Al(OH)_4^- + 2I^- + 4OH^- + 4H_2O \qquad (3.3)$$
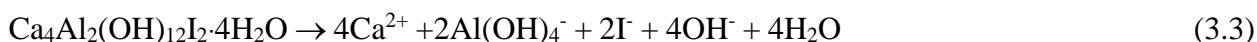
To make sure the dissolution equilibrium, the reactions were continued until 24 h in this work. The XRD patterns of solid residues collected from blank and amino acids tests at different reaction times were presented in **Fig. 3.3**. **Fig. 3.3(a)** shows the result in blank test, where the phase of Ca_2Al-LDH(I) was maintained until 3 h and after that, it was gradually phase-transferred into the metastable phase of calcium aluminum oxide hydrate ($4CaO \cdot Al_2O_3 \cdot xH_2O$ (PDF#02-0077) and $3CaO \cdot Al_2O_3 \cdot xH_2O$ (PDF#02-0083)). After 6 h, the phase of $4CaO \cdot Al_2O_3 \cdot xH_2O$ completely disappeared and $3CaO \cdot Al_2O_3 \cdot xH_2O$ became the end-product, but the Ca^{2+} and $Al(OH)_4^-$ concentrations were kept constant which indicates the ion-exchanging of I^- with OH^- also happened in the simple dissolution process.
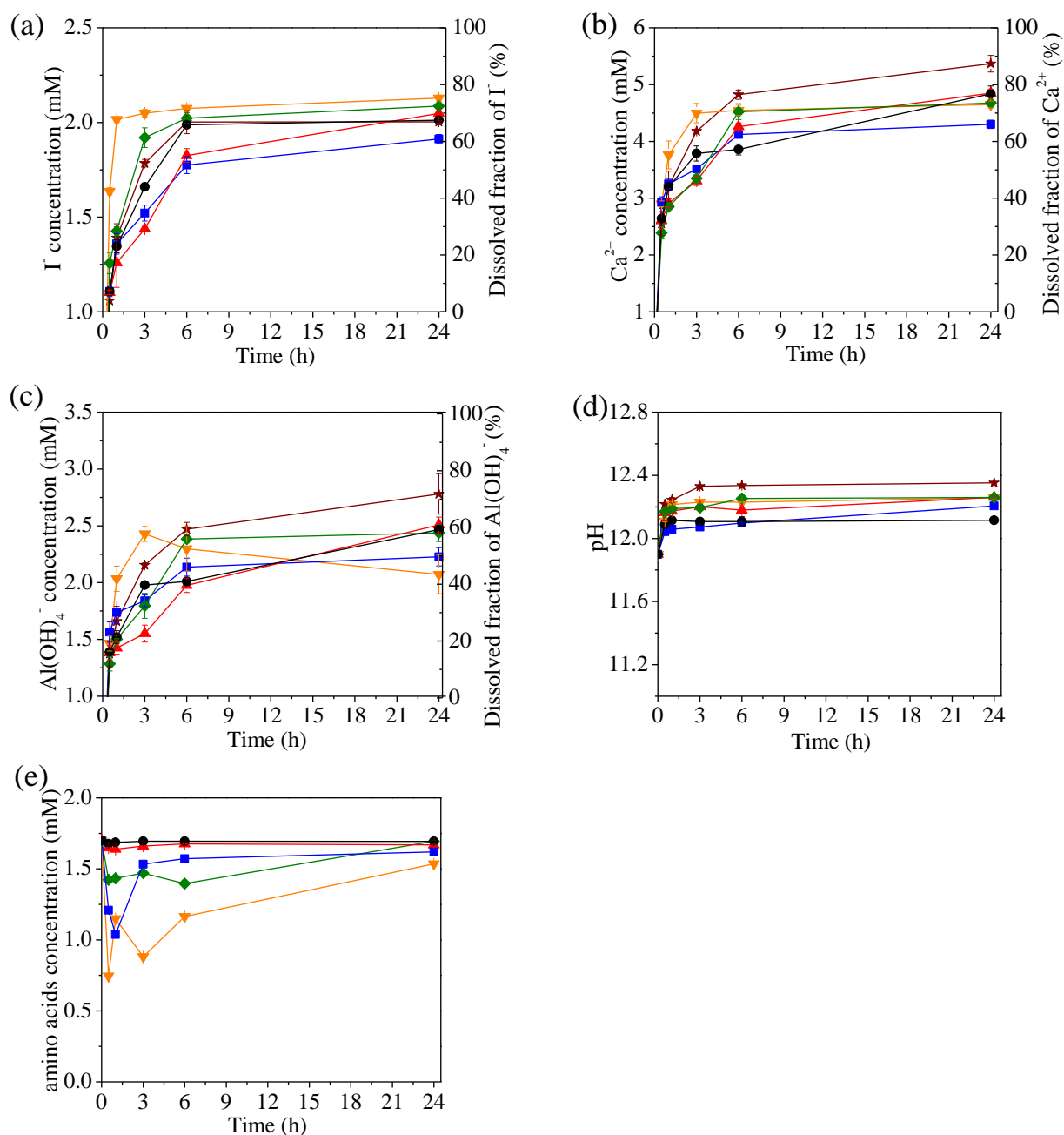
Fig. 3.2 The concentrations of released (a) I⁻, (b) Ca^{2+} (c) $Al(OH)_4^-$ and (d) pH in the presence and absence of 1.7 mM amino acids at different time intervals. Symbols: ★, Blank; ▲, HGly; ◆, H_2Asp; ▼, H_2Cys; ■, HPhe; ●, HTrp.

Amino acids of H_2Cys, H_2Asp, HGly, HTrp, and HPhe with a concentration of 1.7 mM were used to explore the environmental impact of amino acids on the stability of Ca_2Al-LDH(I). As shown in **Fig. 3.2(d)**, the equilibrated pH in all series was higher than 12.0, so the -COOH, $-NH_3^+$,

and thiol (-SH) functional groups in all amino acids were dissociated because of pK_a values of five amino acids. This means H_2Cys, H_2Asp, $HGly$, $HTrp$, and $HPhe$ existed in the form Cys^{2-}, Asp^{2-}, Gly^-, Trp^-, and Phe^- under the present pH. Based on the bond length and bond angle of each amino acid molecule, the size includes length (Å) and width (Å) were estimated (Ching et al., 1989; Weast and Astle, 1979). Glycine (3.9/3.5 Å), cysteine (6.4/3.7 Å), aspartic acid (6.5/3.5 Å), phenylalanine (9.7/4.7 Å), and tryptophan (10.9/5.6 Å), so we can clearly distinguish the phenylalanine and tryptophan have bigger molecular sizes. Combing with the van der Waals volume (Nölting, 2006) of glycine (48 Å^3), cysteine (86 Å^3), aspartic acid (91 Å^3), phenylalanine (135 Å^3), and tryptophan (163 Å^3), so the glycine has the smallest molecular size and cysteine is smaller than aspartic acid.

In the presence of H_2Cys, at 0.5 h and 1 h, the leaching fraction of I^- corresponded to 74.7% (1.637 mM) and 91.9% (2.016 mM), respectively (**Fig. 3.2(a)**). After 24 h, the released amount was 2.128 mM, occupying 97.1% of the original content of I^- in $Ca_2Al-LDH(I)$ and almost I^- was released from $Ca_2Al-LDH(I)$. Therefore, the releasing rate of I^- was much enhanced in the presence of H_2Cys, compared with blank test at all times, and finally, the leaching amount also was larger than 2.003 mM in blank. From **Fig. 3.2(e)**, the changes in H_2Cys concentration indicate a possible ion-exchange mechanism of Cys^{2-} as **Eq. (3.4)**:

$$Ca_4Al_2(OH)_{12}I_2 \cdot 4H_2O + Cys^{2-} \rightarrow Ca_4Al_2(OH)_{12}(Cys) \cdot 4H_2O + 2I^- \tag{3.4}$$

After 0.5 h, the concentration of Cys^{2-} reduced to 0.75 mM, which means 0.95 mM Cys^{2-} was immobilized in solid. According to the charge balance, Cys^{2-} provided 1.9 meq/L negative charges which were enough to substitute with 1.637 mM I^- from $Ca_2Al-LDH(I)$. Also, the XRD patterns verified the expectation. In **Fig. 3.3(b)**, two reflections at d_{003} 10.306 Å (8.58°, 2θ) and 11.694 Å (7.56°, 2θ) after 0.5 h appeared and should be assigned to $Ca_2Al-LDH(Cys)$. After 3 h, the d_{003} peak intensity of $Ca_2Al-LDH(Cys)$ at 8.54° (2θ) decreased and almost disappeared after 24 h resulting in $3CaO \cdot Al_2O_3 \cdot xH_2O$, which is the main phase. The Ca^{2+} and $Al(OH)_4^-$ concentrations

before 6 h in **Fig. 3.2(b), (c)** showed higher values than blank test, this might indicate the ion-exchanging process affected to unstabilize the metallic hydroxide layer of Ca_2Al-LDH(I). After 6 h, the reduction of Ca^{2+} and $Al(OH)_4^-$ concentrations ascribed to the co-precipitation with OH^- to form $3CaO·Al_2O_3·xH_2O$.

H_2Asp showed a bit different trend from H_2Cys, while both amino acids are charged -2 under the present conditions. In the presence of H_2Asp, the released rate of I^- was slower than H_2Cys series but larger than blank test as shown in **Fig. 3.2(a)**. At the suspension time of 0.5 h and 1 h, the releasing concentration of I^- was 1.258 mM (57.4%) and 1.426 mM (65.1%), separately, which is much lower than in H_2Cys series. After 24 h, 2.087 mM I^- was released corresponding to 95.2% of the original amount of I^- in Ca_2Al-LDH(I). The changes in Asp^{2-} concentrations in **Fig. 3.2(e)** showed the adsorbed amounts of Asp^{2-} were smaller than Cys^{2-}. After 0.5 h, the concentration of Asp^{2-} decreased from 1.70 mM to 1.42 mM, so 0.56 meq/L of negative charges were used to ion-exchange with I^-. In **Fig. 3.3(c)**, a phase of Ca_2Al-LDH(Asp) appeared within 0.5 h with the d_{003} value of 11.305 Å (7.82°, 2θ) and was kept until 6 h with a small intensity. Therefore, this solid phases changing process also verified the ion-exchange of Asp^{2-} with I^- as **Eq. (3.5)**:

$$Ca_4Al_2(OH)_{12}I_2·4H_2O + Asp^{2-} \rightarrow Ca_4Al_2(OH)_{12}(Asp)·4H_2O + 2I^- \quad (3.5)$$
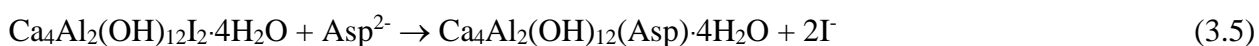
In **Fig. 3.2(b), (c)**, the released amount of Ca^{2+} and $Al(OH)_4^-$ concentrations were always lower than in blank test except in the presence of H_2Cys, demonstrating that leaching of I^- was not caused by simple dissolution. So the residual 0.698 mM I^- at 0.5 h was ascribed to ion-exchange with OH^- in Ca_2Al-LDH(I) to form $3CaO·Al_2O_3·xH_2O$.

As observed in **Fig. 3.3(b), (c)**, the d_{003} diffraction peaks of Ca_2Al-LDH(Cys/Asp) gradually disappeared after 24 h but the released fraction of Ca^{2+} and $Al(OH)_4^-$ concentrations were kept constant. That means Ca_2Al-LDH(Cys/Asp) phases were unstable and changed to $3CaO·Al_2O_3·xH_2O$ phase through ion-exchange of Cys^{2-}/Asp^{2-} with OH^- as **Eq. (3.6)**.

$$Ca_4Al_2(OH)_{12}(Amino\ acid)·4H_2O + yOH^- \rightarrow 3CaO·Al_2O_3·xH_2O + (Amino\ acid)^{2-} + Ca^{2+} \quad (3.6)$$

The different performance of H_2Cys and H_2Asp on the releasing rate of I^- might be caused by their different molecular sizes and the existence of thiol group (-SH) in H_2Cys. Cys^{2-} possesses a little bit smaller molecule than Asp^{2-} under the same alkaline condition made it easier to go the interlayer of hydrocalumite.

However, in the HGly and HTrp series, **Fig. 3.2(a)** showed a similar released amount of I^- to blank test within the initial 0.5 h. During the period of 0.5 h to 6 h, the leaching amount of I^- was lower than in the blank. Furthermore, the released amounts of Ca^{2+} (**Fig. 3.2(b)**) and $Al(OH)_4^-$ (**Fig. 3.2(c)**) were lower than in blank. This means the surface adsorption of Gly^- and Trp^- by electrostatic interaction on hydrocalumite might more easily happen than intercalation of them into $[Ca_2Al(OH)_6]^+$ metallic interlayer. **Fig. 3.2(e)** presents the changes in amino acids concentrations in the period from 0 to 24 h. The adsorption of Gly^- and Trp^- on solid phases were always in very low values over the reaction times, which are consistent with the prediction that only surface adsorption of them happened rather than intercalation. This phenomenon relates to their properties. HGly has the smallest molecular size among these amino acids, but it displayed Gly^- at the present pH. Therefore, the ion-exchange of Gly^- with I^- seems difficult to happen. For HTrp, it possesses a relatively large molecular size, one negative charge, and aromatic group that make it more difficult to go into the hydrocalumite interlayer by substituting with I^-. After adding 1.7 mM HGly, the phase of Ca_2Al-LDH(I) was maintained within 6 h but disappeared and transformed into $3CaO \cdot Al_2O_3 \cdot xH_2O$ as the main product after 24 h (**Fig. 3.3(d)**). It seems that HGly acted to stabilize Ca_2Al-LDH(I) a bit longer, compared with no co-existing amino acids. It seems no d_{003} diffraction peak of Ca_2Al-LDH(Gly) appeared in small diffraction angles, so the intercalation of HGly did not significantly happen. When HTrp was co-existing with Ca_2Al-LDH(I) (**Fig. 3.3(f)**), the intermediate phase of calcium aluminum oxide hydrate of $2CaO \cdot Al_2O_3 \cdot xH_2O$ (PDF#12-0008), $4CaO \cdot Al_2O_3 \cdot xH_2O$, and $3CaO \cdot Al_2O_3 \cdot xH_2O$ appeared after 3

h. However, XRD peaks assigned to $2CaO \cdot Al_2O_3 \cdot xH_2O$ seems to overlap with Ca_2Al-LDH(I) from 3 h to 6 h.

In the presence of HPhe, it showed different suppression results for I^- compare with HGly and HTrp. The released I^- concentration was a little bit larger than in HGly within 3 h, but after 6 h, the leaching rate decreased after 24 h, and the releasing concentration of I^- was 1.913 mM which is lower than in blank tests and other amino acids series. HPhe and HTrp belong to aromatic amino acids which have similar molecular sizes and structures, but within 1 h, the concentration of HPhe decreased to 1.04 mM, indicating that 0.66 mM Phe^- was kept on solid phase. Combined the solution data with the corresponding and XRD patterns, the surface adsorption of Phe^- can be suspected. In **Fig. 3.3(e)**, $3CaO \cdot Al_2O_3 \cdot xH_2O$ became the main phase after 24 h but Ca_2Al-LDH(I) in the solid residues was still maintained. It is obvious that I^- is still preserved in hydrocalumite rather than releasing into solution. This phenomenon is consistent with the solution results in **Fig. 3.2(a)**, indicating that more significantly inhibitory effects of HPhe. As the reaction time going, the concentration of Phe^- in the solid phase decreased as the solid phase changed from Ca_2Al-LDH(I) to $3CaO \cdot Al_2O_3 \cdot xH_2O$, suggesting that HPhe might be likely to adsorb on the surface of Ca_2Al-LDH(I). Based on the above results, HPhe and HTrp showed different effects on the leaching of I^- from Ca_2Al-LDH(I). HPhe and HTrp have one -COOH group and a side chain with an aromatic group to make the hydrophobic property. Initially, the ion-exchange and surface adsorption of negative charged Phe^- and Trp^- are possible to happen on Ca_2Al-LDH(I). The adsorbed Phe^- and Trp^- may modify the surface properties of Ca_2Al-LDH(I) from hydrophilic to hydrophobic in some extent. Under the high concentration of 1.7 mM HPhe and HTrp, more hydrophobic molecules were adsorbed onto the surface rather than stabled in the interlayer. However, HPhe has more strongly hydrophobic property, when Phe^- adsorbed onto the surface by electrostatic interaction, OH^- in solution is difficult to contact with Ca_2Al-LDH(I) so it might prevent the OH^- ion-exchange with I^-.

To make sure the decomposition of Ca_2Al-LDH(I), the particle morphologies of solid residues before and after reaction with different amino acids for 24 h were observed by SEM in **Fig. 3.4**. **Fig. 3.4(c)** shows the morphology of Ca_2Al-LDH(I) solid residue after suspended into alkaline solution in the absence of amino acids. The hexagonal structure, irregular structures, and collapsed layer structure were observed which are characteristic of the typical layered double hydroxides. After suspended into different amino acids solutions, in H_2Cys (**Fig. 3.4(d)**), H_2Asp (**Fig. 3.4(e)**), HGly (**Fig. 3.4(f)**), and HTrp (**Fig. 3.4(h)**) series, there are not only collapsed layer structures but also aggregation and frame of hexagonal structure, suggesting the dissolution of Ca_2Al-LDH(I). For HPhe (**Fig. 3.4(g)**), the layer structure and clear hexagonal-like morphology still existed which is consistent with the XRD pattern at 24 h (**Fig. 3.3(e)**).

Therefore, based on the above results, HGly, HTrp, and HPhe suppressed the dissolution rate of Ca_2Al-LDH(I), and HPhe also suppressed the releasing amount of I^-, while H_2Cys, H_2Asp enhanced the release of I^- from Ca_2Al-LDH(I) to form other solid phases but in different rates. Furthermore, the small amount of Ca_2Al-LDH(I) still existed according to SEM images where hexagonal morphology was maintained.
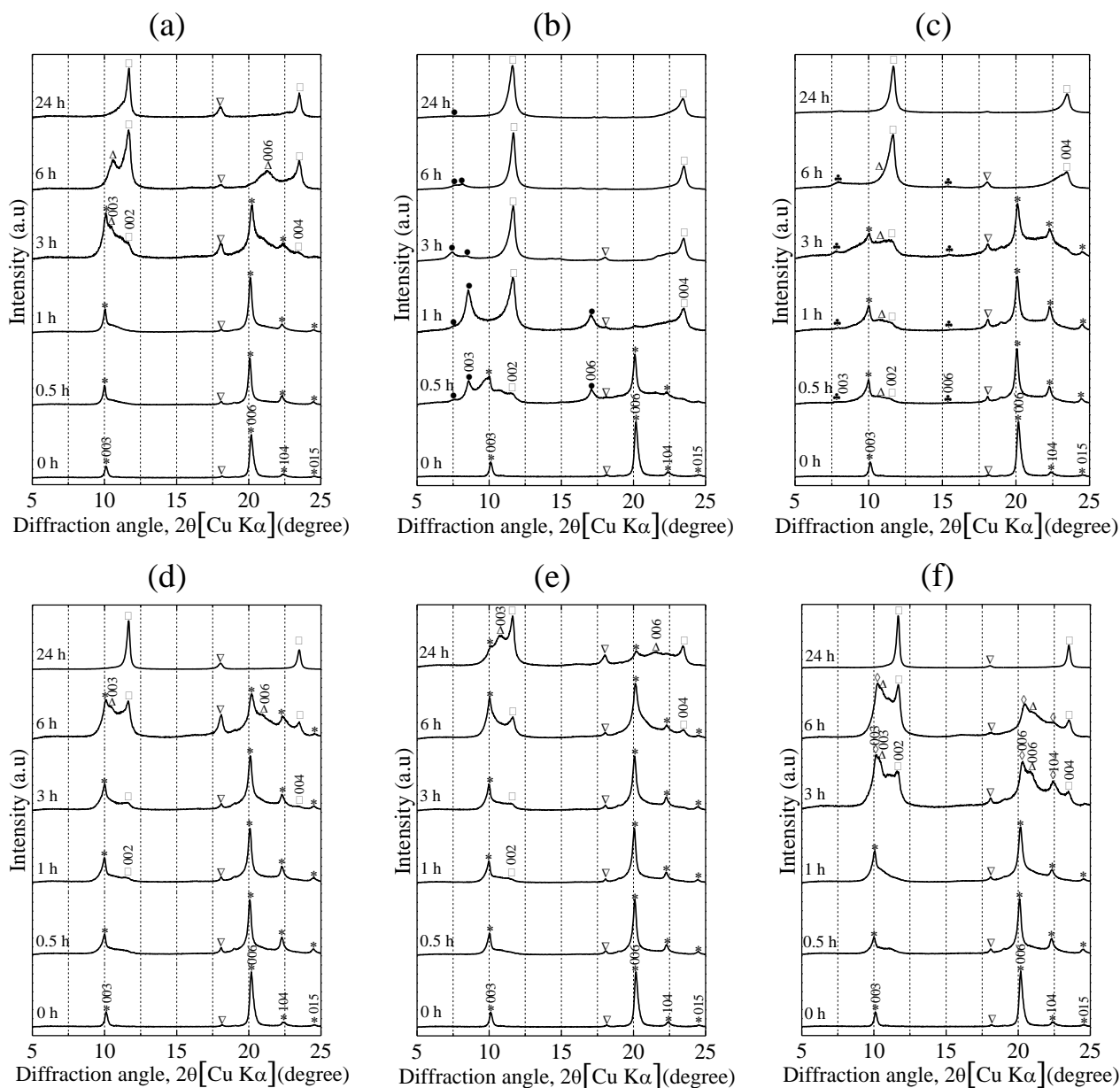
Fig. 3.3 X-ray diffraction patterns of solid residues after reaction with different amino acids at time intervals. (a) Blank, (b) H$_2$Cys, (c) H$_2$Asp, (d) HGly, (e) HPhe, (f) HTrp. Symbols indicate, * calcium aluminum iodide oxide hydrate (3CaO·Al$_2$O$_3$·CaI$_2$·10H$_2$O, PDF#42-1474); □ calcium aluminum oxide hydrate (3CaO·Al$_2$O$_3$·xH$_2$O, PDF#02-0083); ∇ unknown; Δ calcium aluminum oxide hydrate (4CaO·Al$_2$O$_3$·xH$_2$O, PDF#02-0077); ◊ calcium aluminum oxide hydrate (2CaO·Al$_2$O$_3$·6H$_2$O, PDF#12-0008), and/or calcium aluminum iodide oxide hydrate (3CaO·Al$_2$O$_3$·CaI$_2$·H$_2$O); ● Cys-hydrocalumite (Ca$_2$Al-LDH(Cys)); ♣ Asp-hydrocalumite (Ca$_2$Al-LDH(Asp)).
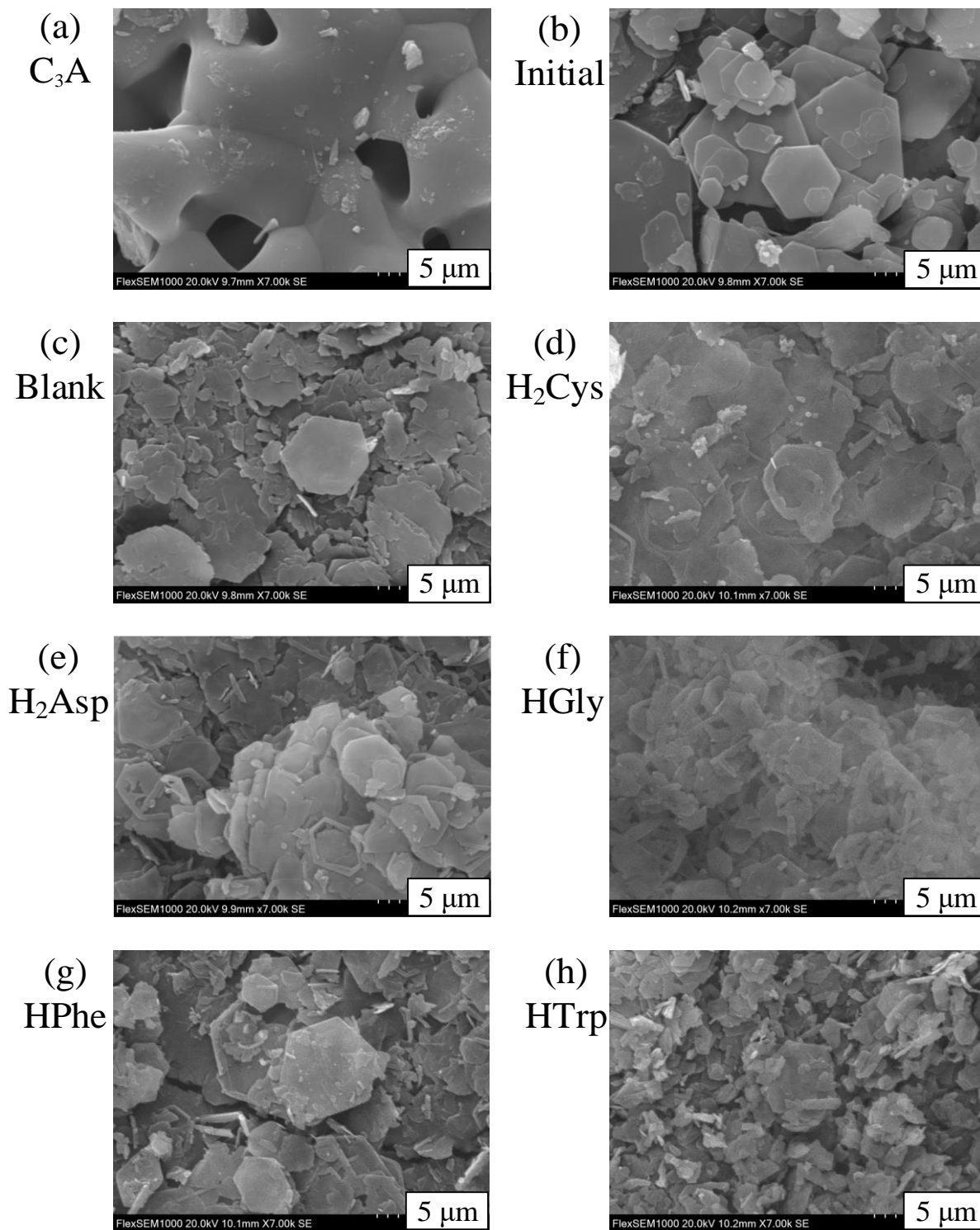
Fig. 3.4 SEM-EDS images of (a) C₃A, (b) original Ca₂Al-LDH(I); and solid residues after suspension of Ca₂Al-LDH(I) in different solutions for 24 h. (c) Blank, (d) HGly, (e) H₂Asp, (f) H₂Cys, (g) HPhe, (h) HTrp.

3.3.3 Behavior of amino acids in Ca_2Al-LDH(I)

To explore the different effects between Cys^{2-} and Asp^{2-} on interaction with Ca_2Al-LDH(I), the total formation energies calculated by DFT considering different configurations of Ca_2Al-LDH(Cys) and Ca_2Al-LDH(Asp) were plotted against their interlayer spacing in **Fig. 3.5**. There is a positive correlation which based on the total formation energies of the system increased with an increase in the interlayer distances. The higher formation energy means a more unstable system. Here, we selected the most stable and most unstable systems which possess the lowest and highest total energies, respectively. In **Fig. 3.6(a)**, the most stable configuration $Ca_4Al_2(OH)_{12}$·Asp (0 kJ/mol) showed the interlayer distance of 7.34 Å with 1 Ca-O bond and 7 hydrogen bonds in one unit cell. In **Fig. 3.6(b)**, the most unstable system $Ca_4Al_2(OH)_{12}$·Asp (103 kJ/mol) showed the layer spacing of 9.21 Å with 1 Ca-O bond and 6 hydrogen bonds between metal hydroxide layers and Asp^{2-} in one unit cell. For H_2Cys, the most stable system of $Ca_4Al_2(OH)_{12}$·Cys with a formation energy of 0 kJ/mol shows a 7.22 Å of interlayer spacing including 1 Ca-O and 3 hydrogen bonds between metal hydroxide layers and Cys^{2-} (**Fig. 3.6(d)**). In the most unstable system, $Ca_4Al_2(OH)_{12}$·Cys showed 8.35 Å of interlayer distance in 86 kJ/mol with 1 Ca-O and 4 hydrogen bonds (**Fig. 3.6(e)**). From these results, the simulation predicted much lower interlayer spacings than the observed XRD results (**Fig. 3.3(b), (c)**). As can be confirmed, the water molecules can cause to expansion of the interlayer spacings in experimental results (Yan et al. 2009; Grégoire et al. 2016). So we considered the new system which includes one water molecule in one unit cell of hydrocalumite including Asp^{2-} as shown in **Fig. 3.6(c)**. In the system of $Ca_4Al_2(OH)_{12}Asp$·$4H_2O$, the corresponding interlayer spacing was 7.99 Å under the lowest formation energy of 0 kJ/mol, which indicates the presence of water molecule can affect to expand the interlayer distances. Therefore, in the real system, the most stable state is possibly be overlapped by the d_{003} peak in XRD assigned to $3CaO$·Al_2O_3·CaI_2·$10H_2O$ in 11.6°, 2θ. The XRD diffraction peaks at 8.54° (2θ), 7.61° (2θ) and 7.92° (2θ) in **Fig. 3.3(b), (c)** might be caused by the

different water molecule numbers included in each system affecting the configurations of Asp^{2-} and Cys^{2-} in metallic hydroxide layer. Another factor might be related to the difference of basal layer charge densities which has been confirmed through the positive correlation relationship between them (Zhang et al., 2017).
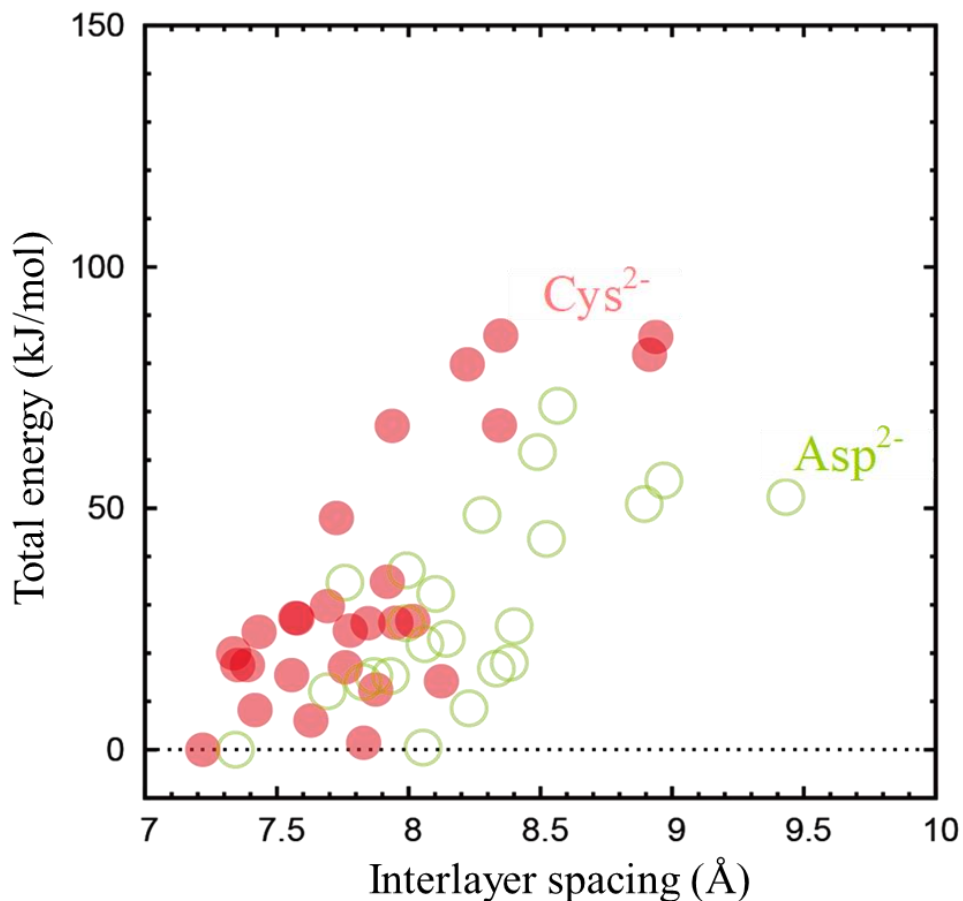
Fig. 3.5 Total energies plotted against interlayer spacing for Ca_2Al-LDH(I) after intercalated Asp^{2-} (green circles) and Cys^{2-} (red circles) with respect to the total energy of the most stable system.

(a) H₂Asp, without H₂O   (b) H₂Asp, without H₂O   (c) H₂Asp, with H₂O

(d) H₂Cys, without H₂O   (e) H₂Cys, without H₂O

Ca   Al   O   C   N   S   H
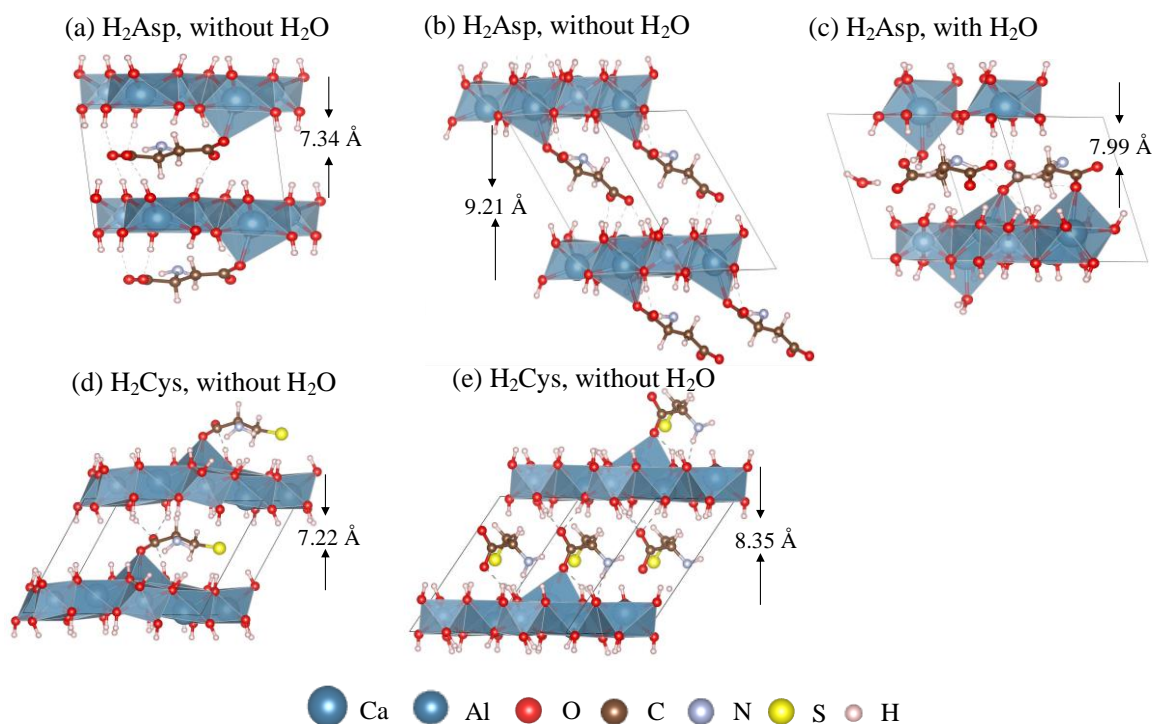
Fig. 3.6 Schematic structures obtained by DFT calculations on the Ca₂Al-LDH with Asp²⁻ and Cys²⁻. The dashed and solid lines indicate hydrogen bonds and Ca-O bonds, respectively. (a) Asp, without H₂O, most stable (0 kJ/mol); (b) Asp, without H₂O, most unstable (103 kJ/mol); (c) Asp, with H₂O, most stable (0 kJ/mol); (d) Cys, without H₂O, most stable (0 kJ/mol); (e) Cys, without H₂O, most unstable (86 kJ/mol).

3.4 Conclusions

The interaction of five selected amino acids with iodide intercalated hydrocalumite was investigated by solid and solution chemistry integrated with DFT simulation. Ca_2Al-LDH(I) was very fragile to cause the dissolution even though under pH 12.0. After suspended into amino acids solutions, the main factors to cause the release of I^- are divided into ion-exchange and simple dissolution. H_2Cys and H_2Asp accelerated the releasing rate of I^- through ion-exchange between Cys^{2-}/Asp^{2-} and I^-. In XRD, the expanded d_{003} spacings were observed, which was different from the other three amino acids. However, the effects of Cys^{2-} and Asp^{2-} on the ion-exchange with I^- in hydrocalumite and the stability of Ca_2Al-LDH(I) were different. Asp^{2-} maintained the structure of Ca_2Al-LDH(I) for a longer time than Cys^{2-}, and Cys-intercalated hydrocalumite showed one

smaller d_{003} spacing than Asp-intercalated hydrocalumite in XRD patterns. This was also verified by DFT simulation. DFT simulation also confirmed that the interlayer spacings might be strongly influenced by the presence of water molecules and the numbers. There are interaction forces between amino acids and hydrocalumite in which the hydrogen and Ca-O bonds contributed to their configurations but the Ca_2Al-LDH(Cys/Asp) system still is unstable. In the presence of HGly, HTrp, and HPhe, the simple dissolution and ion-exchange with OH^- contributed to Ca_2Al-LDH(I) decomposition, and moreover, HPhe showed a little bit inhibitory effects on the release of I^- by surface adsorption. Analogically based, some organic matters negatively charged with a large molecule and less affinity than I^- might make hydrocalumite stable. For iodide isotopes stabilization in cementitious materials, Ca_2Al-LDH(I) may form but the stabilization is strongly influenced by the geochemical environment.

References

Aimoz, L., Wieland, E., Taviot-Guého, C., Dähn, R., Vespa, M., Churakov, S.V., 2012. Structural insight into iodide uptake by AFm phases. Environ. Sci. Technol. 46, 3874-3881.

Ching, C.; Hidajat, K.; Uddin, M.,1989. Evaluation of equilibrium and kinetic parameters of smaller molecular size amino acids on KX zeolite crystals via liquid chromatographic techniques. Sep. Sci. Technol. 24, 581-597.

Choi, W., Ghorpade, P.A., Kim, K., Shin, J., Park, J., 2012. Properties of synthetic monosulfate as a novel material for arsenic removal. J. Hazard. Mater. 227-228, 402-409.

Dai, J.L., Zhang, M., Hu, Q.H., Huang, Y.Z., Wang, R.Q., Zhu, Y.G., 2009. Adsorption and desorption of iodine by various Chinese soils: II. Iodide and iodate. Geoderma 153, 130-135.

Emerson, H.P., Xu, C., Ho, Y., Zhang, S., Schwehr, K.A., Lilley, M., Kaplan, D.I., Santschi, P.H., Powell, B.A., 2014. Geochemical controls of iodine uptake and transport in Savannah River Site subsurface sediments. Appl. Geochem. 45, 105-113.

Gao, K., Chen, G., Wu, D., 2014. A DFT study on the interaction between glycine molecules/radicals and the (8, 0) SiCNT. Phys. Chem. Chem. Phys. 16, 17988-17997.

Grégoire, B., Erastova, V., Geatches, D.L., Clark, S.J., Greenwell, H.C. and Fraser, D.G., 2016. Insights into the behaviour of biomolecules on the early Earth: The concentration of aspartate by layered double hydroxide minerals. Geochimica et Cosmochimica Acta, 176, 239-258.

Li, J., Zhou, H., Wang, Y., Xie, X., Qian, K., 2017. Sorption and speciation of iodine in groundwater system: The roles of organic matter and organic-mineral complexes. J. Contam. Hydrol. 201, 39-47

Momma, K., Izumi, F., 2011. VESTA 3 for three-dimensional visualization of crystal, volumetric and morphology data. J. Appl. Crystallogr. 44, 1272-1276.

Nedyalkova, L., Lothenbach, B., Geng, G., Mäder, U., Tits, J., 2020. Uptake of iodide by calcium aluminate phases (AFm phases). Appl. Geochem. 116, 1-13.

Nölting, B., 2006. Physical interactions that determine the properties of proteins. Springer.

Ong, S.P., Richards, W.D., Jain, A., Hautier, G., Kocher, M., Cholia, S., Gunter, D., Chevrier, V.L., Persson, K.A., Ceder, G., 2013. Python Materials Genomics (pymatgen): A robust, open-source python library for materials analysis. Comput. Mater. Sci. 68, 314-319.

Sánchez-Herrero, M.J., Fernández-Jiménez, A., Palomo, A., 2012. Alkaline Hydration of Tricalcium Aluminate. J. Am. Chem. Soc. 95, 3317-3324.

Sacerdoti, M., Passaglia, E., 1988. Hydrocalumite from Latium, Italy: its crystal structure and relationship with related synthetic phases. Neues Jahrb. für Mineral. Monatshefte. 10, 462-475.

Weast, C., Astle, M., 1979. Handbook of Chemistry and Physics, ; Table D-190. CRC Press, Boca Raton, FL.

Xu, C., Kaplan, D.I., Zhang, S., Athon, M., Ho, Y., Li, H., Yeager, C.M., Schwehr, K.A., Grandbois, R., Wellman, D., 2015. Radioiodine sorption/desorption and speciation transformation by subsurface sediments from the Hanford Site. J. Environ. Radioactiv. 139, 43-55.

Yan, D., Lu, J., Wei, M., Ma, J., Evans, D.G. and Duan, X., 2009. A combined study based on experiment and molecular dynamics: perylene tetracarboxylate intercalated in a layered double hydroxide matrix. Physical Chemistry Chemical Physics, 11(40), 9200-9209.

Zhang, Y., Liu, X., Zhang, C., He, M. and Lu, X., 2017. Interlayer structures and dynamics of arsenate and arsenite intercalated layered double hydroxides: A first principles study. Minerals, 7(4), 53.

Yan, D., Lu, J., Wei, M., Ma, J., Evans, D.G. and Duan, X., 2009. A combined study based on experiment and molecular dynamics: perylene tetracarboxylate intercalated in a layered double hydroxide matrix. Physical Chemistry Chemical Physics, 11(40), 9200-9209.

Zhang, Y., Liu, X., Zhang, C., He, M. and Lu, X., 2017. Interlayer structures and dynamics of arsenate and arsenite intercalated layered double hydroxides: A first principles study. Minerals, 7(4), 53.

Chapter 4 Environmental impact of amino acids on the release of selenate immobilized in hydrotalcite

4.1 Introduction

Se dominates in SeO_4^{2-} and/or SeO_3^{2-} in aqueous environments, which are more mobile than cationic species due to the negative charges of the surface of silicate minerals as major constituents in the earth crust. However, SeO_4^{2-} is more mobile than SeO_3^{2-} in LDHs (Constantino et al., 2017). The immobilization mechanisms of SeO_4^{2-} into LDHs mainly involve surface adsorption, co-precipitation and anionic exchange (Chubar and Szlachta, 2015; Constantino et al., 2017; Zhu et al., 2017). Hydrotalcite (Mg$_2$Al-LDH) belongs to layered double hydroxides (LDHs) family, which possesses the ability to retain SeO_4^{2-} (You et al., 2001; Paikaray et al., 2013; Opiso et al., 2016; Tian et al., 2020b). Meanwhile, there are no reports to investigate the natural effects from biodegraded organic matters on the stability of immobilized anionic radioactive species in Mg$_2$Al-LDH.

Therefore, in the present work, we report here the effect of amino acids on the stability of incorporated SeO_4^{2-} in hydrotalcite, which serves as a model for the chemical environment of the pedosphere. The release behavior of SeO_4^{2-} accompanied with changes in the layer spacing of Mg$_2$Al-LDH was interpreted from the aspects of the configurations and coordination of amino acids in the interlayer of Mg$_2$Al-LDH through density-functional theory (DFT) calculations. The present work provides prospective alarms toward the radioactive waste in repositories and the environmental problems of concrete at low durability.

4.2 Experimental

4.2.1 Materials

Five amino acids, L-tryptophan (HTrp, $C_{11}H_{12}N_2O_2$), L-phenylalanine (HPhe, $C_9H_{11}NO_2$), Glycine (HGly, $C_2H_5NO_2$), L-aspartic acid (H$_2$Asp, $C_4H_7NO_4$), L-cysteine (H$_2$Cys, $C_3H_7NO_2S$) were selected in the present work as shown in **Table 1.1**. They have different functional groups, charges, and molecular sizes. H$_2$Asp includes two carboxyl groups and H$_2$Cys contains one thiol group as well as one carboxyl group in one molecule, which contributes to the formation of negative charges. All of amino acids are in special grade and were purchased from Wako Chemicals (Osaka, Japan).

Inorganic chemicals including $Mg(NO_3)_2 \cdot 6H_2O$ (99%), $Al(NO_3)_3 \cdot 9H_2O$ (98%), NaOH (97%), Na_2SeO_4 (97%), $NaNO_3$ (99%) for the synthesis of Mg$_2$Al-LDH are in analytical grade and supplied from Wako Chemicals (Osaka, Japan). Each solution was prepared using decarbonized water which was prepared by boiling ultra-pure water purged with N_2 gas (99.99%) for 2 h.

4.2.2 Synthesis of Mg$_2$Al-LDH(SeO$_4$)

Firstly, Mg$_2$Al-LDH(NO$_3$) was prepared through the co-precipitation method. 20 mL of the solution including 1 M $Mg(NO_3)_2$ and 0.5 M $Al(NO_3)_3$ (solution A) dropwise into 30 mL 0.33 M $NaNO_3$ (solution B) under vigorous stirring with the pH maintained at 10.0 using 3 M NaOH. Afterward, the obtained slurries were stirred for another 30 min and then transferred into the Teflon vessels which were put in an Ethos Plus microwave (Milestone General, Kawasaki, Japan) oven for 5 h at 373 K. Thereafter, the precipitates were collected by centrifugation at 8000 rpm for 6 min, washed by pure water several times and freeze-dried for 24 h. It should be noted that the whole procedure was conducted under N_2 atmosphere to minimize the contamination of carbon dioxide (CO$_2$).

Secondly, 1.0 g of the above product was suspended into 50 mL 41 mM Na_2SeO_4 and the mixture was stirred at 300 rpm for 24 h. This process was repeated 2 times to maximize the ion exchange with SeO_4^{2-} in Mg_2Al-LDH(NO_3) to get selenate-bearing Mg_2Al-LDH (Mg_2Al-LDH(SeO_4)). The powdery product was obtained at pH 8.0 after going through centrifugation, washing, and drying as mentioned above. All of the procedures were conducted in a glovebox (95% N_2, 5% H_2, COY, M-160, Grass Lake, US).

Both products were characterized by XRD (**2.2.1 section**), ICP-OES (**2.1.1 section**), and ICP-MS (**2.1.2 section**) after HNO_3 decomposition.
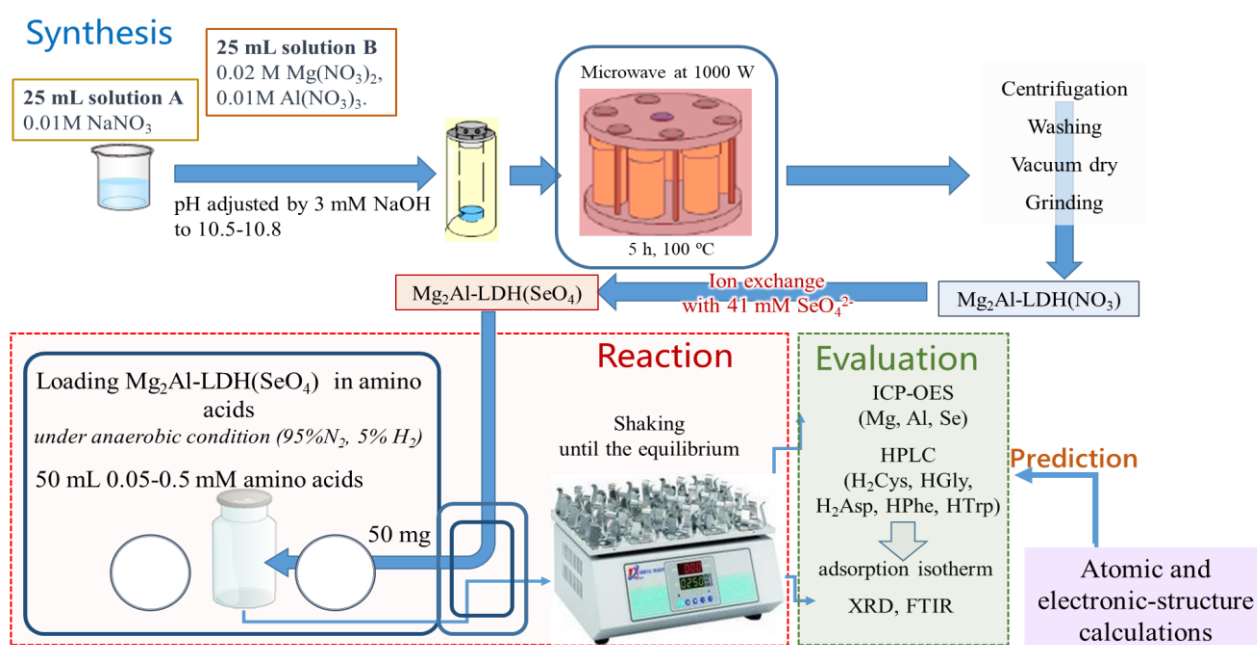
Scheme 4.1 Experimental procedure of Mg_2Al-LDH(SeO_4) with different amino acids.

4.2.3 Reaction of Mg_2Al-LDH(SeO_4) with amino acids

The solutions of HTrp, HPhe, HGly, H_2Asp, and H_2Cys were prepared separately using decarbonized water in the range of 0.0-0.5 mM. According to the pK_a values of the amino group, the pH of each solution was adjusted to 10.8-11.0 using 3 M NaOH to keep the maximum amount of negative charges. 50 mg of the obtained Mg_2Al-LDH(SeO_4) was separately added into 50 mL

of the above amino acid solution with a solid/liquid ratio of 1 g/L. Separately, the blank solution without any amino acids was also prepared as a control. At room temperature, the suspensions were stirred for 24 h and filtrated using 0.2 µm membrane filters to obtain the supernatant for determination of the remaining amino acids concentrations by HPLC (**2.1.4 section**) and the released Se^{6+}, Mg^{2+} and $Al(OH)_4^-$ concentrations by ICP-OES (**2.1.1 section**) and ICP-MS (**2.1.2 section**). It is worth noting that the pH adjustment and solutions transfer were all conducted in a glovebox to minimize CO_2 effects.

The adsorption density of each amino acid was calculated by **Eq. (4.1)**:

$$Q_e = (C_0 - C_e) \cdot V/m \tag{4.1}$$

where Q_e (mmol g^{-1}) is the amino acid sorption amount in Mg_2Al-LDH(SeO$_4$) after 24 h, C_0 (mM) is the initial concentration of amino acid, C_e (mM) is the equilibrium concentration of amino acid after the interaction, V (L) is the volume of solution and m (g) is the mass of Mg_2Al-LDH(SeO$_4$). It was confirmed that the equilibrium was achieved within 24 h.

4.2.4 Chemical analysis and solid characterization

The solid residues were collected to provide for the determination of elemental compositions and measurements of XRD (**2.2.1 section**) and zeta potentials (**2.1.5 section**). The elemental compositions of Mg_2Al-LDH(NO$_3$) and Mg_2Al-LDH(SeO$_4$) were estimated by digesting a specific amount of solid phase in 25 mL 5% HNO$_3$ to collect the solution. Nitrate (NO$_3^-$) was determined by IC (**2.1.3 section**) after the sample was dissolved into 0.1 M HCl. The fourier transform infrared (FTIR) spectroscopy (400-4000 cm^{-1}) of the samples diluted by KBr were collected on a JASCO 670 Plus (Japan) spectrometer at a resolution of 4 cm^{-1}. The carbon (C), hydrogen (H), nitrogen (N) contents in Mg_2Al-LDH(NO$_3$) and Mg_2Al-LDH(SeO$_4$) were determined by a CHN (**2.2.2 section**). The C content was derived from incorporated carbonate caused by CO_2 contamination.

4.2.5 DFT simulation

As shown in 2.3 section.

Electronic-structure calculations using DFT were performed to figure out the stable configurations of amino acids and selenate ions in LDH and the energies of the ion-exchange and complexation reactions. The following states were treated as valence electrons: 1s for H; 2s and 2p for C, N, and O; 3s and 3p for Mg and Al; 4s and 4p for Se. The lattice constants and internal coordinates were optimized until the residual stress and force converged to 0.0044 GPa and 1 meV/Å, respectively. The unit cells used in this study contain a positively charged Mg_2Al-LDH layer ($[Mg_2Al(OH)_6]^+$) and deprotonated HGly monovalent anions ($[CH_2(NH_2)(COO)]^-$) and/or a selenate (SeO_4^{2-}). A wide variety of configurations of HGly and SeO_4^{2-} ions between the LDH layers were considered for input structural models. A 4×4×2 k-mesh was used according to the Monkhorst-Pack scheme (Monkhorst and Pack, 1976) for the unit cells having the composition of $Mg_2Al(OH)_6 \cdot CH_2(NH_2)(COO)$. The formation energies were calculated based on the following ion-exchange reaction:

$Mg_2Al(OH)_6 \cdot 0.5SeO_4 + xCH_2(NH_2)COOH \rightarrow Mg_2Al(OH)_6 \cdot xCH_2(NH_2)COO \cdot 0.5(1-x)SeO_4 + 0.5xH_2SeO_4$ (4.2)
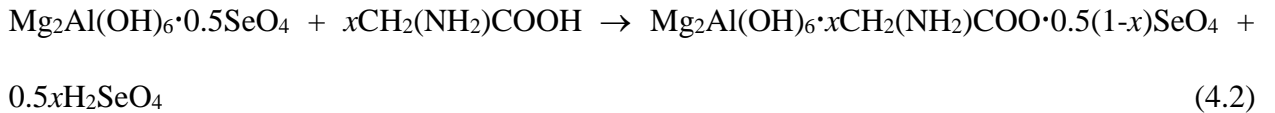
To determine the formation energies, the total energies were independently calculated for the intercalated LDH with the composition of $Mg_2Al(OH)_6 \cdot xCH_2(NH_2)COO \cdot 0.5(1-x)SeO_4$ ($x = 0, 0.5,$ and 1), and H_2SeO_4 and $CH_2(NH_2)COOH$ molecules.

The association energies of Mg^{2+} with deprotonated amino acids ions of Asp^{2-} and Cys^{2-}, are also calculated according to the following reaction:

$Mg^{2+} + A^{2-} \rightarrow Mg\text{-}A$ (4.3)

where A is Asp and Cys, and Mg-A is a complex. During structural optimizations, the dimension of unit cells containing a single ion or a complex was fixed to be 20×20×20 $Å^3$ to keep the ions and complexes isolated. A single k-point sampling at the Γ point was used. For these calculations,

Mg 2s and 2p states are also treated as valence electrons. The HSE06 functional (Heyd et al., 2003; Ge and Ernzerhof, 2006; Krukau et al., 2006) was used for these calculations because it is known to provide a better description for charge density of anions while GGA functional fail to describe negatively charged systems (Kim et al., 2011). Calculated structures for the amino acids ions and complexes were visualized using the VESTA code (Momma and Izumi, 2011).

4.3 Results and discussion

4.3.1 Characterizations of Mg_2Al-LDH(SeO_4)

XRD patterns for two synthesized LDHs are shown in **Fig. 4.1(a)**, indicating the typical layered double hydroxide structure with 003, 006, and 110 reflections. Notably, the value of d_{003} changed from 8.93 Å for Mg_2Al-LDH(NO_3) to 9.10 Å for Mg_2Al-LDH(SeO_4) (Ma et al., 2016; Constantino et al., 2017) and the FWHM at 003, 006 increased after the substitution of NO_3^- with SeO_4^{2-}, as clearly shown in **Fig. 4.1(b)**. FTIR spectra also confirmed the substitution of SeO_4^{2-} with NO_3^- in the Mg_2Al-LDH, as shown in **Fig. 4.1(c)**. The strong band at 1382 cm^{-1} corresponds to the N-O vibration mode in NO_3^- of Mg_2Al-LDH(NO_3) (Wan et al., 2012; Xu et al., 2020). After ion-exchanged with SeO_4^{2-}, the new peak at 872 cm^{-1} and 1369 cm^{-1} were assigned to Se-O vibration and C-O vibration mode, separately (Chubar, 2014; Chubar and Szlachta, 2015), implying some contamination of CO_2 from the air could not be avoided in synthesis.

Table 4.1 Elemental compositions and cell parameters of synthesized Mg_2Al-LDH(NO_3) and Mg_2Al-LDH(SeO_4)

LDHs	Chemical formula	M^{2+}/M^{3+}	a (nm)	c (nm)	d_{003}(nm)
Mg_2Al-LDH(NO_3)	$Mg_{0.77}Al_{0.38}(OH)_{2.32}(NO_3)_{0.34}$ $(CO3)0.015 \cdot 0.79H2O$	2.03	0.3044	2.6779	0.893
Mg_2Al-LDH(SeO_4)	$Mg_{0.72}Al_{0.34}(OH)_{2.29}(SeO_4)_{0.142}$ $(CO_3)_{0.028} \cdot 1.43H_2O$	2.15	0.3038	2.6727	0.910

Combined the elemental compositions, obtained by IC, ICP-OES, and ICP-MS after acid digestion, with CHN analytical results of the solids, the chemical formula of the synthesized LDHs are expressed as $Mg_{0.77}Al_{0.38}(OH)_{2.32}(NO_3)_{0.34}(CO_3)_{0.015}\cdot0.79H_2O$ and $Mg_{0.72}Al_{0.34}(OH)_{2.29}(SeO_4)_{0.142}(CO_3)_{0.028}\cdot1.43H_2O$ (MW 113.3) as summarized in **Table 4.1**. The complete substitution of SeO_4^{2-} with NO_3^- was observed, which is consistent with **Fig. 4.1**, and a small amount of carbonate (CO_3^{2-}) appeared in the Mg_2Al-LDH(SeO_4) sample even though the synthetic procedure was conducted in the N_2 purging glovebox. Lattice parameters and d_{003} values are also listed together in **Table 4.1**. An value of 3.044 Å for Mg_2Al-LDH(NO_3) and 3.038 Å for Mg_2Al-LDH(SeO_4) was found, indicating that the microstructure of the brucite-like sheets was not changed by SeO_4^{2-} intercalation (Constantino et al., 2017).
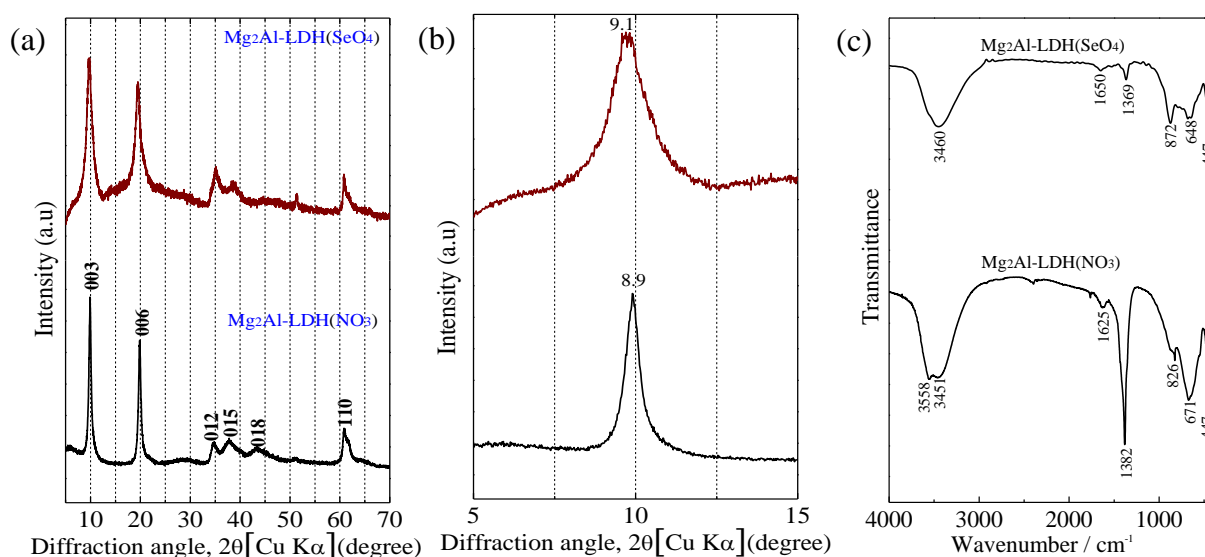
Fig. 4.1 X-ray diffraction patterns ((a), (b)) and FTIR spectra (c) of synthesized Mg_2Al-LDH(NO_3) and Mg_2Al-LDH(SeO_4). Numbers indicate Miller indices in (a) and *d*-values in Å in (b).

4.3.2. Interaction of amino acids with Mg_2Al-LDH(SeO_4)

Without adding any amino acids, the dissolution of Mg_2Al-LDH(SeO_4) was observed at pH 11.0. To evaluate ion-exchange of amino acids with SeO_4^{2-}, the released SeO_4^{2-} in the absence of amino acids caused by simple dissolution of Mg_2Al-LDH(SeO_4) must be deduced.
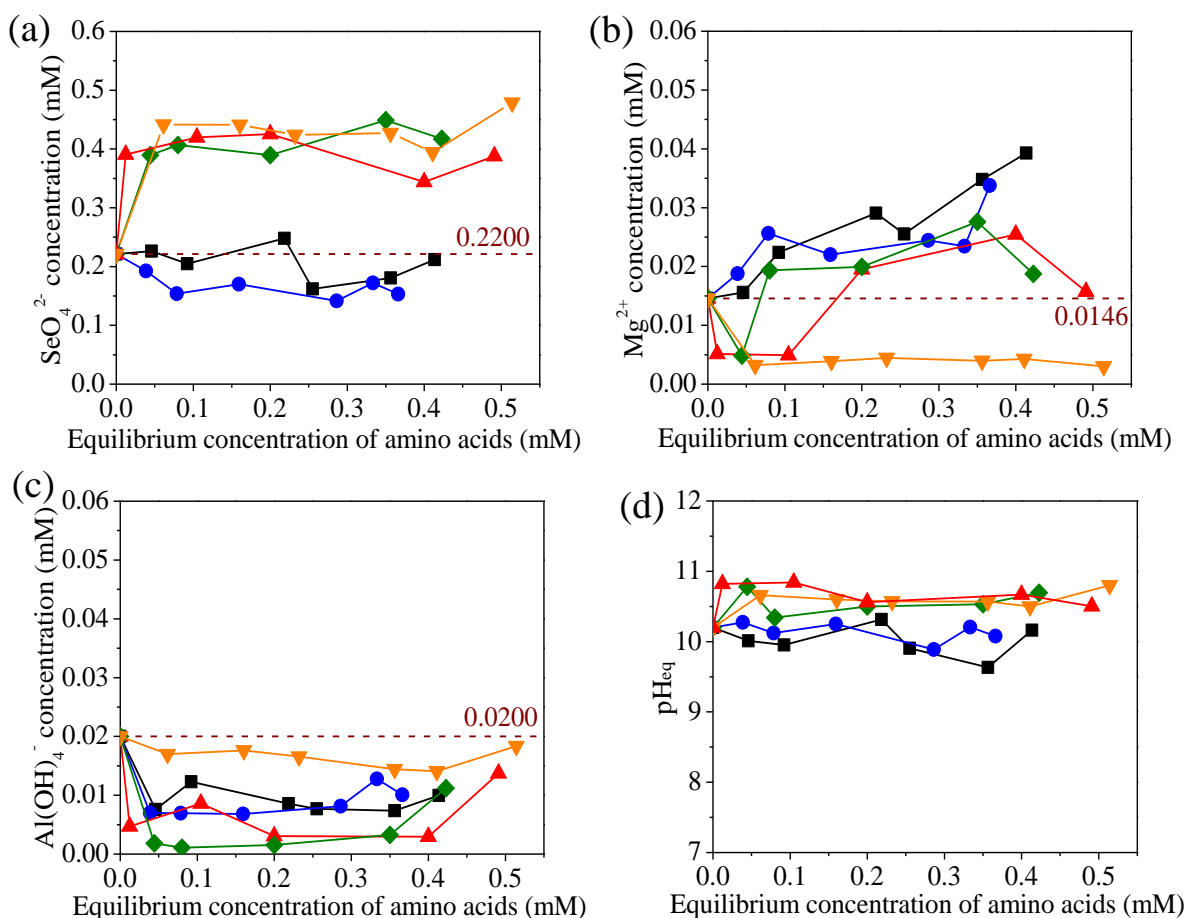
Fig. 4.2 Plots of released concentrations of (a) SeO_4^{2-}, (b) Mg^{2+}, and (c) $Al(OH)_4^-$ from Mg_2Al-LDH(SeO_4) and (d) pH after reacted with HPhe, HTrp, HGly, H_2Asp, and H_2Cys for 24 h against the equilibrated concentrations of amino acids. HPhe (■), HTrp (●), HGly (▲), H_2Asp (◆), and H_2Cys (▼).

Fig. 4.2 presents the dissolved concentrations of SeO_4^{2-}, Mg^{2+}, $Al(OH)_4^-$, and pH after 24 h against the equilibrated amino acids concentrations. Regarding **Fig. 4.2(a)~(c)**, the dissolved amounts after 24 h were normalized for unit initial mass of Mg_2Al-LDH(SeO_4) and shown against the equilibrated amino acids concentrations in **Fig. 4.3**. The simply released concentration of SeO_4^{2-} was 0.2215 mM in the absence of amino acids, corresponding to 15.6% of the initially existing SeO_4^{2-} amounts in Mg_2Al-LDH(SeO_4). This means that two-thirds of the original amounts of SeO_4^{2-} remain in LDH even in the case where the largest concentration of SeO_4^{2-} was released. The simply dissolved concentrations of Mg and Al were 0.0146 and 0.0200 mM **(Fig. 4.1(b, c))** which correspond to 2.02 and 5.88% in the original contents in LDH, respectively. This implies

there is a nonstoichiometric dissolution of LDH with excessively enhanced dissolution of Al under alkaline pH.
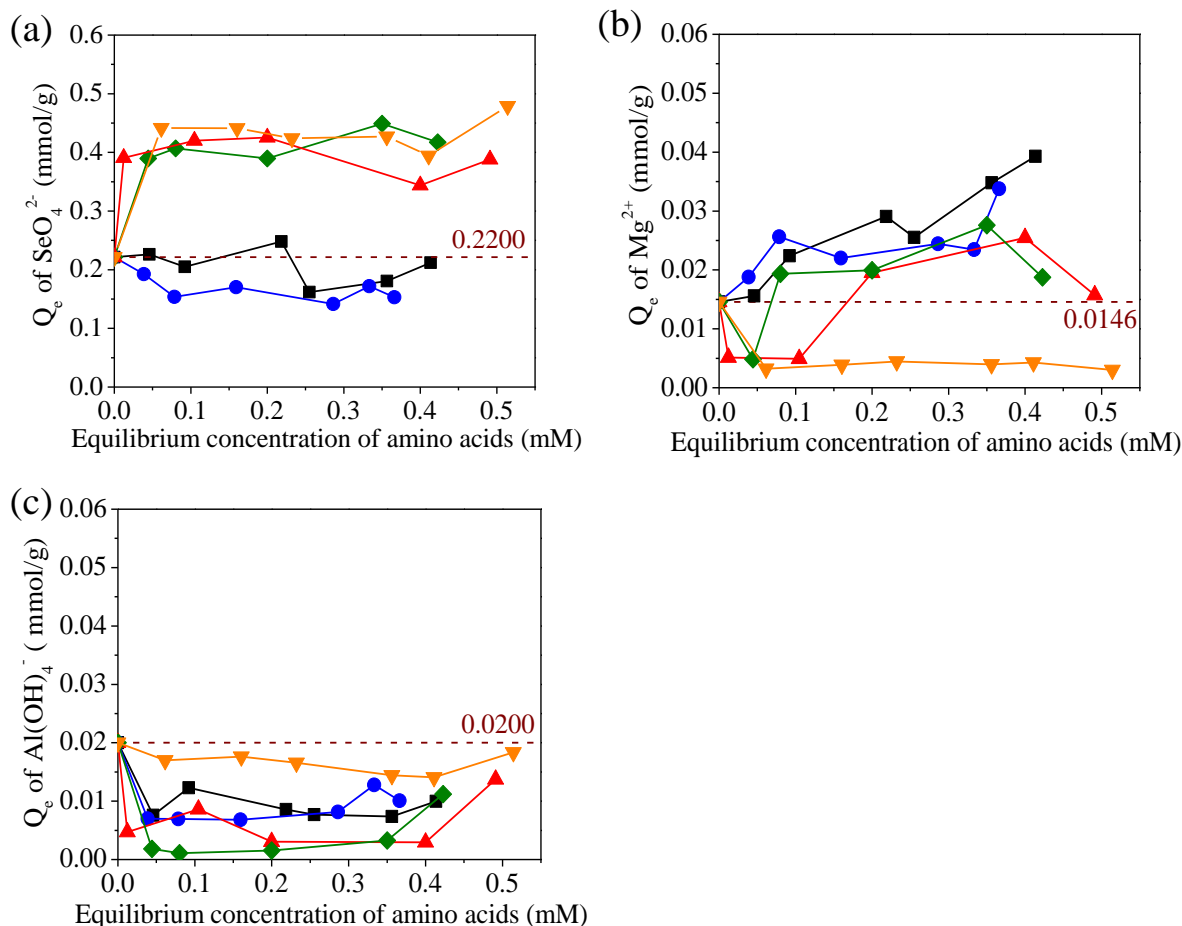
Fig. 4.3 Plots of released concentrations of (a) SeO_4^{2-}, (b) Mg^{2+}, and (c) $Al(OH)_4^-$ from Mg_2Al-LDH(SeO_4) and (d) pH after reacted with HPhe, HTrp, HGly, H_2Asp, and H_2Cys for 24 h against the equilibrated concentrations of amino acids. HPhe (■), HTrp (●), HGly (▲), H_2Asp (◆), and H_2Cys (▼).

Interestingly, the addition of small amounts of several amino acids (HGly, H_2Cys, H_2Asp with $C_0 < 0.05$ mM) stabilized metallic ions in Mg_2Al-LDH(SeO_4), but still release around 0.4 mM SeO_4^{2-}. This suggests a small amount of HGly, H_2Cys and H_2Asp might function to avoid LDH dissolving. Moreover, it is notable that in the presence of H_2Cys with < 0.5 mM the dissolution of Mg^{2+} was suppressed and the behavior of $Al(OH)_4^-$ dissolution was similar to the blank test, leading to the more significantly non-stoichiometric dissolution with excessively released $Al(OH)_4^-$. This implies there might be some specific affinities of H_2Cys with Mg atoms in LDH,

leaving the solid surfaces of LDH with Al deficiency. DFT simulations were performed to corroborate and further explain these findings, as discussed in section **4.3.4**.

After reaction with HPhe and HTrp, the released concentration of SeO_4^{2-} was similar or lower compared with the blank test, suggesting there was almost no ion-exchange of HPhe and HTrp with SeO_4^{2-} and the simple dissolution contributed to SeO_4^{2-} concentrations. The above results are reflected by the interaction of negatively charged carboxylic groups and thiol groups in amino acids with positively charged Mg_2Al-LDH(SeO_4). The median values of the surface charge of Mg_2Al-LDH(SeO_4) were always positive in a range of pH 9.5 to 11.1 (**Fig. 4.4**), which was observed in **Fig. 4.2(d)**.
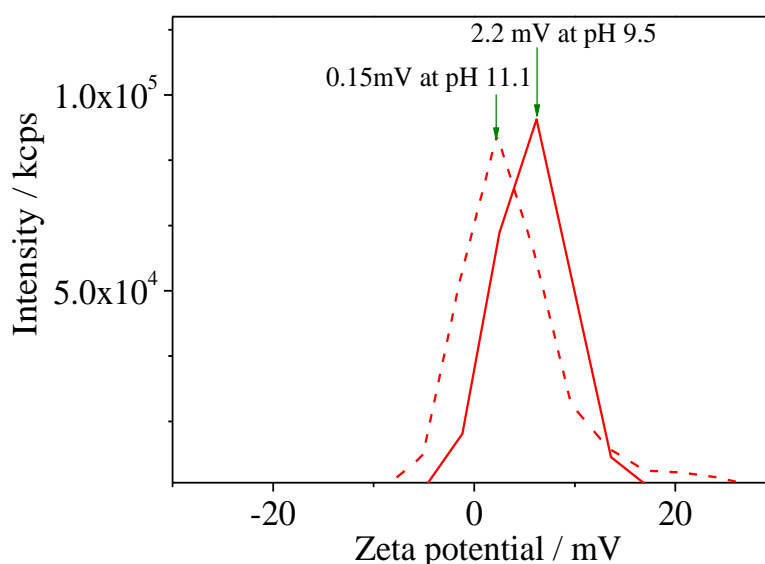
Fig. 4.4 Zeta potential distributions of Mg_2Al-LDH(SeO_4) particle at pH 9.5 and 11.1.

Sorption isotherms of amino acids on Mg_2Al-LDH(SeO_4) are expressed as shown in **Fig. 3.5**. Since the partial dissolution of Mg_2Al-LDH(SeO_4) accompanied as above, where dissolution-reprecipitation (D-R) mechanism might have happened when the dissolved concentrations of Mg^{2+} and $Al(OH)_4^-$ can contribute to the formation of Mg_2Al-LDH with SeO_4^{2-} and/or amino acids anions under the present pH (Xu and Lu, 2005; Takaki et al., 2016; Wan et al., 2019). This also

means $Mg_2Al-LDH(SeO_4)$ is unstable in aqueous solutions, therefore, the sorption data were fitted to Freundlich isotherm instead of Langmuir isotherm. Freundlich model fitting parameters were summarized in **Table 4.2**.
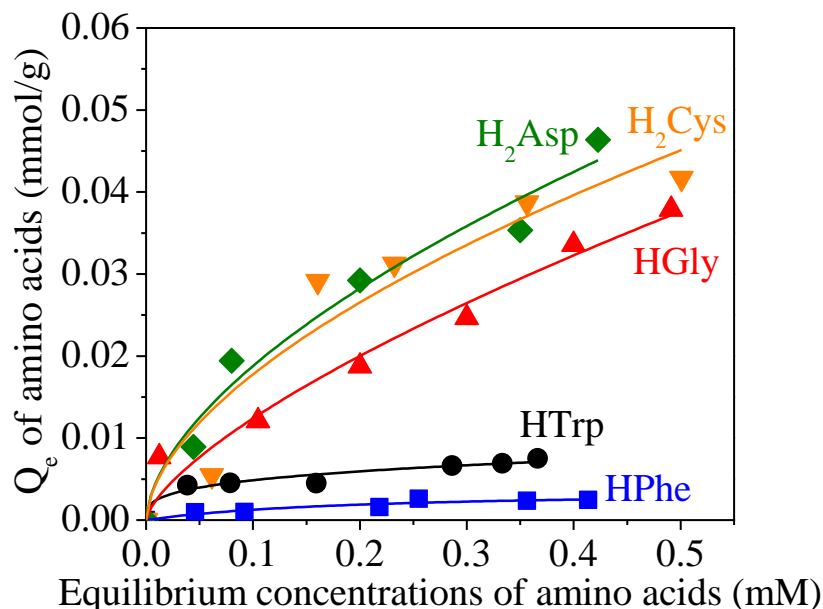
Fig. 4.5 Sorption isotherms of HPhe (■), HTrp (●), HGly (▲), H_2Asp (◆), and H_2Cys (▼) onto $Mg_2Al-LDH(SeO_4)$. Solid lines indicate the fittings to Freundlich isotherms.

Table 4.2 Fitting parameters of Freundlich isotherms in sorption of different amino acids on $Mg_2Al-LDH(SeO_4)$.

Amino acids	K_f	n	R^2
L-phenylalanine	0.0040	1.96	0.9146
L-tryptophan	0.0095	3.42	0.9571
Glycine	0.0607	1.44	0.9732
L-aspartic	0.0728	1.70	0.9738
L-cysteine	0.0673	1.73	0.9241

It is obvious that these behaviors can be divided into two groups: (i) well adsorbed (H_2Cys, HGly, H_2Asp), (ii) less adsorbed (HTrp, HPhe). As shown in **Table 1.1**, HGly is the smallest molecule, and H_2Cys and H_2Asp are a little bit larger than HGly and have -2 charges at pH 11.0, while HTrp and HPhe have an aromatic ring and larger molecular sizes with -1 charge causing the

intercalation into $Mg_2Al\text{-}LDH(SeO_4)$ more difficult. H_2Cys, HGly, and H_2Asp are more hydrophilic and smaller so making energetically favorable to interact with water molecules in interlayers of LDH than HPhe and HTrp (Khenifi et al., 2010; Silvério et al., 2013). While H_2Asp and H_2Cys possess -2 charges and HGly possesses -1 charge, the sorption coefficient values (K_f) for H_2Asp and H_2Cys in $mmol^{(1-1/n)} \cdot g^{-1} \cdot L^{1/n}$ were much lower than twice of HGly (**Table 4.2**). **Fig. 4.2** shows that H_2Cys, HGly, and H_2Asp caused a relatively larger concentration of SeO_4^{2-} released, indicating the release of SeO_4^{2-} is caused by not only ion-exchange but also unstabilization of LDH probably through intercalation of H_2Cys, HGly, and H_2Asp due to their smaller molecular sizes. The released concentration of SeO_4^{2-} was already saturated in case of H_2Cys, HGly, and H_2Asp, when the equilibrated concentrations of amino acids were lower than 0.1 mM (**Fig. 4.2(a)**). As mentioned above, several factors caused the release of SeO_4^{2-}. (1) ion-exchange with H_2Cys, HGly, and H_2Asp, (2) simple dissolution of LDH, (3) unstabilization of LDH by interaction with H_2Cys, HGly, and H_2Asp followed by ion-exchange with carbonate. Based on the above analysis, the chemical stability of hydrotalcite after bearing SeO_4^{2-}, which can be affected by competitive anions, pH, and temperature, becoming an important consideration in a practical circumstance (Constantino et al., 2017; Chubar, 2018). The released amount of selenate, magnesium, and aluminum from $Mg_2Al\text{-}LDH(SeO_4)$ into solution in the presence of HGly, H_2Asp, and H_2Cys may raise the risk in the radioactive anionic pollutant treatment in the practical soil or wastewater. Of note is in the real environment, there are so much SOM including different molecule sizes, structures as well as functional groups, which may significantly affect the ion-exchange ability with SeO_4^{2-} in hydrotalcite. Therefore, detailed interaction information of amino acids with SeO_4^{2-} is necessary.

4.3.3 Characterization of the solid residues after reaction of amino acids with $Mg_2Al\text{-}LDH(SeO_4)$

The XRD patterns of the pristine $Mg_2Al\text{-}LDH(SeO_4)$ and the solid residues after react

without/with 0.5 mM amino acids are shown in **Fig. 4.6(a)**. For the blank experiment, the d_{003} value of solid residues is 9.00 Å which is similar to the pristine value of 9.10 Å (**Fig. 4.6(b)**). The broadening of d_{003} was caused by the simple dissolution of Mg_2Al-LDH(SeO_4). When amino acids were added, Mg_2Al-LDH(SeO_4) is still the dominant phase, because two-thirds of selenate were still present at least in Mg_2Al-LDH. As shown in **Fig. 4.6(b)**, peak separation revealed that two d_{003} values appeared around 10.7-11.0 Å of shoulder peaks and 8.36-8.82 Å of main peaks. This indicates Mg_2Al-LDH(SeO_4) can be expandable by the intercalation with amino acids, which was not observed in Zn_2Al-LDH(SeO_4) under the same condition (unpublished), probably different attraction force depending on the metal combination in LDH.
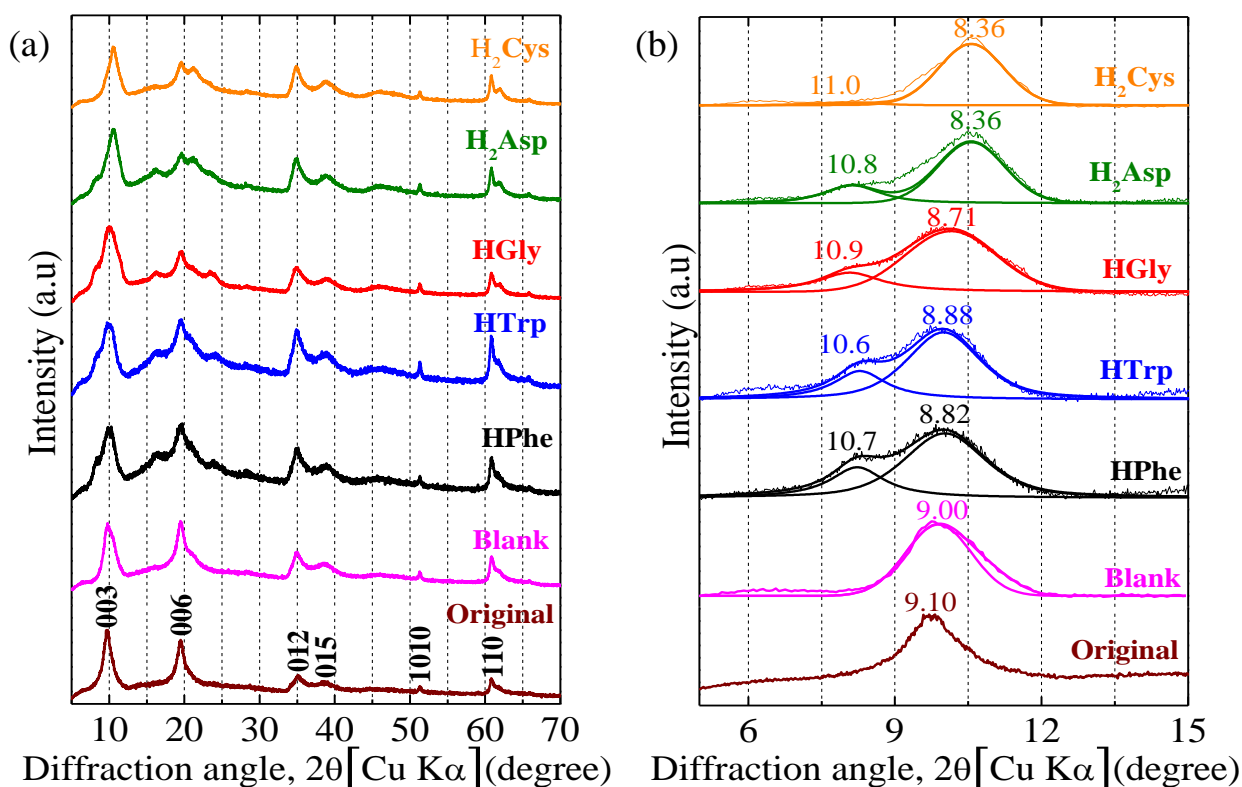
Fig. 4.6 Representative X-ray diffraction patterns of the pristine Mg_2Al-LDH(SeO_4) and solid residues after sorption of 0.5 mM amino acids on Mg_2Al-LDH(SeO_4) in ranges of diffraction angle (2θ) of (a) 5° to 70°, and (b) 5° to 15° with the interlayer distance in Å. Blank means no amino acids.

4.3.4. DFT simulation analysis

We have selected one model of the reacted Mg_2Al-LDH(SeO_4) with glycine (HGly, $C_2H_5NO_2$) to confirm the stable configurations of HGly after intercalation into Mg_2Al-LDH(SeO_4), since HGly is the simplest amino acid and has the smallest molecule size, furthermore, it caused the layer distance of LDH partially expanded as shown in **Fig. 4.6**.

Fig. 4.7 illustrates the representative optimized structures of the intercalated LDHs, Mg_2Al-LDH(SeO_4), Mg_2Al-LDH(SeO_4, Gly), and Mg_2Al-LDH(Gly) with the composition of $Mg_2Al(OH)_6 \cdot xCH_2(NH_2)COO \cdot 0.5(1-x)SeO_4$ ($x = 0$, 0.5, and 1, respectively). **Fig. 4.8(a)** plots the formation energies for the ion-exchange reaction, defined in **Eq. (2)**, against the HGly concentration x. The solid line indicates a convex hull, which connects the lowest formation-energy points for each of the compositions. The convex hull falls to the right, indicating that Gly^- can be readily exchanged with SeO_4^{2-}. A close look at the optimized structures shown in **Fig. 4.7** reveals that the oxide ions of both anionic molecules form hydrogen bonds to the protons of the LDH layers, and/or to those of the molecules leading to intermolecular interactions. The configurations of the molecules are relevant to the formation of hydrogen bonds. **Fig. 4.8(b)** presents the correlation between the formation energies and the number of hydrogen bonds per a formula unit $Mg_2Al(OH)_6 \cdot xCH_2(NH_2)COO \cdot 0.5(1-x)SeO_4$. Here, the O-H bonds that are longer than 1.6 Å and shorter than 2.1 Å are regarded as hydrogen bonds. The intercalated LDHs tend to be more stable with an increase in the number of hydrogen bonds. **Fig. 4.8(c)** plots the formation energies against the interlayer spacing. The interlayer spacing of the pristine Mg_2Al-LDH(SeO_4) ($x = 0$) is about 8.2 Å, and that of Mg_2Al-LDH (SeO_4, Gly) ($x = 0.5$) ranges from 8.1 to 8.7 Å. Thus, there is no significant change in interlayer spacing between $x = 0$ and 0.5. Interestingly, the Mg_2Al-LDH (Gly) ($x = 1$) is classified into two groups in terms of interlayer spacing: one group with short interlayer spacing ranging from 7.6 to 8.8 Å and the other group with long interlayer spacing ranging from 9.9 to 10.5 Å, which is in good agreement with the low-angle shoulder peak

of 003 diffractions (**Fig. 4.6(b)**). In the former group, the HGly molecules are single stacked between the LDH layers as seen in **Fig. 4.7(c).** On the other hand, the latter group has doubly stacked HGly molecules sandwiched by LDH layers as seen in **Fig. 4.7(d)**. The formation energies of the Mg_2Al-LDH(Gly) with doubly stacked HGly molecules are much higher than those of the Mg_2Al-LDH(Gly) with singly stacked HGly molecules. This is because the doubly stacked HGly molecules can form hydrogen bonds only to the protons in one side of the LDH layers, resulting in a smaller number of hydrogen bonds compared to the singly stacked HGly molecules, which can produce hydrogen bonds to the protons in both sides of the LDH layers. The Mg_2Al-LDH(Gly) with doubly stacked HGly molecules has negative formation energies and therefore can be kinetically stabilized to be responsible for the observed lattice expansion by the ion-exchange.

(a) $x = 0$, E_{form} = 0 kJ/mol, d = 8.20 Å   (b) $x = 0.5$, E_{form} = −34.5 kJ/mol, d = 8.36 Å

(c) $x = 1$, E_{form} = −83.6 kJ/mol, d = 7.65 Å   (d) $x = 1$, E_{form} = −15.7 kJ/mol, d = 10.19 Å
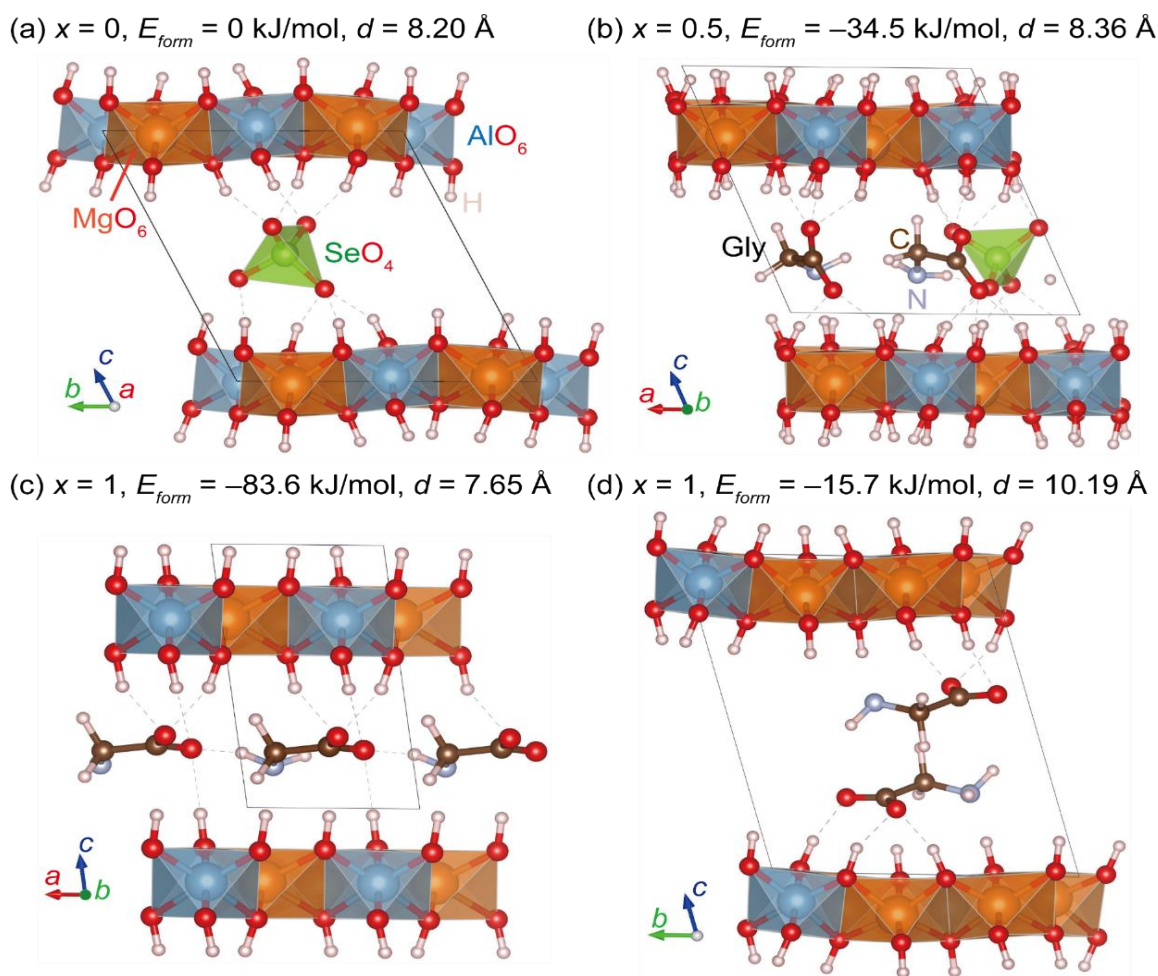
Fig. 4.7 Schematics of representative simulated structures with the composition of $Mg_2Al(OH)_6 \cdot xCH_2(NH_2)COO \cdot 0.5(1-x)SeO_4$ [x = (a) 0, (b) 0.5, (c) and (d) 1] as well as the formation energy, E_{form}, and interlayer spacing, d. The dashed lines indicate hydrogen bonds.
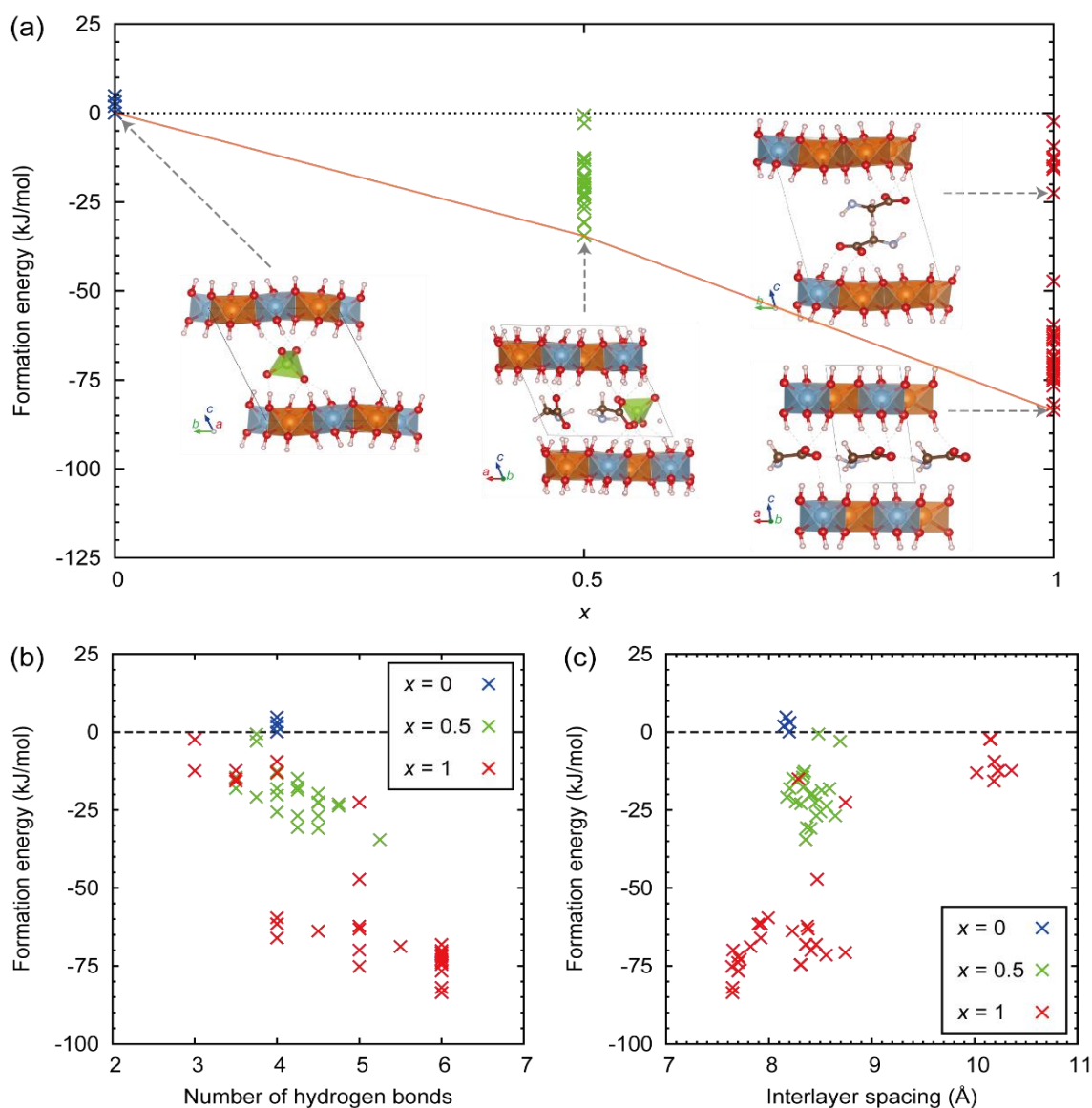
Fig. 4.8 (a) Formation energies for the ion-exchange reaction plotted against (a) the Gly concentration x (blue: x = 0, green: x = 0.5, red: x = 1.0 in $Mg_2Al(OH)_6 \cdot xCH_2(NH_2)COO \cdot 0.5(1-x)SeO_4$), (b) the number of hydrogen bonds, and (c) interlayer spacing. The solid line indicates a convex hull. The representative structures for each composition are also displayed in the inset.

It was suggested that there is a strong affinity of Cys^{2-} with Mg than other amino acids, since Mg was stabilized in solid phase in the presence of H_2Cys (**Fig. 4.2(b)**) and no shoulder peaks appeared in XRD pattern for the solid residues after reaction with H_2Cys (**Fig. 4.6(b)**). To confirm the strong affinity between Cys^{2-} and Mg from first principles, two structural models of Mg-Cys

complexes were created as shown in **Fig. 4.9**, as well as structural models of deprotonated amino acids ions of Asp^{2-} and Cys^{2-}. For comparison, a model of the Mg-Asp complex was also added for calculation of the formation energy. First, formation energies for two configurations of Mg-Cys complexes were derived from **Eq. (4.3)** to compare, where Mg atom is coordinated by one O atom from the carboxyl group, S atom from thiol group, and N atom of the amino group (Mg-Cys1 in **Fig. 4.9(d)**), and Mg atom is coordinated by two O atoms from carboxyl group and S atom from thiol group (Mg-Cys2 in **Fig. 4.9(e)**). The formation energies were -2522.2 kJ/mol for the former and -2447.7 kJ/mol for the latter. The more stable configuration of Mg-Cys1 (**Fig. 4.9(d)**) is quite similar to the previously reported model (Shankar et al., 2011). For comparison with H_2Asp, as a representative example which showed the similar trend with other amino acids in **Fig. 4.2(b, c)**, the formation energy of Mg-Cys1 was smaller than that of Mg-Asp complex (Mg-Asp in **Fig. 4.9(c)**) which was -2481.0 kJ/mol. This suggests there is a specific affinity between Cys^{2-} and Mg in a form of Mg-Cys1. Our calculations imply that the distribution of electron densities of Cys^{2-} molecule tends to stabilize only Mg on the surface of LDH specifically releasing $Al(OH)_4^-$ and selenate to the solution. This phenomenon should happen on the surface of LDH. Due to the strongly bound Cys^{2-} with Mg atoms on the surface of LDH, the doubly stacked configuration of Cys^{2-} in LDH interlayer is unlikely to happen in XRD pattern for the solid residues after reaction (**Fig. 4.6(b)**). This effect of H_2Cys may also help selenate immobilization.
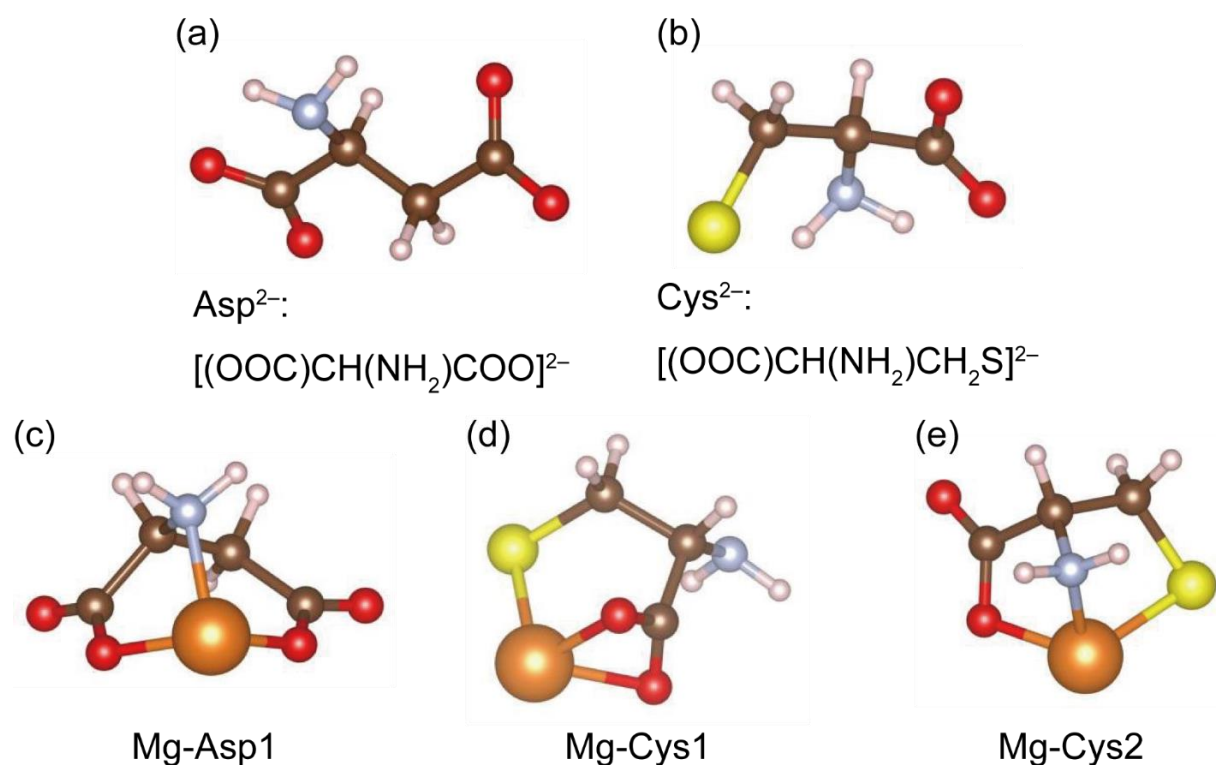
Fig. 4.9 Structural models for deprotonated (a) Asp^{2-} and (b) Cys^{2-} ions and (c) Mg-Asp and (d), (e) Mg-Cys complexes.

4.4 Conclusions

The effect of amino acids on unstabilization of SeO_4^{2-} in Mg_2Al-LDH(SeO_4) was studied by experimental analysis integrated with DFT modeling. The released amount of SeO_4^{2-} from Mg_2Al-LDH(SeO_4) in the absence of amino acids corresponded to 15.6% of the initially existing SeO_4^{2-} in the solids. HGly, H_2Asp, and H_2Cys promoted the release of SeO_4^{2-} by ion-exchange and unstabilization of LDH during the intercalation process of HGly, H_2Asp and H_2Cys. Through the intercalation, amino acids expanded the interlayer spacing of Mg_2Al-LDH(SeO_4) to 10.7-11.0 Å except for H_2Cys, but Mg_2Al-LDH(SeO_4) phase still is dominant. The DFT simulation using HGly as a model revealed that the singly stacked HGly was the most stable configuration and the layer spacing expansion of LDH was caused by the doubly stacked configuration of HGly. The intercalated LDHs tend to be more stable with increase in the number of hydrogen bonds between H atoms in metallic layers of LDH and O atoms in selenate and/or carboxyl groups in HGly.

Notably, the dissolution of Mg^{2+} was suppressed by complexation with thiol, carboxyl, and amine groups in H_2Cys which was verified by the formation energy calculated from DFT. The strong affinity of Cys^{2-} with Mg might contribute to destabilizing the surface structure of LDH releasing not only $Al(OH)_4^-$ but also SeO_4^{2-}. This work raises important environmental questions regarding the transportation and immobilization of anionic species of low-level radionuclide wastes in repositories, where anionic amino acids of smaller molecular size can potentially intercalate. Engineering countermeasures are necessary to stabilize selenate using, for example, barriers such as iron minerals, especially when the concentration of selenate is relatively high in the radioactive wastes.

References

Chubar, N., 2014. EXAFS and FTIR studies of selenite and selenate sorption by alkoxide-free sol-gel generated Mg-Al-CO$_3$ layered double hydroxide with very labile interlayer anions. J. Mater. Chem. A 2, 15995-16007.

Chubar, N., Szlachta, M., 2015. Static and dynamic adsorptive removal of selenite and selenate by alkoxide-free sol-gel-generated Mg-Al-CO$_3$ layered double hydroxide: effect of competing ions. Chem. Eng. J. 279, 885-896.

Cohen, S.A., Bidlingmeyer, B.A., Tarvin, T.L., 1986. PITC derivatives in amino acid analysis. Nature 320, 769-770.

Constantino, L.V., Quirino, J.N., Monteiro, A.M., Abrão, T., Parreira, P.S., Urbano, A., Santos, M.J., 2017. Sorption-desorption of selenite and selenate on Mg-Al layered double hydroxide in competition with nitrate, sulfate and phosphate. Chemosphere 181, 627-634.

Ge, H.J.S., Ernzerhof, M., 2006. Erratum:"Hybrid functionals based on a screened Coulomb potential"[J. Chem. Phys. 118, 8207 (2003)]. J. Chem. Phys. 124, 219906.

Grimme, S., Antony, J., Ehrlich, S., Krieg, H., 2010. A consistent and accurate ab initio parametrization of density functional dispersion correction (DFT-D) for the 94 elements H-Pu. J. Chem. Phys. 132, 154104.

Grimme, S., Ehrlich, S., Goerigk, L., 2011. Effect of the damping function in dispersion corrected density functional theory. J. Comput. Chem. 32, 1456-1465.

Gunawan, S., Walton, N.Y., Treiman, D.M., 1990. High-performance liquid chromatographic determination of selected amino acids in rat brain by precolumn derivatization with phenylisothiocyanate. J. Chromatogr. A 503, 177-187.

Heinrikson, R.L., Meredith, S.C., 1984. Amino acid analysis by reverse-phase high-performance liquid chromatography: precolumn derivatization with phenylisothiocyanate. Anal. Biochem. 136, 65-74.

Heyd, J., Scuseria, G.E., Ernzerhof, M., 2003. Hybrid functionals based on a screened Coulomb potential. J. Chem. Phys. 118, 8207-8215.

Khenifi, A., Derriche, Z., Mousty, C., Prévot, V., Forano, C., 2010. Adsorption of glyphosate and glufosinate by Ni$_2$AlNO$_3$ layered double hydroxide. Appl. Clay Sci. 47(3-4), 362-371.

Kim, M.-C., Sim, E., Burke, K., 2011. Communication: Avoiding unbound anions in density functional calculations. J. Chem. Phys. 134, 171103.

Krukau, A.V., Vydrov, O.A., Izmaylov, A.F., Scuseria, G.E., 2006. Influence of the exchange screening parameter on the performance of screened hybrid functionals. J. Chem. Phys. 125, 224106.

Lippincott, S.E., Friedman, A.L., Siegel, F.L., Pityer, R.M., Chesney, R.W., 1988. HPLC analysis of the phenylisothiocyanate (PITC) derivatives of taurine from physiologic samples. J. Am. Coll. Nutr. 7, 491-497.

Ma, L., Wang, Q., Islam, S.M., Liu, Y., Ma, S., Kanatzidis, M.G., 2016. Highly selective and efficient removal of heavy metals by layered double hydroxide intercalated with the MoS_4^{2-}ion. J. Am. Chem. Soc. 138, 2858-2866.

Momma, K., Izumi, F., 2011. VESTA 3 for three-dimensional visualization of crystal, volumetric and morphology data. J. Appl. Cryst. 44, 1272-1276.

Monkhorst, H.J., Pack, J.D., 1976. Special points for Brillouin-zone integrations. Phys. Rev. B 13, 5188.

Opiso, E.M., Sato, T., Yoneda, T., 2016. Immobilization of selenium by Mg-bearing minerals and its implications for selenium removal from contaminated water and wastewater. Appl. Clay Sci. 123, 121-128.

Paikaray, S., Hendry, M.J., Essilfie-Dughan, J., 2013. Controls on arsenate, molybdate, and selenate uptake by hydrotalcite-like layered double hydroxides. Chem. Geol. 345, 130-138.

Scholze, H., 1985. Determination of phenyltiocarbamyl amino acids by reversed-phase high-performance liquid chromatography. J. Chromatogr. A 350, 453-460.

Silvério, F., Dos Reis, M.J., Tronto, J., Valim, J.B., 2013. Sorption of aspartic and glutamic aminoacids on calcined hydrotalcite. Springerplus 2, 211.

Takaki, Y., Qiu, X., Hirajima, T., Sasaki, K., 2016. Removal mechanism of arsenate by bimetallic and trimetallic hydrocalumites depending on arsenate concentration. Appl. Clay Sci. 134, 26-33.

Tian, Q., Guo, B., Sasaki, K., 2020b. Immobilization mechanism of Se oxyanions in geopolymer: Effects of alkaline activators and calcined hydrotalcite additive. J. Hazard.Mater. 387, 121994.

Wan, B., Yan, Y., Huang, R., Abdala, D.B., Liu, F., Tang, Y., Tan, W., Feng, X., 2019. Formation of Zn-Al layered double hydroxides (LDH) during the interaction of ZnO nanoparticles (NPs) with γ-Al_2O_3. Sci. Total Environ. 650, 1980-1987.

Wan, D., Liu, H., Liu, R., Qu, J., Li, S., Zhang, J., 2012. Adsorption of nitrate and nitrite from aqueous solution onto calcined (Mg-Al) hydrotalcite of different Mg/Al ratio. Chem. Eng. J.195-196, 241-247.

Xu, S., Zhang, L., Zhao, J., Cheng, J., Yu, Q., Zhang, S., Zhao, J., Qiu, X., 2020. Remediation of chromium-contaminated soil using delaminated layered double hydroxides with different divalent metals. Chemosphere 254, 126879.

Xu, Z.P., Lu, G.Q., 2005. Hydrothermal synthesis of layered double hydroxides (LDHs) from mixed MgO and Al_2O_3: LDH formation mechanism. Chem. Mater. 17, 1055-1062.

You, Y., Vance, G.F., Zhao, H., 2001. Selenium adsorption on Mg-Al and Zn-Al layered double hydroxides. Appl. Clay Sci. 20, 13-25.

Zhu, L., Zhang, L., Li, J., Zhang, D., Chen, L., Sheng, D., Yang, S., Xiao, C., Wang, J., Chai, Z., 2017. Selenium sequestration in a cationic layered rare earth hydroxide: a combined batch experiments and EXAFS investigation. Environ. Sci. Technol. 51, 8606-8615.

Chapter 5 Environmental impact of amino acids on the release of selenate immobilized in hydrocalumite

5.1 Introduction

Ca$_2$Al-LDH possesses surface adsorption capacity and ion-exchange ability (Perkins and Palmer, 2001; Baur and Johnson, 2003b; Christensen et al., 2004; Moon et al., 2009; Li et al., 2017; Yao et al., 2017). Therefore, Ca$_2$Al-LDH has been widely explored from aspects of its immobilization mechanisms for Se oxyanion species and phase transformation boundary. Moon et al. (2009) reported selenium-bearing phase appeared calcium selenite hydrate and selenate-ettringite in the soil-cement system. Zhang and Reardon (2003) confirmed that Ca$_4$Al$_2$(OH)$_{12}$(OH)$_2$·6H$_2$O can reduce SeO$_4^{2-}$ concentration below the drinking water standard and the uptake amount was larger than ettringite. Baur and Johnson (2003b) explored SO$_4$-monosulfate possibly removes SeO$_4^{2-}$ through substitution with SO$_4^{2-}$ in the cement paste. Li et al. (2020) found the adsorption of SeO$_4^{2-}$ onto Ca-Al LDHs was controlled by the chemisorption and can be reused at least three times with the adsorption capacity still keeping 88%. Yet, the stability of hydrocalumite after immobilized Se oxyanions in the presence of environmental factors is still unknown.

Considering the real environmental factors in cement systems and the practical purity of SeO$_4$-hydrocalumite, selenate- and carbonate-bearing hydrocalumite (Ca$_2$Al-LDH) was obtained by co-precipitation method in the present work. Five amino acids were selected to react with it. Releasing concentrations of SeO$_4^{2-}$ from Ca$_2$Al-LDH after suspended into amino acids solutions were determined and sorption isotherms of the amino acids were obtained. XRD patterns of Ca$_2$Al-LDH solid residues were analyzed through peak separation to give the peak assignments assisted by Density Functional Theory (DFT) simulation. Also, DFT was applied to predict the possible

mechanisms to release SeO_4^{2-} and possible interactions of amino acids with hydroxide layers of Ca_2Al-LDH.

5.2 Experimental

5.2.1 Materials

Inorganic chemicals including $Ca(OH)_2$ (96.0%), $NaAlO_2$ ($Al_2O_3 > 42.0\%$), Na_2SeO_4 (97.0%), NaOH (97.0%) and organic chemicals including L-tryptophan (HTrp, $C_{11}H_{12}N_2O_2$, 99.0%), L-phenylalanine (HPhe, $C_9H_{11}NO_2$, 99.0%), glycine (HGly, $C_2H_5NO_2$, 99.0%), L-aspartic acid (H_2Asp, $C_4H_7NO_4$, 99.0%) and L-cysteine (H_2Cys, $C_3H_7NO_2S$, 99.0%) in a special grade were purchased from FUJIFILM Wako Pure Chemicals Co. Ltd. (Osaka, Japan). Decarbonized water was prepared by simultaneously boiling the ultrapure water under the N_2 bubbling for 2 h.

5.2.2 Synthesis of Ca_2Al-LDH

Selenate-bearing hydrocalumite (Ca_2Al-LDH) was prepared by co-precipitation method. First, 0.012 mol $NaAlO_2$ was dissolved into 50 mL 10 mM Na_2SeO_4 for 10 min (solution A). $Ca(OH)_2$ suspension was prepared using 0.024 mol $Ca(OH)_2$ dissolved in 200 mL 10 mM Na_2SeO_4 (solution B). Then solution A was added into solution B to react for 1 h to avoid the SeO_4-ettringite formation in a glovebox (95% N_2, 5% H_2, COY, M-160, USA). After washing 2 times by ultrapure water and freeze-drying for 12 h, powdery Ca_2Al-LDH was obtained and stored inside the drying shelf for further use.

5.2.2 Reaction of Ca_2Al-LDH with amino acids

First, 50 mg of Ca_2Al-LDH was added into 50 mL decarbonized water at pH 11.0 without any amino acids to shake for an appropriate time from 0.5 h to 24 h at 25 °C. The suspensions were collected at different time intervals using disposable syringes and solid residues were separated by

filtration using 0.2 μm membrane filters, and then drying solid samples for further characterization. The remaining Ca^{2+}, $Al(OH)_4^-$, and SeO_4^{2-} concentrations in the solution were determined by ICP-OES (**2.1.1 section**). The dissolved fraction of SeO_4^{2-} was calculated by **Eq. (5.1).**

$$Dissolution\ (\%)\ =\ Q_t \cdot 100/Q_0 \tag{5.1}$$

where the Q_0 (mmol/g) and Q_t (mmol/g) are the initial amounts and final amount at t h of SeO_4^{2-}, respectively.

Then, the reaction of Ca_2Al-LDH with different amino acids including HPhe, HTrp, HGly, H_2Asp, and H_2Cys at a concentration range from 0 to 7 mM was performed in a glovebox to avoid contamination from CO_2. 50 mg of Ca_2Al-LDH was added into 50 mL of the above sole amino acid solution for 24 h at 25 °C. The solution and solid samples were collected in the same manner as above to provide for the determination of dissolved species concentrations and solid characterization, respectively.
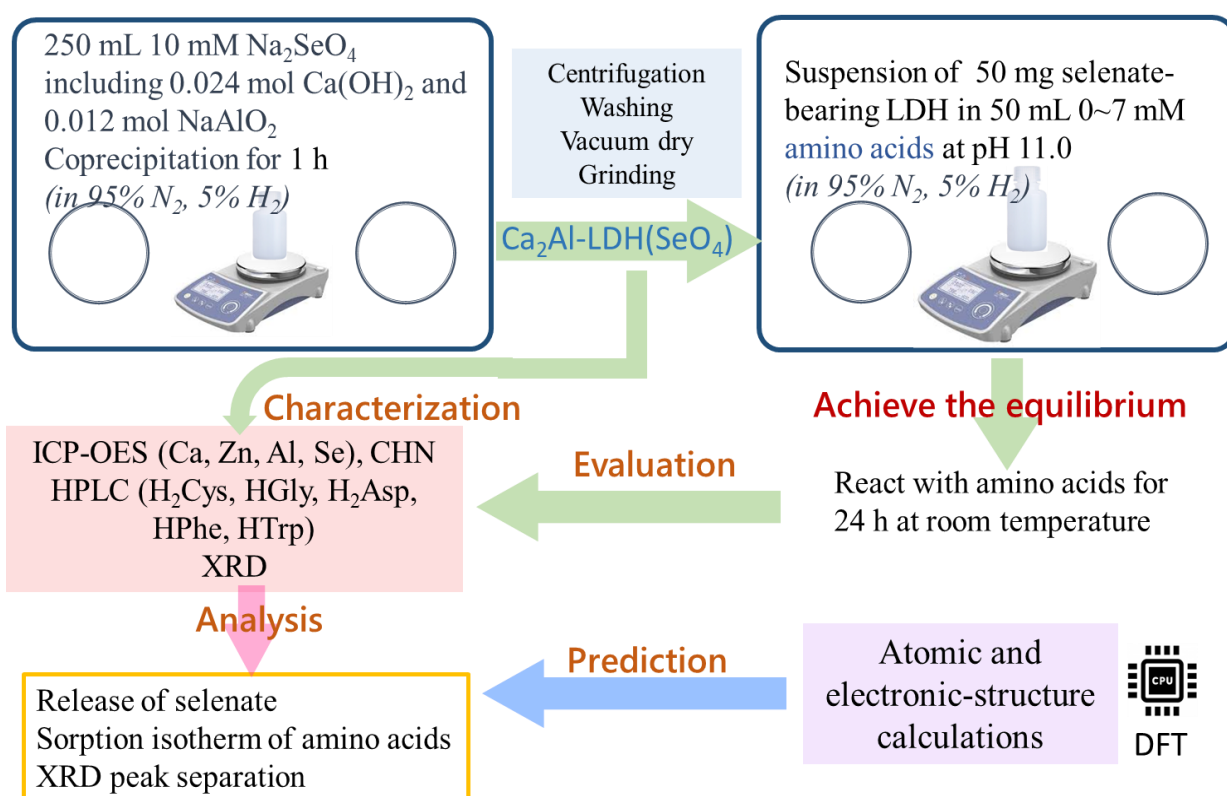
Scheme. 5.1 Experimental procedure of Ca_2Al-LDH(SeO_4) with different amino acids.

5.2.3 Chemical analysis and solid Characterizations

As shown in 2.1 and 2.2 sections.

5.2.4 DFT simulation

As shown in 2.3 section.

Our density functional theory (DFT) simulation was performed to calculate the formation energies of the products in ion-exchanges of SeO_4^{2-} with amino acids and of CO_3^{2-} with amino acids by changing the reacted fractions. Considering the equivalent negative charges with SeO_4^{2-}, H_2Asp and H_2Cys were selected as amino acids models in the present work to figure out their ion-exchanging ability depending on the formation energies and the possible configurations of Ca_2Al-LDH including different anions.

We treated the following states as valence electrons: 1s for H; 2s and 2p for C, N, and O; 3s and 3p for Al and S; 3p and 4s for Ca; 4s and 4p for Se. Initial structural models were prepared as follows. Firstly, the structural model of positively charged hydroxides layers for Ca_2Al-LDH was constructed for the computer simulation. The hydroxide layers of Ca_2Al-LDH used in the simulations were set using atomic coordinates extracted from the previously reported crystal structure of hydrocalumite with the composition of $[Ca_8Al_4(OH)_{24}(CO_3)(Cl)_2 \cdot 10H_2O]$ (Sacerdoti and Passaglia, 1988). By removing the intercalated carbonate (CO_3^{2-}) and chloride (Cl^-) ions and water (H_2O) molecules, an "empty" LDH model was created. Since the composition of the LDH layer is $[Ca_2Al(OH)_6]^+$, the number of Al atom corresponds to the positive charge of the empty LDH model. Secondly, SeO_4^{2-}, CO_3^{2-}, Asp^{2-} and Cys^{2-} anions are placed in the gallery space of the empty LDH with random positions and rotation angles by using the pymatgen python library (Ong et al., 2013) so as to neutralize the positive charges. Thus, more than ten simulated unit cells consisting of the positively charged hydroxide layers of $[Ca_2Al(OH)_6]^+$ and desired intercalated anions were constructed.

Relaxation of lattice constants and internal coordinates was performed until the residual stress and force decreased to 4 MPa and 1 meV/Å, respectively. The pymatgen python library was used to extract the structural information such as interlayer spacing and the number of chemical bonds from the optimized structures (Ong et al., 2013). The VESTA code was used to visualize the optimized structures (Momma and Izumi, 2011).

The total energies of the Ca_2Al-LDH incorporating the anions as well as those of H_2Asp, H_2Cys, H_2SeO_4, and H_2CO_3 neutral molecules were calculated to obtain the formation energies of the products in ion-exchange of SeO_4^{2-} and CO_3^{2-} with Asp^{2-} and Cys^{2-} as expressed as **Eqs. (5.2)~(5.5)**, where the values of x are 0, 0.5, and 1.

$$Ca_2Al(OH)_6 \cdot 0.5(SeO_4) + 0.5xH_2Asp \rightarrow Ca_2Al(OH)_6 \cdot 0.5(1-x)\ SeO_4 \cdot 0.5xAsp + 0.5xH_2SeO_4 \qquad (5.2)$$

$$Ca_2Al(OH)_6 \cdot 0.5(SeO_4) + 0.5xH_2Cys \rightarrow Ca_2Al(OH)_6 \cdot 0.5(1-x)SeO_4 \cdot 0.5xCys + 0.5xH_2SeO_4 \qquad (5.3)$$

$$Ca_2Al(OH)_6 \cdot 0.5(CO_3) + 0.5xH_2Asp \rightarrow Ca_2Al(OH)_6 \cdot 0.5(1-x)CO_3 \cdot 0.5xAsp + 0.5xH_2CO_3 \qquad (5.4)$$

$$Ca_2Al(OH)_6 \cdot 0.5(CO_3) + 0.5xH_2Cys \rightarrow Ca_2Al(OH)_6 \cdot 0.5(1-x)CO_3 \cdot 0.5xCys + 0.5xH_2CO_3 \qquad (5.5)$$
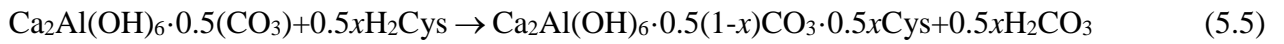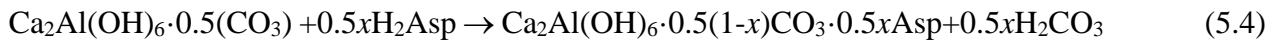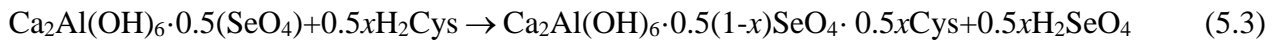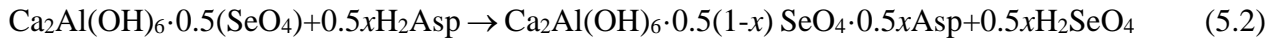
Moreover, ion-exchanging of SeO_4^{2-} in ternary anionic systems (SeO_4^{2-}/ CO_3^{2-}/ amino acid) was also explored to predict the effect of CO_3^{2-} on the release of SeO_4^{2-} from Ca_2Al-LDH in the presence of amino acids. Formation energies of the products in **Eqs. (5.6), (5.7)** were simulated at $x = 0$ and 0.5.

$$Ca_2Al(OH)_6 \cdot 0.5(0.5SeO_4 \cdot 0.5Asp) + 0.5xH_2CO_3$$
$$\rightarrow Ca_2Al(OH)_6 \cdot 0.5((0.5-x)SeO_4 \cdot 0.5xCO_3 \cdot 0.5Asp) + 0.5xH_2SeO_4 \qquad (5.6)$$

$$Ca_2Al(OH)_6 \cdot 0.5(0.5SeO_4 \cdot 0.5Cys) + 0.5xH_2CO_3$$
$$\rightarrow Ca_2Al(OH)_6 \cdot 0.5((0.5-x)SeO_4 \cdot 0.5xCO_3 \cdot 0.5Cys) + 0.5xH_2SeO_4 \qquad (5.7)$$
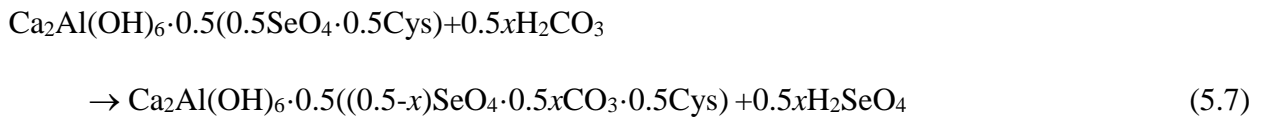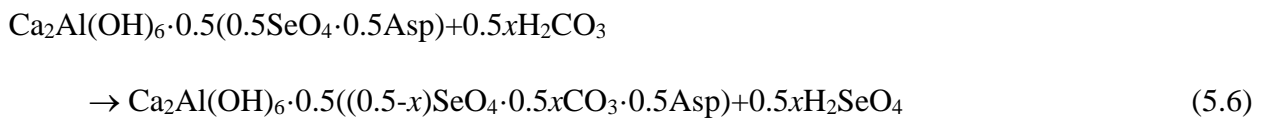
5. 3 Results and discussion

5.3.1 Characterizations of synthesized Ca_2Al-LDH

The chemical formula of Ca_2Al-LDH in a composition of $Ca_{0.872}Al_{0.402}(OH)_{2.4}(SeO_4)_{0.093}(CO_3)_{0.063} \cdot 10H_2O$ was obtained by combining with ICP-OES and CHN analytical results, indicating the molar ratio of Ca/Al is 2.17. Considering the difficulty to synthesize pure selenate-bearing hydrocalumite, SeO_4^{2-} and CO_3^{2-} co-intercalated hydrocalumite was obtained. The reagent $NaAlO_2$ in which $NaCO_3$ seems to be contained as an impurity caused the CO_3^{2-} as an intercalator for the produced LDH.
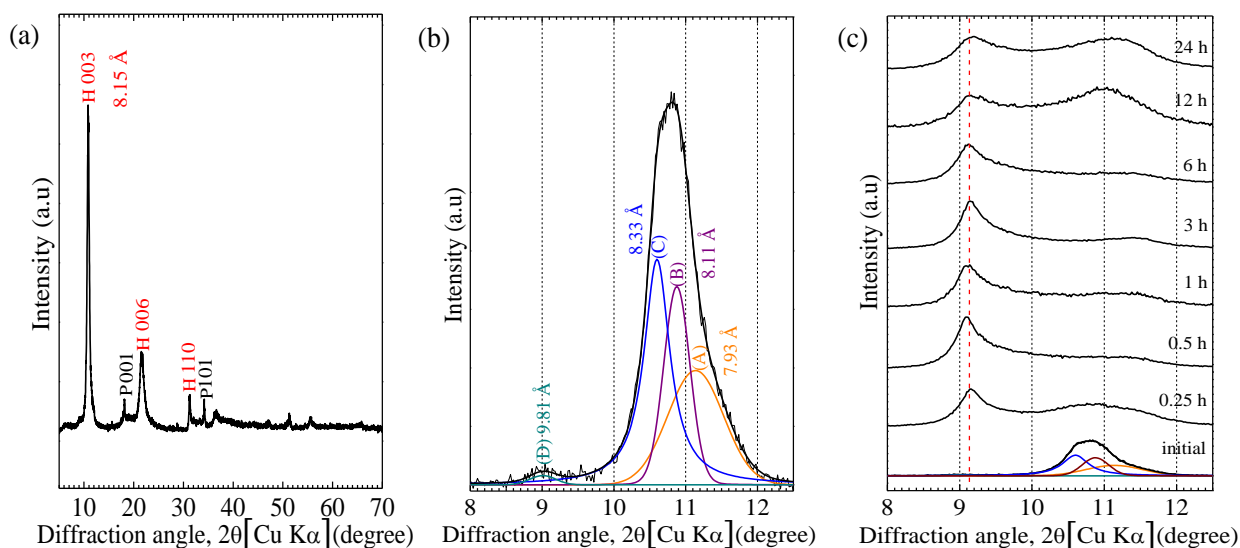
Fig. 5.1 X-ray diffraction patterns of synthesized Ca_2Al-LDH in a region of (a) 5° to 70°, (b) 8° to 12.5° in 2θ, (c) changes in XRD patterns of Ca_2Al-LDH over suspending time in alkaline solutions. Symbols in (a): H, hydrocalumite (PDF#42-0063); P, portlandite (PDF#72-0156) and in (b): (A), Ca_2Al-LDH (unknown); (B)~(D), Ca_2Al-LDH(SeO_4).

Fig. 5.1(a) shows the XRD pattern of synthesized Ca_2Al-LDH. The interlayer spacing at d_{003} was 8.15 Å which was consistent with the previous reports by experimental studies (Baur and Johnson, 2003b; Baur et al., 2004). Two weak peaks of portlandite $Ca(OH)_2$ (PDF # 72-0156) were also detected around 18.1° and 34.8° in 2θ. Due to the existence of CO_3^{2-} derived from air, peak separation of 003 plane in **Fig. 5.1(a)** was carried out as shown in **Fig. 5.1(b)**. There are four

components which can be assigned to (A) Ca$_2$Al-LDH (unknown) at d_{003} = 7.93 Å, (B)~(D) Ca$_2$Al-LDH(SeO$_4$) with different water molecule numbers in hydration of SeO$_4^{2-}$ at d_{003} = 8.11 Å, 8.31 Å, and 9.81 Å (Baur and Johnson, 2003b; Zhang, 2003), where the component (A) should include SeO$_4^{2-}$ and CO$_3^{2-}$ possibly as intercalators.

5.3.2 Suspension of Ca$_2$Al-LDH in alkaline solution

Changes in the released SeO$_4^{2-}$, Ca^{2+}, and Al(OH)$_4^-$ concentrations over time are shown in **Fig. 5.2(a)~(c)** when the synthesized Ca$_2$Al-LDH was suspended into alkaline solutions without any amino acids. Simple dissolution caused 0.34 mM SeO$_4^{2-}$ released from Ca$_2$Al-LDH within 15 min, then the concentration gradually raised to 0.45 mM at the equilibrium around 6 h, where 4.4 mM Ca^{2+} and 1.8 mM Al(OH)$_4^-$ were dissolved. The pH values immediately increased from 11.0 to 12.0 (**Fig. 5.2(d)**). This means Ca$_2$Al-LDH is much more fragile than Mg$_2$Al-LDH which in our previous report (Wang et al., 2021).

Fig. 5.1(c) shows the changes in XRD patterns of the solid residues at different suspending time intervals in the absence of amino acids. After 15 min, the main peak position (003 plane) of Ca$_2$Al-LDH shifted from 10.7° to 9.14° in 2θ corresponding to the interlayer spacing expanded from 8.15 Å to 9.66 Å. The peak intensity at 9.14° in 2θ increased from 15 min to 6 h and then partially shifted to 11.0° in 2θ after 12 h. The dominant interlayer spacing of Ca$_2$Al-LDH in the solid residues was always kept around 9.66 Å which is probably due to the hydration of SeO$_4^{2-}$ in interlayer without amino acids. Also, the interlayer spacing of Ca$_2$Al-LDH(SeO$_4$) is strongly dependent on the number of coordinated water molecules.
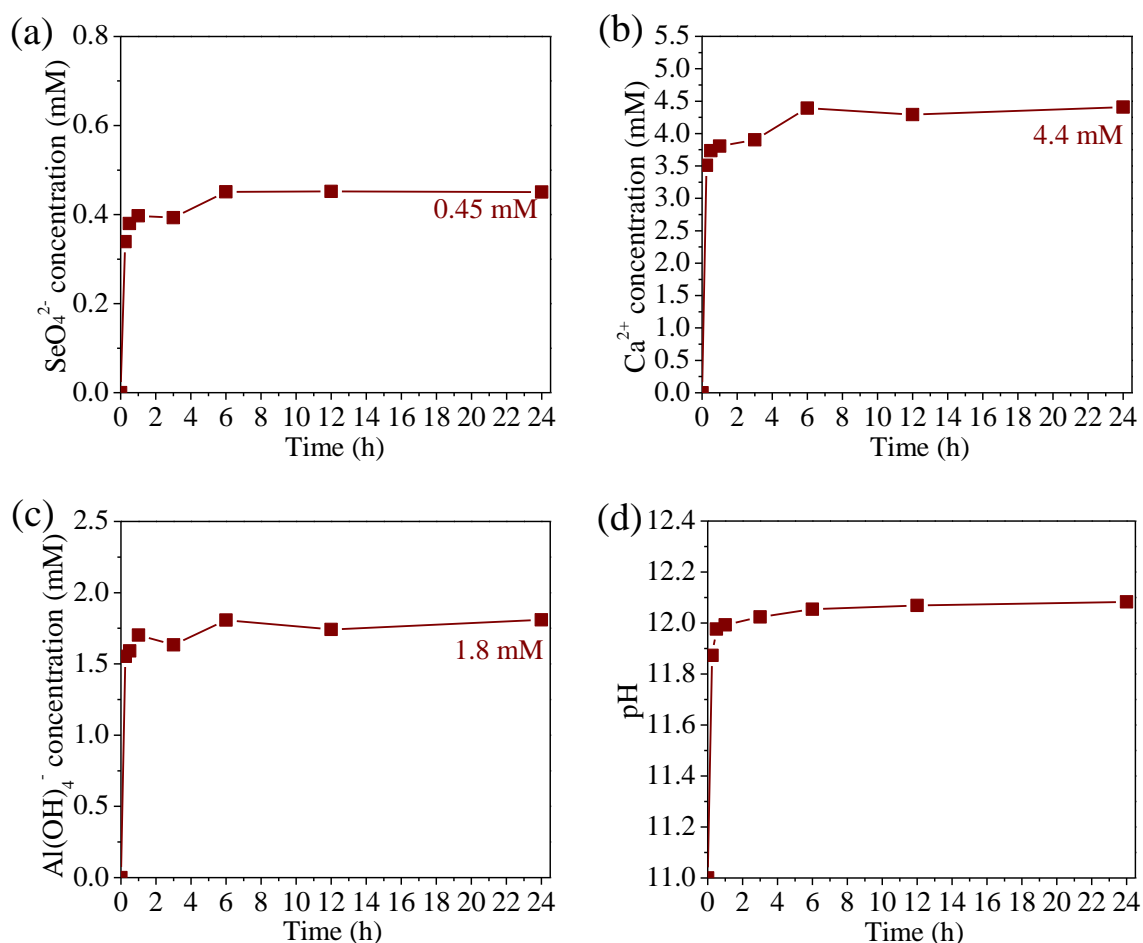
Fig. 5.2 Dissolution kinetics of (a) SeO_4^{2-}, (b) Ca^{2+}, and (c) $Al(OH)_4^-$ concentrations from synthesized Ca_2Al-LDH and (d) pH after suspended into alkaline solutions without amino acids.

The bond length of Se-O in SeO_4^{2-} is around 1.644 Å and it can possess various bond length values when combined with different numbers of water molecules in the aqueous solution. It has been reported that the Se-O bond length was 1.674 Å for hexa-hydrated selenate, however, the length is changeable from 1.655 to 1.701Å for tri-hydrated selenate (Pye and Walker, 2011; Eklund and Persson, 2014). Therefore, when SeO_4^{2-} is hydrated in LDH, the Se-O bond length tends to increase to different extents and is possible to expand the interlayer spacing of Ca_2Al-LDH.

5.3.3 Interaction of Ca_2Al-LDH with amino acids

After adding the synthesized Ca_2Al-LDH into amino acids solutions at pH 11.0, the releasing behaviors of SeO_4^{2-}, Ca^{2+} and $Al(OH)_4^-$ showed different trends compared with the blank test. As shown in **Fig. 5.3(a)**, with increase in the concentrations of HPhe and HTrp to 5.0 mM, the released concentration of SeO_4^{2-} was maintained around 0.47 mM which is close to in the blank, indicating that the HPhe and HTrp did not promote the release of SeO_4^{2-} from Ca_2Al-LDH. On the other hand, HGly, H_2Asp, and H_2Cys enhanced SeO_4^{2-} releasing progressively with an increase in the concentrations, compared with in the blank (C_0 for amino acid = 0). The equilibrated SeO_4^{2-} concentrations reached 0.687 mM in H_2Asp, 0.623 mM in HGly, and 0.592 mM in H_2Cys which correspond to 73.8%, 66.9% and 63.7% in the original contents of SeO_4^{2-} in LDH. In the presence of amino acids, the release of Ca^{2+} and $Al(OH)_4^-$ was lower than in the blank test, suggesting that amino acids might stabilize the hydroxide layer of Ca_2Al-LDH (**Fig. 5.3(b), (c)**). HPhe and HTTrp molecules have one amino and one carboxyl group with an aromatic group in a side-chain that possesses the hydrophobic property. Under alkaline conditions, HPhe and HTrp are deprotonated to be Phe^- and Trp^- because of the pK_a values of carboxyl groups. However, ion-exchange of SeO_4^{2-} with Phe^- and Trp^- in interlayer spaces did not happen significantly, probably due to their larger molecular sizes and hydrophobicity. H_2Asp, H_2Cys, and HGly are relatively hydrophilic amino acids, where H_2Asp and H_2Cys are dissociated to Asp^{2-}, Cys^{2-} under alkaline conditions to cause the same negative charge numbers with SeO_4^{2-}. While Gly would get one negative charge but it has the smallest molecular size making it more easily intercalated into Ca_2Al-LDH. Based on the above properties of each amino acid molecule, HGly, H_2Asp, and H_2Cys might have promoted the release of SeO_4^{2-} from Ca_2Al-LDH interlayer through ion-exchange, this behavior affects the stability of SeO_4^{2-} in Ca_2Al-LDH.
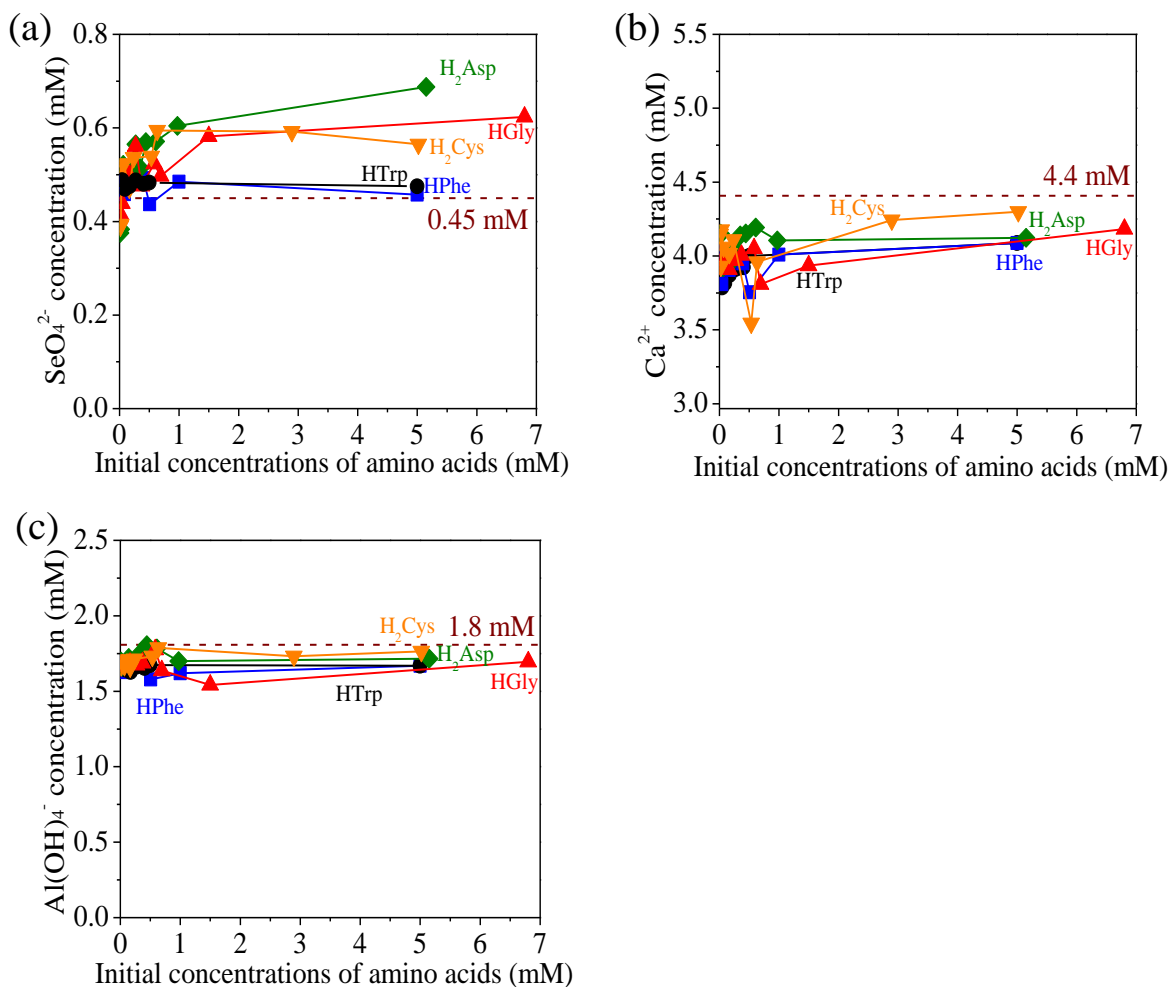
Fig. 5.3 Plots of (a) SeO_4^{2-}, (b) Ca^{2+}, and (c) $Al(OH)_4^-$ concentrations dissolved from Ca_2Al-LDH against the initial concentrations of amino acids. Dotted lines indicate the equilibrated concentrations in the absence of amino acids ($C_0 = 0$).
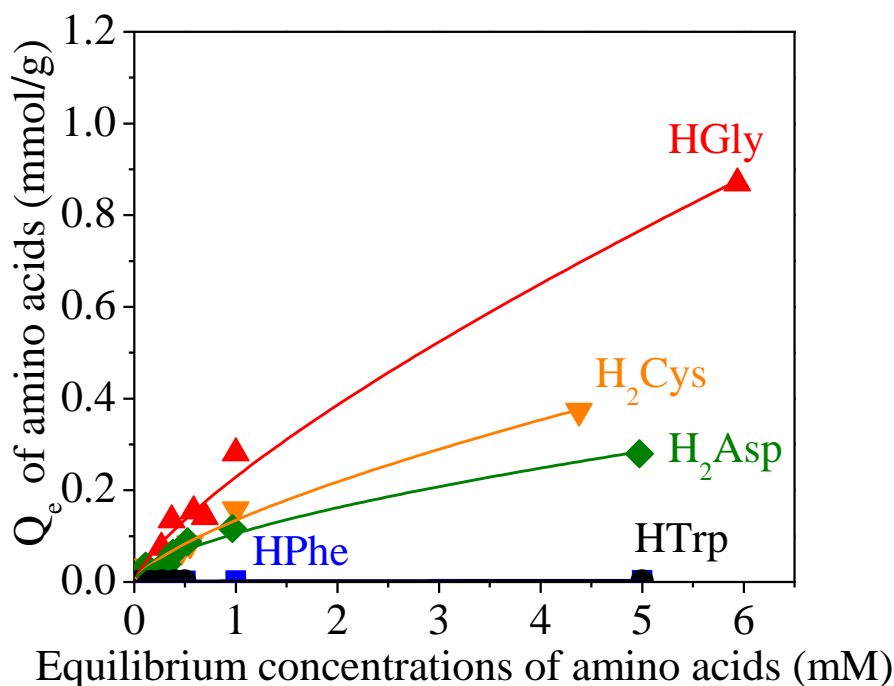
Fig. 5.4 Sorption isotherms of HGly (▲), H₂Asp (◆), H₂Cys (▼), HPhe (■), and HTrp (●) onto Ca₂Al-LDH. Solid lines indicate the fittings to Freundlich model.

Since the partial dissolution happened with Ca₂Al-LDH, the sorption data of amino acids onto Ca₂Al-LDH were fitted to Freundlich model (**Eq. (5.8)**) rather than Langmuir model, as shown in **Fig. 5.4**.

$$Q_e = K_f C_e^{1/n} \tag{5.8}$$

where C_e (mM) is the equilibrium concentration, Q_e (mmol/g) is the adsorption density, K_f represents the adsorption capacity, $1/n$ represents the adsorption intensity ($0 < 1/n < 1$). Fitting results are summarized in **Table 5.1**. The Freundlich sorption constants (K_f) were in the order of HGly > H₂Cys > H₂Asp > HTrp > HPhe, indicating that HGly has a significantly higher affinity than other amino acids, especially compared with HPhe and HTrp (Yan et al., 2008; Chen et al., 2010). The molecular size is more important to affect the intercalation than charge numbers, probably due to the different steric hindrance they caused (Santos et al., 2017). In HGly, H₂Asp, and H₂Cys series, they showed high adsorption densities which might be contributed by their

intercalation. This also implies that the possible mechanism to enhance SeO_4^{2-} release from Ca_2Al-LDH by HGly, H_2Asp, and H_2Cys might be a partial substitution with SeO_4^{2-} in the interlayer.

Table 5.1 Fitting results to Freundlich isotherms in sorption of different amino acids on Ca_2Al-LDH.

Amino acids	K_f	n	R^2
L-phenylalanine	0.0024	3.99	0.967
L-tryptophan	0.0044	3.92	0.932
Glycine	0.2291	1.33	0.988
L-aspartic	0.1057	1.62	0.978
L-cysteine	0.1348	1.44	0.990

5.3.4 XRD peak separation at 003 plane reflections for Ca_2Al-LDH solid residues

XRD patterns of each solid residue of Ca_2Al-LDH after interacting with different amino acids were collected and its peak separation was performed to explore the effect of amino acids on the stability of SeO_4^{2-} in Ca_2Al-LDH as shown in **Fig. 5.5**. XRD patterns for Ca_2Al-LDH after interacted with HGly, H_2Asp, and H_2Cys series were changed depending on the initial amino acids concentrations (**Fig. 5.5(a)~(c)**). As the loading amount of amino acids increasing, the 003 peak position was shifted to larger angles in 2θ gradually. In all XRD patterns except for H_2Asp-1 (**Fig. 5.5(b)**), the largest layer spacing component at $d_{003} = 9.81$ Å (component (D)) disappeared while it was observed clearly in the blank test (**Fig. 5.1(c)**). Due to the relatively large adsorption amounts of HGly, H_2Asp, and H_2Cys in Ca_2Al-LDH (**Fig. 5.4**) and their enhanced leaching effects on SeO_4^{2-} (**Fig. 5.3**), amino acids should be considered as one of the intercalators in peak separation process. In the low concentration range of amino acids (from 0.00 to 0.03 mM), the adsorption amount of them almost can be ignored as shown in **Fig. 5.4**, hence, the intercalation of HGly, H_2Asp, and H_2Cys into Ca_2Al-LDH seemed not occur in this range. Taking this into consideration, the separation of 003 peak in **Fig. 5(a)~(c)** was carried out in the same manner as the original material (**Fig. 5.1(b)**) which only include the component of Ca_2Al-LDH(unknown) and Ca_2Al-

LDH(SeO$_4$). As the concentrations of amino acids increasing to [HGly]$_0$ > 0.16 mM (HGly-3), [H$_2$Asp]$_0$ > 0.06 mM (H$_2$Asp-3), and [H$_2$Cys]$_0$ > 0.03 mM (H$_2$Cys-3), the main peak position started shift to larger diffraction angles. Also, the adsorption amount of them started increasing, there appeared two additional components after the separation of d_{003} with interlayer spacing in 2θ present as component (E) with 7.70 Å (11.5°, 2θ) and component (F) with 7.83 Å (11.28°, 2θ). Components of (B) and (C) were identified in the original material, but the peak assignment of (A), (E), and (F) are still unclear. At the highest concentrations of HGly and H$_2$Asp, component (E) seems to have become the predominant phase which indicates the main intercalator has been transited from SeO$_4^{2-}$ to other anions.

(a)

(b)

(c)

(d)
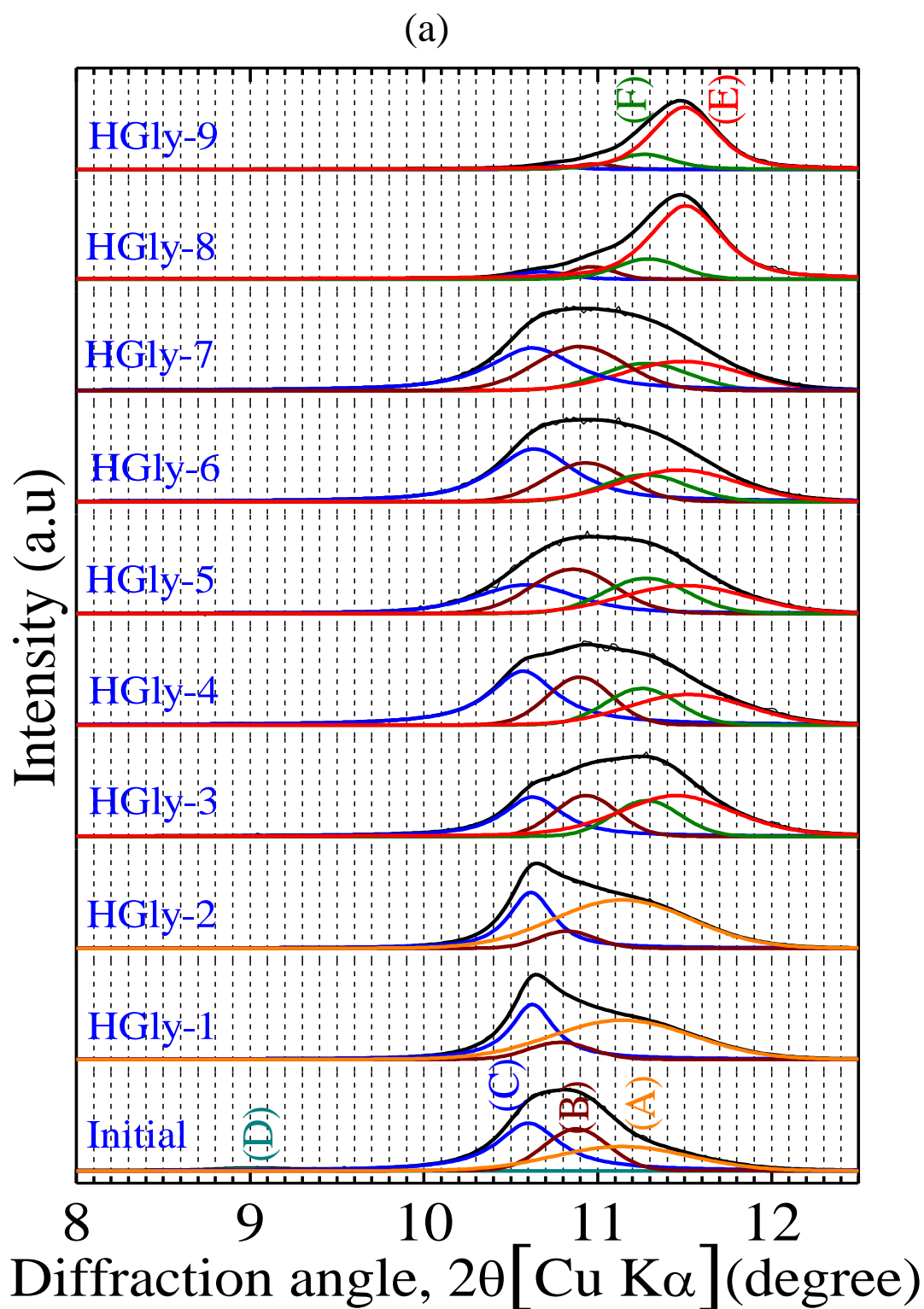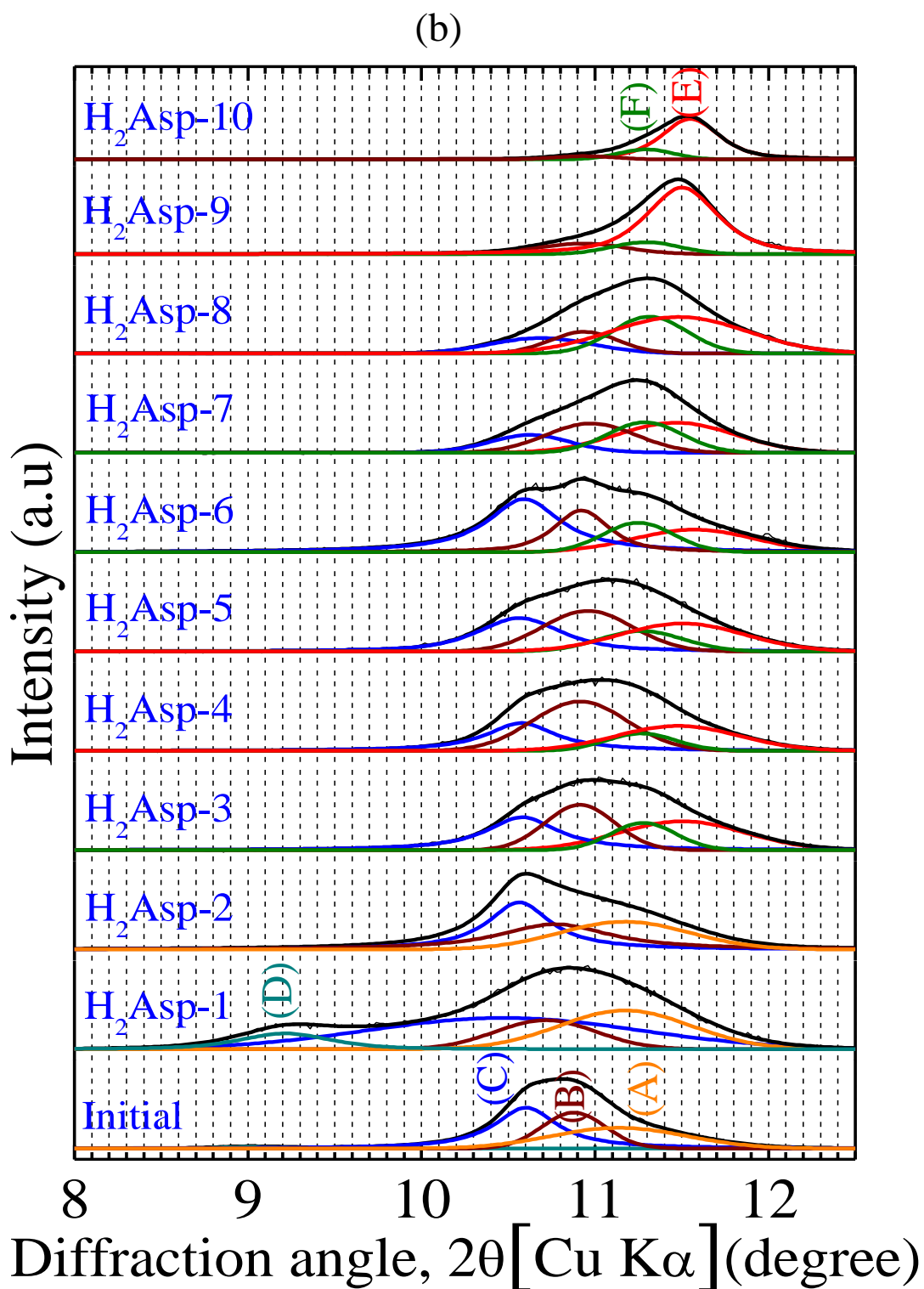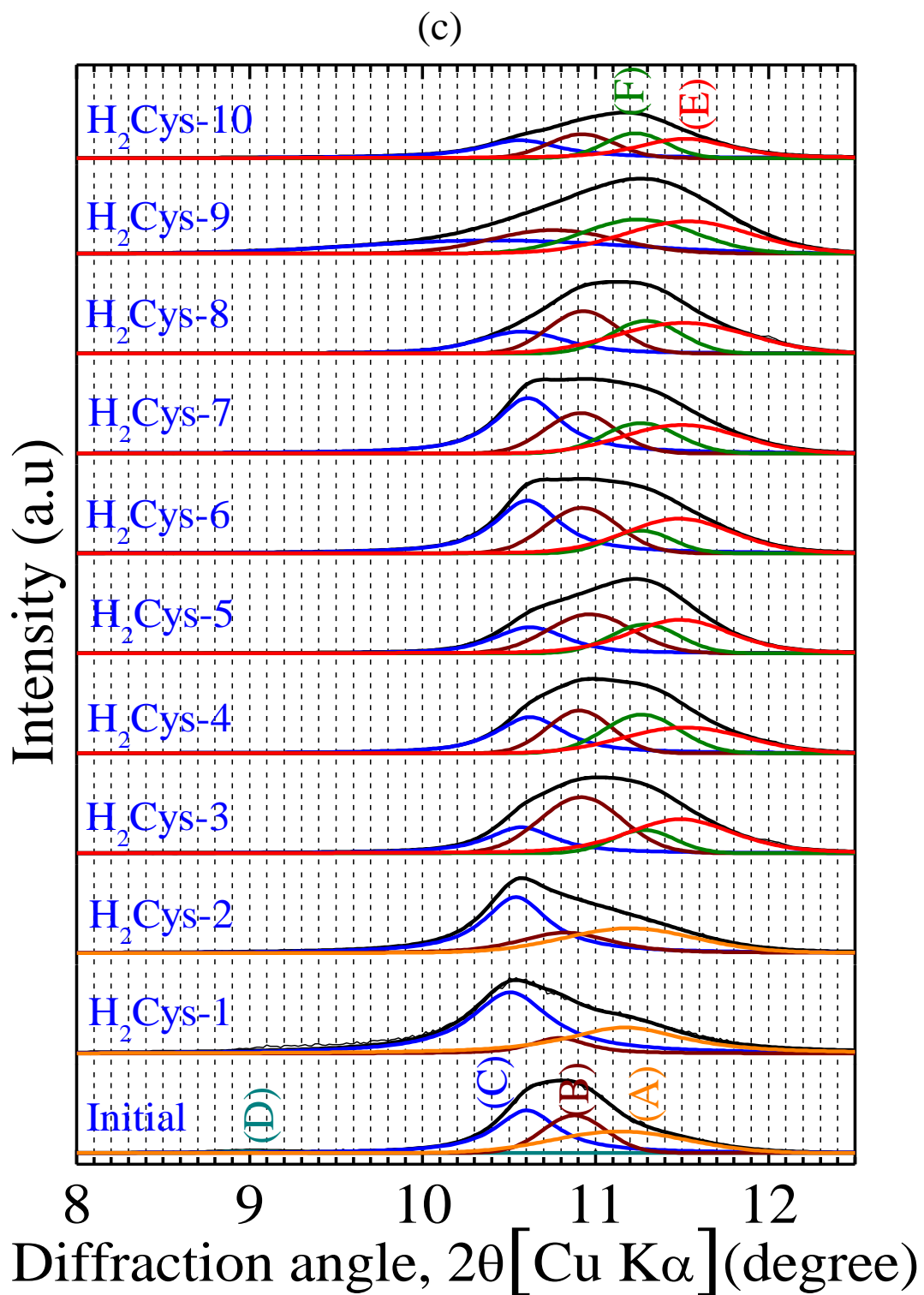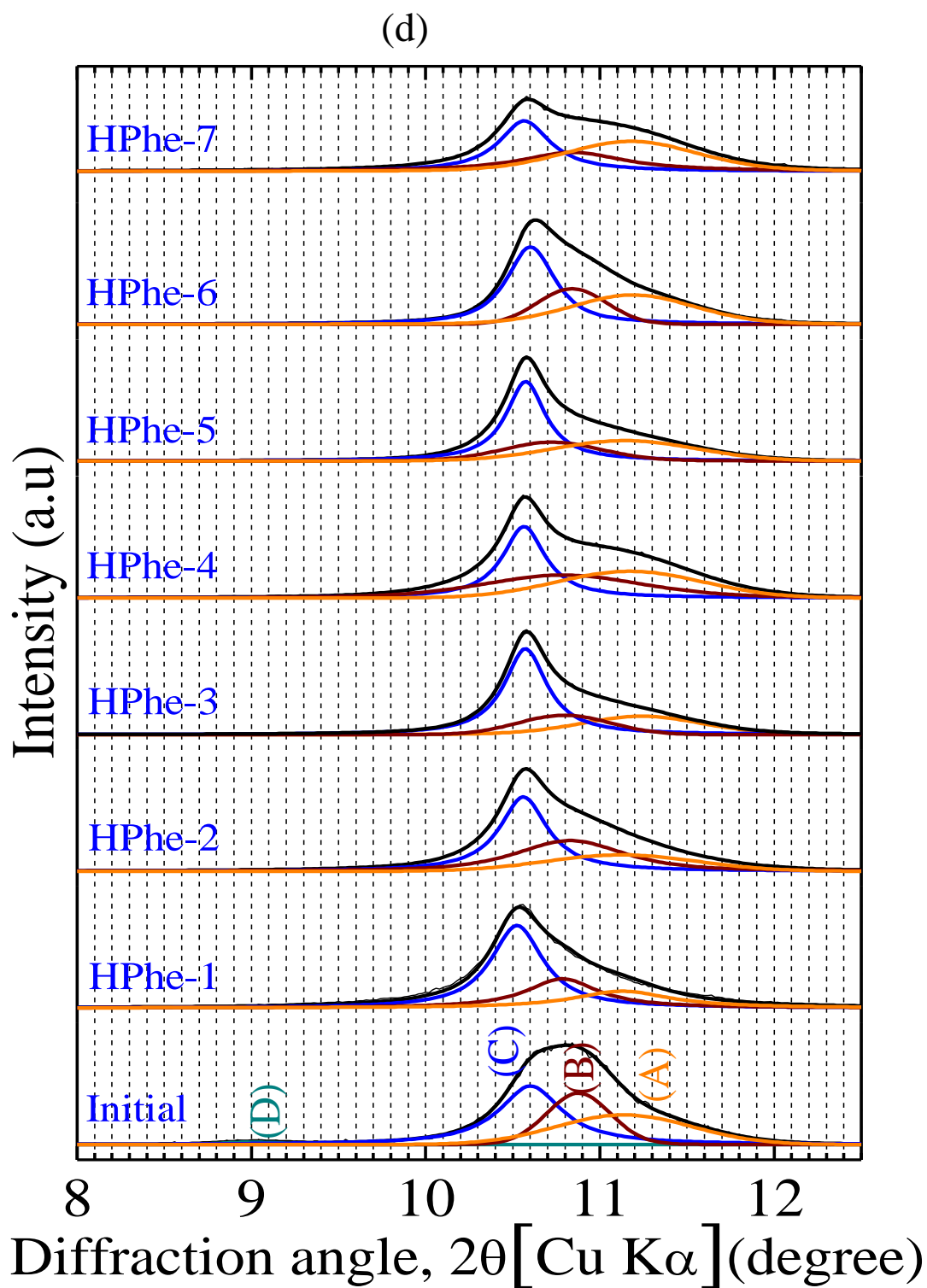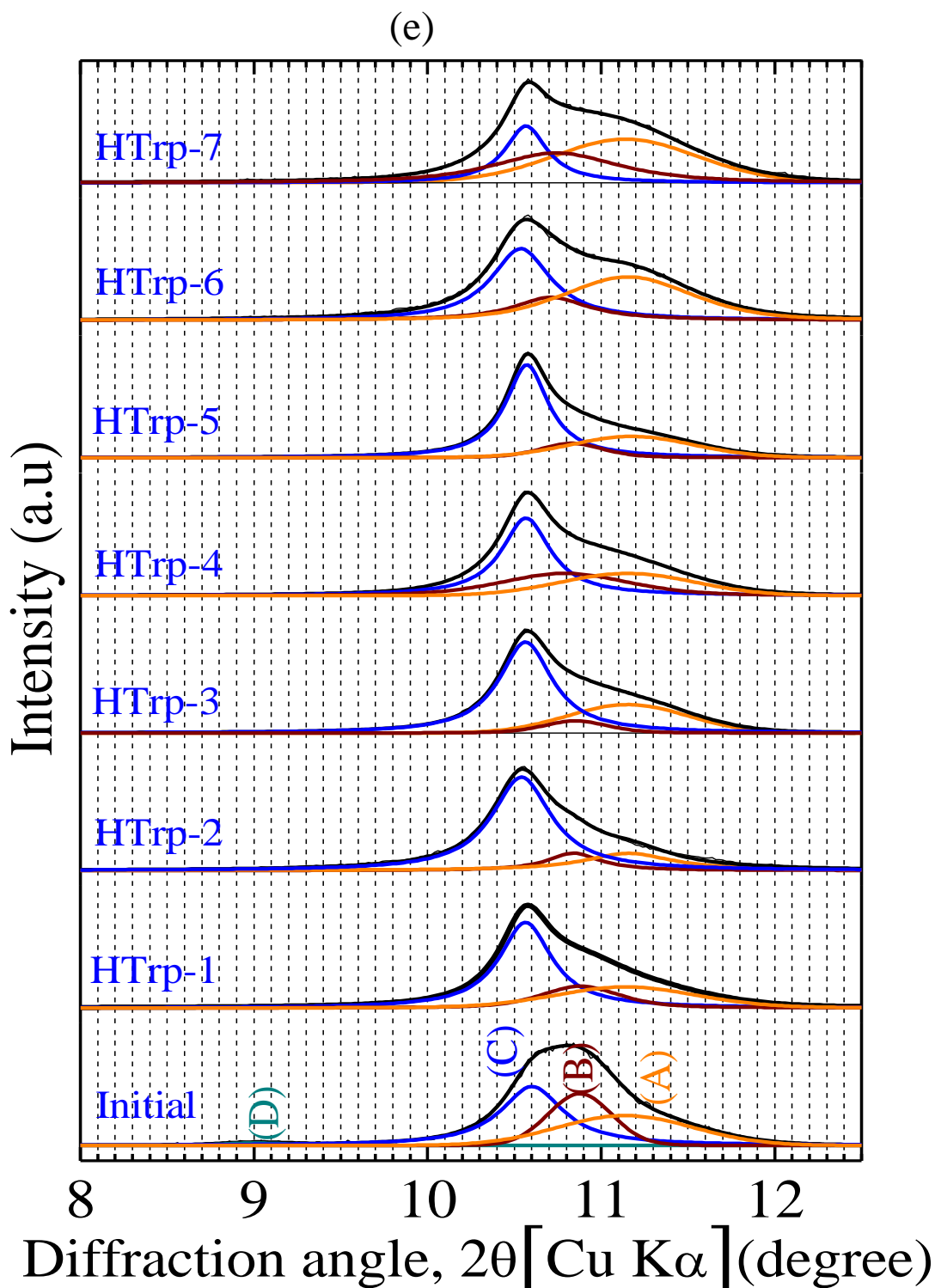
Fig. 5.5 X-ray diffraction patterns of Ca_2Al-LDH solid residues after suspended in different concentrations of amino acids. Component E, Ca_2Al-LDH (amino acid, CO_3) (d_{003} = 7.70 Å); F, Ca_2Al-LDH (amino acid) (d_{003} = 7.83 Å); A, Ca_2Al-LDH(unknown) (d_{003} = 7.93 Å); B, Ca_2Al-LDH(SeO$_4$) (d_{003} = 8.11 Å); C, Ca_2Al-LDH(SeO$_4$) (d_{003} = 8.31 Å) and D, Ca_2Al-LDH(SeO$_4$) (d_{003}

= 9.81 Å). Initial concentrations: (a) HGly-1, 0.01 mM; HGly-2, 0.04 mM; HGly-3, 0.16 mM; HGly-4, 0.27 mM; HGly-5, 0.37 mM; HGly-6, 0.58 mM; HGly-7, 0.69 mM; HGly-8, 1.0 mM; HGly-9, 6.8 mM,

(b) H_2Asp-1, 0.01 mM; H_2Asp-2, 0.02 mM; H_2Asp-3, 0.06 mM; H_2Asp-4, 0.14 mM; H_2Asp-5, 0.27 mM; H_2Asp-6, 0.35 mM; H_2Asp-7, 0.44 mM; H_2Asp-8, 0.61 mM; H_2Asp-9, 0.97 mM; H_2Asp-10, 5.15 mM,

(c) H_2Cys-1, 0.01 mM; H_2Cys-2, 0.02 mM; H_2Cys-3, 0.03 mM; H_2Cys-4, 0.07 mM; H_2Cys-5, 0.17 mM; H_2Cys-6, 0.24 mM; H_2Cys-7, 0.54 mM; H_2Cys-8, 0.63 mM; H_2Cys-9, 2.89 mM; H_2Cys-10, 5.02 mM.

(d) HPhe-1 0.04 mM; HPhe-2, 0.08 mM; HPhe-3 0.16 mM; HPhe-4, 0.39 mM; HPhe-5, 0.51 mM; HPhe-6,1.0 mM; HPhe-7, 5.0 mM.

(e) HTrp-1, 0.04 mM; HTrp-2, 0.08 mM; HTrp-3, 0.25 mM; HTrp-4, 0.30 mM; HTrp-5, 0.50 mM; HTrp-6, 1.0 mM; HTrp-7, 5.0 mM.

XRD patterns for the solid residues after suspension of Ca_2Al-LDH in 0~5 mM HPhe and HTrp did not show the components (D), (E), and (F) at all. Considering the trace amount of adsorption of HPhe and HTrp in Ca_2Al-LDH (as shown in **Fig. 5.4**), the intercalation of HPhe and HTrp should not be considered in the peak separation of XRD patterns for the solid residues. Therefore, there were still three components (A), (B), (C) of 003 reflections in all of XRD patterns as depicted in **Fig. 5.5(d), (e)**, which are the same as original material. Based on the peak assignment in **Fig. 5.1(b)**, the components of (B) and (C) are assigned to Ca_2Al-LDH(SeO_4) (d_{003} = 8.11 Å) and Ca_2Al-LDH(SeO_4) (d_{003} = 8.31 Å) with different hydrations, and the component (A) is assigned to Ca_2Al-LDH(unknown) (d_{003} = 7.93 Å).

For a better understanding of the components of (E) and (F), which were observed in **Fig. 5.5(a)~(c)**, DFT simulations were performed. Since there are similar trends in changes of XRD patterns between HGly and H_2Asp series but different from H_2Cys series, anions of Asp^{2-}, Cys^{2-}, SeO_4^{2-} and CO_3^{2-} in solutions were selected to simulate the possible interactions among anions in Ca_2Al-LDH and the corresponding interlayer spacings as well as formation energies. Under the present alkaline condition, H_2Asp and H_2Cys were dissociated to be Asp^{2-} and Cys^{2-}. In the unit cell of Ca_2Al(OH)$_6$·0.5SeO_4, the ion-exchange of amino acids with SeO_4^{2-} was simulated in **Fig. 5.6(a), (b)**. Atomic and electronic structure calculations predicted that SeO_4^{2-} is preferable to

remain in the interlayer of Ca_2Al-LDH than Asp^{2-} and Cys^{2-} because the greater x values lead to the larger formation energies. Since CO_3^{2-} also was included in the unit cell of $Ca_2Al(OH)_6 \cdot 0.5CO_3$, the ion-exchange of Asp^{2-} and Cys^{2-} with CO_3^{2-} also was calculated by changing x values as shown in **Fig. 5.6(c), (d)**. In the unit cell of $Ca_2Al(OH)_6 \cdot 0.5(1-x)CO_3 \cdot 0.5xAsp$ at $x = 1$ after intercalation of Asp, the formation energies were lower than $Ca_2Al(OH)_6 \cdot 0.5(1-x)CO_3 \cdot 0.5xCys$ at $x = 1$. This indicates that Asp^{2-} can be more easily ion-exchanged than Cys^{2-}, and that Asp^{2-} is likely to occupy the adsorption sites in the interlayer of Ca_2Al-LDH than CO_3^{2-}. Therefore, based on the above results, the selectivity of ion-exchange sites in Ca_2Al-LDH interlayer can be expected in the order of $SeO_4^{2-} > Asp^{2-} > Cys^{2-} \cong CO_3^{2-}$.

Regarding possible combinations of a couple of anions in the unit cell of $Ca_2Al(OH)_6(X, Y)$ including different configurations of amino acids, SeO_4^{2-} and CO_3^{2-}, the distribution of interlayer spacing values in angstrom (Å) were obtained as shown in **Fig. 5.7**. When the single anion exists in one unit cell, there were four systems of Ca_2Al-LDH including $Ca_2Al(OH)_6 \cdot 0.5Asp$, $Ca_2Al(OH)_6 \cdot 0.5Cys$, $Ca_2Al(OH)_6 \cdot 0.5CO_3$, and $Ca_2Al(OH)_6 \cdot 0.5SeO_4$. For $Ca_2Al(OH)_6 \cdot 0.5Asp$ and $Ca_2Al(OH)_6 \cdot 0.5Cys$, the calculated values were distributed in wider ranges of interlayer spacing of 7.3 to 9.5 Å and 7.2 to 9.0 Å (**Fig. 5.7(a),(d)**), respectively, than inorganic anions intercalated LDH (**Fig. 5.7(g)~(i)**). $Ca_2Al(OH)_6 \cdot 0.5CO_3$ and $Ca_2Al(OH)_6 \cdot 0.5SeO_4$ showed a relatively narrow range of interlayer spacing with 6.2 to 6.5 Å and 7.5 to 8.1 Å, respectively. This indicates amino acids molecules are in a large variety of configurations in LDH layers. When the mixed anions exist in one unit cell ($x = 0.5$), including amino acids, four systems also were calculated. In the unit cell of $Ca_2Al(OH)_6 \cdot 0.5(1-x)SeO_4 \cdot 0.5xAsp$ ($x = 0.5$) and $Ca_2Al(OH)_6 \cdot 0.5(1-x)SeO_4 \cdot 0.5xCys$ ($x = 0.5$), interlayer spacing of 7.7 to 8.5 Å (**Fig. 5.7(b)**) and 7.5 to 8.3 Å (**Fig. 5.7(e)**) were obtained, which were larger than pure SeO_4^{2-} systems but smaller than pure Asp^{2-} and Cys^{2-} systems. In the system of amino acids mixed with CO_3^{2-}, 6.9 to 8.3 Å for Asp^{2-} (**Fig. 5.7(c)**) and 6.9 to 8.4 Å for Cys^{2-} (**Fig. 5.7(f)**) which are a little bit smaller than SeO_4^{2-} mixed with amino acids. Notably, there

is a trend that as the interlayer spacing increasing, the formation energy also increased. The wide ranges distribution of spacing may lead to the entropy contribution to free energy. This may stabilize the amino acids-including systems.
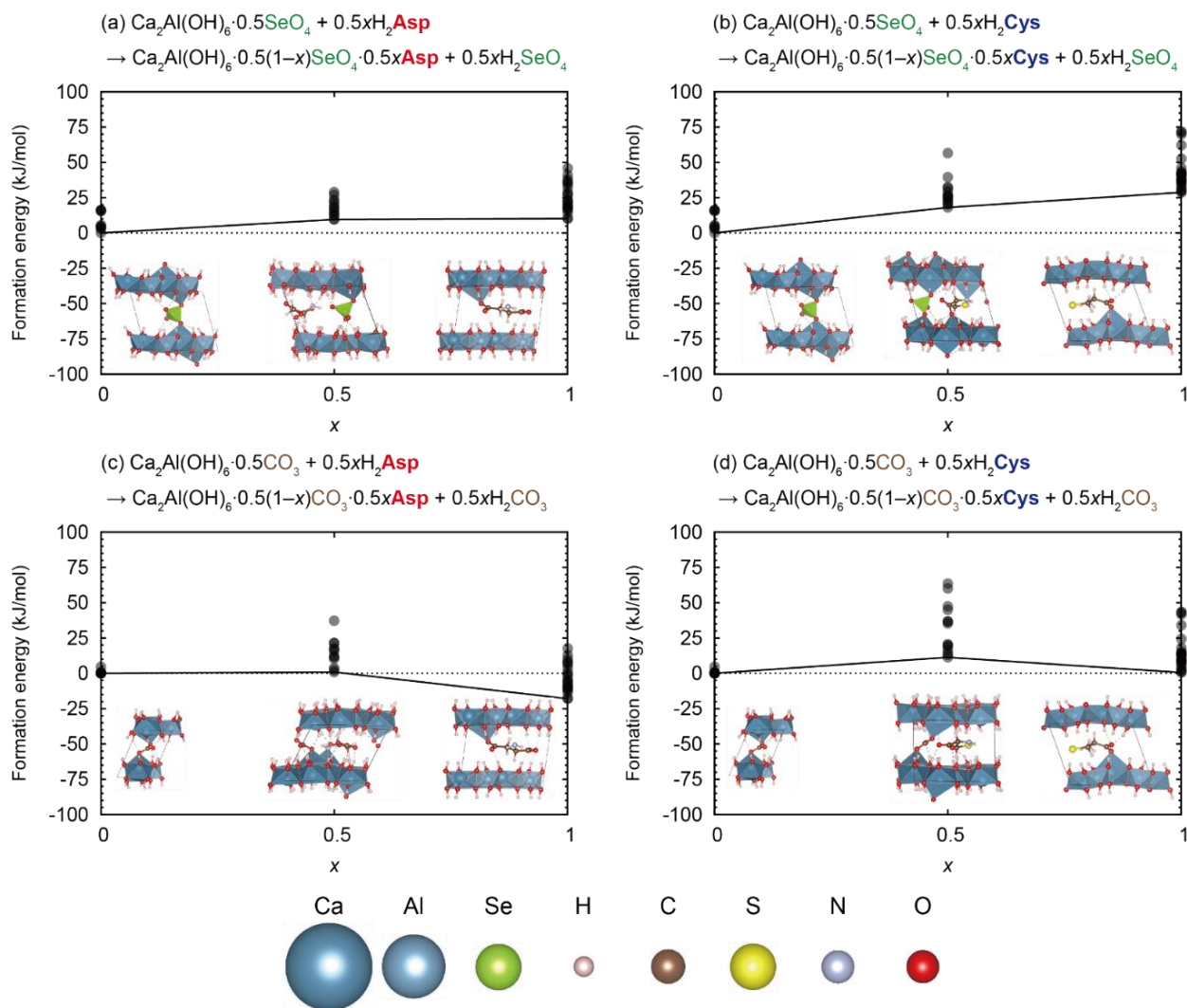
Fig. 5.6 Formation energies of (a) $Ca_2Al(OH)_6 \cdot 0.5(1-x)SeO_4 \cdot 0.5xAsp$, (b) $Ca_2Al(OH)_6 \cdot 0.5(1-x)SeO_4 \cdot 0.5xCys$, (c) $Ca_2Al(OH)_6 \cdot 0.5(1-x)CO_3 \cdot 0.5xAsp$, and (d) $Ca_2Al(OH)_6 \cdot 0.5(1-x)CO_3 \cdot 0.5xCys$, ($x = 0, 0.5, 1$) via the ion-exchange reactions of SeO_4^{2-} and CO_3^{2-} with Asp^{2-} and Cys^{2-}. The schematic structures with the lowest formation energies are illustrated in the insets.
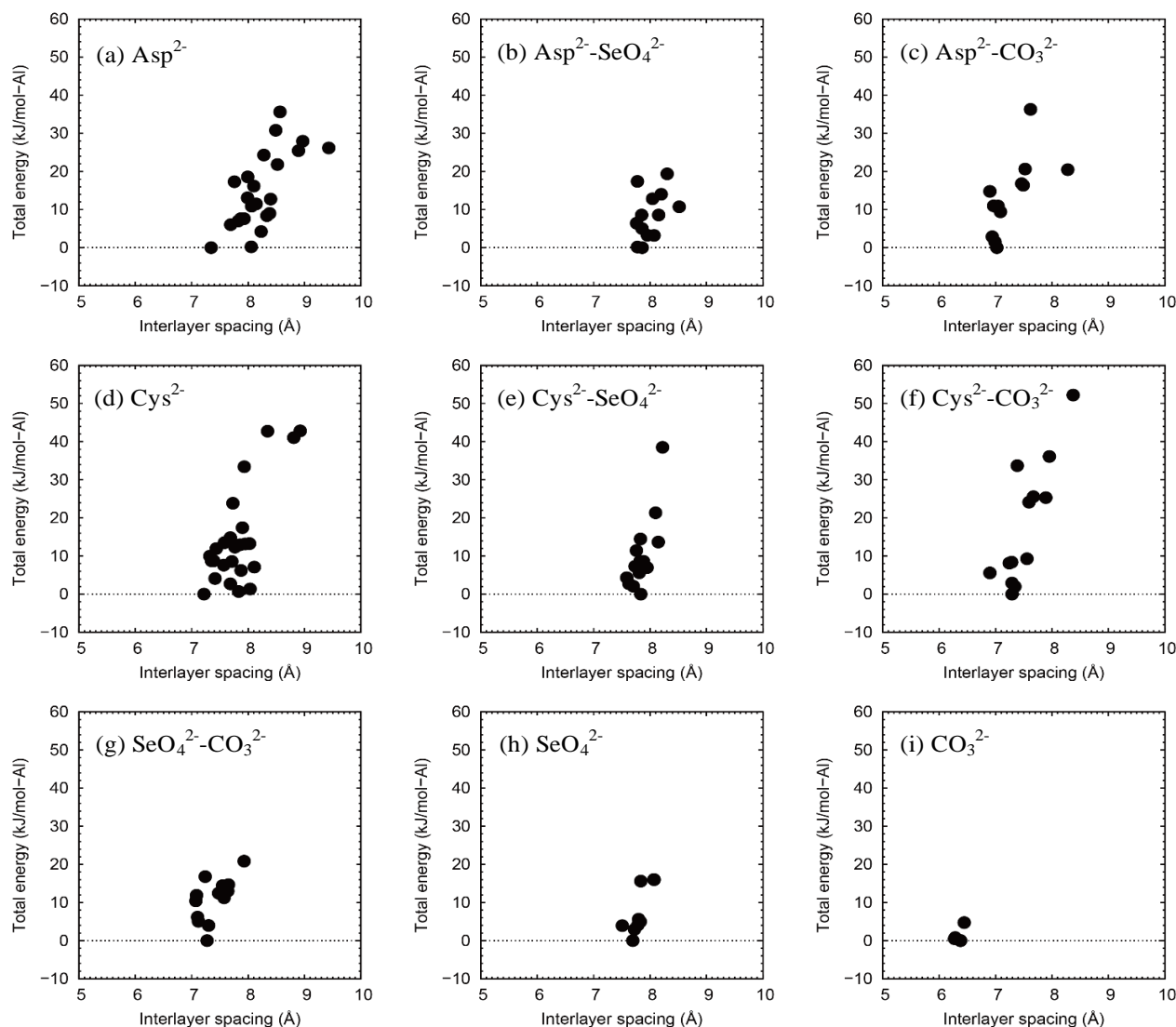
Fig. 5.7 Total energies plotted against interlayer spacing for Ca_2Al-LDH including (a) Asp^{2-}, (b) Asp^{2-}-SeO_4^{2-}, (c) Asp^{2-}- CO_3^{2-}, (d) Cys^{2-}, (e) Cys^{2-}- SeO_4^{2-}, (f) Cys^{2-}- CO_3^{2-}, (g) SeO_4^{2-}- CO_3^{2-}, (h) SeO_4^{2-}, (i) CO_3^{2-}.

Here, we selected interlayer spacing with the lowest formation energy in each system to compare with our experimental results in **Fig. 5.5(c)~(e)**. Taking into account the anhydrous systems in the present simulation, the involvement of water molecules in the real system should affect the interlayer spacing through the host-guest interaction as well as water molecules supply a more flexible space (Yan et al., 2009; Brian et al., 2016). So the computational interlayer values in anhydrous state should be smaller than the experimental results. Therefore, the component (F) in **Fig. 5.5** can be possibly assigned to d_{003} of 7.35 Å in Ca_2Al-LDH(Asp) and 7.20 Å in Ca_2Al-

LDH(Cys) in DFT simulation (**Fig. 5.7 (a), (d)**). The d_{003} is smaller in component (E) than component (F), so the smaller interlayer spacing values from computational results in **Fig. 5.7 (c)** of 7.0 Å and **Fig. 5.7 (f)** of 7.3 Å are likely to be assigned. The differences between simulated interlayer spacings and experimentally obtained values are 0.4 - 0.7 Å. In addition to the water molecules effect, the more complex stacking modes of the layers than simplified unit cell also contributed to the differences. Therefore, based on the above analysis, peak assignments of (E) and (F) in **Fig. 5.5(c)~(e)** are likely to be Ca_2Al-LDH(Gly/Asp/Cys+CO_3) and Ca_2Al-LDH (Gly/Asp/Cys), respectively. Pure Ca_2Al-LDH(CO_3), where sole CO_3^{2-} is an intercalator in a unit cell of LDH, was excluded from the peak assignments here because the simulated values are too small far from the observed values.

Further, the converged configurations of $Ca_2Al(OH)_6 \cdot 0.25xCO_3 \cdot 0.5Asp$ ($x = 0.5$), $Ca_2Al(OH)_6 \cdot 0.25CO_3 \cdot 0.5Cys$ ($x = 0.5$), $Ca_2Al(OH)_6 \cdot 0.5Asp$ ($x = 1$), and $Ca_2Al(OH)_6 \cdot 0.5Cys$ ($x = 1$) showed the possible interaction of Asp^{2-} and Cys^{2-} between Ca_2Al-LDH sheets in **Fig. 5.8**. Hydrogen bonds can be formed through carboxyl and amine groups in amino acids to hydroxide layers, and also Ca-O bonds can be created through the oxygen atoms in the carboxyl groups of amino acids with Ca atoms in $[Ca_2Al(OH)_6]^+$. Formation of chemical bonds of Ca-O between the carboxyl groups and Ca atoms in LDH has been predicted by DFT at the first time as long as we know, although it has been predicted by the single crystal XRD (Renaudia et al., 1999). Such a formation of Mg-O chemical bond was not predicted in hydrotalcite (Mg_2Al-LDH) by DFT (Wang et al., 2021), because the atomic size of Ca is enough large to be bared on the hydroxide layers of LDH (**Fig. 5.8(c), (d)**). These chemical bonds promoted amino acids molecules oriented in a horizontal direction with their longest axis approximately parallel to the plane of the $[Ca_2Al(OH)_6]^+$. Unexpectedly, direct interaction between amino acids molecules and CO_3^{2-} was not predicted in binary systems of Asp^{2-}-CO_3^{2-} and Cys^{2-}-CO_3^{2-} (**Fig. 5.8(a), (b)**). Neither chemical

bonds nor hydrogen bonds were projected through thiol groups (-SH) in H$_2$Cys and the hydroxide

layers [Ca$_2$Al(OH)$_6$]$^+$ to stabilize the unit cell of Ca$_2$Al(OH)$_6$·0.5Cys (**Fig. 5.8(d)**).
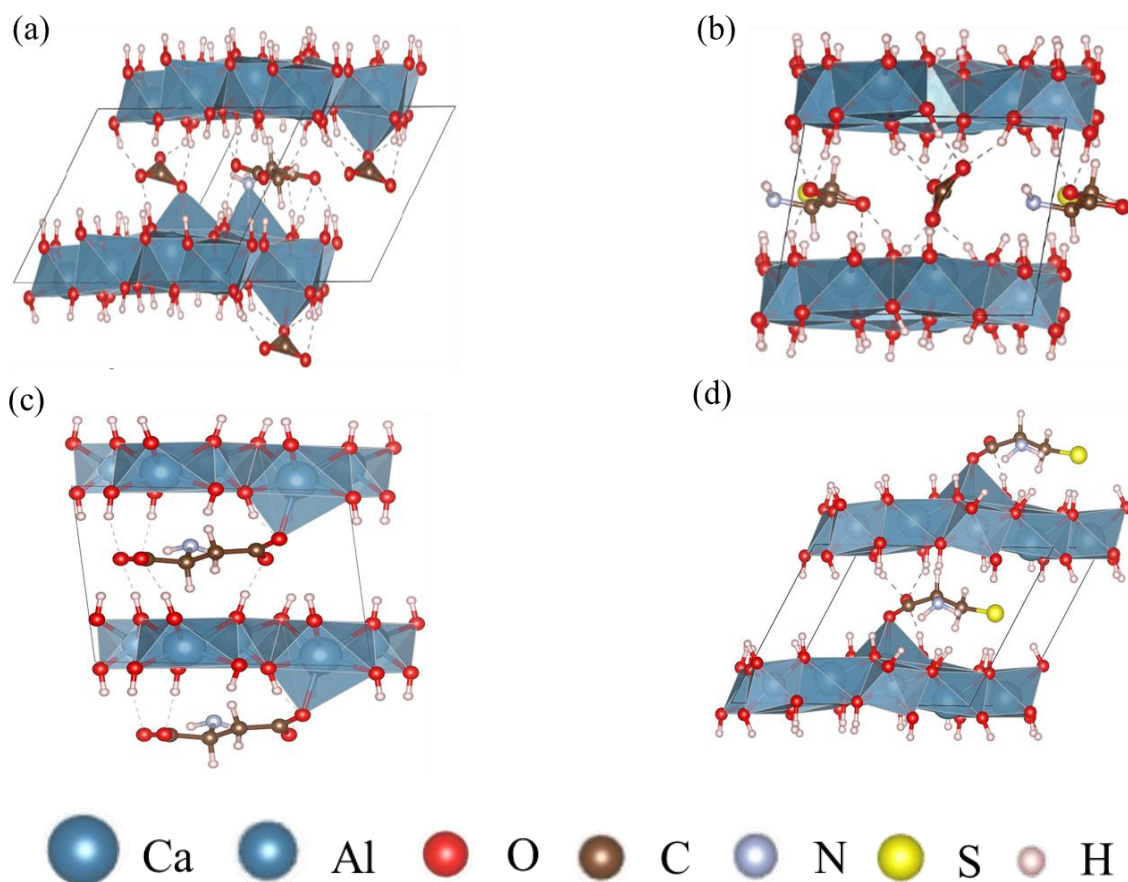
Fig. 5.8 Simulated results of different anions in a model of Ca$_2$Al-LDH without water molecules. The dashed and solid lines indicate hydrogen bonds and Ca-O bonds, respectively. (a) Asp^{2-}- CO$_3^{2-}$, (b)Cys^{2-}-CO$_3^{2-}$, (c) Asp^{2-}, (d) Cys^{2-}.

5.3.5 Effect of CO$_3^{2-}$ on the release of SeO$_4^{2-}$

The changes in relative XRD intensities of each component depending on the sorption densities

of amino acids were analyzed to further confirm the peak assignment and SeO$_4^{2-}$ unstabilizing

mechanism. To observe the compositional trends of each interlayer anion depending on amino

acids loading amounts into Ca$_2$Al-LDH, relative intensities of d_{003} in XRD (**Fig. 5.5**) were plotted

against the Q_e values (**Fig. 5.4**) as shown in **Fig. 5.9**.
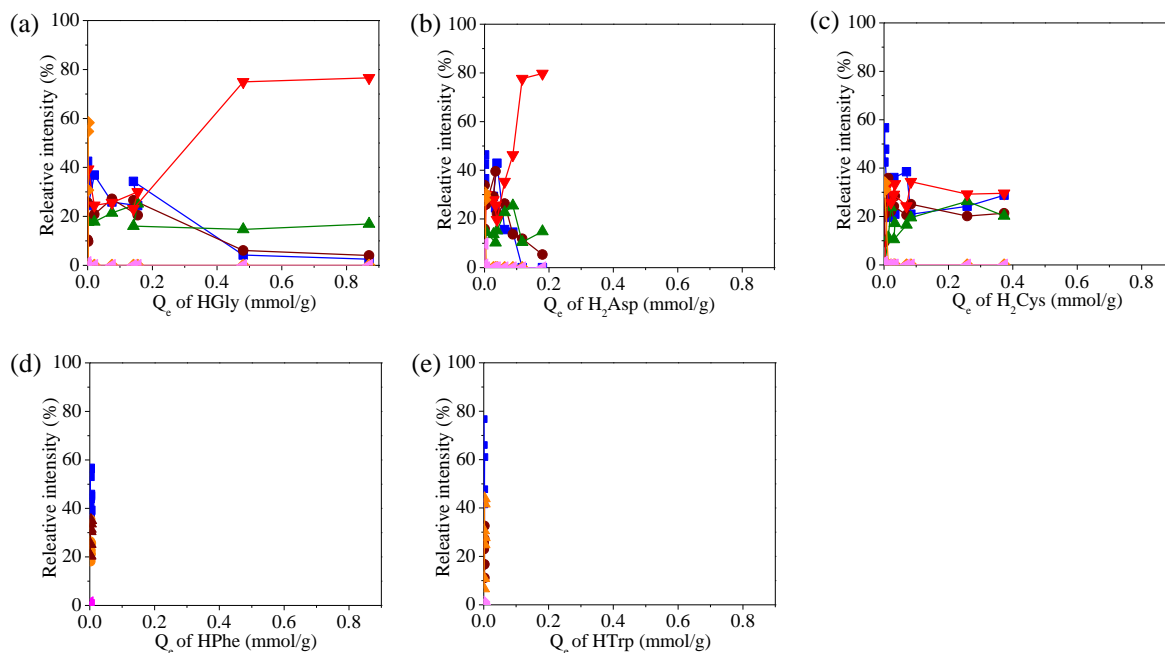
Fig. 5.9 Plots of relative intensities of each XRD peak components in d_{003} derived from Ca$_2$Al-LDH solid residues after reaction with different concentrations of amino acids against Q_e values.

♦, Ca$_2$Al-LDH (SeO$_4$, CO$_3$) (d_{003} = 0.793 Å), corresponding to (A) in **Fig. 5.5**; ●, Ca$_2$Al-LDH(SeO$_4$) (d_{003} = 0.811 Å), corresponding to (B) in **Fig. 5.5**; ■, Ca$_2$Al-LDH(SeO$_4$) (d_{003} = 0.831 Å), corresponding to (C) in **Fig. 5.5**; ◄, Ca$_2$Al-LDH(SeO$_4$) (d_{003} = 0.981 Å), corresponding to (D) in **Fig. 5.5**; ▼, Ca$_2$Al-LDH (amino acid, CO$_3$) (d_{003} = 7.70 Å), corresponding to (E) in **Fig. 5.5**; ▲, Ca$_2$Al-LDH (amino acid) (d_{003} = 7.83 Å), corresponding to (F) in **Fig. 5.5**.
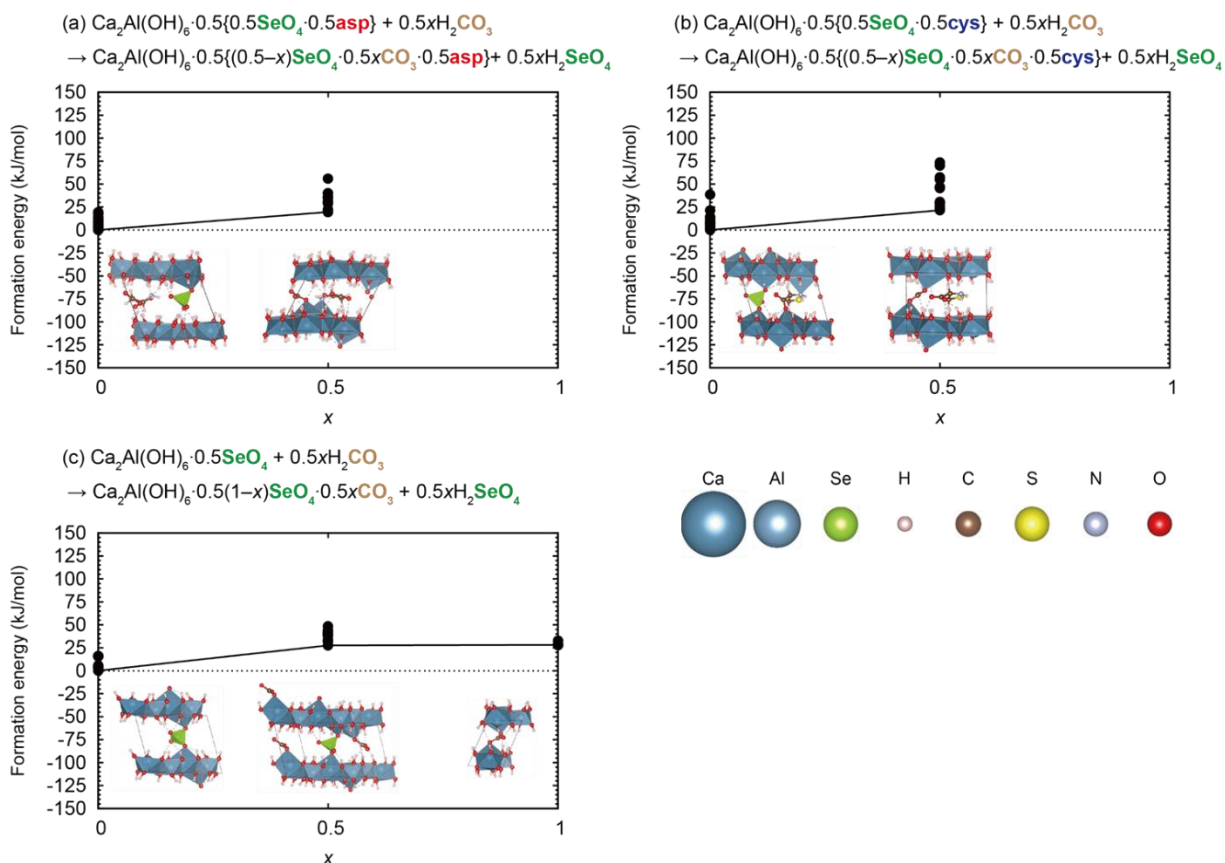
Fig. 5.10 Formation energy in different systems after ion-exchange of CO_3^{2-} with SeO_4^{2-}.
(a) $Ca_2Al(OH)_3 \cdot 0.5(0.5-x)SeO_4 \cdot 0.5xCO_3 \cdot 0.5Asp$,
(b) $Ca_2Al(OH)_3 \cdot 0.5(0.5-x)SeO_4 \cdot 0.5xCO_3 \cdot 0.5Cys$ and in the absence of amino acids,
(c) $Ca_2Al(OH)_3 \cdot 0.5(1-x)SeO_4 \cdot 0.5xCO_3$ (x = 0, 0.5).

HPhe and HTrp were almost not intercalated in the interlayer of Ca_2Al-LDH ($Q_e \sim 0$ in **Fig. 5.9(d), (e)**). Even at the highest initial concentrations of HPhe and HTrp, SeO_4^{2-} was still maintained 64% in Ca_2Al-LDH (**Fig. 5.3(a)**). However, the relative intensities of two configurations (B), (C) of Ca_2Al-LDH(SeO_4) decreased in HGly, H_2Asp, and H_2Cys series as the sorption densities (Q_e) of amino acids increased (**Fig. 5.9(c)~(e)**). The relative intensities of Ca_2Al-LDH(amino acid, CO_3) also increased in HGly and H_2Asp series with an increase in Q_e, but not significant in H_2Cys series (**Fig. 5.9(c)**). Saturated relative intensities of Ca_2Al-LDH(Asp, CO_3) and Ca_2Al-LDH(Gly, CO_3) reached 79.7% and 76.5%, respectively. This indicates not only amino acids intercalation happened but also CO_3^{2-} was induced to substitute with SeO_4^{2-} from Ca_2Al-

LDH. In the H_2Cys series, the relative intensities of Ca_2Al-LDH(Cys, CO_3) was 30%. However, the adsorption amount of H_2Cys showed a little bit larger value than H_2Asp in **Fig. 5.4**, therefore, the difference should be caused by the intercalating amount of CO_3^{2-} which is suppressed in the presence of H_2Cys. Therefore, to verify this hypothesis, the formation energies of trinary system Ca_2Al-LDH(SeO_4, CO_3, amino acids) and binary system Ca_2Al-LDH(SeO_4, CO_3) were predicted by DFT simulation, as shown in **Fig. 5.10**. The lowest formation energies after CO_3^{2-} ion-exchanged with SeO_4^{2-} in the presence of H_2Asp and H_2Cys were 19.3 and 21.4 kJ/mol ($x = 0.5$), respectively, which are smaller than 27.6 kJ/mol without amino acids. This means the substitution of CO_3^{2-} with SeO_4^{2-} was slightly more facilitated by the presence of H_2Asp and H_2Cys, furthermore, the presence of H_2Asp was prone to induce more CO_3^{2-} than H_2Cys. This suggests the presence of "reactive" amino acids like HGly, H_2Asp, and H_2Cys might affect unstabilize SeO_4^{2-} in Ca_2Al-LDH.

5.4 Conclusions

In the present study, the stability of hazardous SeO_4^{2-}-bearing hydrocalumite in the presence of different amino acids was investigated by experimental observation integrated with DFT simulation.

(1) In the absence of amino acids, the simple dissolution of SeO_4-intercalated Ca_2Al-LDH caused 0.44 mM SeO_4^{2-} release corresponding to 48.3% of the initially existing SeO_4^{2-} in Ca_2Al-LDH. HGly, H_2Asp, and H_2Cys enhanced the release of SeO_4^{2-} from Ca_2Al-LDH, reached 73.8 % at the maximum by ion-exchange with SeO_4^{2-} as well as simple dissolution. While almost no intercalation of HPhe and HTrp happened with Ca_2Al-LDH even though at a high concentration of 5 mM due to their large molecular sizes and more hydrophobic property.

(2) The 003 reflections of XRD patterns for Ca_2Al-LDH after reacted with HGly, H_2Asp, and H_2Cys were analyzed by peak separation into four components. Combing with DFT simulation,

peak assignment of Ca$_2$Al-LDH(amino acid) with d_{003} = 7.83 Å, Ca$_2$Al-LDH(amino acid, CO$_3$) with d_{003} = 7.70 Å were determined. The amino acids molecules are predicted to stabilize in the horizontal orientation in Ca$_2$Al-LDH interlayer through the formation of Ca-O and hydrogen bonds between amino acids and hydroxide layer [Ca$_2$Al(OH)$_6$]$^+$.

(3) The intercalation of CO$_3^{2-}$ might also contribute to the release of SeO$_4^{2-}$ through ion-exchanging. But the presence of H$_2$Asp facilitated the substitution between them and was prone to more stably co-exist with CO$_3^{2-}$ than H$_2$Cys, supported by DFT prediction.

Comprehensively, "reactive" amino acids such as HGly, H$_2$Asp, and H$_2$Cys enhanced the release of SeO$_4^{2-}$ from Ca$_2$Al-LDH by unstabilization of hydroxide layers and ion-exchange in interlayer.

References

Baur, I., Johnson, C.A., 2003a. The solubility of selenate-AFt ($3CaO \cdot Al_2O_3 \cdot 3CaSeO_4 \cdot 37.5\ H_2O$) and selenate-AFm ($3CaO \cdot Al_2O_3 \cdot CaSeO_4 \cdot xH_2O$). Cem. Concr. Res. 33, 1741-1748.

Baur, I., Johnson, C.A., 2003b. Sorption of selenite and selenate to cement minerals. Environ. Sci. Technol. 37, 3442-3447.

Baur, I., Keller, P., Mavrocordatos, D., Wehrli, B., Johnson, C.A., 2004. Dissolution-precipitation behaviour of ettringite, monosulfate, and calcium silicate hydrate. Cem. Concr. Res. 34, 341-348.

Christensen, A.N., Jensen, T.R., Hanson, J.C., 2004. Formation of ettringite, $Ca_6Al_2(SO_4)_3$ $(OH)_{12} \cdot 26H_2O$, AFt, and monosulfate, $Ca_4Al_2O_6(SO_4) \cdot 14H_2O$, AFm-14, in hydrothermal hydration of Portland cement and of calcium aluminum oxide-calcium sulfate dihydrate mixtures studied by in situ synchrotron X-ray powder diffraction. J. Solid State Chem. 177, 1944-1951.

Eklund, L., Persson, I., 2014. Structure and hydrogen bonding of the hydrated selenite and selenate ions in aqueous solution. Dalton Trans. 43, 6315-6321.

Li, D., Yan, W., Guo, X., Tian, Q., Xu, Z., Zhu, L., 2020. Removal of selenium from caustic solution by adsorption with CaAl layered double hydroxides. Hydrometallurgy 191, 105231.

Li, M., Farmen, L.M., Chan, C.K., 2017. Selenium removal from sulfate-containing groundwater using granular layered double hydroxide materials. Ind. Eng. Chem. Res. 56, 2458-2465.

Moon, D.H., Grubb, D.G., Reilly, T.L., 2009. Stabilization/solidification of selenium-impacted soils using Portland cement and cement kiln dust. J. Hazard. Mater. 168, 944-951.

Momma, K., Izumi, F., 2011. VESTA 3 for three-dimensional visualization of crystal, volumetric and morphology data. J. Appl. Cryst. 44, 1272-1276.

Ong, S.P., Richards, W.D., Jain, A., Hautier, G., Kocher, M., Cholia, S., Gunter, D., Chevrier, V.L., Persson, K.A. and Ceder, G., 2013. Python Materials Genomics (pymatgen): A robust, open-source python library for materials analysis. Comput. Mater. Sci 68, 314-319.

Pye, C.C., Walker, V.E., 2011. Ab initio investigation of the hydration of the tetrahedral perchlorate, perbromate, selenate, arsenate, and vanadate anions. J. Phys. Chem. A 115, 13007-13015.

Perkins, R.B. and Palmer, C.D., 2001. Solubility of chromate hydrocalumite ($3CaO \cdot Al_2O_3 \cdot CaCrO_4 \cdot n H_2O$) 5-75° C. Cem. Concr. Res 31(7), 983-992.

Renaudin, G., Francois, M., Evrard, O., 1999. Order and disorder in the lamellar hydrated tetracalcium monocarboaluminate compound. Cem. Concr. Res 29(1),63-69.

Sacerdoti, M., Passaglia, E., 1988. Hydrocalumite from Latium, Italy: its crystal structure and relationship with related synthetic phases. Neues Jahrb für Mineral. 462-475.

Santos, R., Tronto, J., Briois, V., Santilli, C., 2017. Thermal decomposition and recovery properties of ZnAl-CO$_3$ layered double hydroxide for anionic dye adsorption: insight into the aggregative nucleation and growth mechanism of the LDH memory effect. J. Mater. Chem. A 5, 9998-10009.

Wang, M., Akamatsu, H., Dabo, I., Sasaki, K., 2021. Environmental impact of amino acids on the release of selenate immobilized in hydrotalcite: Integrated interpretation of experimental and density-functional theory study. Chemosphere 274, 129927.

Yan, D., Lu, J., Wei, M., Ma, J., Evans, D.G. and Duan, X., 2009. A combined study based on experiment and molecular dynamics: perylene tetracarboxylate intercalated in a layered double hydroxide matrix. Phys. Chem. Chem. Phys. 11(40), 9200-9209.

Yao, W., Wang, J., Wang, P., Wang, X., Yu, S., Zou, Y., Hou, J., Hayat, T., Alsaedi, A., Wang, X., 2017. Synergistic coagulation of GO and secondary adsorption of heavy metal ions on Ca/Al layered double hydroxides. Environ. Pollut. 229, 827-836

Zhang, M., Reardon, E.J., 2003. Removal of B, Cr, Mo, and Se from wastewater by incorporation into hydrocalumite and ettringite. Environ. Sci. Technol. 37, 2947-2952

Chapter 6 Leaching behavior of anionic pollutants from fly ash blended cement in the presence of selected amino acids

6.1 Introduction

Fly as blended cement can be a good model to simulate selenium immobilized in hydrocalumite, which is produced in an aging period. Fly ash including selenium in some extent, is produced from coal power plants and the worldwide generation of it is in a large amount (WWCCPN, 2011). The rich amount of lime (CaO), silica (SiO_2), alumina (Al_2O_3), and iron oxide (Fe_2O_3) in fly ash make it either exhibit self-cementing capabilities by reacting with water or react with an activator to produce supplementary cementitious compounds. During these process, hydration reaction would like to happen to produce hydration products, like hydrocalumite ($Ca_4Al_2(OH)_{12}SO_4·6H_2O$), ettringite ($Ca_6Al_2(OH)_{12}(SO_4)_3·26H_2O$), and calcium silicate hydrate (C-S-H) which contribute to the solidification/stabilization (S/S) of anionic species (Guo et al., 2019; Sasaki et al., 2021). Therefore, it can be used in waste S/S mixing with cementitious materials and construction projects to reduce construction costs, save valuable landfill spacing and reuse waste resources (Li et al., 2001; Izquierdo and Querol, 2012). However, the usage of fly ash in cementitious materials may cause new environmental problems due to they usually contain harmful heavy and trace elements (Akar et al., 2012; Lu et al., 2019; Mahedi and Cetin, 2019; Sasaki et al., 2021). Some of them like Se, As, B, Cr, and F species have received significant attraction due to they are in high mobility and harmful to humans, animals as well as plants. And also the changing of environment can cause the leaching behavior of hazardous elements. Halim C.E et al. (2003) investigated the parameters which can affect the leaching behavior of elements in cementitious materials, especially pH controls the leachability of Pb and Cd through affecting their solubility. Same thing also is confirmed by Malviya and Chaudhary (2006).

Therefore, the affecting factors to the stability of pollutants should be clear. In the hydration process of fly ash mixing with cement, the amount of calcium (Ca) contributes to the alkaline condition of the hydration system where great majority heavy and trace elements present a pH-dependent solubility (Reardon and Della Valle, 1997; Izquierdo and Querol, 2012)(Maria,2012). The presence of Ca dictates of the formation of ettringite, hydrocalumite and other secondary Ca-hydrated phases which paly an irreplaceable role in the incorporation and immobilization of Se, As, B, Cr and F elements. Ca exists in fly ash in a large amount of presence, especially provided from lime. The leaching concentrations of Ca are in a wide range over several orders of magnitude but Ca is not considered as an element of concern. Therefore, different Ca additives have been studied to explore their inhibition mechanisms. Guo et al. (2019) selected lime, gypsum, slag, and 60% hydroxylated calcined dolomite (HCD 60) to mix with coal fly ash, the additives of Ca not only as the alkaline sources but also contributed to the formation of ettringite as well as precipitation of calcium salts. Guo and Reardon (2012) used calcined dolomite to reduce the leaching concentrations of oxyanions from fly ash, the results showed the formation of hydrocalumite and hydrotalcite were the main suppression mechanisms. Tian et al. (2019) compared hydroxylated calcined dolomites (HCD60) ($Ca(OH)_2$, 60% $Mg(OH)_2$, 40% MgO) and HCD100 ($Ca(OH)_2$, 100%$Mg(OH)_2$) and lime additives on the leachability anionic species from fly ash, which implied that HCD60 and HCD100 showed better results than sole lime. The exist of $Mg(OH)_2$ and MgO produced more hydration products which act as effective candidates for anionic elements. However, their leach-ability after adding additives still should be determined. In the real field, geochemical properties and intrinsic properties of the cement blocks affect the leaching ability of hazardous elements. Therefore, the effects of amino acids on the leaching behavior of anionic species should be examined.

In this work, the leaching behaviors of anionic species from fly ash blended cement blocks were investigated under SOM existing conditions. SOM possess complicated structures and different

molecular weights, so amino acids were selected as simplified models. Here, we selected cement blocks after added different additives including lime ($Ca(OH)_2$), gypsum ($CaSO_4$), metal clear (HCD60) as Ca sources. The leaching behaviors of Se(IV), As(V), B(III), Cr(VI), and F^- from cement blocks were evaluated in amino acids solutions with pH 4.7 and 12.0. This work is corresponding with our lab scale model experiment about hydrocalumite (Se).

6.2 Experimental

6.2.1 Materials

Fly ash was provided by an anonymous thermal power plant in Japan. Elemental compositions were determined by X-ray fluorescence spectroscopy (XRF, Rigaku ZSX Primus II, Tokyo) as shown in **Table 6.1**: 0.70 MgO, 24.68 Al_2O_3, 59.44 SiO_2, 0.53P_2O_5, 0.73 SO_3, 1.87 K_2O, 2.30 CaO, 2.23 TiO_2, 0.08 MnO, 6.69 Fe_2O_3, 0.06 V_2O_5, 0.01 Cr_2O_3. From **Table 6.2**, the leaching concentration of Cr(VI) and Se(IV), were detected much higher than regulatory limits which indicates the existing risks of fly ash application. Blast furnace cement (type B, around 10 μmφ) which contains 46.44% blast furnace slag was used in this work. Three Ca additives, lime ($Ca(OH)_2$), gypsum ($CaSO_4$), metal clear (HCD60) were selected.

Table 6.1 Elemental composition of fly ash in the present work (wt%).

Na_2O	MgO	Al_2O_3	SiO_2	P_2O_5	SO_3	K_2O	CaO	TiO_2	MnO	Fe_2O_3	V_2O_5	others
0.72	0.89	23.94	50.93	0.28	1.48	2.57	4.47	2.46	0.18	11.24	0.10	0.74

All amino acids in this work including L-cysteine (Cys, $C_3H_7NO_2S$, 99%), L-aspartic acid (Asp, $C_4H_7NO_4$, 99%), glycine (Gly, $C_2H_5NO_2$, 99%), L-tryptophan (Trp, $C_{11}H_{12}N_2O_2$, 99%), and L-phenylalanine (Phe, $C_9H_{11}NO_2$, 99%) are used in a special grade. For high performance liquid chromatography (HPLC) analysis, the phenyl isothiocyanate (PITC, 98%) in a special grade, acetonitrile, methanol, *n*-hexane in HPLC grade were used. All the solutions were prepared using

decarbonized Milli-Q water (integral water purification system, Millipore) boiled with purging N_2

gas for 2 h.

Table 6.2 Leaching results of the original fly ash.

	Cr/ppm	As/ppm	Se/ppm	F/ppm	B/ppm
FA	0.240	0.025	0.57	3.3	2.1
No.46	≤ 0.05	≤ 0.01	≤ 0.01	≤ 0.8	≤ 1

(No.46: Environemntal announcement No.46 (Japan); Maximum Concentrations Limit (MCL).)

6.2.2 Preparation of fly ash blended cement blocks

Cement blocks containing 40 kg/m^3 each above Ca additives were prepared to enhance the immobilization of hazardous elements in fly ash. Therefore, in this work, standard cement block (S) means without any Ca additives. With 40 kg/m^3 Ca(OH)$_2$, CaSO$_4$, and metal clear additives, the fly ash-blended cement blocks are expressed in C40, G40, and M40 series, respectively. The solid/water mass ratio was fixed to 0.323, as shown in **Table 6.3**. The required amounts of cement, fly ash, and Ca additives were mixed using a Hobart type mixer N50 (Hobart Japan, Tokyo, Japan) for 15 s. Subsequently, water was added to the mix for 30s, and the mixture was kneaded for 120 s. the product was packed in a mold with 5.0 cm and 10.0 cm diameter and height, respectively, and compacted on a table vibrator to remove air bubbles for the specimen preparation. After compaction, the sealing cure was performed at 20 °C under 60% of humidity until it aged 2 days. After demolding, curing was performed in water at 20°C for 28 days. The cured cement blocks were separately ground into samples under 280 mesh (53 μm) to supply for XRD and TCLP test according to the Environmental Agency Notification No.46 in Japan.

Table 6.3 Added amount of each material to prepare the fly ash blended cement blocks (kg/m^3).

	S	C40	G40	M40
Water	424	424	424	424
Cement	94	94	94	94
Fly ash No.8	1219	1219	1219	1219
Ca additives	0	40	40	40

6.2.3 Dissolution test

According to Environmental Agency Notification No. 46 in Japan, toxicity characteristic leaching procedure (TCLP) test where the ratio of ground solid powder to aqueous solution (S/L) is 10.0 was conducted to determine the leaching concentrations of anionic species from raw fly ash. The TCLP was followed as a regulatory tool to determine whether the cement blocks waste could be classified as hazardous or not.

The solution pH for TCLP was adjusted to 4.7 using 1 mM acetate buffer. 5 mM of five amino acids, HTrp, HPhe, HGly, H_2Asp, and H_2Cys were included in the leaching solution. To simulate the alkaline condition, the solution at pH 12.0 was also prepared by direct using 3 M NaOH. Capped polypropylene centrifuge tubes were used to perform the extraction experiments where 1g ground cement blocks powder was suspended into 10 mL prepared solution rotating at 200 rpm 25 °C for 6 h according to Environmental Agency Notification No.46 in Japan. All experiments were carried out in duplicate. After rotation, the leachate solutions were kept and solid residues were filtered through 0.45 μm pore size disposable filter and then dried for further analysis. The leachate was provided to measure pH and hazardous elements.

6.2.4 Chemical analysis and solid characterizations

The Se, As, B, and Cr concentrations were measured using ICP-MS (**2.1.2 section**). IC (**2.1.3 section**) was used to determine the concentration of F. XRD patterns of solid samples were

collected (**2.2.1 section**). For XRD measurement, Rietveld method using corundum (α-Al$_2$O$_3$) as an internal standard was used to determine the mass contents in each phase.

6.3 Results and discussion

6.3.1 Characterization of fly ash blended cement powder with different Ca additives

Following the previous work (Sasaki et al., 2021), the cement, fly ash and different Ca additives including lime, gypsum, and metal clear were mixed for curing 28 d to get the fly ash blended cement blocks. As usual, the pozzolanic reaction in the mixing system of cement, fly ash, and Ca additives was happened and related XRD patterns of each series were shown in **Fig. 6.1**.

Ettringite was formed in each system with the (100) plane at 9.0 ° in 2θ, (110) plane at 15.7° in 2θ. The hydrocalumite also was formed with the main peak of (002) plane at 11° except in G40 series. A very broad peak appeared around 25° (2θ) in all series which is assigned to (004) due to pozzolanic reaction. In the presence of lime, hydrocalumite was well developed than ettringite, while in the presence of gypsum, only ettringite was formed. This indicates the formation of hydrocalumite is induced by Ca additives, the sufficient CaSO$_4$ facilitated the formation of ettringite but if CaSO$_4$ was consumed, ettringite will be converted to hydrocalumite(SO$_4$) (Christensen et al., 2004). Ettringite and hydrocalumite are well known for their ion-exchange ability, thus depending on the anionic species in cement systems, the different anions can be immobilized into them (Guo et al., 2017; Guo et al., 2019; Sasaki et al., 2021). Furthermore, the phase transformation between ettringite and hydrocalumite also probably happens.
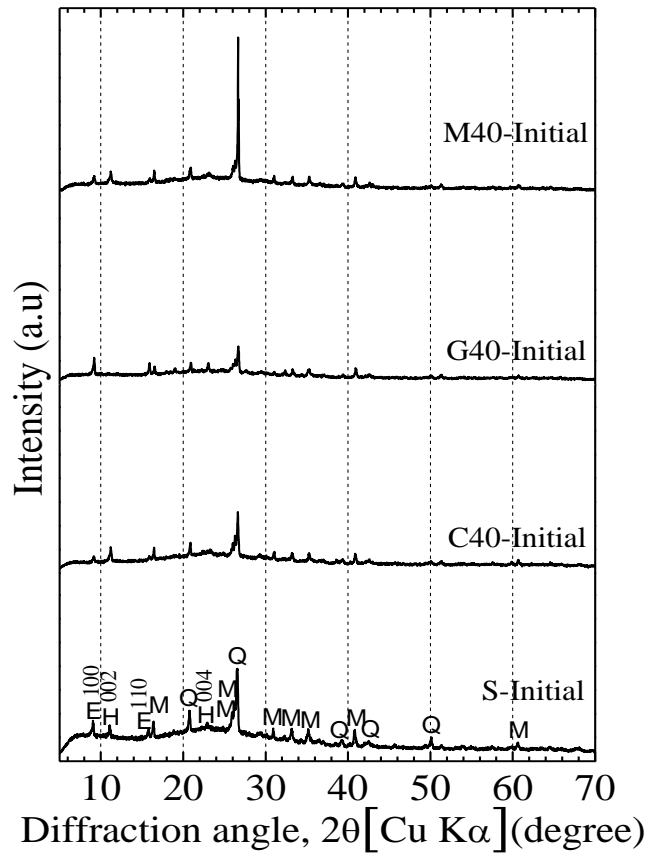
Fig. 6.1 XRD patterns of four cement blocks with S, C40, G40, M40 additives curing for 28 d.

6.3.2 Effects of pH on the leaching ability of anionic species without amino acids

According to previous works (Guo et al., 2019; Sasaki et al., 2021), the mainly leaching species of each element from initial fly ash should be SeO_3^{2-}, CrO_4^{2-}, AsO_4^{3-}, $B(OH)_4^-$, and F^-. These undesirable elements of four cement blocks were determined using TCLP test without any amino acids under pH 4.7 and 12.0 as shown in **Fig. 6.2**. The blue dash lines represent the criteria values for cement leaching.

Under pH 4.7, after added Ca additives, the releasing concentrations of Se, As, B, and Cr were reduced. Moreover, As, B, Cr in C40 series, B and Cr in M40, and B, F in G40 were lower than the MCL. Therefore, the additives of Ca and Mg resulted in immobilization to some extent, especially, the leached concentration of B was reduced in all the series. In the cement systems, Ca

was in an excess amount which was enough to produce insoluble Ca salts. Therefore, except the coprecipitation of anionic species in ettringite and hydrocaumite, the precipitation of $Ca_3(AsO_4)_2$ ($K_{sp} = 6.4 \times 10^{-19}$), $CaSeO_3$ ($K_{sp} = 5.4 \times 10^{-8}$), CaF_2 ($K_{sp} = 4.0 \times 10^{-11}$) also contributed their removal in the presence of cement and Ca additives. According to previous works, $B(OH)_4^-$ is difficult to precipitate to be Ca salt but the ettringite was found significantly contributed to its immobilization than hydrocalumite (Kumarathasan et al., 1989; Duchesne and Reardon, 1999; Qiu et al., 2015; Guo et al., 2019; Sasaki et al., 2021). Under pH 4.7 after 6 h, the final pH of S-Blank, C40-Blank, G40-Blank, and M40-Blank were increased to 9.39, 11.06, 9.20, and 10.65, separately. Mynenia et al. (1998) explored the effects of pH on the solubility of ettringite, which indicated below pH 10.7 ettringite still can exist but was influenced by gypsum and Al-hydroxide until at near neutral pH the complete dissolution would like to happen.

To analyze the amount of ettringite and hydrocalumite quantitively, the Rietveld method was applied to the mixture of each cement solid residues including corundum (α-Al_2O_3) in 10% as an internal standard in XRD (**Fig. 6.1**). After added different additives, the amounts of ettringite in each solid residue were different. With G40, the content of ettringite in cement blocks was reached 6.09% which is higher than with S (2.16%), M40 (1.81%), and C40 (1.09%) series (**Fig. 6.8**). While in each blank tests without amino acids, the amounts of ettringite were corresponded to S (1.20%), C40 (0.85%), G40 (1.52%), and M40 (1.23%). In the presence of C40 and M40, hydrocalumite were formed around 6.08 % and 4.12%, separately, which were much higher than without any additives. In G40 series all of SO_4^{2-} and Ca were consumed to form ettringite. However, the excess amount of SO_4^{2-} in G40 series provided for ettringite formation and also plays a competitive role with Se, As, B, and Cr in ettringite adsorption sites (Guo et al., 2017), so even though the amount of ettringite was large, the leaching of Se, As, B, Cr were still higher than C40 and M40. In all of the series, the leaching of F^- was lower than the MCL, this might be caused by the CaF_2 (K_{sp} 4.0×10^{-11}) formation (Guo et al., 2019).

In S, C40, G40, and M40 series, the release of Se, As, B, and Cr from cement were decreased with the increase of initial pH from 4.7 to 12.0, while F increased (**Fig. 6.2**). This indicates that the alkalization of cement system strongly affects the immobilization of Se, As, B, Cr, and F (Sasaki et al., 2021). Under pH 12.0, As, B, Cr in all of the series (C40, G40, M40) were below the MCL, while Se and F were always higher than the MCLs in any series. In XRD for the ground fly ash blended cement (**Fig. 6.7**), at the higher initial pH condition, the peak of ettringite and hydrocalumite still exist in some amount to contribute to the reducing of Se, As, B, and Cr (**Fig. 6.2**). However, the releasing of Se in all series were higher than the MCL due to its higher mobility. The anion exchange selectivity is in the order of $AsO_4^{3-} > SeO_3^{2-} > B(OH)_4^- > CrO_4^{2-} > F^-$ in ettringite (Myneni et al., 1998; Zhang and Reardon., 2003; Guo et al., 2017; Sasaki et al., 2021), and $AsO_4^{3-} > SeO_3^{2-} > SO_4^{2-} > CrO_4^{2-} > F^- > B(OH)_4^-$ in hydrocalumite (Thesis et al., 2013; Sasaki et al., 2021). Usually, the immobilization of anionic species in hydrocalumite is accompanied with dissolution-precipitation (DR) mechanism due to its higher solubility, hence, under alkaline condition, the precipitation ability of F^- in ettringite and hydrocalumite was small.
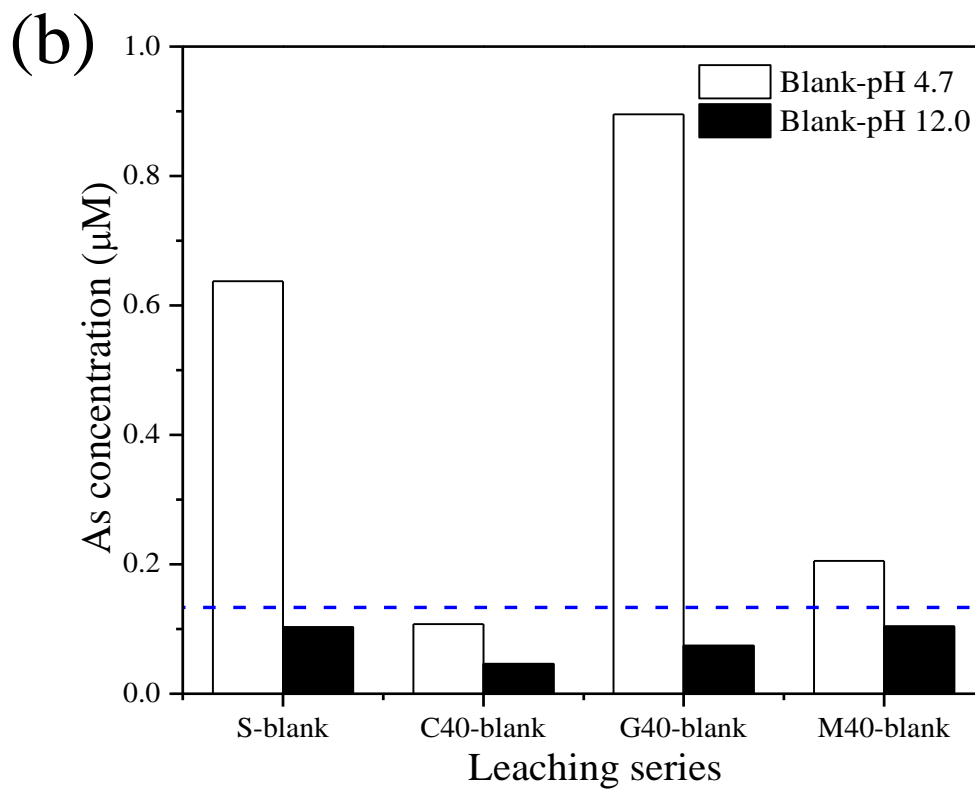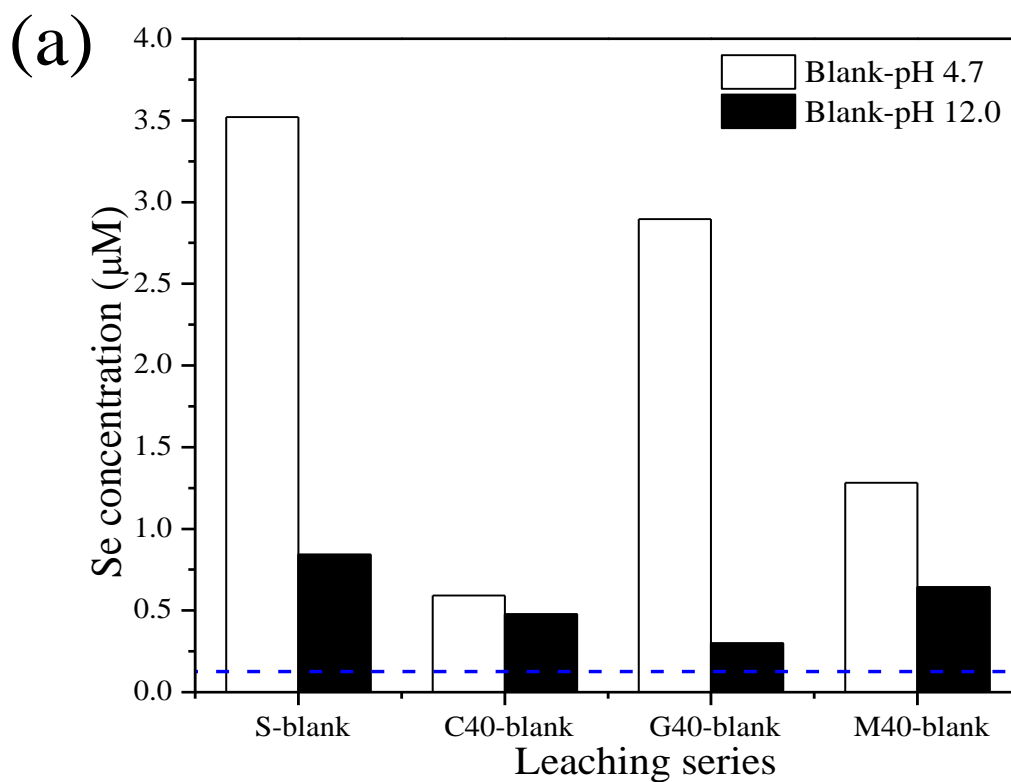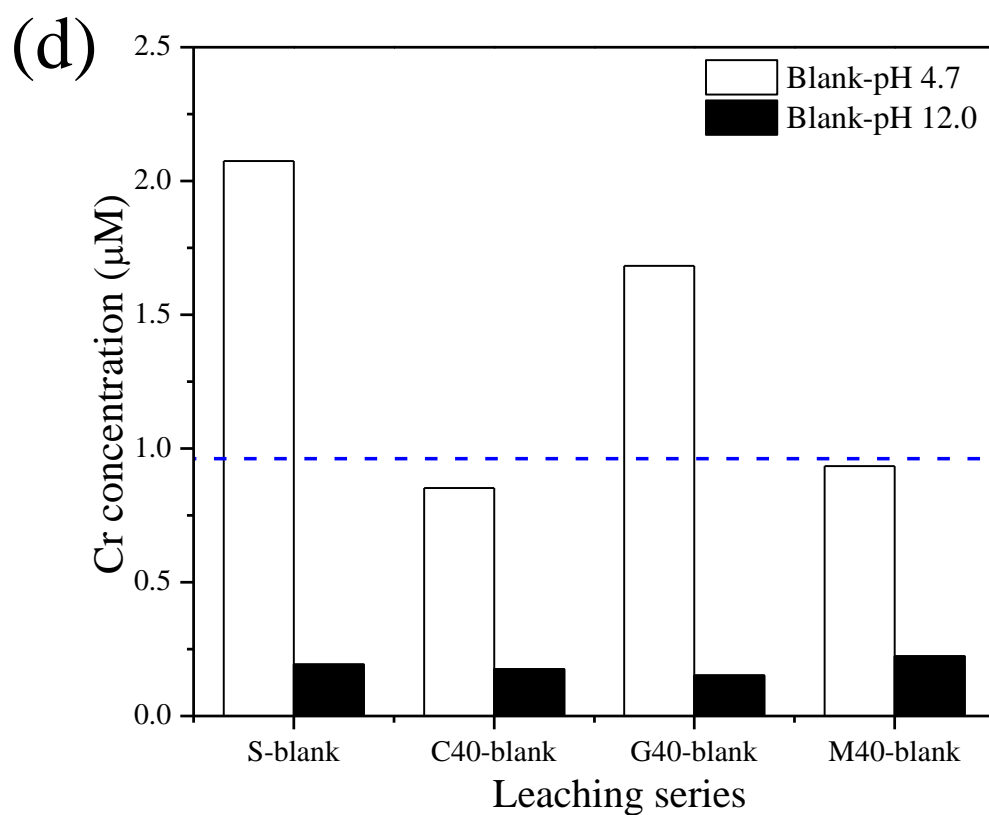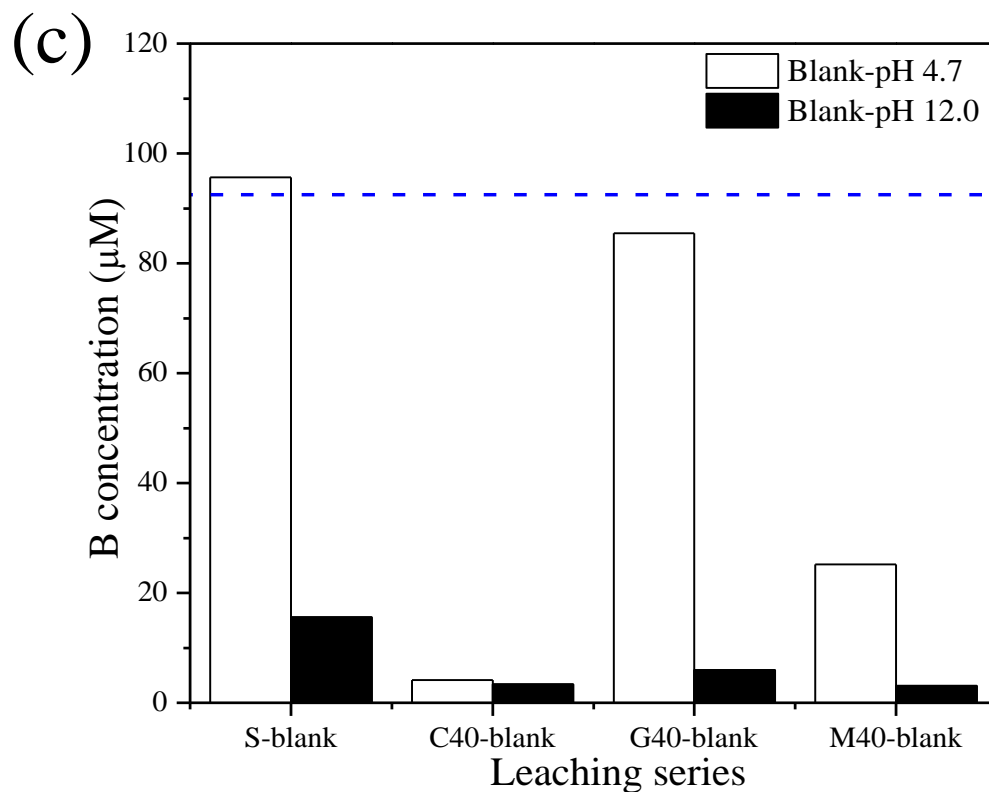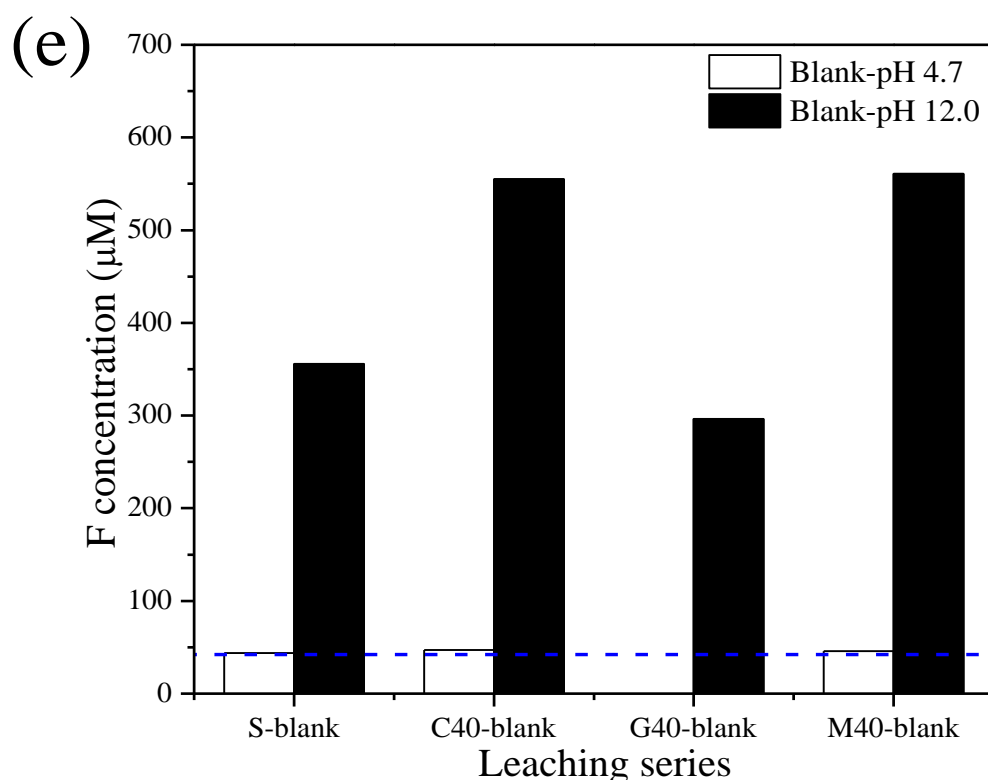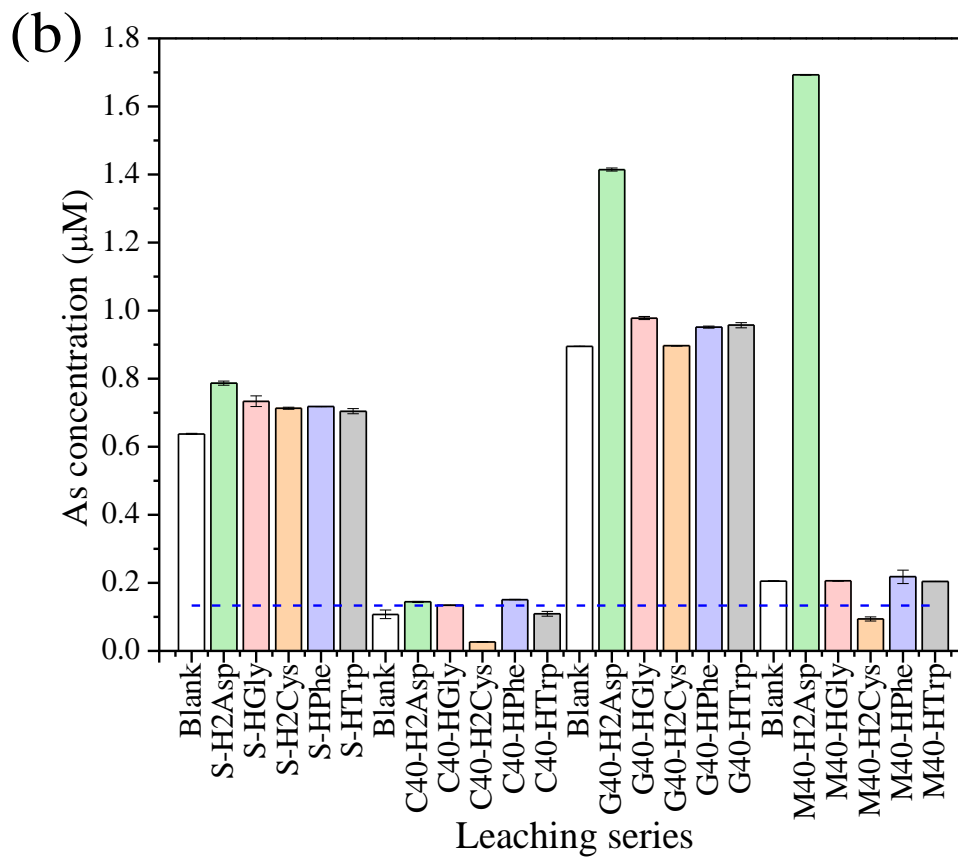
Fig. 6.2 Leaching results of (a) Se, (b) As, (c) B, (d) Cr, and (e) F from the ground cement powders S, C40, G40, M40 under pH 4.7 and 12.0 without adding any amino acids.

6.3.3 Effects of the amino acids on the leaching ability of anionic elements under different pH conditions

The leaching of anionic species SeO_3^{2-}, AsO_4^{3-}, $B(OH)_4^-$, CrO_4^{2-}, and F^- of each cement blocks solid residue were detected in the presence of 5 mM HGly, H_2Asp, H_2Cys, HPhe, and HTrp, shown in **Fig. 6.3** (pH 4.7) and **Fig. 6.4** (pH 12.0). Under initial pH 4.7, amino acids showed different influences on the leaching of anionic species. H_2Asp enhanced the release of SeO_3^{2-}, AsO_4^{3-}, $B(OH)_4^-$, and CrO_4^{2-} in S, C40, G40, and M40 series in different extents, while for F species showed suppressing effects. For Se (**Fig. 6.3(a)**), H_2Asp and HGly promoted the releasing of it in all series. Meanwhile, in S and G40 series, H_2Cys played an inhibiting role, the leaching concentration of Se decreased from 2.89 μM to 1.76 μM compare with blank.
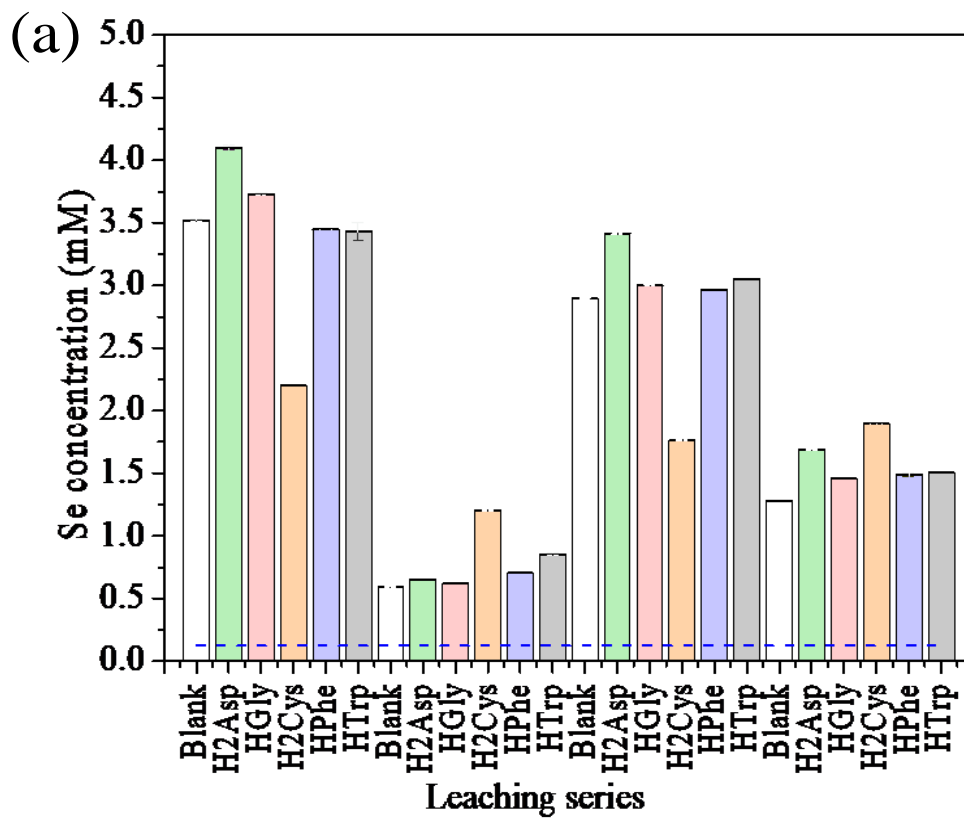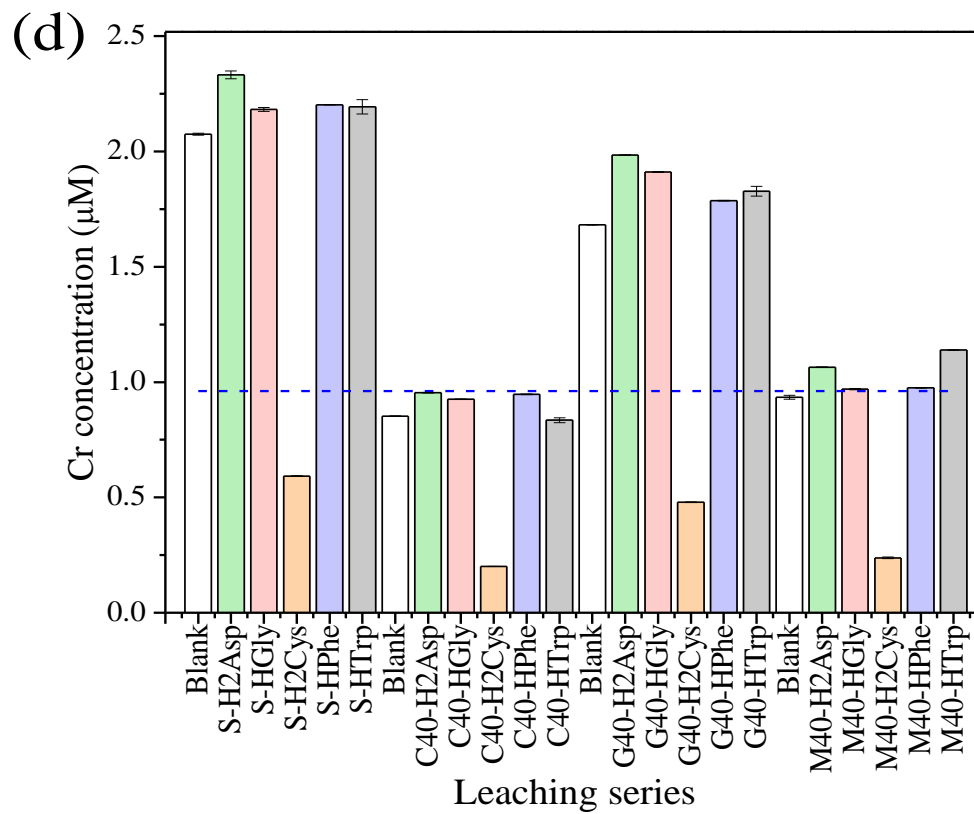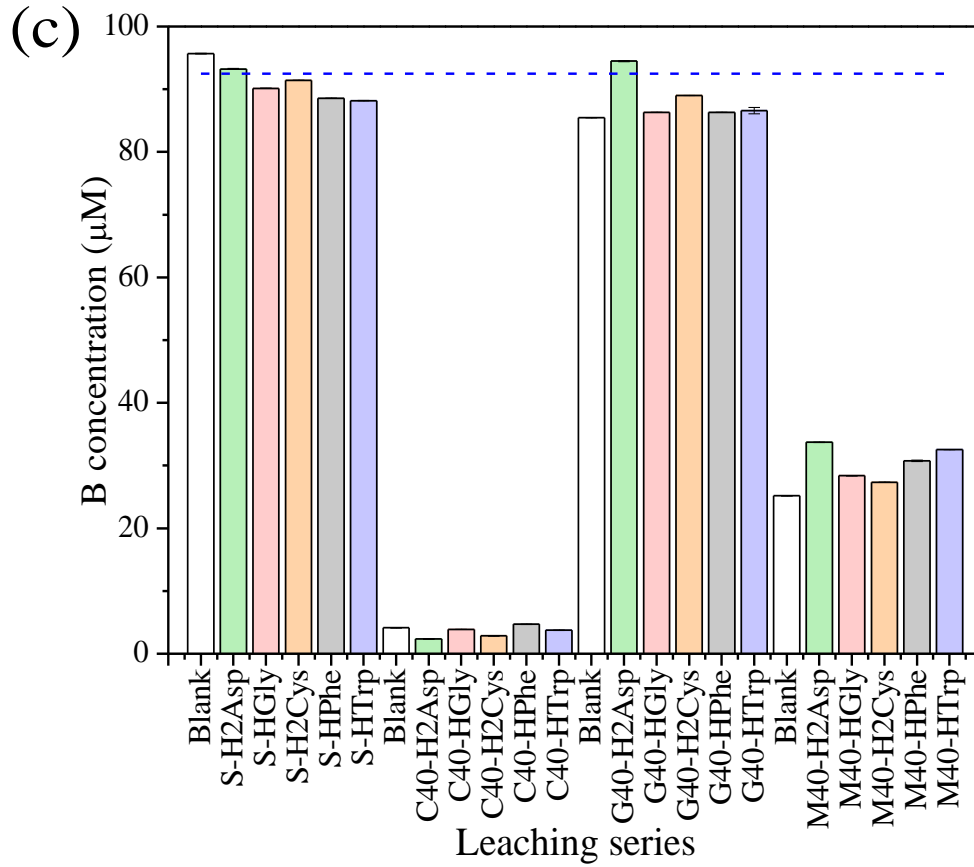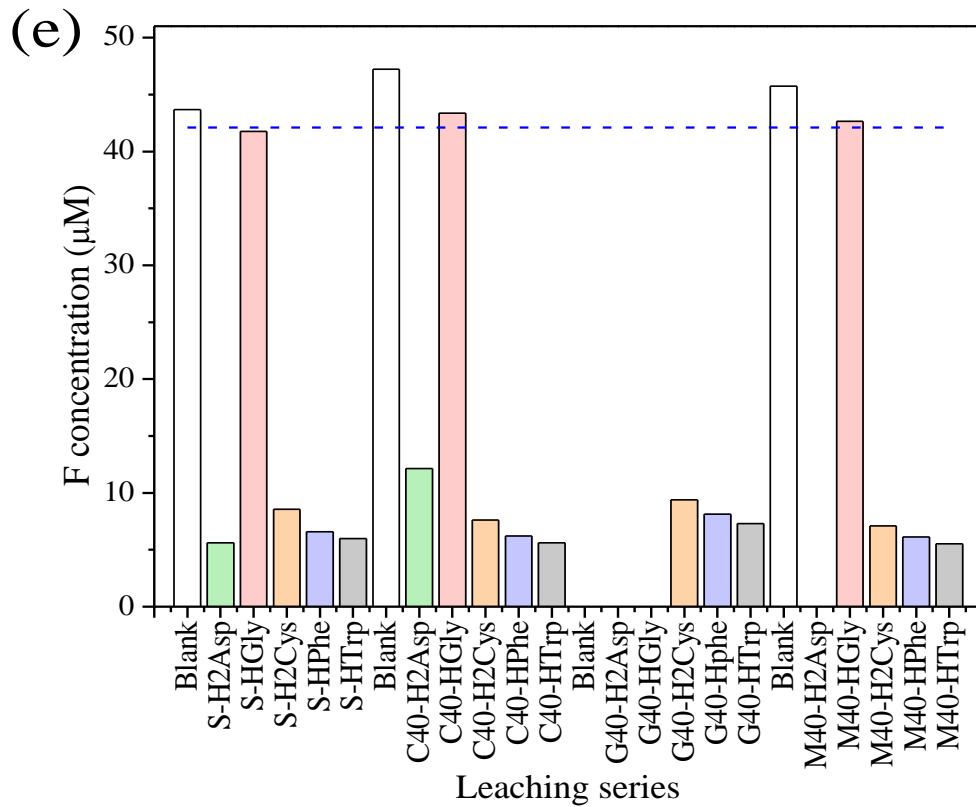
Fig. 6.3 Leaching results of (a) Se, (b) As, (c) B, (d) Cr, and (e) F, from S, C40, G40, M40 ground cement powder after TCLP tests with different amino acids H₂Asp, HGly, H₂Cys, HPhe and HTrp under pH 4.7.

After 6 h suspension, the final pH was increased to be weakly alkaline shown in **Fig. 6.5(a)** because of simple dissolution of hydrocalumite and ettringite at acidic conditions. Under neutral and weakly alkaline conditions, H₂Cys is likely to be oxidized in which the disulfide bond (S-S) between two cysteine molecules will be formed and produce cysteine dimers. Therefore, during the oxidization of H₂Cys, the reduction of SeO_3^{2-}/SeO_4^{2-} might have happened. The related reactions with the standard oxidation-reduction potential (E^0) are presented in **Eqs. (6.1)~(6.3)**. The value E^0 of **Eq. (6.1)** is -0.23 V which is lower than E^0 in **Eq. (6.2),** but higher than **Eq. (6.3)**. This means in the initial fly ash material, SeO_3^{2-} is the main form of Se but still SeO_4^{2-} in the minor. But in C40 and M40 series, leached Se decreased. That might be caused by the addition of C40 and M40, resulting in the immobilization of Se by formation of hydrocalumite. The dissolved concentration of Se might be not enough to contact with H₂Cys to happen oxidization-reduction

reaction. On the other side, SO_4^{2-} is competitive ion with SeO_3^{2-}, AsO_4^{3-}, and CrO_4^{2-} to incorporate

into ettringite or form Ca precipitates, which caused further dissolution of them in G40 series.

$$2C_3H_7NO_2S = C_6H_{12}N_2O_4S_2 + 2e + 2H^+ \quad (\textbf{\textit{E}}^0 = \textbf{-0.23 V}) \tag{6.1}$$

$$SeO_4^{2-} + H_2O + 2e = SeO_3^{2-} + 2OH^- \qquad (\textbf{\textit{E}}^0 = \textbf{0.05 V}) \tag{6.2}$$

$$SeO_3^{2-} + 3H_2O + 4e = Se^0 + 6OH^- \qquad (\textbf{\textit{E}}^0 = \textbf{-0.366 V}) \tag{6.3}$$
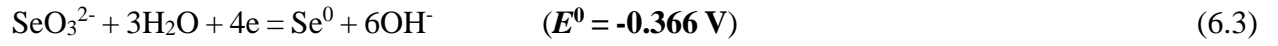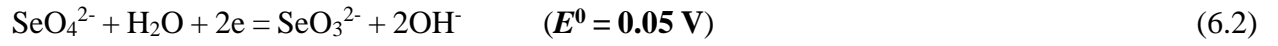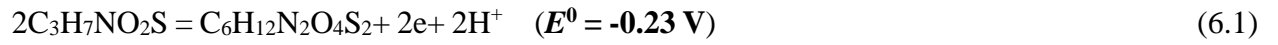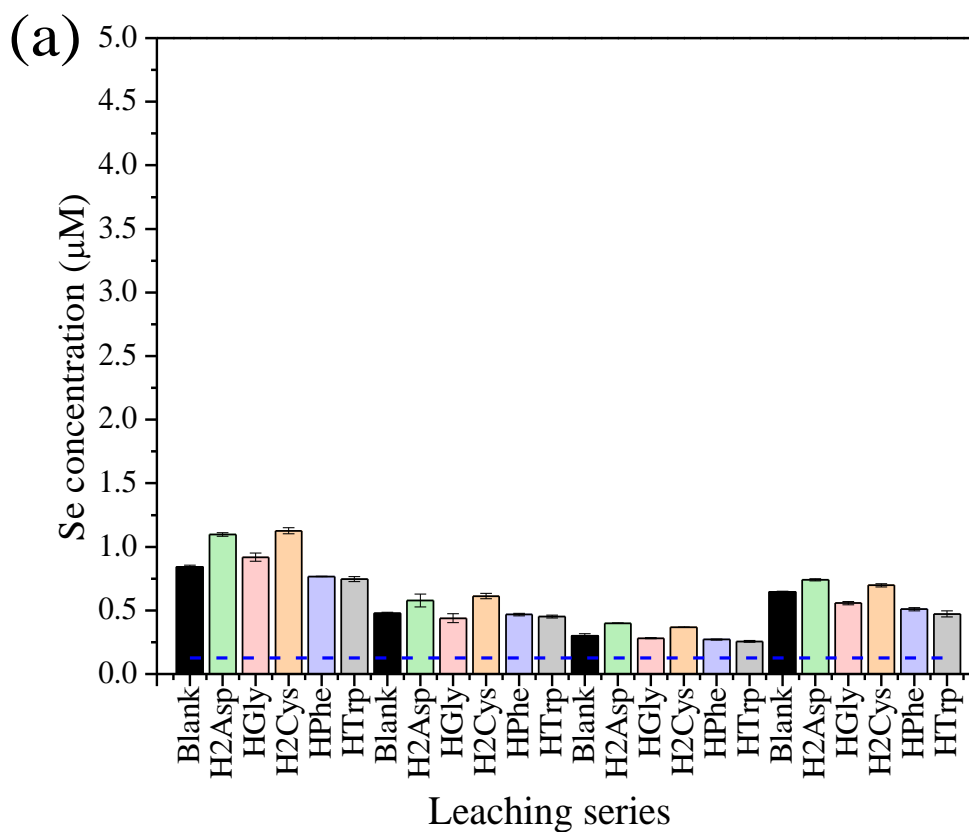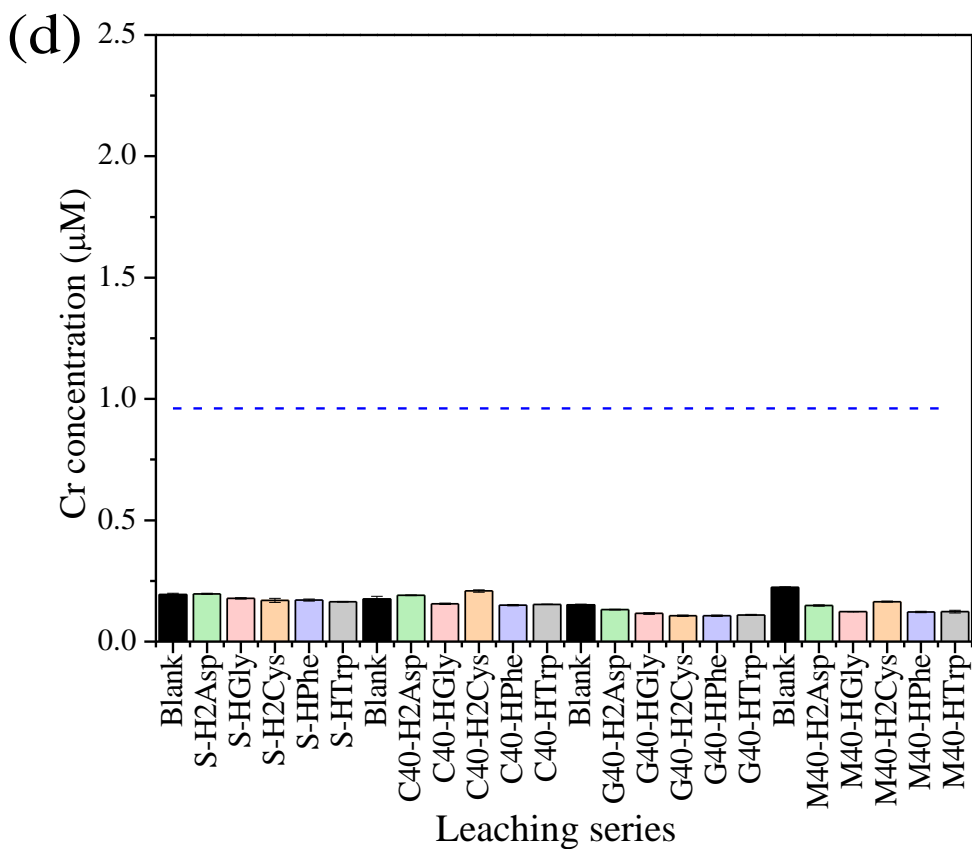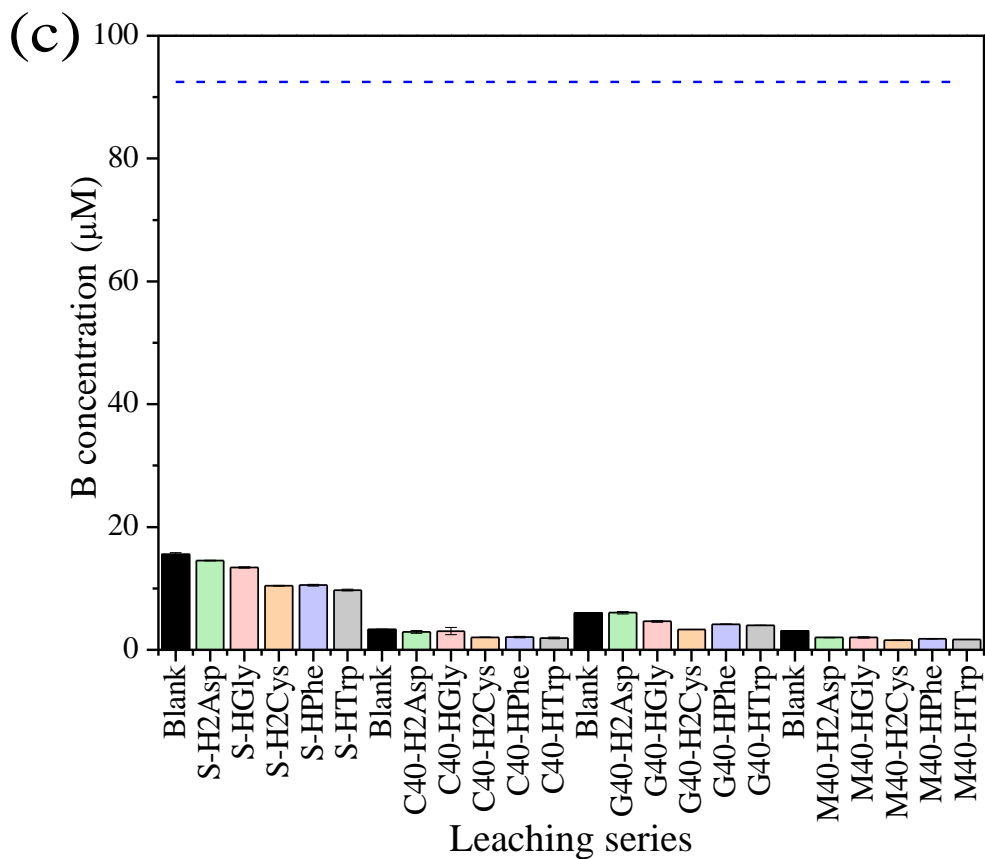
Fig. 6.4 Leaching results of (a) Se, (b) As, (c) B, (d) Cr, and (e) F from ground cement powders S, C40, G40, M40 with different amino acids H_2Asp, HGly, H_2Cys, HPhe and HTrp under pH 12.0.
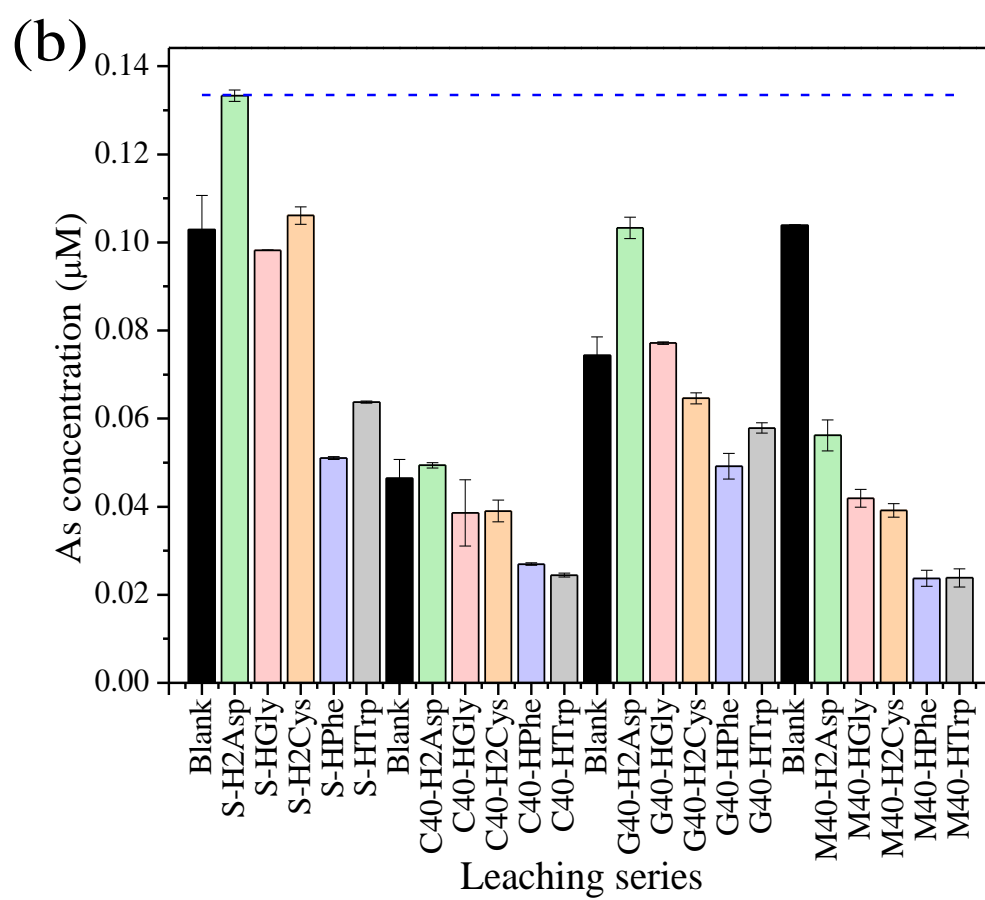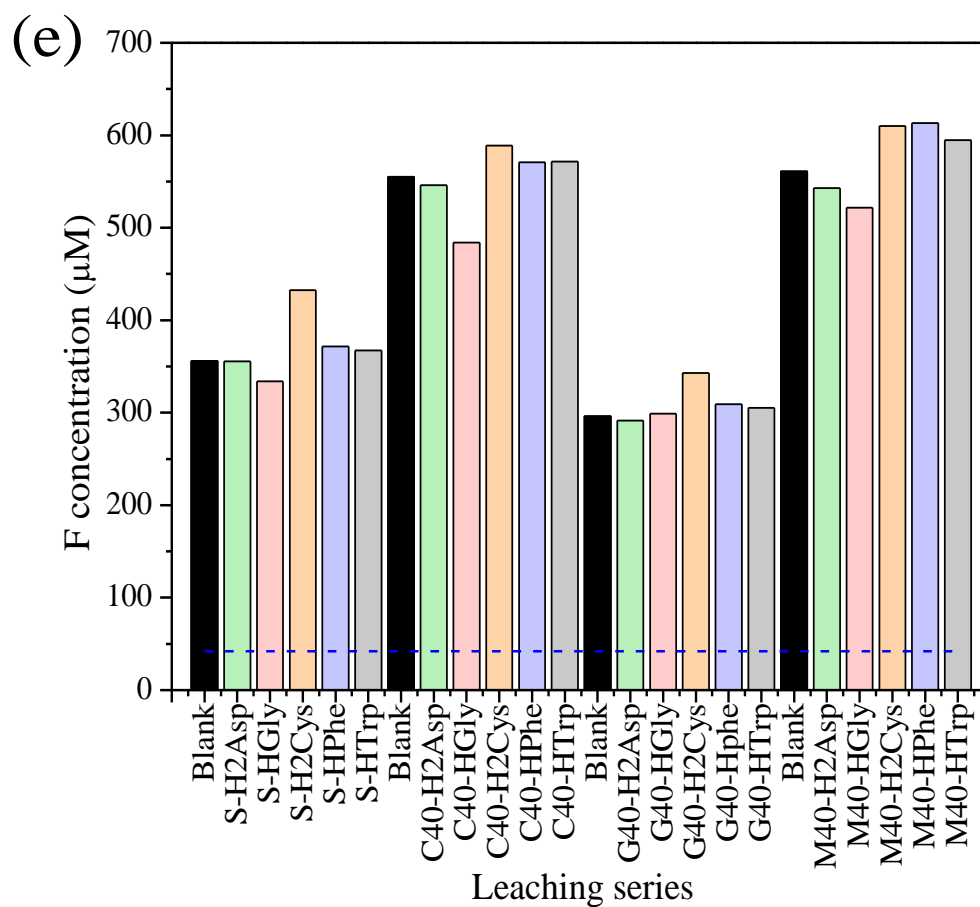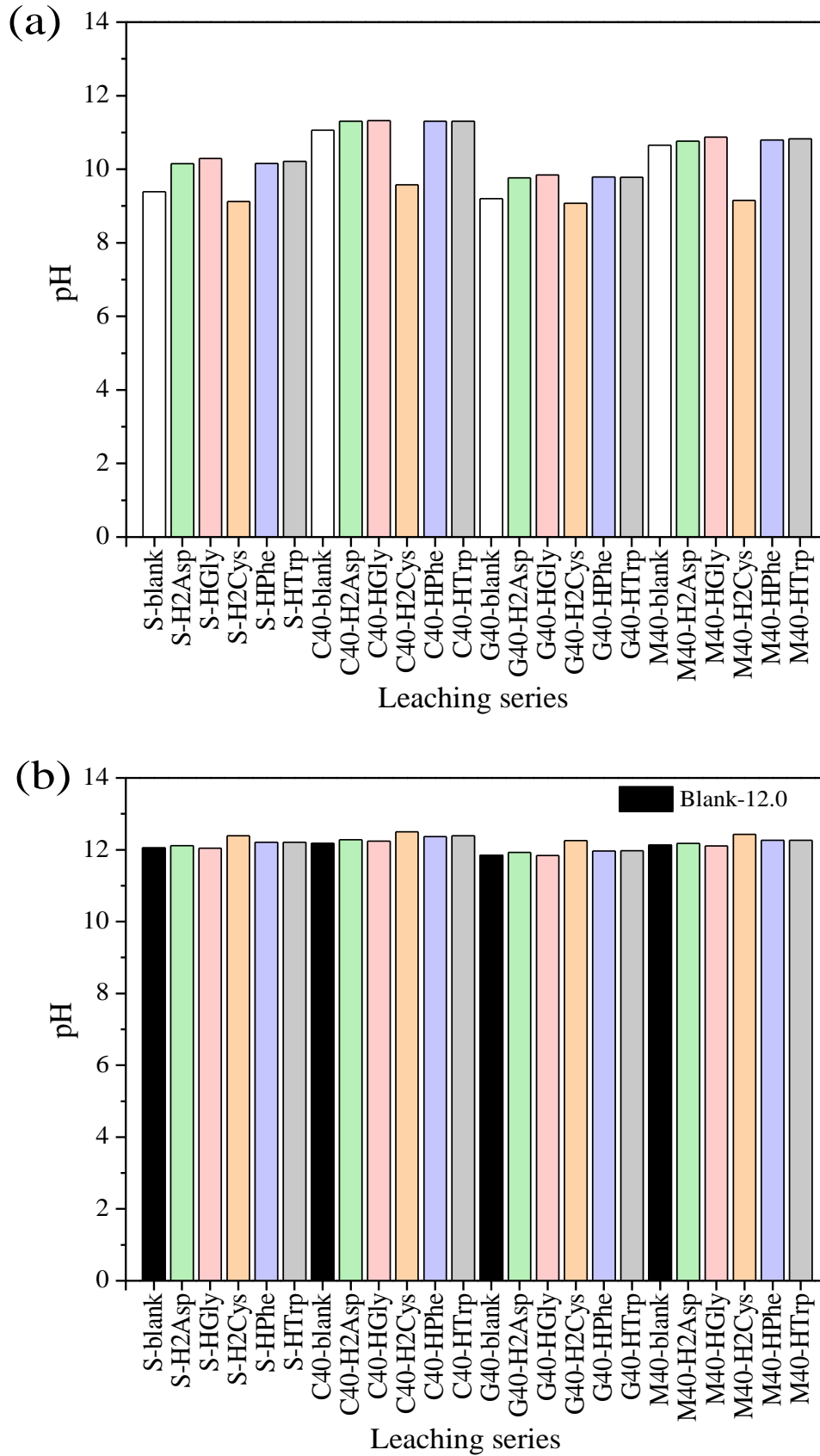
Fig. 6.5 The equilibrated pH of the solution after suspended S, C40, G40, M40 ground cement powder into different amino acids H_2Asp, HGly, H_2Cys, HPhe and HTrp.

In **Fig. 6.3(b)**, H$_2$Asp enhanced the releasing of As significantly comparing with other amino acids. In the cement systems, the immobilization of As involving coprecipitation with ettringite and precipitation of Ca$_3$(AsO$_4$)$_2$. The enhancement might be caused by the electrostatic attraction between -NH$_3^+$ and AsO$_4^{3-}$ on the surface of fly ash to prevent the immobilization. On the other hand, the K_{sp} of Ca$_3$(AsO$_4$)$_2$ is 6.8×10^{-19} which means it is easy to be formed in the absence of amino acids. However, -COOH group in amino acids can be complexed with Ca^{2+} in Ca$_3$(AsO$_4$)$_2$. Due to one H$_2$Asp molecule possess two -COOH groups, so H$_2$Asp prevents immobilizing As more than other amino acids under the same condition. The hydrogen bonds between -COOH and H$_2$AsO$_4^-$ also exist. For H$_2$Cys, it showed inhibitory effects on As like on Se through oxidization and reduction reaction but was in the presence of C40 and M40 series. Due to the main species of arsenic is arsenate, so the form of AsO$_4^{3-}$ and H$_3$AsO$_4$ existed. But for As(III), it is difficult to be precipitated. So one conceived complexes including H$_2$Cys, cystine, arsenite is expected.

Amino acids did not show significant effects on the releasing B it compared with blank tests (**Fig. 6.3(c)**). However, for Cr in **Fig. 6.3(d)**, H$_2$Cys inhibited its releasing in all of additives series to below the criteria, while other amino acids enhanced. The leaching forms of Cr from fly ash mainly are CrO$_4^{2-}$ and HCrO$_4^-$, so it is possible to happen reduction (**Eq. (6.4)**) in the presence of H$_2$Cys. For F in **Fig. 6.3(e)**, the additive of G40 contributed to the immobilization of F$^-$ effectively than C40 and M40. The additives as the Ca sources contributed to precipitate CaF$_2$. Also, CaSO$_4$ provided excess amount of SO$_4^{2-}$ to form ettringite, even though around pH 9-10 as shown in **Fig. 6.6(c)**, which indicates the ettringite also immobilized F$^-$ after it released from fly ash. In **Fig. 6.6(a)~ (d)**, the (100) plane of ettringite at 9.0° (2θ) almost disappeared unlike in **Fig. 6.6(c)**.

$$CrO_4^{2-} + 4H_2O + 3e = Cr(OH)_3 + 5OH^- \qquad (E^0 = \textbf{-0.13 V}) \tag{6.4}$$
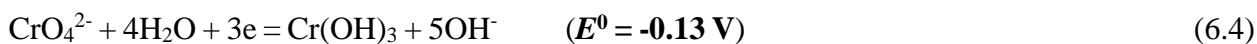
Under pH 12.0, the leaching amount of Se (**Fig. 6.4(a)**), As (**Fig. 6.4(b)**), B (**Fig. 6.4(c)**), and Cr (**Fig. 6.4(d)**) much decreased compared with pH 4.7 while Se still exceeds the MCL. From XRD patterns (**Fig. 6.7**) for the solid residues, after suspended for 6 h, the phases of each solid

residue after suspended into amino acids solutions were same as the original solid phases. Ettringite and hydrocalumite are more stable existing under 12.0 than 4.7, but the amounts of them were different as shown in **Fig. 6.8 (c), (d)**. In the G40 series, after suspended into different amino acids solutions, the amount of ettringite was still higher than S, C40, M40 series. The leaching amount of F^- was increased with the increasing of pH, suggesting the formation of ettringite where other co-existing anionic species are preferable to co-precipitate than F^-. H_2Asp and H_2Cys played an enhancing effect on the leaching of Se in different amount, other amino acids HGly, HPhe and HTrp suppressed the release of Se. After cement blocks suspended into solutions with the initial pH 12.0 for 6 h, the final pH was around 12.0 as shown in **Fig. 6.5(b)**, only in the presence of G40 showed relatively lower pH than other additives. This is consistent with the previous report that the Ca sources also play a role as an alkaline reagent to increase system pH (Guo et al., 2019). For selenite, the immobilization mechanisms mainly ascribe to the formation of hydrocalumite and ettringite which can immobilize SeO_3^{2-} in their crystal structures (Gougar et al., 1996; Ma et al., 2017; Ma et al., 2018). So under 12.0, H_2Asp and H_2Cys dissociated into Asp^{2-} and Cys^{2-}, the ion-exchange might happen between amino acids and SeO_3^{2-} from hydrocalumite interlayer. Other amino acids, HGly, HPhe and HTrp dissociated into Gly^-, Phe^-, and Trp^- with one negative charge in each molecule which the ion-exchanging ability were lower than SeO_3^{2-}. Due to the positively charged surface of ettringite and hydrocalumite, the surface adsorption of amino acids can happen and this might inhibit the simple dissolution of ettringite and hydrocalumite. That is why amino acids can decrease the leaching of some anionic species.
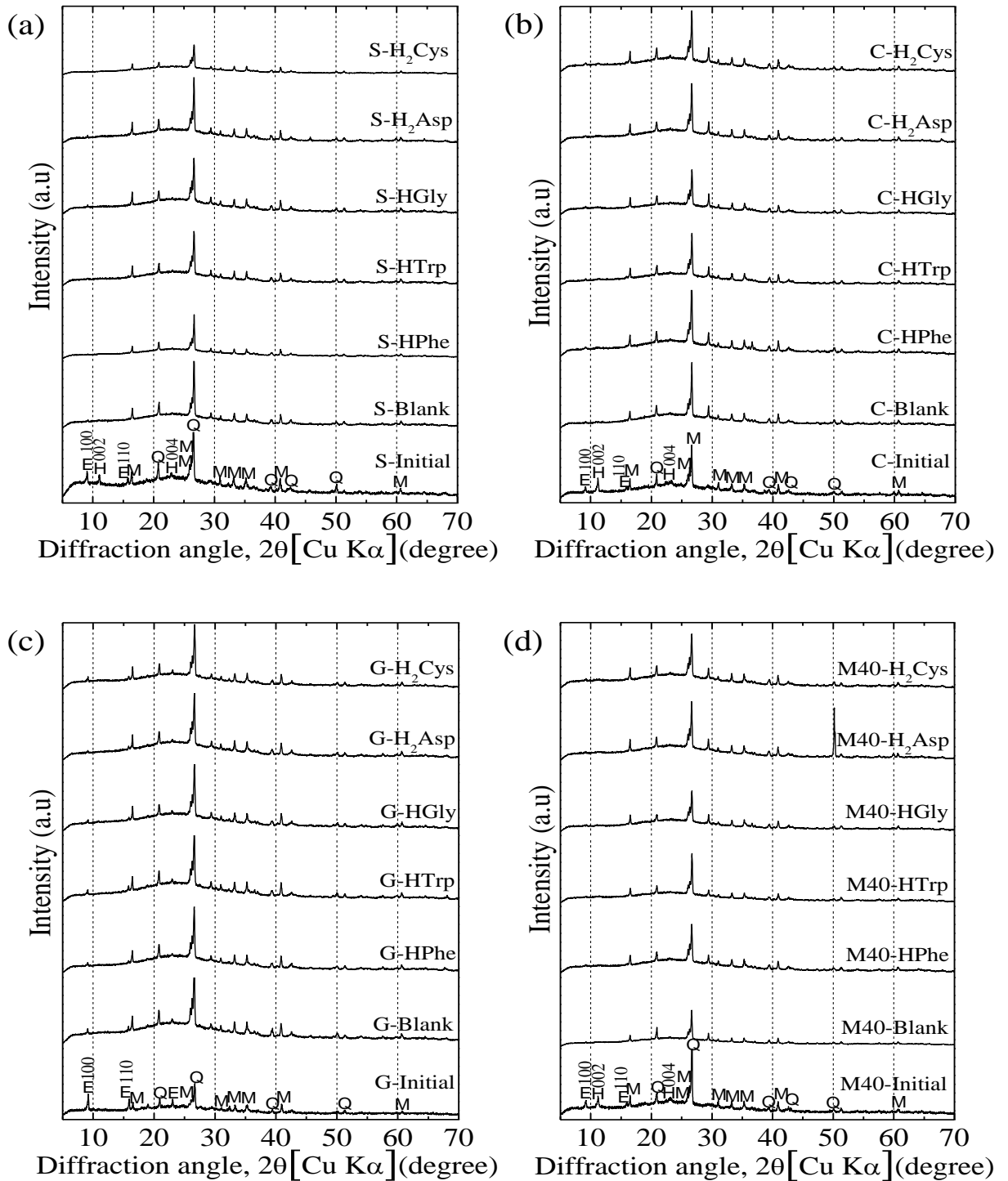
Fig. 6.6 XRD patterns of four ground cement powder in (a) S, (b) C40, (c) G40, (d) M40 series in the presence of amino acids under pH 4.7.

Fig. 6.7 XRD patterns of four ground cement powder in (a) S, (b) C40, (c) G40, (d) M40 series in the presence of amino acids under pH 12.0.
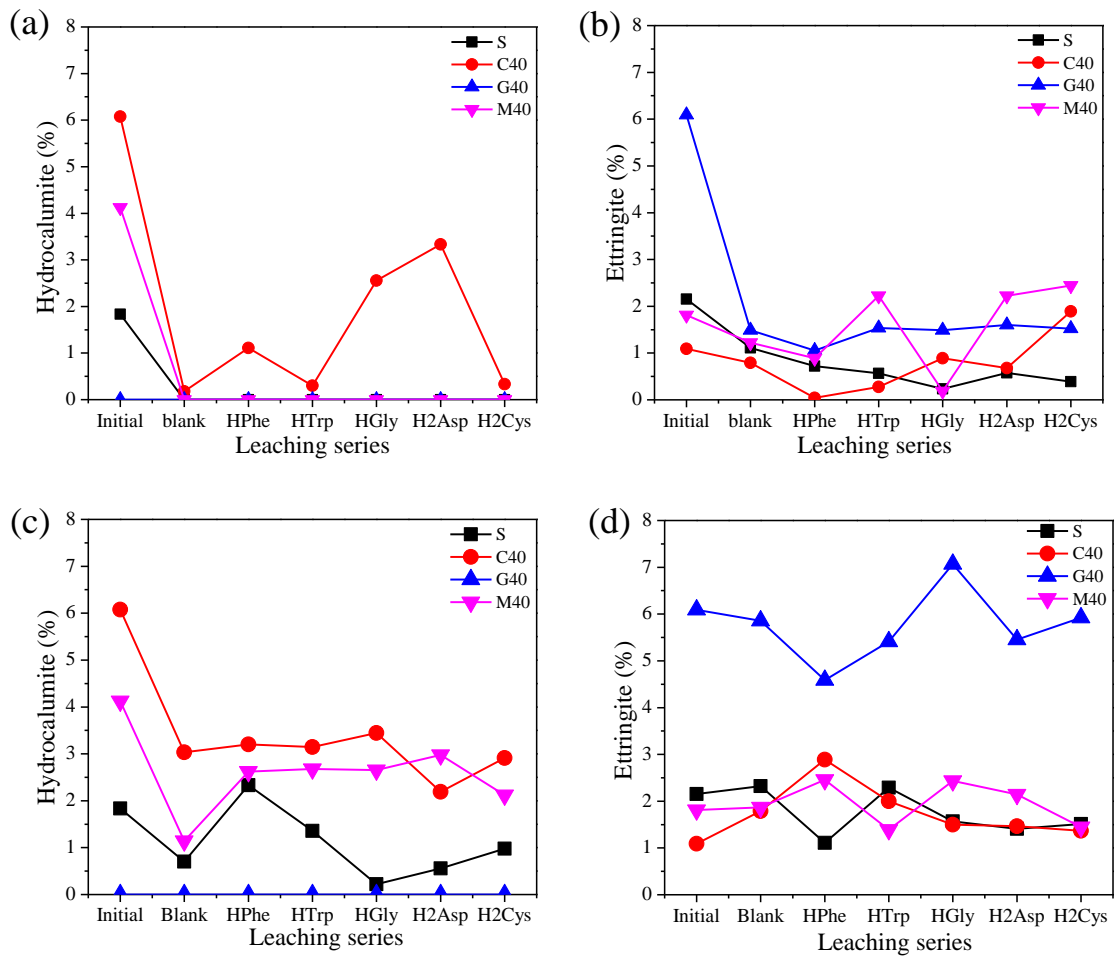
Fig. 6.8 Rietveld analysis of ettringite and hydrocalumite in each ground cement powder before and after amino acids TCLP tests under pH 4.7 and 12.0. (a) ettringite under pH 4.7, (b) hydrocalumite under 4.7, (c) ettringite under pH 12.0, (d) hydrocalumite under pH 12.0.

6.4 Conclusions

In the present work, the leaching behavior of Se, As, B, Cr, F from fly ash blended cement blocks after added different Ca additives were determined using TCLP in the presence of amino acids. After added Ca additives, the formation of ettringite and hydrocalumite were increased in all series of C40, G40, M40. The leaching of Se, As, B, Cr were decreased to some extent but Se was still higher than the MCL even in high pH 12.0. The leaching of Se, As, B, Cr were decreased as the pH increased from 4.7 to 12.0. Under pH 4.7, H_2Asp increased the leaching of Se, As, Cr in all of series, while H_2Cys played an inhibiting role through oxidization. Under pH 12.0, H_2Asp

and H_2Cys enhanced the releasing of Se from cement blocks whereas HGly, HPhe, and HTrp suppressed the leaching but still over the MCL. Therefore, environmental conditions such as pH, control the effects of amino acids on the leaching behavior of anionic species from cement blocks and the necessary methods should be developed to improve selenium immobilization.

References

Akar, G., Polat, M., Galecki, G., Ipekoglu, U., 2012. Leaching behavior of selected trace elements in coal fly ash samples from Yenikoy coal-fired power plants. Fuel Process. Technol. 104, 50-56.

Amiri, F., Yaghmaei, S., Mousavi, S.M., 2011. Bioleaching of tungsten-rich spent hydrocracking catalyst using Penicillium simplicissimum. Bioresour. Technol. 102, 1567-1573.

Christensen, A.N., Jensen, T.R., Hanson, J.C., 2004. Formation of ettringite, $Ca_6Al_2(SO_4)_3(OH)_{12} \cdot 26H_2O$, AFt, and monosulfate, $Ca_4Al_2O_6(SO_4) \cdot 14H_2O$, AFm-14, in hydrothermal hydration of Portland cement and of calcium aluminum oxide-calcium sulfate dihydrate mixtures studied by in situ synchrotron X-ray powder diffraction. J. Solid State Chem. 177, 1944-1951.

Duchesne, J., Reardon, E.J., 1999. Lime treatment of fly ash: characterization of leachate composition and solid/water reactions. Waste Manage. 19, 221-231.

Gougar, M.L.D., Scheetz, B.E., Roy, D.M., 1996. Ettringite and C-S-H Portland cement phases for waste ion immobilization: A review. Waste Manage. 16, 295-303.

Guo, B., Nakama, S., Tian, Q., Pahlevi, N.D., Hu, Z., Sasaki, K., 2019. Suppression processes of anionic pollutants released from fly ash by various Ca additives. J. Hazard. Mater. 371, 474-483.

Guo, B., Sasaki, K., Hirajima, T., 2017. Characterization of the intermediate in formation of selenate-substituted ettringite. Cem. Concr. Res. 99, 30-37.

Guo, Q., Reardon, E.J., 2012. Calcined dolomite: alternative to lime for minimizing undesirable element leachability from fly ash. Ind. Eng. Chem. Res. 51, 9106-9116.

Halim, C.E., Amal, R., Beydoun, D., Scott, J.A., Low, G., 2003. Evaluating the applicability of a modified toxicity characteristic leaching procedure (TCLP) for the classification of cementitious wastes containing lead and cadmium. J. Hazard. Mater. 103, 125-140.

Izquierdo, M., Querol, X., 2012. Leaching behaviour of elements from coal combustion fly ash: an overview. Int. J. Coal Geol. 94, 54-66.

Kalembkiewicz, J., Sitarz-Palczak, E., 2015. Efficiency of leaching tests in the context of the influence of the fly ash on the environment. J. Ecol. Eng. 16(1).

Kumarathasan, P., McCarthy, G.J., Hassett, D.J., Pflughoeft-Hassett, D.F., 1989. Oxyanion substituted ettringites: synthesis and characterization; and their potential role in immobilization of As, B, Cr, Se and V. MRS Online Proceedings Library (OPL) 178.

Li, X.D., Poon, C.S., Sun, H., Lo, I., Kirk, D.W., 2001. Heavy metal speciation and leaching behaviors in cement based solidified/stabilized waste materials. J. Hazard. Mater. 82, 215-230.

Lu, C., Hsu, M.H., Lin, Y., 2019. Evaluation of heavy metal leachability of incinerating recycled aggregate and solidification/stabilization products for construction reuse using TCLP, multi-final pH and EDTA-mediated TCLP leaching tests. J. Hazard. Mater. 368, 336-344.

Ma, B., Fernandez-Martinez, A., Grangeon, S., Tournassat, C., Findling, N., Carrero, S., Tisserand, D., Bureau, S., Elkaïm, E., Marini, C., Aquilanti, G., Koishi, A., Marty, N.C.M., Charlet, L., 2018. Selenite Uptake by Ca-Al LDH: A Description of Intercalated Anion Coordination Geometries. Environ. Sci. Technol. 52, 1624-1632.

Ma, B., Fernandez-Martinez, A., Grangeon, S., Tournassat, C., Findling, N., Claret, F., Koishi, A., Marty, N.C.M., Tisserand, D., Bureau, S., Salas-Colera, E., Elkaïm, E., Marini, C., Charlet, L., 2017. Evidence of Multiple Sorption Modes in Layered Double Hydroxides Using Mo As Structural Probe. Environ. Sci. Technol. 51, 5531-5540.

Mahedi, M., Cetin, B., 2019. Leaching of elements from cement activated fly ash and slag amended soils. Chemosphere 235, 565-574.

Malviya, R., Chaudhary, R., 2006. Leaching behavior and immobilization of heavy metals in solidified/stabilized products. J. Hazard. Mater. 137, 207-217.

Myneni, S.C., Traina, S.J., Logan, T.J., 1998. Ettringite solubility and geochemistry of the Ca $(OH)_2$-$Al_2(SO_4)_3$-H_2O system at 1 atm pressure and 298 K. Chem. Geol. 148, 1-19.

Qiu, X., Sasaki, K., Takaki, Y., Hirajima, T., Ideta, K. and Miyawaki, J., 2015. Mechanism of boron uptake by hydrocalumite calcined at different temperatures. J. Hazard. Mater, 287, 268-277.

Reardon, E.J., Della Valle, S., 1997. Anion sequestering by the formation of anionic clays: lime treatment of fly ash slurries. Environ. Sci. Technol. 31, 1218-1223.

Sasaki, K., Nakama, S., Tian, Q., Guo, B., Wang, M., Takagi, R., Takahashi, T., 2021. Elution characteristics of undesirable anionic species from fly ash blended cement in different aqueous solutions. J. Environ. Chem. Eng. 9, 105171.

Tian, Q., Guo, B., Nakama, S., Zhang, L., Hu, Z., Sasaki, K., 2019. Reduction of undesirable element leaching from fly ash by adding hydroxylated calcined dolomite. Waste Manage. 86, 23-35.

Zhang, M. and Reardon, E.J., 2003. Removal of B, Cr, Mo, and Se from wastewater by incorporation into hydrocalumite and ettringite. Environ. Sci. Technol. 37(13), 2947-2952.

Theiss, F.L., Ayoko, G.A. and Frost, R.L., 2013. Removal of boron species by layered double hydroxides: A review. J. Colloid Interface Sci. 402, 114-121.

Chapter 7 Effects of zero valent iron on the leaching behavior of anionic species from cement blocks in the presence of H_2Asp and H_2Cys

7.1 Introduction

According to **Chapter 6**, Ca additives like lime(Ca(OH)$_2$), gypsum (CaSO$_4$) play a significant role in prohibiting the leaching of anionic species, but the leaching of Se was always higher than the MCL in Environmental Agency Notification No.46 in Japan. Zero valent iron (Fe^0, ZVI) is a common reducing agent used to solidify contaminants from waste by reductive precipitation ((Zhang et al., 2005; Triszcz et al., 2009; Guo et al., 2016; Zhang et al., 2020). In the cementitious systems, ZVI acts as a strong reducing agent as well as low-cost and potentially available materials to reduce the As, Cr, and Se to enhance their immobilization.

In this chapter, the fly ash-blended cement blocks were prepared with Ca(OH)$_2$, and CaSO$_4$ as Ca additives, and varying ZVI amounts. The effects of ZVI on the immobilization of Se, As, B, and Cr were discussed, furthermore, the leaching behavior of Se, As, B, and Cr from cement blocks after the addition of ZVI was evaluated using TCLP tests under the pH 4.7 and 12.0.

7.2 Experimental

7.2.1 Materials

In this work, two amino acids of H$_2$Asp and H$_2$Cys were focused. The cement, fly ash and other materials are same as shown in **6.2.1** section.

7.2.2 Preparation of fly as-blended cement blocks with ZVI

The specific experimental conditions are named as shown in **Table. 7.1**. Blank: 0.94 g cement +12.19 g fly ash; C-0: 0.94 g cement +12.19 g fly ash +0.4 g lime; C-0.1: 0.94 g cement +12.19 g

fly ash +0.4 g lime +0.1 g ZVI; C-0.5: 0.94 g cement +12.19 g fly ash +0.4 g lime +0.5 g ZVI; C-1: 0.94 g cement +12.19 g fly ash +0.4 g lime +1.0 g ZVI; G-0: 0.94 g cement +12.19 g fly ash +0.4 g gypsum; G-0.1: 0.94 g cement +12.19 g fly ash +0.4 g gypsum +0.1 g ZVI; G-0.5: 0.94 g cement +12.19 g fly ash +0.4 g gypsum +0.5 g ZVI; G-1: 0.94 g cement +12.19 g fly ash +0.4 g gypsum +1.0 g ZVI. The solid/water mass ratio was fixed to 0.323. Firstly, the cement and fly ash were mixed, and then ZVI was added for mixing. Finally, a specific amount of ultra-pure water was added using a vortex oscillator to shake for 10 mins. After curing for 28 days under 70% of humidity, the cured cement blocks were separately ground into samples under 280 mesh (53 μm) to supply for XRD and TCLP test according to the environmental Agency Notification No.46 in Japan.

Table 7.1 Specific mixing conditions of different fly ash-blended cement blocks.

	Cement	Fly ash	Lime	Gypsum	ZVI
Blank	0.94 g	12.19 g	/	/	/
C-0	0.94 g	12.19 g	0.4 g	/	/
C-0.1	0.94 g	12.19 g	0.4 g	/	0.1 g
C-0.5	0.94 g	12.19 g	0.4 g	/	0.5 g
C-1	0.94 g	12.19 g	0.4 g	/	1.0 g
G-0	0.94 g	12.19 g	/	0.4 g	/
G-0.1	0.94 g	12.19 g	/	0.4 g	0.1 g
G-0.5	0.94 g	12.19 g	/	0.4 g	0.5 g
G-1	0.94 g	12.19 g	/	0.4 g	1.0 g

7.2.3 Dissolution test

As shown in 6.2.3 section.

7.2.4 Chemical analysis and solid characterizations

The compressive strengths of the obtained cement blocks were determined using a 200 kN capacity CLP-200KNS1 testing machine (Osaka, Japan). As shown in **Chapter 6**, the leaching solutions were provided for ICP-MS to check the concentrations of elements of Se, As, B, and Cr. XRD was used to characterize the cement blocks solid residues.

7.3 Results and discussion

7.3.1 Characterization of fly ash blended cement blocks

As expected, the pozzolanic reaction in the mixing of cement, fly ash, Ca additives systems have happened and related XRD patterns of each cement block were shown in **Fig. 7.1**.
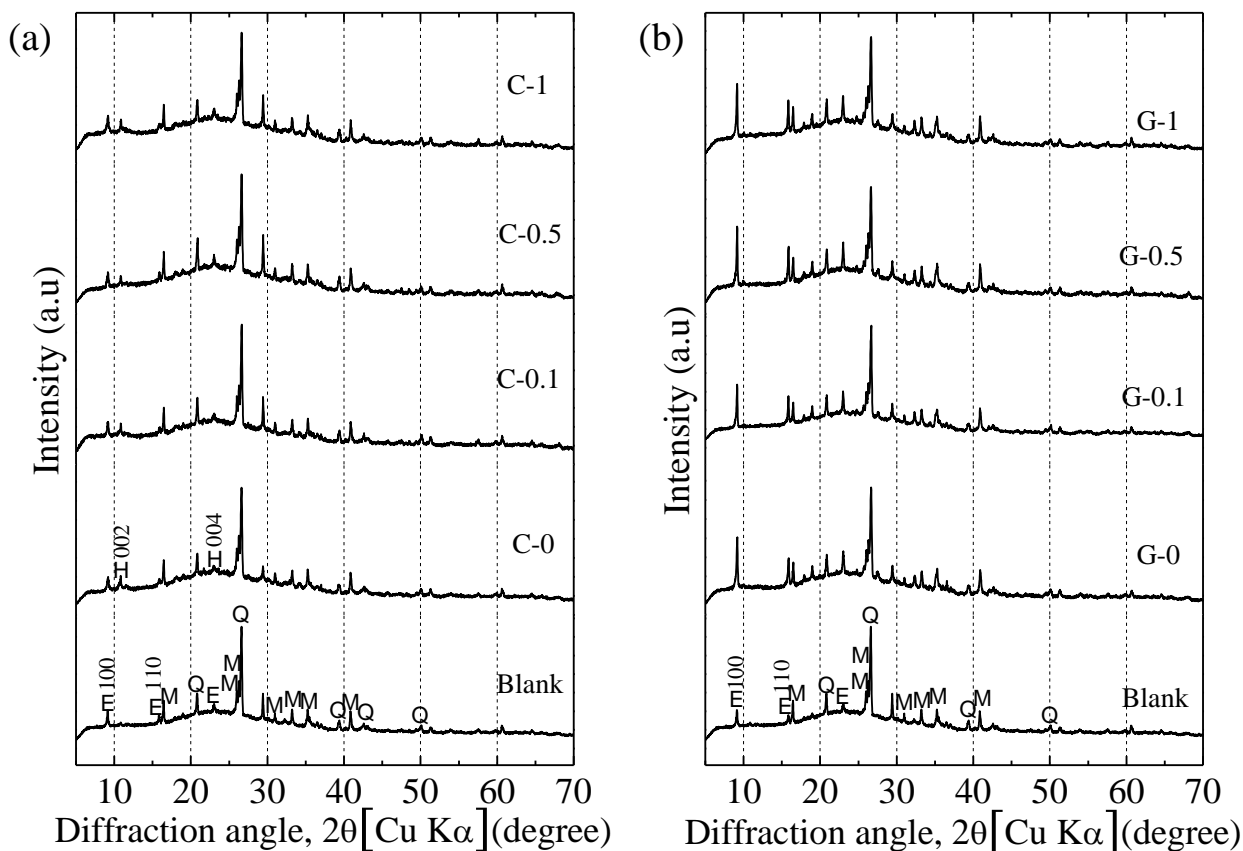

Fig. 7. 1 XRD patterns of fly ash-blended ground cement powder with different amounts of ZVI after curing for 28 d, (a) lime as an additive, (b) gypsum as an additive.

For blank, without any Ca additives, only ettringite, quartz, and mullite formed. After added Ca(OH)$_2$, hydrocalumite was formed, and ettringite and hydrocalumite were still produced even though after the addition of ZVI. In **Fig. 7.1(b)**, the addition of CaSO$_4$ enhanced the formation of ettringite but no hydrocalumite formed cause an excess of SO$_4^{2-}$ consumed Ca to produce ettringite. Ettringite and hydrocalumite both are well known for their immobilizing ability of Se, As, B, and Cr as cement hydration products (Baur and Johnson, 2003; Bonhoure et al., 2006; Triszcz et al., 2009; Mončeková et al., 2016; Fan et al., 2018; Maaouia et al., 2018; Guo et al., 2019; Wang et al., 2019; Zhang et al., 2020; Sasaki et al., 2021).

Compressive strength is an important factor in the S/S of radioactive cement blocks, and **Fig. 7.2** shows the observed compressive strength of each fly ash-blended cement blocks samples. After added Ca(OH)$_2$ and CaSO$_4$, the compressive strengths of C-0 and G-0 were increased to around 6.0. With the different amounts of ZVI, it seems the compressive strengths decreased but still were higher than the blank series.
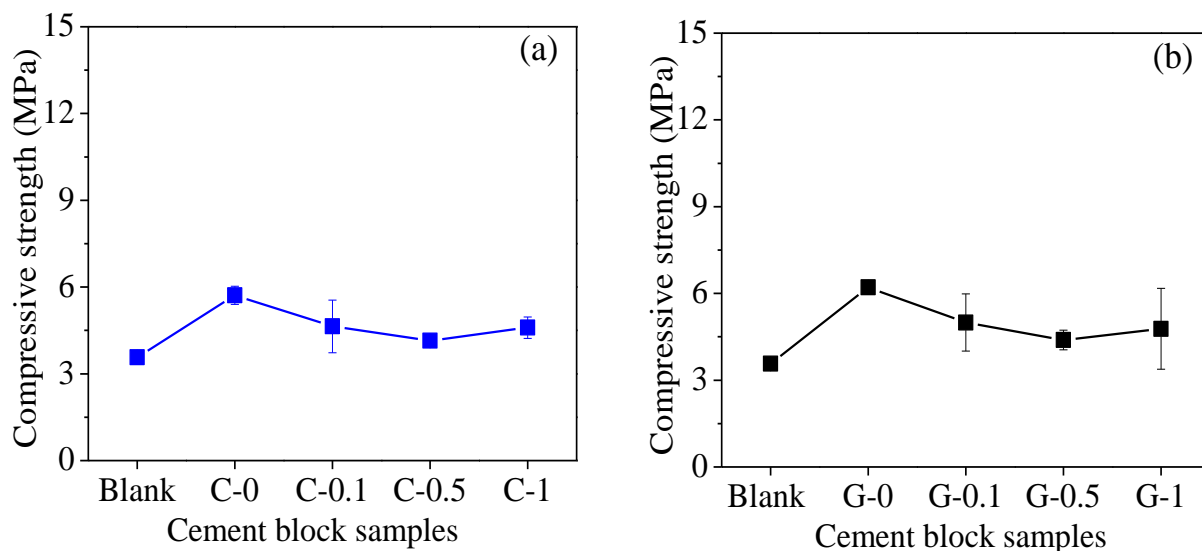

Fig. 7. 2 Compressive strength of fly ash-blended cement blocks samples after 28 d curing.

7.3.2 Effects of Ca additives on the leaching of anionic species

From **Fig. 7.1**, after added Ca(OH)$_2$ and CaSO$_4$, the formation of ettringite and hydrocalumite were enhanced. As shown in **Fig. 7.3** and **Fig. 7.4**, the leaching of Se, As, B, and Cr was significantly inhibited under pH 4.7 and 12.0 in the absence of amino acids. The alkalinity of the solution environment also had a strong influence on their leaching, as leaching concentrations decreased with the pH increased from 4.7 to 12.0. Under pH 12.0, Ca(OH)$_2$ and CaSO$_4$ suppressed the leaching of As (**Fig.7.4(b)**) and B (**Fig.7.4(c)**) to below the MCL. However, Se (**Fig.7.4(a)**) and Cr (**Fig.7.4(d)**) were still higher than criteria values.
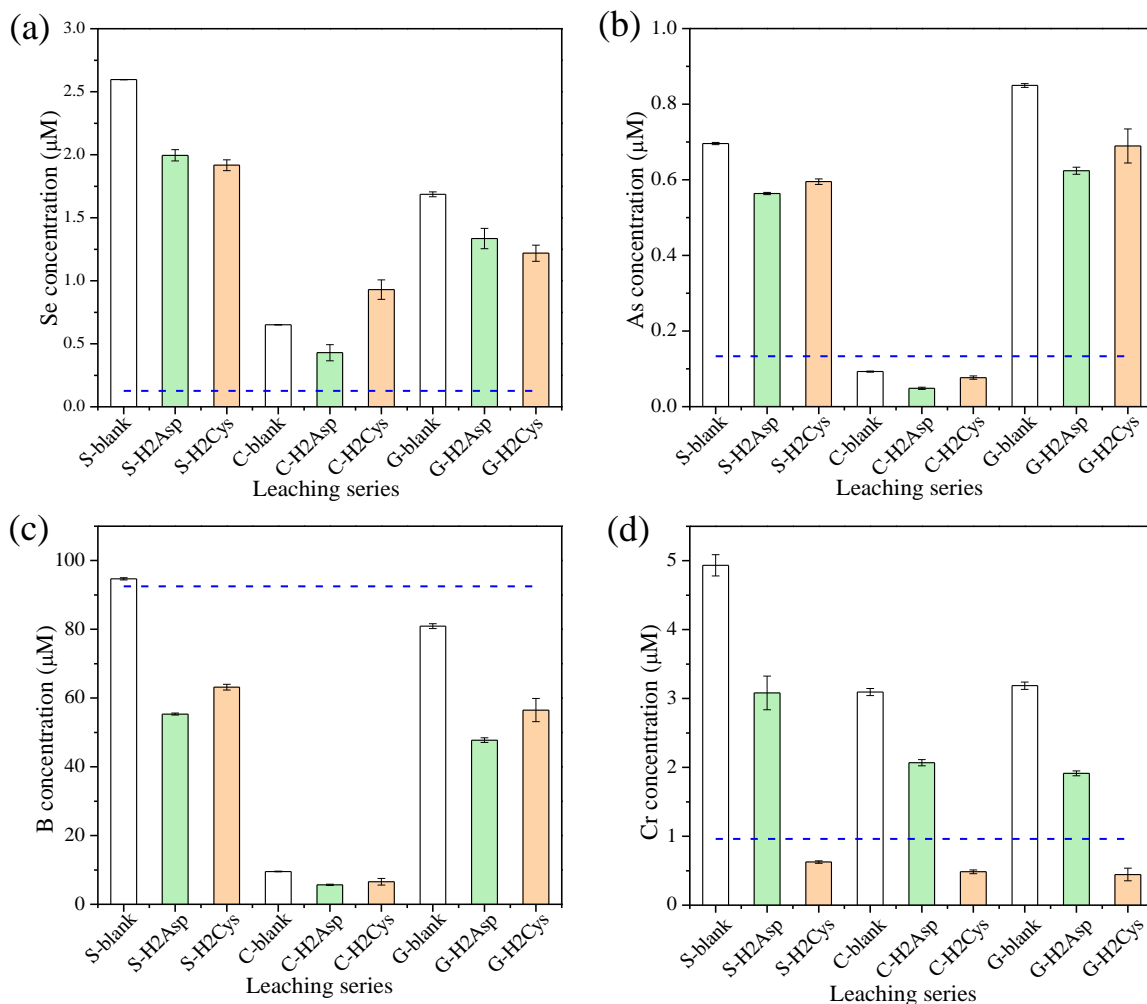

Fig. 7. 3 Leaching results of (a) Se, (b) As, (c) B, and (d) Cr from ground cement powder without the addition of ZVI under pH 4.7.

In the TCLP leaching tests with amino acids, under pH 12.0, H_2Asp and H_2Cys both enhanced the releasing concentration of Se **(Fig. 7.4(a))**, As **(Fig. 7.4(b))**, and Cr **(Fig. 7.4(d))**, while B **(Fig. 7.4(c))** seems no obvious changing. The ion-exchanging of Asp^{2-} and Cys^{2-} with anionic species happened from hydrocalumite interlayer which also is confirmed in **Chapters 5 and 6**. However, under pH 4.7, the amino acids showed suppression effects of Se **(Fig. 7.3(a))**, As **(Fig. 7.3(b))**, B **(Fig. 7.3(c))**, and Cr **(Fig. 7.3(d))**. This may be caused by surface adsorption of amino acids on the hydrocalumite to inhibited its dissolution. While $[Cr(OH_2)_6]^{3+}$ is only present in acidic conditions (pH < 3.6), the solid phase $Cr(OH)_3$ predominates in the pH range of 6.5-11.4 (Rai et al., 1987). Therefore, another reason might ascribe to the oxidization of H_2Cys to cystine and caused the reduction of Cr(VI) to be Cr(III) to decrease its solubility.
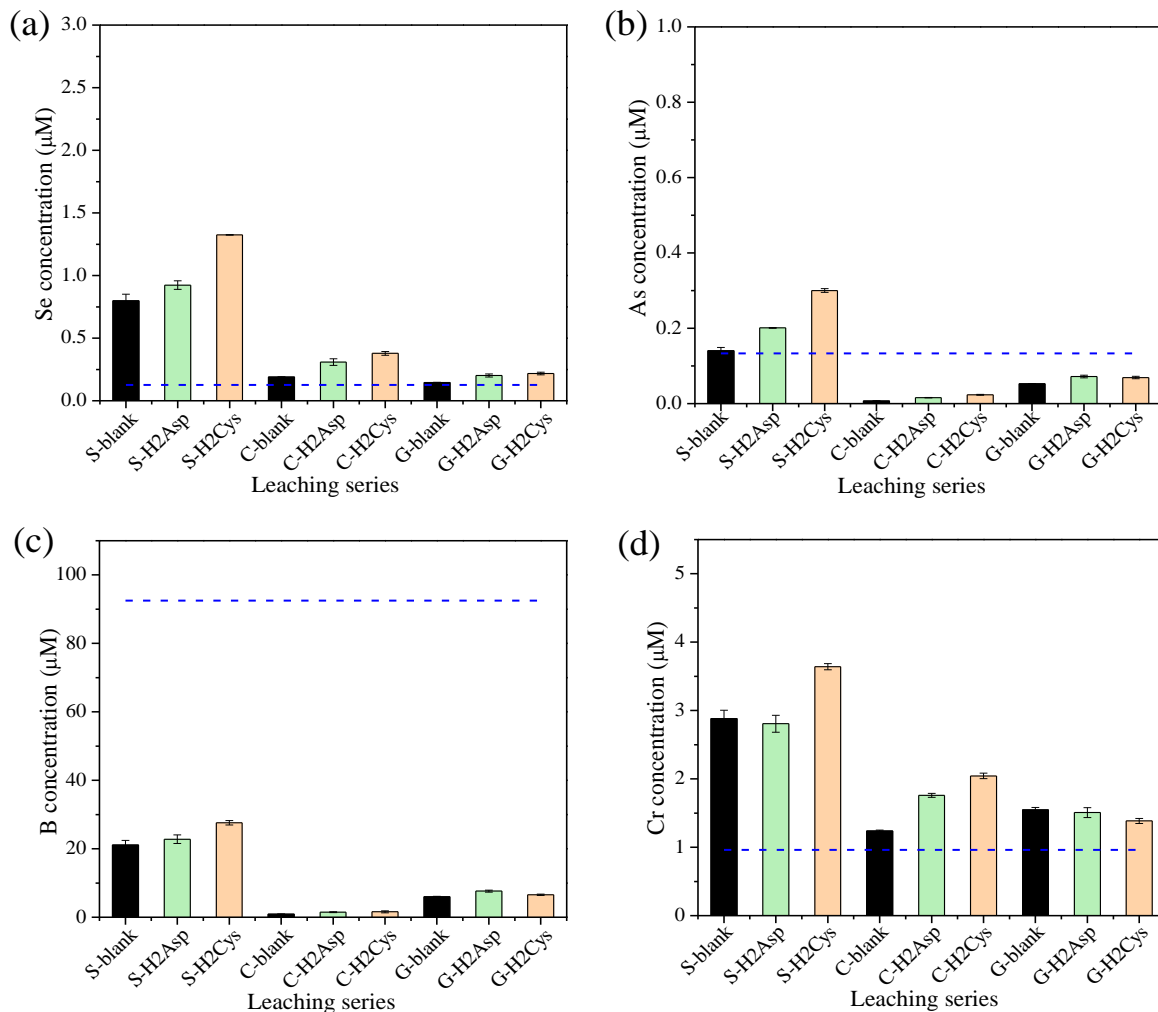
Fig. 7. 4 Leaching results of (a) Se, (b) As, (c) B, and (d) Cr from cement blocks without the addition of ZVI under pH 12.0.

7.3.3 Effects of ZVI on the leaching of anionic species

ZVI as the reduction agent was mixed into cement blocks. After curing 28 d, TCLP solution with and without amino acids was used for their suspension. **Fig. 7.5** shows the leaching results in the presence of H_2Asp and H_2Cys under pH 12.0. Under this condition, the addition of ZVI did not show inhibition effects on the leaching of Se **(Fig. 7.5(a))**, As **(Fig. 7.5(b))**, and B **(Fig. 7.5(c))**,. On the contrary, the enhancing influences appeared. For hydrocalumite and ettringite, the immobilization involved dissolution and re-precipitation mechanisms. Hence, during the re-precipitation process, the dissolved Fe(III) was possible to be involved in the formation of CaFe-

LDH. So SeO_3^{2-}/SeO_4^{2-} was released into solution instead of co-precipitation into hydroclaumite.

The oxidization of Fe(0) was affected by the values of pH and Eh. The capacity of ZVI is severely limited in an alkaline environment and the oxidant was reduced more efficiently in an acid medium by ZVI (Cao and Zhang, 2006; Fiúza et al., 2010). The related oxidization reaction with standard oxidation-reduction potential (E^0) is presented in **Eqs. (7.1), (7.2)**. The value E^0 of Fe(0) to be Fe(II) is -0.447 V (**Eq. (7.1)**) which is lower than -0.037 V in **Eq. (7.2)**. Under the initial alkaline pH 12.0, a small amount of Se **(Fig. 7.5(a))**, As **(Fig. 7.5(b))**, and Cr **(Fig. 7.5(d))** were released into solution from ettringite and hydrocalumite, thus, the oxidant was much lower than reducing agent and reduced the Eh value in cement systems. Another reason might be the release amount of oxidant was too small to contact with ZVI particles.

For Cr, the release of it was decreased as the addition amount of ZVI increased in the presence of $CaSO_4$ which might be related to the precipitate of Cr(III). In the presence of $CaSO_4$, excess amount of SO_4^{2-} competed with CrO_4^{2-} to form ettringite, causing more CrO_4^{2-} to be released into solutions which increase the possibility of it contacting ZVI. As shown in **Eq. (7.6)**, the E^0 of Cr(VI)/Cr(III) in -0.13 V is higher than other equations which indicate the reduction of Cr(VI) to be Cr(III) primarily happened than the reduction of Se(VI)/Se(IV) and As(V). The amino acids of H₂Asp and H₂Cys played the obvious enhanced effects on the release of Se in all leaching series through ion-exchange with ionic species from hydrocalumite interlayer, and Cr in the addition of Ca(OH)₂. Also the release of As and B was enhanced but only in the absence of Ca additives cement blocks.

$$Fe^0 = Fe^{2+} + 2e \qquad (E^0 = \textbf{-0.447 V}) \qquad (7.1)$$

$$Fe^0 = Fe^{3+} + 3e \qquad (E^0 = \textbf{-0.037 V}) \qquad (7.2)$$

$$SeO_4^{2-} + H_2O + 2e = SeO_3^{2-} + 2OH^- \qquad (E^0 = \textbf{0.05 V}) \qquad (7.3)$$

$$SeO_3^{2-} + 3H_2O + 4e = Se^0 + 6OH^- \qquad (E^0 = \textbf{-0.366 V}) \qquad (7.4)$$

$$AsO_4^{3-} + 2H_2O + 2e = AsO_2^- + 4OH^- \qquad (E^0 = \textbf{-0.71 V}) \qquad (7.5)$$

$$CrO_4^{2-} + 4H_2O + 3e = Cr(OH)_3 + 5OH^- \qquad (E^0 = -0.13 \text{ V}) \tag{7.6}$$
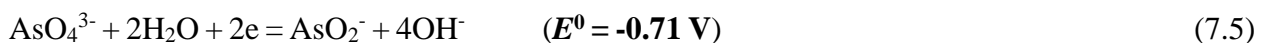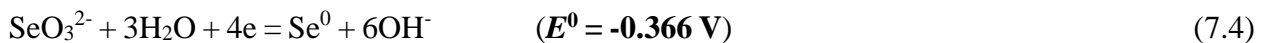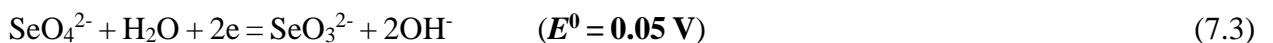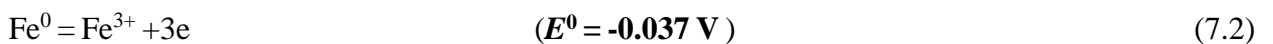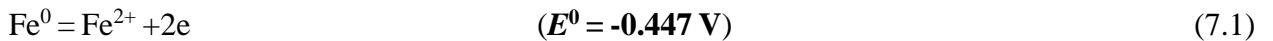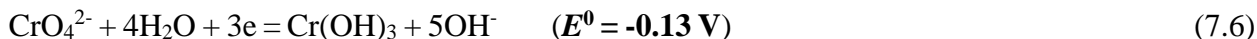
Under the condition of pH 4.7, H_2Asp and H_2Cys in all of the leaching series showed suppression effects **(Fig. 7.6)**. For Se, as the addition amount increasing of ZVI, the release of Se also was increased **(Fig. 7.6(a))**. The release of B was not affected by ZVI **(Fig. 7.6(c))**. The release of element As **(Fig. 7.6(b))** in the presence of $Ca(OH)_2$ also was not be affected by ZVI but in the addition of $CaSO_4$ reduction of As(V) to be As(III) might have happened to reduce the leaching. However, for Cr, it seems the reduction reaction has happened in all of the leaching series either in the presence of $Ca(OH)_2$ or $CaSO_4$ **(Fig. 7.6(d))**. Depending on the E^0 values in **Eqs. (7.3)~(7.6)**, Cr(VI) was primarily reduced during the oxidation process of Fe(0). It was possible that the ZVI surface was consumed by the Cr(VI)/Cr(III) and was not available for other elements, furthermore, the E^0 of Se(IV)/Se(0) is too low to happen reduction in the presence of Cr(VI). Except for $Cr(OH)_3$, in the presence of dissolved Fe(III), Cr(III) readily precipitates as mixed Fe(III)-Cr(III) hydroxides when pH higher than 4.0 (Fiúza et al., 2010). The H_2Cys also possibly happened oxidation as shown in **Fig. 7.6(d)**, cause in the presence of H_2Cys, the releasing of Cr was much lower than blank and H_2Asp series.
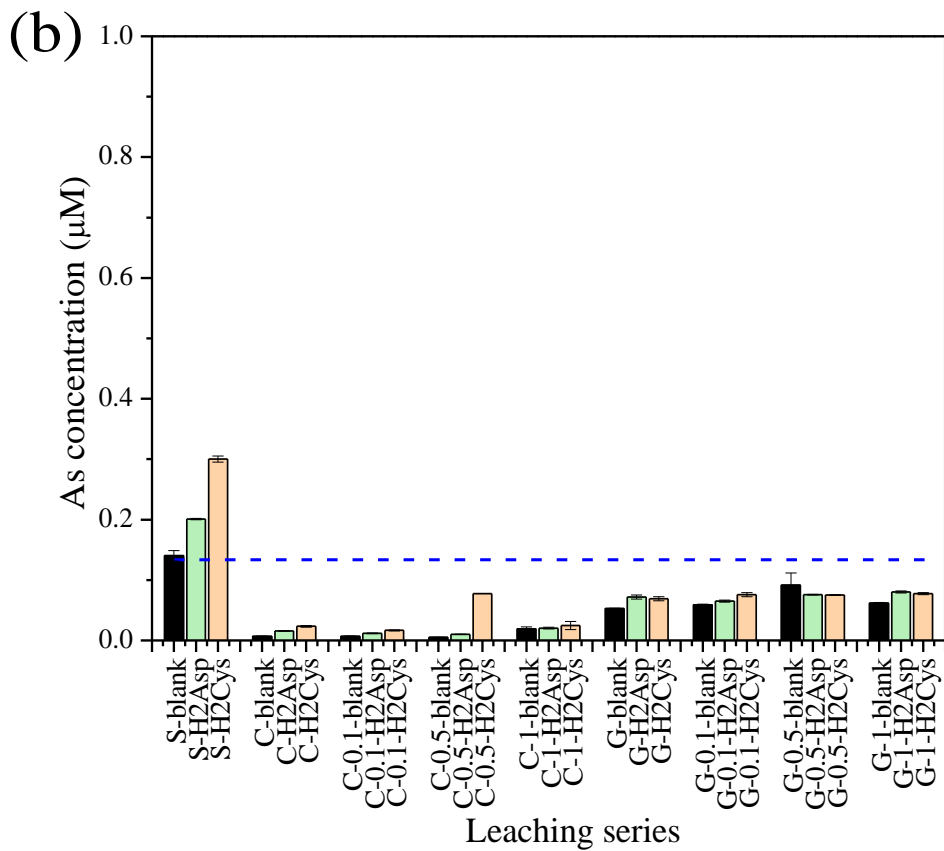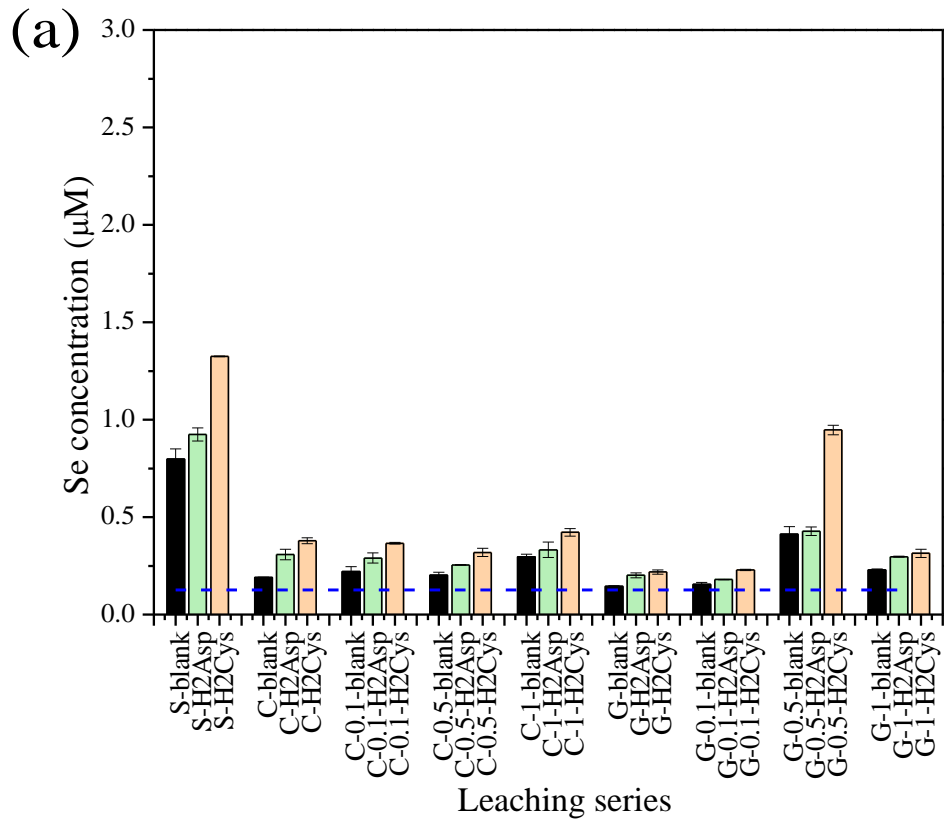
Fig. 7.5 Leaching results of (a) Se, (b) As, (c) B, and (d) Cr from ground cement powder with addition of ZVI under pH 12.0.

Based on the above results, the oxidization process of ZVI did not enhance the immobilization of Se. Several reasons can be expected according to the results. (i) After the oxidation of Fe(0), Fe(III) was produced and it can be consumed to form hydrocalumite and decreased the immobilization amount of SeO_3^{2-}/SeO_4^{2-}. (ii) The released concentration of Se was too low to contact ZVI to precipitate. (iii) Due to the relatively higher E^0 value of Cr(VI)/Cr(III) than Se(IV)/Se(0), it seems the ZVI surface was consumed by Cr(VI) reduction. (iv) The E^0 value of Se(IV)/Se(0) makes the reduction reaction of Se(IV) to be Se(0) is unpreferable in the presence of Cr(VI) and As(V) depending on the results.
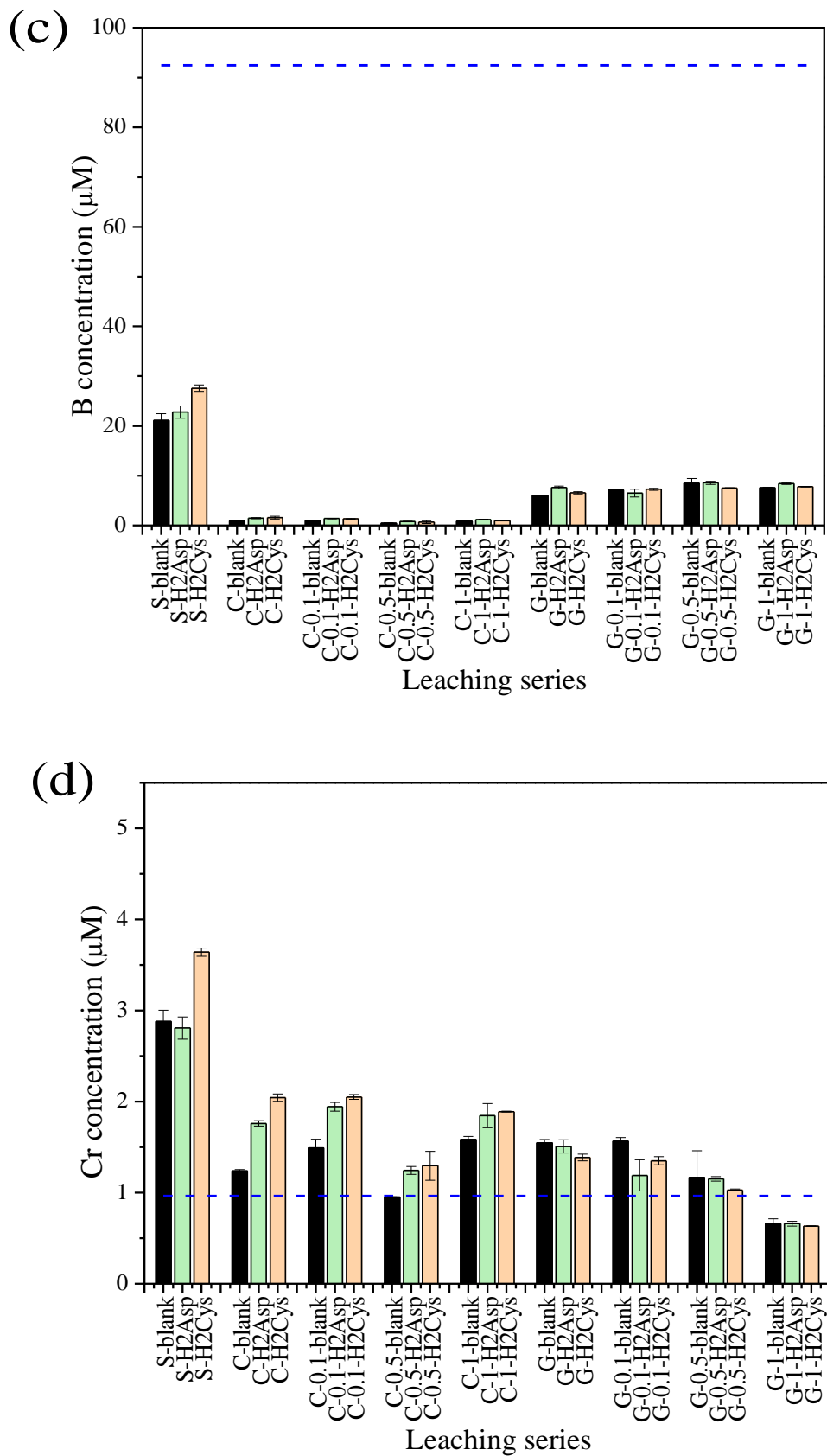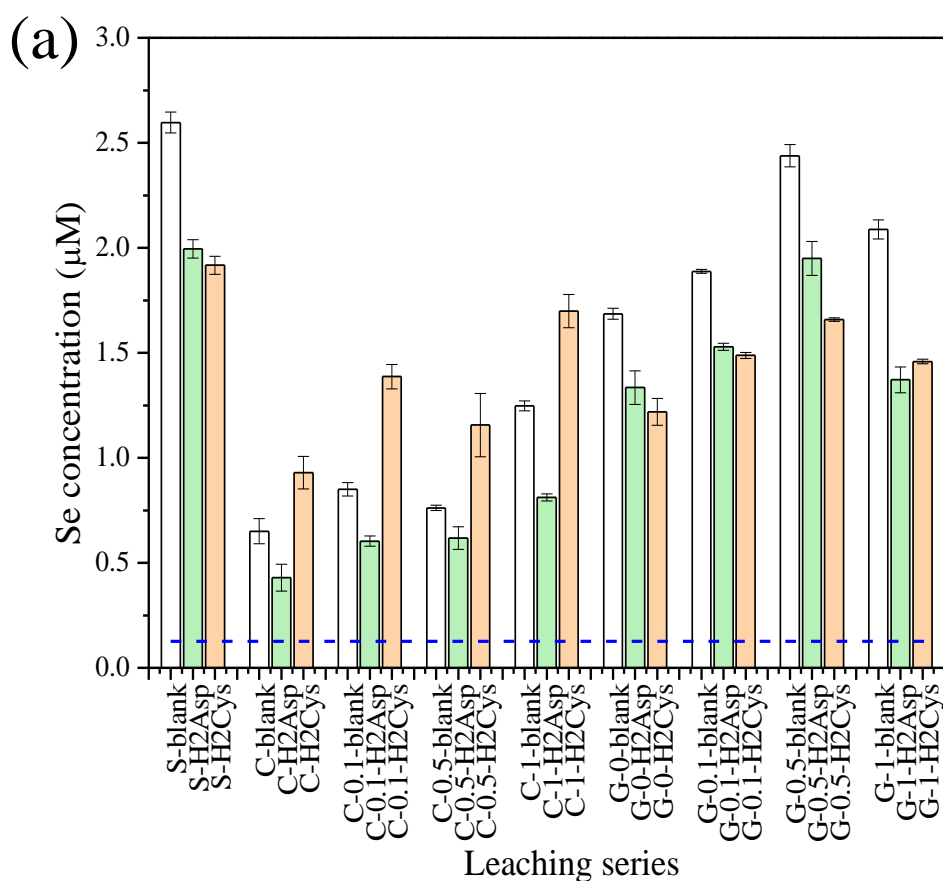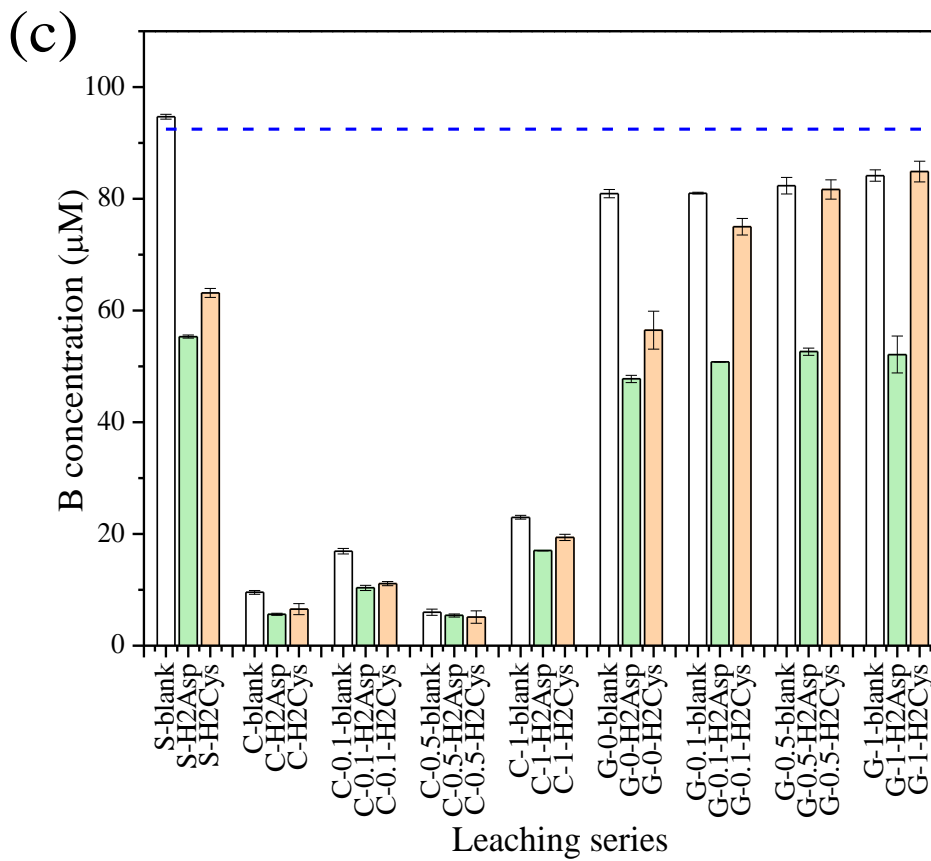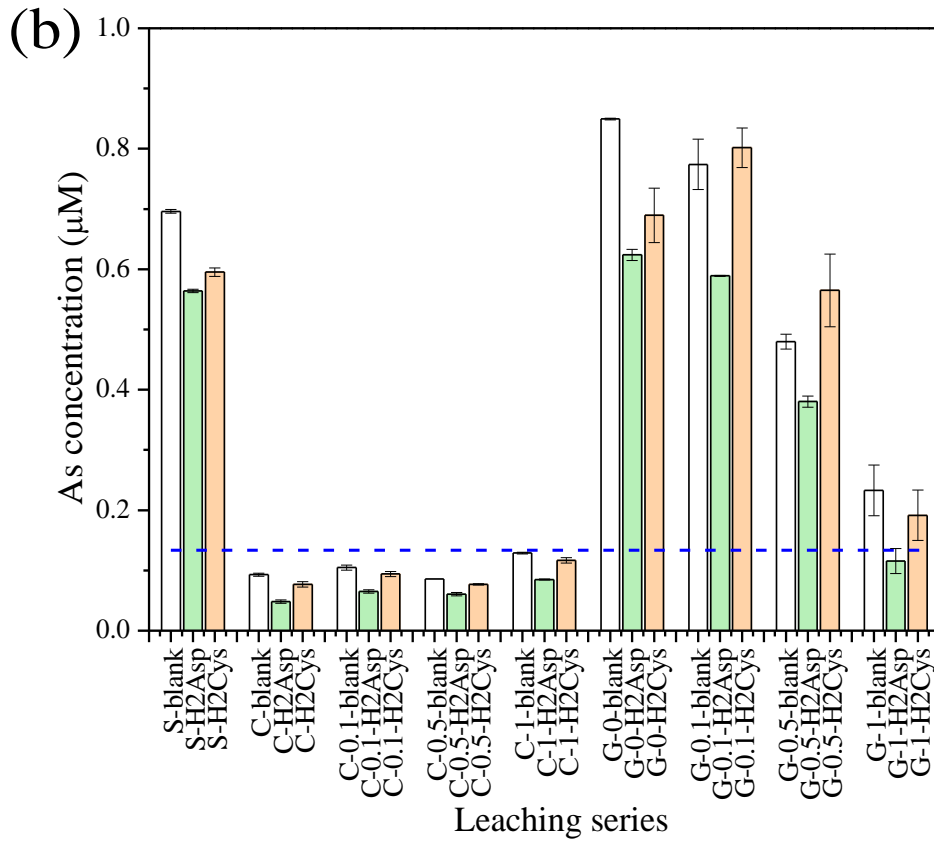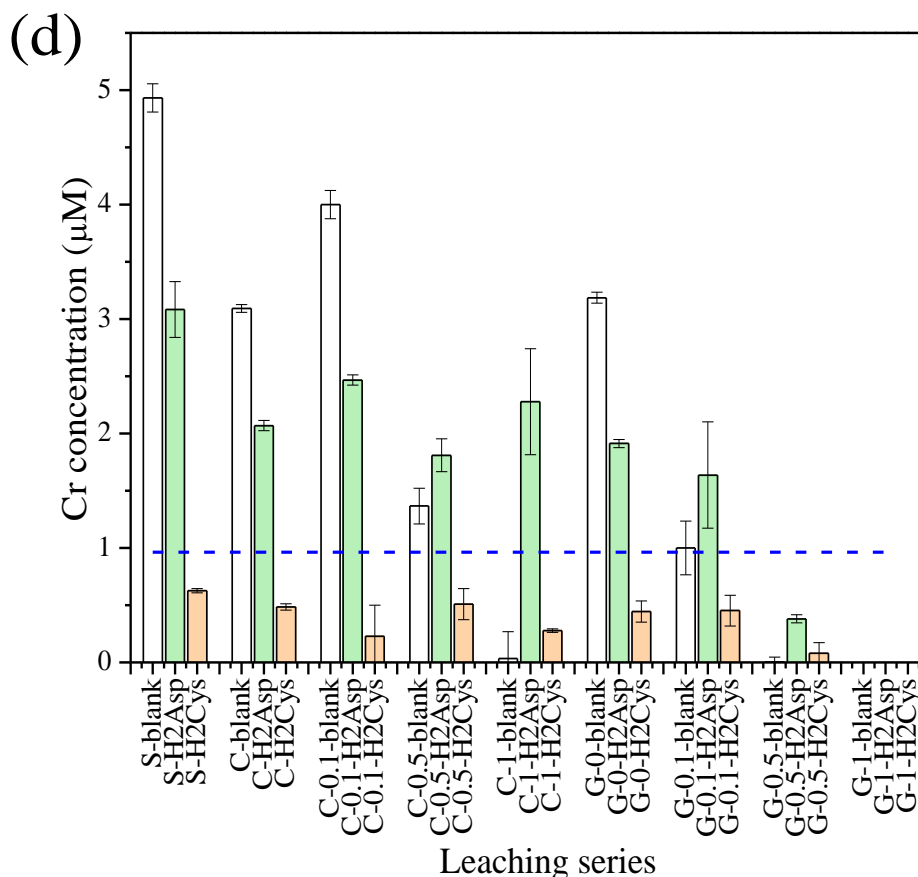
Fig. 7.6 Leaching results of (a) Se, (b) As, (c) B, and (d) Cr from ground cement powder with

the addition of ZVI under pH 4.7.

Therefore, suggestions to improve the immobilization of Se in cement systems can be proposed. In the cement systems, selenium-containing waste might be more effective immobilized with the addition of ZVI than several types of anionic species co-existed wastes, like chromium. However, in the solid waste where chromium and arsenic ions coexist, the E^0 of Se(VI)/Se(0) is higher than Se(IV)/Se(0) indicating Se(VI) is more easily to be reduced than Se(IV) (Sasaki et al., 2008; Sasaki et al., 2008), hence, the oxidant can be used to transfer Se(IV) to be Se(VI) before added ZVI. Furthermore, from the point of view of ZVI, an excessive amount of it can be added but the compressive strength of cement blocks should be paying attention to.

7.4 Conclusions

In the present work, the effects of ZVI on the leaching behavior of Se, As, B, and Cr from fly ash blended cement blocks after added lime and gypsum additives were explored using TCLP tests under the condition of with and without amino acids. The leaching of Se, As, B, and Cr were decreased as the pH increased from 4.7 to 12.0. After added lime and gypsum, the leaching of Se, As, B, Cr were decreased to some extent. In this work, the reduction of Se(IV) to be Se(0) seemed not to happen due to its relatively lower E^0 values. However, ZVI reduced the leaching amount of Cr and As through oxidation reaction, but it seems to be dependent on the releasing amount of anionic species to provided ZVI surface for reduction. Under pH 12.0, H₂Asp and H₂Cys enhanced the releasing of Se from ground cement powder through ion-exchanging, however, under pH 4.7, they suppressed the releasing of Se, As, B, and Cr by surface adsorption and H₂Cys oxidation. The immobilizing effects of ZVI might be more obvious when the releasing amount of Se is enough high, the existing species of Se is almost Se(VI), or in the absence or trace amount of Cr(VI) in the system.

References

Baur, I., Johnson, C.A., 2003. The solubility of selenate-AFt ($3CaO \cdot Al_2O_3 \cdot 3CaSeO_4 \cdot 37.5 \ H_2O$) and selenate-AFm ($3CaO \cdot Al_2O_3 \cdot CaSeO_4 \cdot xH_2O$). Cem. Concr. Res. 33, 1741-1748.

Bonhoure, I., Baur, I., Wieland, E., Johnson, C.A., Scheidegger, A.M., 2006. Uptake of Se (IV/VI) oxyanions by hardened cement paste and cement minerals: An X-ray absorption spectroscopy study. Cem. Concr. Res. 36, 91-98.

Cao, J., Zhang, W., 2006. Stabilization of chromium ore processing residue (COPR) with nanoscale iron particles. J. Hazard. Mater. 132, 213-219.

Fan, C., Wang, B., Zhang, T., 2018. Review on cement stabilization/solidification of municipal solid waste incineration fly ash. Adv. Mater. Sci. Eng.

Fiúza, A., Silva, A., Carvalho, G., António, V., Delerue-Matos, C., 2010. Heterogeneous kinetics of the reduction of chromium (VI) by elemental iron. J. Hazard. Mater. 175, 1042-1047.

Guo, B., Nakama, S., Tian, Q., Pahlevi, N.D., Hu, Z., Sasaki, K., 2019. Suppression processes of anionic pollutants released from fly ash by various Ca additives. J. Hazard. Mater. 371, 474-483.

Guo, X., Yang, Z., Dong, H., Guan, X., Ren, Q., Lv, X., Jin, X., 2016. Simple combination of oxidants with zero-valent-iron (ZVI) achieved very rapid and highly efficient removal of heavy metals from water. Water. Res. 88, 671-680.

Maaouia, O.B., Hamzaoui, R., Bennabi, A., Colin, J., Colina, H., 2018. Chromium stabilization and trapping in the cement matrix of recycled concrete aggregates. Constr. Build. Mater. 191, 667-678.

Mončeková, M., Novotný, R., Koplík, J., Kalina, L., Bílek, V., Šoukal, F., 2016. Hexavalent chromium reduction by ferrous sulphate heptahydrate addition into the Portland clinker. Procedia. Eng. 151, 73-79.

Rai, D., Sass, B.M., Moore, D.A., 1987. Chromium (III) hydrolysis constants and solubility of chromium (III) hydroxide. Inorg. Chem. 26, 345-349.

Sasaki, K., Blowes, D.W., Ptacek, C.J., 2008. Spectroscopic study of precipitates formed during removal of selenium from mine drainage spiked with selenate using permeable reactive materials. Geochem. J. 42, 283-294.

Sasaki, K., Blowes, D.W., Ptacek, C.J., Gould, W.D., 2008. Immobilization of Se (VI) in mine drainage by permeable reactive barriers: column performance. Appl. Geochem. 23, 1012-1022.

Sasaki, K., Nakama, S., Tian, Q., Guo, B., Wang, M., Takagi, R., Takahashi, T., 2021. Elution characteristics of undesirable anionic species from fly ash blended cement in different aqueous solutions. J. Environ. Chem. Eng. 9, 105171.

Triszcz, J.M., Porta, A., Einschlag, F.S.G., 2009. Effect of operating conditions on iron corrosion rates in zero-valent iron systems for arsenic removal. Chem. Eng. J. 150, 431-439.

Wang, L., Cho, D., Tsang, D.C., Cao, X., Hou, D., Shen, Z., Alessi, D.S., Ok, Y.S., Poon, C.S., 2019. Green remediation of As and Pb contaminated soil using cement-free clay-based stabilization/solidification. Environ. Int. 126, 336-345.

Zhang, M., Yang, C., Zhang, Z., Zhu, X., Huang, W., Zhao, M., Yang, K., Yu, L., 2020. Understanding the binding and leaching of Cr (VI) in calcium aluminate cement based solidified/stabilized pastes. Constr. Build. Mater. 262, 120040.

Zhang, W., Oswal, H., Renew, J.E., Gallagher, B., Ellison, K., Huang, C., 2020. Solidification/stabilization of flue gas desulfurization brine and coal fly ash for heavy metals and chloride immobilization: Effects of S/S conditions and zero-valent-iron pretreatment. J. Hazard. Mater. 384, 121463.

Zhang, Y., Amrhein, C., Frankenberger Jr, W.T., 2005. Effect of arsenate and molybdate on removal of selenate from an aqueous solution by zero-valent iron. Sci. Total Environ. 350, 1-11.

Chapter 8 Conclusions

^{79}Se and ^{129}I as radioactive isotopes with 3.77×10^5 years and 1.57×10^7 years half-life, which as low-level radioactive nuclides have been explored for their environmental behavior in the pedosphere. Their anionic species of SeO_4^{2-} and I^- have high mobility in the soil environment and are difficult to be adsorbed using natural minerals. Based on cementitious materials for the safe disposal of low-level radioactive wastes which contain low-level radionuclides and then be buried in the shallow underground zone, LDHs have been widely studied for their immobilizing ability of SeO_4^{2-} and I^-. LDHs have been confirmed that they play an important role in the adsorption of radioactive oxyanions in cement systems. However, only a few studies have been conducted on their stability when they are exposed to environmental SOM. Thus, in this thesis, we chose five different types of amino acids to represent a SOM model to investigate the stability of LDHs after immobilized SeO_4^{2-} and I^-. To clarify the environmental behavior of amino acids in LDHs, DFT simulation was combined using Gly^-, Asp^{2-}, and Cys^{2-} as models.

In **Chapter 1**, at first, the low-level radionuclides wastes, SOM information, and ^{79}Se and ^{129}I species were illustrated. Then, the basic information of LDHs for removing anionic species of radionuclides and the existing problems were shown. Finally, DFT simulation was introduced for calculating the ion-exchange energies to support the experimental results, and also simulated the possible interactions between SeO_4^{2-}, CO_3^{2-}, amino acids ions and LDHs metallic layers.

The used solution analysis methods, solid characterization methods, and related DFT simulation methods were shown in **Chapter 2**, including ICP-OES, ICP-MS, IC, HPLC, XRD, SEM, CHN.

In **Chapter 3**, the simple dissolution of Ca_2Al-LDH(I) happened immediately even though under pH 12. After suspended into amino acids solutions, the main factors to cause the release of I^- are divided into ion-exchange and simple dissolution. Amino acids of H_2Cys and H_2Asp existed in the form of Cys^{2-} and Asp^{2-}, which accelerated the releasing rate of I^- through ion-exchange with I^-. In XRD, the expanded d_{003} spacings were observed, which was different from the other

three amino acids. However, the effects of Cys^{2-} and Asp^{2-} on the ion-exchange with I^- in hydrocalumite and the stability of I-hydrocalumite were different. Asp^{2-} maintained the structure of I-hydrocalumite for a longer time than Cys^{2-}, and Cys-intercalated hydrocalumite showed one smaller d_{003} spacing than Asp-intercalated hydrocalumite in XRD patterns. This was also verified by DFT simulation. DFT simulation also confirmed that the interlayer spacings might be strongly influenced by the presence of water molecules and the numbers. There are interaction forces between amino acids and hydrocalumite in which the hydrogen and Ca-O bonds contributed to their configurations but the Asp/Cys-hydrocalumite system still is unstable. In the presence of HGly, HTrp, and HPhe, the simple dissolution and ion-exchange with OH^- contributed to I-hydrocalumite decomposition, and HPhe showed a little bit inhibitory effects on the release of I^- by surface adsorption. Analogically based, some organic matters negatively charged with a large molecule and less affinity than I^- might make hydrocalumite stable. For iodine isotopes stabilization in cementitious materials, I-hydrocalumite may form but the stabilization is strongly influenced by the geochemical environment.

In **Chapter 4,** the released amount of SeO_4^{2-} from Mg_2Al-LDH(SeO_4) in the absence of amino acids corresponding to 15.6% of the initially existing SeO_4^{2-} in the solids. HGly, H_2Asp, and H_2Cys promoted the release of SeO_4^{2-} by ion-exchange and destabilization of LDH during the intercalation process of HGly, H_2Asp and H_2Cys. Through the intercalation, amino acids expanded the interlayer spacing of Mg_2Al-LDH(SeO_4) to 10.7-11.0 Å except for H_2Cys, but Mg_2Al-LDH(SeO_4) phase still is dominant. DFT simulation revealed that the singly stacked HGly was the most stable configuration and the layer spacing expansion of LDH was caused by the doubly stacked configuration of HGly molecule. The intercalated LDHs tend to be more stable with an increase in the number of hydrogen bonds between H atoms in metallic layers of LDH and O atoms in SeO_4^{2-} and/or -COOH groups in HGly. Notably, the dissolution of Mg^{2+} was suppressed by complexation with -SH, -COOH, and $-NH_3^+$ groups in H_2Cys which were verified by the

formation energy calculated from DFT. The strong affinity of Cys^{2-} with Mg^{2+} might contribute to destabilizing the surface structure of LDH releasing not only $Al(OH)_4^-$ but also SeO_4^{2-}. This study indicates potential limitations to the stability of low-level radioactive wastes of ^{79}Se in repositories which are affected by smaller molecules of amino acids released through degradation of organic matters in the pedosphere.

In **Chapter 5,** without amino acids, the released concentration of SeO_4^{2-} from Ca_2Al-LDH was 0.44 mM corresponding to 48.3% of the initially existing SeO_4^{2-}, however, the layer spacing of Ca_2Al-LDH was expanded, because of hydration of SeO_4^{2-}. Almost no intercalation of HPhe and HTrp happened with Ca_2Al-LDH even though at a high concentration of 5 mM due to their large molecular size and more hydrophobic property. HGly, H_2Asp, and H_2Cys enhanced the release of SeO_4^{2-} from Ca_2Al-LDH, reached 73.8 % at the maximum by ion-exchange with SeO_4^{2-} as well as simple dissolution. The 003 reflections of XRD patterns for Ca_2Al-LDH after reacted with HGly, H_2Asp, and H_2Cys were analyzed by peak separation into four components. With an increase in sorption densities of amino acids, the relative intensities of d_{003} at large diffraction angles increased. H_2Cys series showed a different trend from HGly and H_2Asp series. Combining with DFT simulation, peak assignment of Ca_2Al-LDH(amino acid) with $d_{003} = 7.83$ Å, Ca_2Al-LDH(amino acid, CO_3) with $d_{003} = 7.70$ Å were determined. The amino acids molecules are predicted to stabilize in the horizontal orientation in Ca_2Al-LDH interlayer through the formation of Ca-O and hydrogen bond between amino acids and hydroxide layer $[Ca_2Al(OH)_6]^+$. The intercalation of CO_3^{2-} might also contribute to the release of SeO_4^{2-} through ion-exchanging. But the presence of H_2Asp facilitated the substitution between them and was prone to more stably co-exist with CO_3^{2-} than H_2Cys, supported by DFT prediction. Therefore, in the real environmental systems, two negative charges and/or relatively smaller molecular amino acids like HGly, H_2Asp, and H_2Cys might have a threat to the stability of SeO_4^{2-} in hydrocalumite and during their intercalation process some competitive ions like CO_3^{2-} might be induced.

In **Chapter 6**, the real cement blocks were considered in this section. Based on the TCLP leaching tests, the leaching of SeO_3^{2-}, AsO_4^{3-}, $B(OH)_4^-$, and CrO_4^{2-} from fly ash blended cement blocks powder were decreased to some extent after added Ca additives. In S, C40, G40, and M40 series, the leaching of SeO_3^{2-}, AsO_4^{3-}, $B(OH)_4^-$, and CrO_4^{2-} were decreased as the pH increased from 4.7 to 12.0. However, the release of Se in all series was higher than the criteria value due to its higher mobility even though under pH 12.0. In the presence of amino acids, under pH 4.7, H_2Asp increased the leaching of Se, As, Cr in all of series, while through oxidation, the two H_2Cys molecules formed disulfide bond (S-S) to produce cystine molecules. During this process, the reduction of selenite (SeO_3^{2-})/selenate (SeO_4^{2-}) happened, but it seems the higher releasing concentration made the reduction happen more easily. Under pH 12.0, H_2Asp and H_2Cys enhanced the releasing of Se from cement blocks, whereas HGly, HPhe, and HTrp suppressed its leaching but still over the MCL. The dissociation forms of Asp^{2-} and Cys^{2-} substituted the SeO_3^{2-} from hydrocalumite interlayer by ion-exchanging. While Gly^-, Phe^-, and Trp^- with one negative charge in each molecule just happened surface adsorption which weakens the simple dissolution of ettringite and hydrocalumite. Therefore, environmental conditions such as pH, decide the effects of amino acids on the leaching behavior of anionic species from cement blocks and the necessary methods should be developed to improve selenium immobilization.

Therefore, in **Chapter 7,** the effects of ZVI on the leaching behavior of SeO_3^{2-}, AsO_4^{3-}, $B(OH)_4^-$, and CrO_4^{2-} from fly ash blended cement blocks after added lime and gypsum additives were explored using TCLP tests under the condition of with and without amino acids. As observed in **Chapter 6**, lime and gypsum play an important inhibition role in the anionic species leaching from fly ash blended cement blocks through enhancing the formation of ettringite and hydrocalumite. Also, the leaching of Se, As, B, Cr were decreased as the pH increased from 4.7 to 12.0. After added different amounts of ZVI, it seems not to cause the reduction of Se(IV) to be Se(0) due to its relatively lower E^0 value. It was possible that the ZVI surface was consumed by the Cr(VI)

161

reduction reaction and was not available for other elements, furthermore, the E^0 of Se(IV)/Se(0) is too low to happen reduction in the presence of Cr(VI) and As(V). Also, it seems the released concentration of Se was too low to contact ZVI. When the releasing amount of Se is sufficiently high or the existing species is almost in Se(VI), the immobilization effects of ZVI may be more obvious. Therefore, on the one hand, selenium-containing waste might be more effective immobilized with the addition of ZVI than several types of anionic species co-existed wastes, like chromium, arsenic. On the other hand, the oxidant can be used to transfer Se(IV) to be Se(VI) before added ZVI.

In **Chapter 8,** the main conclusions of this work were summarized. Amino acids have been confirmed the different roles on the stability of LDHs after immobilized SeO_4^{2-} and I^-. Comprehensively, "reactive" amino acids like HGly, H_2Asp, and H_2Cys enhanced the release of I^- from hydrocalumite, SeO_4^{2-} from Mg_2Al-LDH and Ca_2Al-LDH by destabilization of hydroxide layers and ion-exchange in the interlayer. DFT simulation confirmed the intercalation of amino acids by calculating the ion-exchange energies and provided the possible configurations of them between host layers of LDHs. Also, the stability of each system was explored by calculating the formation energies. In addition, the TCLP leaching tests of fly ash blended cement blocks in application scale confirmed the influence behavior of amino acids. This work raises important environmental questions regarding the transportation and immobilization of anionic species of low-level radionuclide wastes in repositories, where anionic amino acids of smaller molecular size can potentially intercalate. Engineering countermeasures are necessary to stabilize iodine and selenium using, for example, barriers such as iron minerals, especially when the concentration of selenium is relatively high in radioactive wastes. Some inhibitors like, ZVI, can be used in the cement systems for suppressing anionic species leaching. But effectiveness can be influenced by the co-existing ions and the Se leaching amount which could raise more thinking about the engineering application of ZVI in low-level radioactive wastes systems.

Acknowledgments

My deepest gratitude goes first and foremost to my respectable supervisor, Prof. Keiko Sasaki, for her constant encouragement, high standard requirements, guidance, kindness, and support. One quote from Yu Han in Tang Dynasty: the progress of studies comes from hard work and is retarded by frivolities, doing a good job lies in thinking over, and destroyed by random. From Sasaki Sensei's rigorous scientific research attitude and behavior, I better understand the meaning of this sentence. She always guided me with practical academic advice and feasible instructions and enlightened me during the doctoral period. At the beginning of my doctoral period, the failed experiments always made me disappointed, but she always helped me to analyze the cause to find the solution, further, her words of encouragement always regained my confidence. She has offered me lots of valuable suggestions in my academic studies, and her insightful ideas and meaningful inspirations have benefited me a lot. Her incisive comments and constructive criticisms have greatly contributed to the completion of this thesis. Without her strong support, this thesis cannot have reached its present form.

I am also grateful to Prof. Kazuya Idemitsu (Department of Applied Quantum Physics and Nuclear Engineering), Prof. Takeshi Tsuji (Department of Earth Resources Engineering), and Associate Prof. Hirofumi Akamatsu (Department of Applied Chemistry) who belong to my thesis defense committee. Also, my thanks to Prof. Ismaila Dabo (Department of Materials Science and Engineering, The Pennsylvania State University) who given a lot of discussions for DFT simulations. Their insightful criticisms and suggestions on my dissertation greatly help me to improve this work. Here, I want to express my thanks to Associate Prof. Hirofumi Akamatsu. He has made a lot of help to the work of DFT simulation and discussed with me so many times with great patience and kindness, which have a positive impact on my attitude toward scientific research.

Then, I would like to express my appreciation to Prof. Tsuyoshi Hirajima, Assoc. Prof. Naoko Okibe, Assoc. Prof. Hajime Miki, and Assistant Prof. Moriyasu Nonaka, who always give me kind

helps in my academic research. Also, I would like to express thanks to Ms. Makiko Semba who invariably edits and files many kinds of documents for us silently.

In our laboratory, as a Ph.D. candidate, I spent the majority of my time with other members of the Mineral Processing, Recycling and Environmental Remediation laboratory, and I received enormous help from them. I would like to express my most sincere thanks to them and list their names as bellows: Dr. Binglin Guo, Dr. Quanzhi Tian, Dr. Kojo Twum Konadu, Dr. Chitiphon Chuaicham, Dr. Gde Pandhe Wisnu Suyantara, Dr. Santisak Kitjanukit, Dr. Pawar Radheshyam Rama, Dr. Balakumar Vellaichamy, Dr. Keishi Oyama, Dr. Karthikeyan Sekar, Li Zhang, Diego Moizes Mendoza Flores, Ryoutaro Sakai, Kohei, Nonaka, Yu Tanaka, Cindy, Kaito Hayashi, Yuki Semoto, Masaya Fujita, Shingo Nakama, Shunsuke Imamura, Ryohei Nishi, Haruki Noguchi, Tsubasa Oji, Yuta Orii, Zenta Shirozu, Taiki Kondo, and Takumi Inoue. Thank you for sharing with me. Many thanks to Dr. Binglin Guo, Dr. Quanzhi Tian, and Dr. Kojo Twum Konadu they always give me help in the laboratory work.

Last but not least, I would like to appreciate the scholarship provided by China Scholarship Council (No.201806350035). Without the CSC scholarship, I cannot put all of my efforts into academic research. In addition, all of my academic works were supported by Prof. Keiko Sasaki by the Japan Society for the Promotion of Science (JSPS) KAKENHI (No. JP19H00883). I am very grateful for the opportunity to study for a Ph.D. degree at Kyushu University.

Finally, I appreciate my parents and brother for their understandable and spiritual support. I met so many problems in my Lab works, and some life confusion in Japan due to it is my first time to stay abroad and live alone. My parents always enlighten my thinking, reduce my anxiety and stress, and give me strong power to continue my study in Japan. I am also really thankful to my boyfriend Ph.D. candidate Xi Wang who gives me a lot of understanding and encouragement, sometimes accepts my negative emotions and complaints. We never thought of giving up on this road but keep walking side by side.